UNIVERSITÀ
DEGLI STUDI
DI PADOVA

Sede Amministrativa: Università degli Studi di Padova

Dipartimento Territorio e Sistemi Agro Forestali (TeSAF)

SCUOLA DI DOTTORATO IN:

TERRITORIO, AMBIENTE, RISORSE E SALUTE

Indirizzo: Idronomia Ambientale

Ciclo XXII°

Radar Hydrology and Flash Flood Event Analysis

Direttore della Scuola: Ch.mo Prof. Vasco Boatto

Coordinatore d'indirizzo: Ch.mo Prof. Mario Aristide Lenzi

Supervisore: Ch.mo Prof. Marco Borga

Dottorando: dott. Francesco Zanon

Contents

Introduction

A flash flood is a flood that follows the causative storm event in a short period of time. The term "flash" reflects a rapid response, with water levels in the drainage network reaching a crest within minutes to a few hours after the onset of the rain event, leaving extremely short time for warning [Creutin and Borga, 2003; Borga *et al.*, 2008]. Flash floods are localized phenomena that occur in watersheds of few hundred kilometres or less, with response times of a few hours or less [Creutin and Borga, 2003; O'Connor and Costa, 2004]. Such basins respond rapidly to intense rainfall because of steep slopes and impermeable surfaces, saturated soils, or because of human (i.e., urbanization) or fire-induced alterations to the natural drainage. Causative events are generally excessive storms, but can also be the sudden release of water impounded by a natural jam (i.e., formed by ice or rock, mud, and wood debris) or human-made dam or levee. This thesis focuses on flash flood events associated with heavy rainfall.

Europe experienced several catastrophic flash floods in the last decades. Data concerning a number of these floods occurred during the last 15 years have been reported in Marchi *et al.* (2010). Examination of these data and references therein shows that:

- Flash floods occur in any of the hydroclimatic regions of Europe, even though three regions appear to be characterized by high flash flood potential: Mediterranean, Alpine Mediterranean, and Inland Continental Europe;
- Heavy rainfall accumulation is a necessary but not sufficient condition for flash floods, since hydrology critically controls flash-flood-triggering. Without hydrological analysis, it is impossible to evaluate the flood potential of storms, particularly in the fringe of the flood/no flood threshold;
- Flash flood hazard is related to both stream response (flood) and landscape response (landslide and erosion). The intense erosion and solid transport associated with these extreme events add to the hazard and strongly influence the quality of soils, waters and ecosystems.

The twofold consequence of the above observations is that forecasting of flash-floods:

- Depends critically on meso-scale storm forecasting, with a specific attention to the processes leading to slow movement of the precipitation system;

- Necessitates real time hydrological modelling, with a specific attention to the runoff generation processes over a wide range of scales.

Although they are seldom all deployed at the same time, the technical requirements for a hydrometeorological flash flood forecasting system include:

- A numerical weather prediction (NWP) model, capable to provide short-range Quantitative Precipitation Forecasts (QPF);
- A remote sensing based (radar, satellites) precipitation detection system, for storm monitoring and for the possible initialization and conditioning of the NWP model, and
- A hydrological-hydraulic forecasting model, capable to forecast the stream response from the rain input.

These requirements are similar to those of more common riverine flood forecasting systems. However, some features characterise flash flood forecasting with respect to riverine flood forecasting and point out to their larger uncertainty. These are:

- The short lead time, which implies both the integration of meteorological and hydrologic forecast, and the difficulties of using data assimilation procedures based on real time observed discharges to reduce uncertainty in hydrologic predictions;
- The need to provide local forecasts, which means that, on one hand, the rainfall must be monitored and forecasted on a wide range of space/time scales, and, on the other hand, every tributary of a monitored basin can be considered as a potential target for flood warning.

Estimation of extreme rainfall rates by weather radar at the appropriate time and space scales is the cornerstone of flash flood analysis and forecasting. A large body of research work has greatly improved in the last two decades radar technology and algorithms for rain quantification. This work has shown that well maintained conventional radar systems can estimate rainfall at ground level provided that a number of precautions are taken, and in particular:

- The siting of the instrument and its scanning protocol must be carefully selected and analysed;
- The quality of the instrument must be routinely checked;
- The signal processing must take into account the physics of the instrument as well as the properties of the atmospheric and ground targets. A downstream control of the radar rainfall processing can rely on rain-gauge measurements at ground level using a variety of methods.

When these precautions are taken, different studies have shown that radar-based rainfall estimates are reliable and may be used as input in rainfall-runoff models for flood modelling and forecasting [Borga *et al.*, 2000; Delrieu *et al.*, 2005; Borga *et al.*, 2002]. These very positive results must not be hiding some weaknesses:

- Most of these results never had the opportunity to be *coherently validated over a significant number of flash floods events*. The use of *specific experiments* or of limited operational radar data sets is insufficient to test complex combinations of algorithms, especially if high rain intensities are of interest.
- Very few results have been *translated into operational hydrologic applications*.

This thesis aims to investigate the use of weather radar for the purpose of understanding the hydrometeorological mechanisms leading to flash floods, and then for flash flood forecasting.

The outline of the thesis work is as follows. Chapter 1 provides a literature review of the rainfall estimation by weather radar for flash flood-generating storms. Chapter 2 describes a number of procedures for the rainfall estimation at the ground during flash flood events in mountainous catchments. A metric for the analysis of the rainfall field spatial patterns is proposed in Chapter 3, in the context of the analysis of a number of Romenian flash floods. This metric is used for the analysis of two flash flood events, respectively occurred in 2003 in the Eastern Italian Alps (Chapter 4) and in Western Slovenia (Chapter 5). Major conclusions from the work are reported in Chapter 6.

Introduzione

Una piena improvvisa[1] è una piena che segue l'evento precipitativo che la ha causata entro un breve periodo di tempo. Il termine "improvvisa o flash" riflette una risposta rapida, con il picco di piena che si verifica nella rete di drenaggio nel volgere di alcuni minuti fino a poche ore dopo l'inizio dell'evento di pioggia. Questo fatto lascia intendere quanto poco tempo ci sia per l'allerta [Creutin and Borga, 2003; Borga *et al.*, 2008]. Questo tipo di bacini rispondo rapidamente ad una precipitazione intensa a causa di pendii ripidi e superfici impermeabili, terreni saturi, o a per fattori determinati dall'uomo (vedi per esempio l'urbanizzazione) o a causa di alterazioni del drenaggio naturale del terreno dovuto ad incendi. Gli eventi scatenanti le piene improvvise sono generalmente precipitazioni che portano all'eccesso di drenaggio, ma questo tipo di piene possono anche essere scatenate dal rilascio improvviso di acqua trattenuta da impedimenti naturali (per esempio formati da ghiaccio e roccia, fango e detriti di legno) o di tipo artificiale come dighe e argini. Questa tesi si concentra su eventi di piena improvvisa associati a precipitazioni intense.

L'Europa ha conosciuto diverse inondazioni catastrofiche negli ultimi decenni. I dati relativi un certo numero di queste inondazioni che si sono verificate nel corso degli ultimi 15 anni sono riportati da Marchi *et al.* (2010). Dall'analisi di questi dati e di queste fonti risulta che:

- Una piena improvvisa si può verificare in qualsivoglia regione idroclimatica dell'Europa, anche se tre regioni sembrano essere caratterizzate da una grande incidenza di di piene improvvise: l'area Mediterranea, quella Alpino-Mediterranea, e quella Continentale;

- Una gran quantità di pioggia accumulata è una condizione necessaria ma non sufficiente al verificarsi di una piena improvvisa, dal momento che l'idrologia controlla in modo decisivo l'innesco della piena improvvisa. Senza un'analisi di tipo idrologico, risulta impossibile valutare la probabilità che una data precipitazione scateni una piena, in praticolare in termini di una soglia oltre la quale si verifica la piena;

- La pericolosià delle piene improvvise è collegata sia alla risposta del fiume (la piena) che alla risposta del terreno (fenomeni di tipo franoso ed erosivo). L'intensa erosione ed il trasporto solido associati

[1] Flash flood, in inglese.

a questi fenomeni estremi si aggiungono alla pericolosità ed influenzano in modo significativo la qualità dei terreni, delle acque e degli ecosistemi.

La duplice conseguenza delle osservazioni appena fatte è che la previsione di piene improvvise:

- Dipende in modo determinante dalle previsioni delle precipitazioni che si sviluppano alla meso-scala, con una attenzione specifica ai processi che frenano la circolazione del sistema di precipitazione;
- Richiedone modelli idrologici che lavorino in tempo reale, con una particolare attenzione ai processi du generazione del deflusso a vasta scala.

Anche se raramente sono tutti utilizzati contemporaneamente, i requisiti tecnici per un sistema di previsione idrometeorologica per le piene improvvise comprendono:

- Un modello numerico di previsione (NWP[2]), in grado di fornire previsioni quantitative di pioggia a corto raggio (QPF[3]);
- Un sistema di rilevamento in remoto per la pioggia (radar, satellite), per il monitoriraggio dei fenomeni temporaleschi e la possibilie inizializzazione e condizionamento del modello NWP, e
- Un modello di previsione idrologico-idraulico, in grado di prevedere la risposta del corso d'acqua all'input pioggia.

Tali requisiti sono simili a quelli più comuni utilizzati per la previsione delle alluvioni dei sistemi fluviali. Tuttavia, alcuni elementi caratterizzano la previsione delle piene improvvise rispetto alla previsione delle alluvioni e ne sottolineano la grande incertezza. Questi sono:

- Il breve periodo durante il quale questi processi si sviluppano, che implica sia l'integrazione di un sistema di previsione di tipo meteorologico e idrologico, che la difficoltà nell'utilizzo di procedure di assimilazione di dati basate sull'osservazione in tempo reale delle portate al fine di ridurre l'incertezza nelle previsioni idrologiche;
- La necessità di fornire previsioni a scala locale, il che significa da una parte che la pioggia deve essere monitorata e prevista su una vasta scala spazio-temporale, all'altra che ciascun tributario del bacino monitorato può essere considerato come un bersaglio potenziale per un allarme di piena.

La stima di fenomeni precipitativi estremi tramite l'utilizzo del radar meteorologico alla appropriata scala spazio-temporale è una pietra miliare dell'analisi e della previsione delle piene improvvise. Una grande branca della ricerca in questo campo ha favorito un notevolmente migliorato, negli ultimi due decenni,

[2]Numerical Weather Prediction.
[3]Quantitative Precipitation Forecasts.

delle tecnologie radar e degli algoritmi per la stima di pioggia. Questo lavoro ha dimostrato che anche utilizzando sistemi radar convenzionali si possono ottenere stime di precipitaziona a livello del suolo, a condizione che vengono adottate una serie di precauzioni, in particolare:

- L'ubicazione dello strumento e del suo protocollo di scansione devono essere attentamente selezionati ed analizzati;
- La qualità dello strumento deve essere sottoposta a controlli ordinari;
- L'elaborazione del segnale deve tener conto della fisica dello strumento così come delle proprietà atmosferiche e dei bersagli di terra. Un controllo a valle del trattamento delle precipitazioni radar può essere fatto tramite misurazioni da pluviometro a livello del suolo utilizzando una varietà di metodi.

Quando si sono prese queste precauzioni, diversi studi hanno dimostrato che le stime di precipitazione basate su radar meteorologico sono affidabili e possono essere utilizzate come input di modelli afflusso-deflusso per la modellazione e la previsione delle piene [Borga *et al.*, 2000; Delrieu *et al.*, 2005; Borga *et al.*, 2002]. A fronte di questi risultati molto positivi non devono però essere nascosti alcuni punti deboli:

- La maggior parte di questi risultati non hanno mai la possibilità di essere *coerentemente convalidati su un numero significativo di eventi di piena improvvisa*. L'utilizzo di *esperimenti specifici* o di una banca dati limitata di dati radar è insufficiente a testare la combinazione complessa degli algoritmi utilizzati, specialmente se si è interessati ad intensità di pioggia elevata.
- Un numero molto limitato di risultati positivi è stato *tradotto in applicazioni idrologiche operative.*

Questa tesi si propone di esaminare l'uso del radar meteorologico ai fini della comprensione dei meccanismi idrometeorologici che portano alla formazione di piene improvvise, e quindi alla loro previsione.

L'organizzazione del lavoro di tesi è la seguente. Il Capitolo 1 fornisce una revisione della letteratura sul tema della stima di precipitazione tramite radar meteorologico per le precipitazioni che causano la formazione di piene improvvise. Il Capitolo 2 descrive una serie di procedure per la stima delle precipitazioni al suolo durante gli eventi di piena improvvisa in bacini montani. Una metrica per l'analisi spaziale del campo di pioggia viene proposta nel Capitolo 3, nel contesto dell'analisi di una serie di piene improvvise verificatesi in Romania. Questa metrica è utilizzata per l'analisi di due eventi di piena, accaduti rispettivamente nel 2003 nelle Alpi Italiane friulane e nella parte ovest della Slovenia (Capitolo 5). Le conclusioni principali del lavoro di tesi sono riportate nel Capitolo 6.

1. Literature review of the rainfall estimation problem in the context of extreme storms

Weather radar offers an unprecedented opportunity to improve our ability of observing extreme storms and quantifying their associated precipitation. These events trigger floods and flash-floods, debris flow, and landslides.

1.1 Limitation of raingauge sampling of flash flood triggering extreme storm events

Due to their characterising space and time scales, flash flood events are difficult to monitor. These events generally develop at space and time scales that conventional measurement networks of rain and river discharges are not able to sample effectively [Creutin and Borga, 2003] (see Table 1.1).

As these events are locally rare, they are also difficult to capture during classical fieldbased experimen-

Physiologic unit	**Minimum density per station [area in km^2 per station]**		
	Raingauge nonrecording	*Raingauge recording*	*Streamgauge recording*
Costal	900	9000	2750
Mountainous	250	2500	1000
Interior plains	575	5750	1875
Hilly-undulating	575	5750	1875
Small island	25	250	-
Urban areas		10-20	300
Polar-arid	10000	100000	20000

Table 1.1: Recommended raingauge and streamgauge density, WMO (1994).

tation, designed to last a few months over a given region, or on experimental catchments with drainage areas of a few km^2 . This explains why the investigation of flash flood events is by necessity event-based and opportunistic as opposed to driven by observations from carefully designed field campaigns. Post-event surveys play therefore a critical role in gathering essential observations concerning flash floods.

Traditionally, indirect peak discharge estimates and collection of rainfall maxima have been used to document these events, as well as to provide an answer to the questions that are invariably asked after a major flood: why did such a major flood occur? And how frequently might such a flood be expected to occur? Collection of these studies contributed to the establishment of regional peak discharges envelope curves and to the development of more understanding of regional behaviour of extreme floods. However, focusing just on peak discharges and point rainfall maxima alone provides limited insight into the hydrological controls of flash flood response.

Flash flood monitoring requires rainfall estimates at small spatial scales (1 km or finer) and short time scales (15-30 minutes, and even less in urban areas). These requirements are generally met by weather radar networks. This is shown schematically in Figure 1.1, which reports typical monitoring scales of weather radar systems and raingauge networks together with the time and space scales of a number of flash flood generating storms observed in Europe in the last 15 years [Borga *et al.*, 2008].

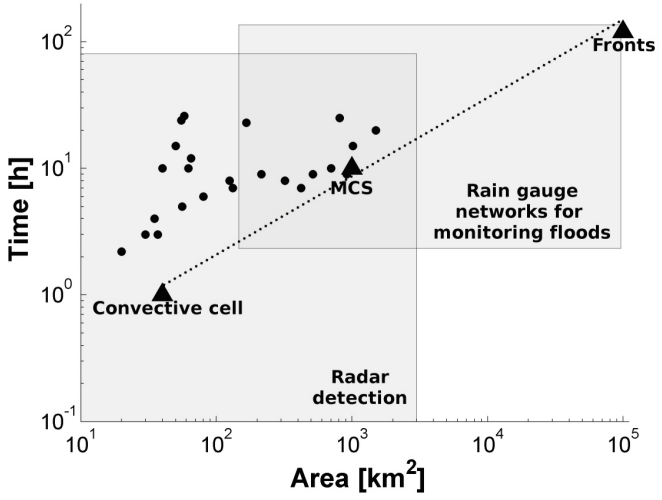

Figure 1.1: Schematic of flash-flood space-time scale versus monitoring capabilities of weather radar and raingauge networks. Dots represent time and space scales of a number of flash flood generating storms observed in Europe in the last 15 years Borga *et al.* (2008). Scales of convective cells, Mesoscale Convective Systems (MCS) and fronts are taken from Orlanski (1975).

Rapidly increasing availability of good quality weather radar observations is greatly expanding our ability to measure and monitor the rainfall distribution at the space and time scales which characterise the flash flood events [Borga *et al.*, 2007]. These technical advances have the potential to enhance the information content of post-event surveys. The awareness of this potential encourages the development of

a methodology for flash flood response survey which goes beyond the collection of indirect peak discharge estimates with the aim of rebuilding the flood time sequences (in term of local intense precipitations as well as of hydrograph peak in distributed cross section along river network) and of collecting observations about phenomena (i.e., debris flow, landslides, woody debris) related to the flood.

Whereas progress has been made in the last decade in the integration of meteorological forecasts and radar observations in flash flood surveillance, lack of observations hamper advances in understanding the hydrological processes at work during flash floods, and, consequently, in forecasting the stream response to extreme precipitations. Process understanding is required for flash flood forecasting, due to the fact that the small basins prone to flash-floods are rarely gauged and must be modelled without prior calibration. Furthermore, the dominant processes of runoff generation may change with the increase of storm severity, and therefore the understanding based on analysis of moderate flood events may be questioned when applied to forecast the response to extreme storms. In this sense, flash flood forecasting exemplifies the ungauged basin problem under extreme conditions.

Observational limitations mainly stem from the fact that flash floods develop at space and time scales that conventional observation systems of rain and river discharges are not able to monitor. Due to these limitations existing knowledge on flash flood events is relatively sparse. Improvement of understanding of rainfall-runoff dynamics during flash floods requires the development of an observational strategy capable to provide high-resolution data on storm and stream/landscape response during flash floods.

Hydrologic models are simplified, conceptual representations of a part of the hydrologic cycle; in particular they have as input rainfall data and as output discharge data. They are primarily used for hydrologic predictions and for understanding hydrologic processes. In the last decades several models with different complexity levels have been developed for different aims. Models are generally divided in two conceptual steps: the first is the rainfall-runoff generation and the second is water transport (on the surface and in the ground). Each step may be lumped (averaged answer of the watershed) or distributed (computed in each cell with a certain resolution, in witch the basin is divided) and have coarser of finer assumptions. More complex models are theoretically closer to reality, but they need a greater number of calibration parameters, that means heavier terrain surveys and longer series of hydrological data [Sivapalan, 2006].

Flood modelling requires knowledge about terrain features and initial moisture conditions. These two aspects are crucial to simulate a correct runoff generation dynamic, but often in flash flood cases, it is not easy to collect this kind of data. Detailed soil classification requires long time, hence uncertainties and lack of time imposes to use a simple sorting based on land use maps. In addition, a solid scientific modelling should compare simulations of different floods in the same basin using the same calibration parameters. For flash floods it is uncommon to have significant historical flood data beside the analyzed case and therefore the only solution is to calibrate the model at the event scale.

The choice of a distributed input is needed for the high spatial gradient of rainfall fields during flash flood events.

1.2 Temporal and spatial scales of urban catchments

A catchment can be seen as a low pass filter which integrates a main input (rainfall) and produces a time series output (discharge). The characteristic time associated to such a filter defines its temporal dynamics. This temporal scale determines the minimum time resolution needed for the input signal to avoid smoothing the filter response

$$\Delta t = \frac{t_c}{4} \tag{1.1}$$

where Δt is the time resolution and t_c, the characteristic time of the system. The factor 4 is an order of magnitude and it depends on the catchment studied and the wished accuracy [Schilling, 1991].

For hydrological applications, the temporal and spatial resolution of rainfall measurements depends on the catchment to be studied. First, a catchment imposes the minimum temporal resolution necessary to correctly reproduce its dynamics. A relation between the surface of the catchment and its characteristic temporal scale has been estimated by Berne *et al.* (2004). Therefore we have a relation between the size of the catchment (surface S in ha) and the temporal resolution required (Δt in min):

$$\Delta t = 0.75 S^{0.3} \tag{1.2}$$

Also the spatial scale of rainfall has been linked to the temporal resolution for Mediterranean climate. [Berne *et al.*, 2004] investigated the spatial structure of rainfall using spatial climatological variograms derived from a band X radar (in RHI mode, see sec. 1.3) and the rain gauge measurements. It can be noticed that the evolution of the range is consistent between the two different types of sensor (radar and rain gauge). The simple relation:

$$r = 4.5\sqrt{\Delta t} \tag{1.3}$$

fits correctly the data.

Although the range is relevant to describe the spatial structure, it does not represent the domain over which a point value is representative of the average. Since the variogram increases symmetrically but rather quickly from the pivot point, a diameter of $r/3$ (where r is the range) can be retained for the

spatial resolution. Journel and Huijbregts (1978) calculated the variance of the error when estimating the mean value over a square (which size is function of the range) knowing only the central point value and using a spherical model. It is of 0.13 for a size of $r/3$ which means 87% of the information is captured (this value is lower when the nugget effect is positive). Using Eq. 1.3, it finally leads to a relation between the temporal and the spatial resolution of rainfall measurement required for urban hydrology:

$$r = 1.5\sqrt{\Delta t} \tag{1.4}$$

For a given catchment surface, the temporal resolution is directly proportional to the ratio between the temporal resolution Δt and the characteristic time t_c. For a given catchment surface and a given ratio $\Delta t/t_c$, the spatial resolution is directly proportional to the ratio between the spatial resolution Δr and the range of the variogram r. Because the exponent is lower than 1 in Eq. 1.4, the ratio $\Delta r/r$ has a more significant influence on the estimation of the spatial resolution than the ratio $\Delta t/t_c$ (for $\Delta t > 1$ min).

If rainfall is measured by a rain gauge network, the spatial resolution corresponds to the mean interdistance between two gauges. A representative surface (S_r) can be associated to one rain gauge. Considering the disc which radius is half of the spatial resolution, it comes for the representative surface

$$S_r = \pi \left[\frac{\Delta r}{2}\right]^2 \tag{1.5}$$

on which the rainfall is relatively homogeneous at the considered time step. Then it is interesting to compare the representative surface S_r and the catchment surface S. Three cases are possible:

1. $S_r > S$: the rainfall field is homogeneous over a surface larger than the catchment surface. A lumped modelling approach is relevant (from the rain input point of view) and the mean rain depth over the catchment can be used as input for hydrological models. Rain measurements at the catchment scale are not required because information can be deduced from outside of the catchment. For example one rain gauge close enough (in a way that the catchment is embedded in S_r) is sufficient;

2. $S_r \sim S$: the rainfall field is homogeneous over a surface similar to the catchment one. A lumped modelling approach is still relevant and the mean rain depth over the entire catchment can still be used as input for hydrological applications. However, rain measurements at the catchment scale are required. For example, at least one rain gauge (with a "central" location in the catchment) is needed;

3. $S_r < S$: the rainfall field is homogeneous over a surface smaller than the catchment one. A lumped modelling approach is no more relevant and the rain depth must be spatially distributed. Rain

measurements at a smaller scale than the catchment one are required. For example several rain gauges must be deployed within the catchment.

So using Eq. 1.5, it is possible to calculate the spatial resolution corresponding to an existing rain gauge network.

1.3 Weather radar fundamental

RADAR is an acronym of RAdio Detection and Ranging and it is essentially a tool able to generate and detect electromagnetic waves that are reflected by objects hit by the radar beam. After World War II radarmeteorology had an intense impulse due to the surplus of war radar working at frequencies adequate to detect rain drops in the atmosphere. Several researchers realized that radars are able to describe meteorological features with spatial and temporal scales much more fine-grained than any other tool. Since late 50's radars have been used to follow convective cell systems and cyclones evolution and, in some counties, they have been employed to alert authorities and population. With computer evolution in the 70's radar potential were amplified by the possibility of storing and elaborating great amount of data.

Weather radar antennae, used for specific meteorological objectives, have a circular-parabolic shape that permit to direct the radar signal to a specific direction. Radars are able to move in two orthogonal directions: azimuthally and vertically. Consequently, different ways to detect atmospheric conditions are possible (see Figure 1.2).

- PPI (Plan Position indicator) when elevation angle is constant and radar can rotate around its vertical axis; this procedure allows to screen a conical area that is then projected in a horizontal plane;
- RHI (Range Height Indicator) when azimuth direction is constant and detection is limited to a vertical profile;
- CAPPI (Constant Altitude Plan Position Indicator) is a complex procedure that allows to map the atmosphere at a constant plane level; this result is possible when the entire volume is already scanned, and therefore only in a post analysis phase, while the other procedures can be obtained in nowcasting.

Electromagnetic waves interact with objects when their length is comparable with object dimension. Wavelength is tied to frequency so that the product of the two values give the propagation velocity ($c=3\times10^8$ m s^{-1}). The ideal wavelength for rainfall detection is a compromise between rainfall drop size (up to few millimetres) and the will to minimizes attenuation process (due to interaction with rainfall and other particles), so that weather radars usually work in microwaves range in X, C and S bands (see Table 1.2). X band radars have the advantages that they need quite small antenna so that they

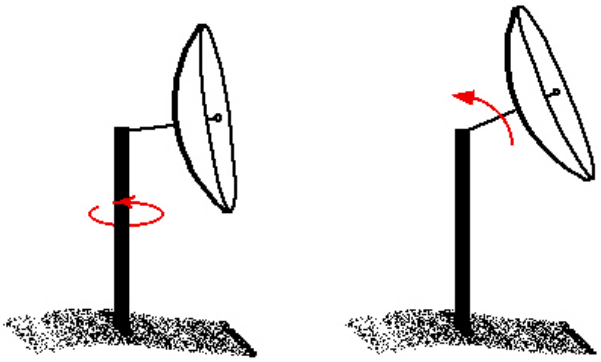

(a) (b)

Figure 1.2: Representation of the two radar working procedure: a) PPI and b) RHI

Band	Frequency [GHz]	Wavelength [cm]
L	1-2	30-15
S	2-4	15-8
C	4-8	8-4
X	8-12	4-2.5

Table 1.2: Typical wavelengths and frequencies for weather radar.

are quite cheep to build and they can be located in mobile structures; on the other hand short X band microwaves actively interact with atmospheric particles and are affected by strong attenuation so that these tools work well only in a 50 km range. On the other extreme S band antennae need big structures, they are more expensive, but less affected by attenuation, since they work with longer wavelengths, and they are able to give information about rainfall spatial distribution up to 200 km. C band radars behave in an intermediate way and are the most common tools used by public administration and are able to provide good precipitation estimation in a 120 km range.

When a radar beam hits an object along its propagation path, the electromagnetic wave is scattered so part of its energy returns back to the receiver. This back-scattering radiation has much less power than the transmitted one, and the total power return signal increases with the number of the detected objects and with their dimension. The double of the distance (direct and return paths) of the hit object is obtained by multiplying velocity c by the time that the signal needs to arrive back to the receiver. Spatial resolution depends on beam wideness, object distance and impulse duration: typical values of 1 μs leads to 150 m length resolution; a beam 0.2° wide means 350 m at 100 km distance. Temporal resolution depends on the antenna rotation velocity and it is generally around few minutes. Whether radar theory is based on the assumption that most of the scattering in the atmosphere is due to raindrops so the power of the return signal is an indicator of rainfall intensity.

The power of the return signal P_r is measured by the receiver and converted in the reflectivity Z according to equation 1.6 on the following page, where C depends on radar proprieties (i.e., power, wavelength) and it is constant, r is the distance from the radar to the targets (i.e., rainfall drops) while k is the imaginary part of the refraction index and depends on target surface: $|\kappa|^2$ is about 0.93 for rainfall drops at 0° C and 0.176 for ice particles.

$$Z = \frac{P_r r^2}{C|\kappa|^2} \tag{1.6}$$

Electromagnetic scattering has been studied exhaustively by Mie, but in the case in witch the dimension of the targets D is smaller that the wavelength (specifically D<0.16 λ), as for whether radar, Rayleigh simplifications (early 1900) are used. These lead to the reflectivity dependency on the drop size distribution $N(D)$ as:

$$Z = \int_0^\infty D^6 N(D) dD \tag{1.7}$$

This last equation shows that reflectivity is very sensible to the dimension of the raindrops, since there is a 6 power factor in the relationship: an adequate study of drop size distribution (DSD) is needed before starting with quantitative rainfall estimation. Since Z varies in a wide range, reflectivity value is usually reported in a logarithmic scale $dBZ = 10 \log_{10} Z$.

DSD is usually modelled according predefined distribution equations. The simplest is the one-parameter exponential model, but its assumption lead to overestimation on the number of both smallest and biggest drops [Joss and Gori, 1978; Waldvogel, 1974]. Ulbrich (1983) proposed the three parameter (N_0, μ, and Λ) gamma function:

$$N(D) = N_0 D^\mu e^{-\Lambda D} \tag{1.8}$$

that is capable of describing a broader range of raindrop size than an exponential distribution (a special case of the gamma distribution with $\mu = 0$ and N_0 tied to Λ). The three parameters of the gamma DSD can be obtained from three independent remote measurements such as disdrometer or vertical reflectivity profile measurements (see sec. 1.5).

1.3.1 Z-R relation for rainfall estimation

The main objective of weather radars, from hydrological point of view, is providing spatially distributed quantitative estimations on rainfall rate. The reflectivity maps have to be converted in rainfall fields, but this is a process that contains different types of uncertainties and error sources. In general reflectivity up to 15-20 dBZ means no or light rainfall (higher no rainfall values correspond to cloud reflectivity), and reflectivity values between 40 and 50 dBZ generally means convective precipitation. Reflectivity values grater than 60 lead to the assumption of hail presence, due to the fact that ice reflects much more than water surface. The conversion from reflectivity to rainfall rate can be accomplished using many different approaches, the most popular, however, is the use of a power type function with two coefficients a and b.

$$Z = aR^b \tag{1.9}$$

Relationships of this type should be regarded as empirical although strong theoretical justification exists for this choice: both radar reflectivity and rainfall rate can be expressed as moments of drop size distribution within a radar sampling volume. This is where the first problem appears with using raingauge observations for parameter estimation of Z-R relationship. Most rain gauges do not measure rainfall rate but rather, rainfall accumulation. The radar sampling volume is often located at elevation as high as 1-2 km, with potentially significant time displacement (up to several minutes) which creates difficulties in time and space synchronization of the two measurements [Krajewski, 1995]. Also, the radar sampling volume is much larger than the raingauge one. These problems, when combined with extremely high space and time variability of rainfall, indicate that one should not expect an high correlation between the raingauge observed values and the radar-estimated amounts at short time scales.

The idea of a relation between reflectivity Z and rainfall rate R started with early weather radar studies [Marshall and Palmer, 1948], but this relation is not unique, but event dependent (mainly due to different DSD) so that many other empirical parameterisation of the same equation are commonly used. Table 1.3 shows different sets of parameters found by other researchers [Joss and Waldvogel, 1968], the third one calibrated specifically for convective precipitation [Sekhon and Srivastava, 1970]. Figure 1.3 on the following page reports 69 empirical parameterizations collected by Battan (1973) in a logarithmic graph, and indicate the ideal goal to have a specific parameter estimation for each studied event. This would be theoretically possible if the disdrometer network would be denser, but since these instruments are quite costly it is not practically feasible.

Since DSD is not constant in the same event some studies suggest spatially and temporally distinction within the same event: Steiner *et al.* (1995) proposed a storm classification method to separate convective and stratiform regions within the rainfall event based on the intensity and sharpness of the peaks to

Researchers	a	b
Marshall and Palmer, 1948	200	1.6
Joss and Waldvogel, 1968	300	1.5
Sekhon and Srivastava, 1970	300	1.35

Table 1.3: Different empirical parameterizations for Z-R power relationship: R in mm h^{-1} and Z in mm^6 m^{-3}.

echo intensity. Good results are found using different methodologies in different events, but complex procedures that perfectly fit in one case may not provide satisfying rainfall fields in other cases. In this study physically based assumption are considered, and parameter calibration is done, where possible, with punctual comparison between raingauge and radar precipitation values. This technique is the oldest one and probably still the most common. Even with limitation due to comparison between punctual (raingauge) and mean volumetric (radar) data, this procedure provides a simple tool to validate precipitation fields from radar processing. Radar and raingauge data can be displayed in a dispersion graph at the event scale or at finer ones (e.g., hourly). When data are linearly well correlated with unitary slope, raingauge and radar give coherent spatial observations; if correlation is good but slope scientifically differs from 1, radar overestimation or underestimation is probable: all rainfall fields can be multiplied by a factor to reduce or eliminate bias between radar and raingauges; if the graph shows no correlation it should lead to consider different hypothesis (e.g., parameters, physical correction, raingauge errors) and hopefully to conclude with more coherent results.

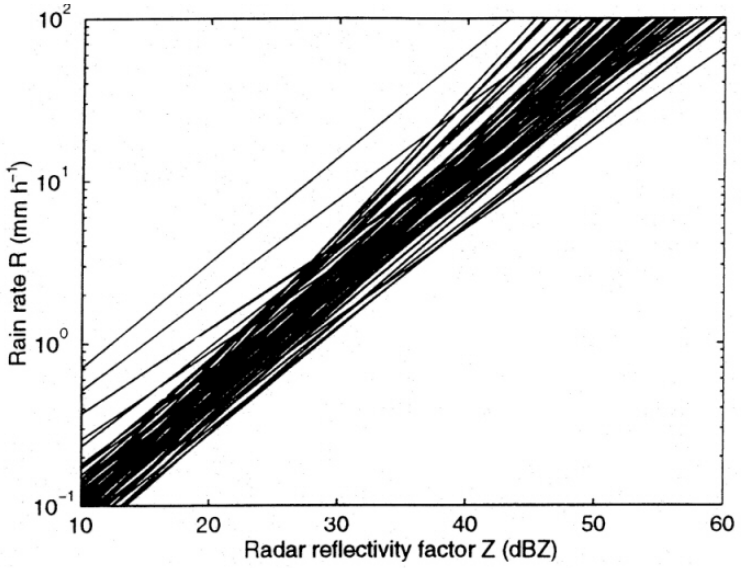

Figure 1.3: 69 Z-R relation collected by Battan (1973).

1.3.2 Bias

Identifying and quantifying bias is perhaps the most important step in characterizing the error structure of radar-rainfall estimates. By "bias" we mean the systematic departure from the true, and unknown, rainfall. There are numerous causes of radar-rainfall bias, including miscalibrated radar, overshooting the cloud systems, improper Z-R relationship, and subcloud evaporation of raindrops. All will cause systematic departure of estimated rainfall from the true rainfall. In the following discussion we approach the problem of bias identification from the real-time estimation point of view. This is because in the off-line mode, with the availability of sufficiently large sample the problem of bias adjustment is much simpler.

We also recognize that identification of the bias due to any or all of the above causes is difficult due to the existence of significant spatial and temporal variability of rainfall and the sampling area mismatch of radar and rain gauge sensors. To eliminate the effects of random factors which include in addition to the rainfall variability, the reflectivity and rain gauge measurement errors on bias identification, radar-rainfall and rain gauge rainfall accumulation should be integrated over a certain time scale prior to a meaningful comparison. What is that scale? There is no simple answer to this question. If the scale is too short, for example 15 min, clearly significant spatial variability of rainfall will mask the effect of the bias. From one period to the next, from one gauge to the next, we could have large positive and negative differences between the radar and rain gauge estimates of rainfall. As we allow time integration of the data, the random effects average out, and the bias, if present, becomes more obvious. On the other hand, if we wait too long, we may be mixing seasonal effects. The bias in the cold season is likely to be different from that of the warm season as the typical vertical extent of the cloud system and the DSDs are quite different [Anagnostou *et al.*, 1998; Smith *et al.*, 1996b].

In the past, the problem of bias estimation and correction in real-time has been approached in the meanfield sense, i.e. trying to ensure that the entire rainfall field in view of a radar does not deviate from that represented by rain gauges. Several authors conducted studies of statistical techniques for this approach, including [Anagnostou *et al.*, 1998; Smith and Krajewski, 1991]. Recently, we note a tendency documented in the literature towards eliminating some of the range dependent biases based on their physical causes Seo *et al.* (2000). In particular, Vignal *et al.* (1999, 2000); Vignal and Krajewski (2001) demonstrated good performance of a vertical profile of reflectivity correction that mitigates the effect of bright band, among other effects. As these effects operate on a short time scale, their effects should be corrected also on such a scale. Vignal and Krajewski (2001) also report decrease of random effects in the VPR-corrected radar-rainfall estimates. This is understandable since some of the effects work in the opposite directions, as we discussed above, and thus, when taken together, they "look" random. Anagnostou *et al.* (1998), Mc Collum *et al.* (2002) and Seo and Breidenbach (2002), attempted to investigate the effect of different time scales on the effectiveness of the bias removal. Still, due to the lack of long-term high-quality radar and rain gauge data sets the question remains largely unanswered. A

Monte Carlo simulation study would be an alternative to provide some guidance but its realism is likely to be compromised by the fact that we know little about the statistical characterization of the errors of radar-rainfall.

1.3.3 Polarimetric methods

Research conducted over the past 20 years indicates that radar-rainfall estimation may be improved with additional radar measurements. Research radar systems simultaneously measure reflectivity and phase at horizontal (H) and vertical (V) polarization [Bringi *et al.*, 1982; Zrnic and Ryzhkov, 1999]. The physical concept behind polarization diversity measurements exploits the fact, that under aerodynamical stress, falling raindrops take oblate shapes, and as a result impact differently the propagation and backscattering of an incoming H and V electromagnetic radar wave. The most common polarimetric radar measurements are:

1. The reflectivity factors at H and V polarization (Z_H, Z_V);
2. The differential reflectivity factor (Z_{DR});
3. The propagation differential phase (Φ_{DP}). These measurements provide information that can be related to DSD characteristics, and in turn provide improved rainfall estimate.

Additionally, the polarimetric measurements provide new means for classifying precipitating particles (rain, hail, graupel and snow) and for distinguishing the ground echo due to local clutter and anomalous propagation conditions from precipitation. The two most beneficial aspects of polarimetric measurements may be the elimination of hail contamination effects in heavy rainfall and improved detection of ground returns.

Use of polarimetric measurements in an operational setting presents a host of new challenges. It is not our goal to discuss them herein as others have already done this effectively (e.g. [Hubbert and Bringi, 1995; Keenan, 1998; Zrnic and Ryzhkov, 1999]). Some of the challenges deal primarily with radar system design. Other issues concern the fundamental physics of propagation and interaction of radar waves with precipitating medium.

Our goal is to bring attention to the issue of estimation. The polarimetric measurements are not a panacea to many of radar-rainfall uncertainty sources (with the possible exception of hail contamination). Within-beam variability, subcloud evaporation, cloud overshooting, etc., cannot be solved with the polarimetric measurements. Also, the measurements of some of the polarimetric variables are associated with significant uncertainties. For example, estimation of specific differential phase shift (K_{DP}) is subject to random phase errors of the Φ_{DP} measurements and the backscattering phase shift (δ), which cannot be readily separated from Φ_{DP}. The δ value, which increases with an increase in raindrop size, can be

significant at high rainfall intensities and high radar frequencies. This non-Rayleigh effect can introduce serious complications in the evaluation of K_{DP} at the X-band and moderate to high rainfall intensities, and requires careful investigation [Matrosov *et al.*, 1999].

Studies on radar polarimetry have concentrated mainly on the S-band frequency and shown that K_{DP} based radar estimators are not affected by radar calibration errors and partial beam occlusion (e.g. [Vivekanandan *et al.*, 1999; Zrnic and Ryzhkov, 1996, 1999]). However, at S-band, these estimators are characterized by relatively low sensitivity to rainfall rate and this, consequently, has negative impact on the product resolution. Since Φ_{DP} sensitivity to the raindrop size is proportional to the radar wavelength, one would expect that at X-band, these limiting values could be lowered by a factor of three. Consequently, the use of X-band wavelength should allow more accurate estimation of light to moderate rainfall rates at higher spatial resolutions. These improvements are primarily important for the accurate prediction of floods in small to medium size watersheds with rapid response to precipitation and for real-time urban water management. Furthermore, partial signal attenuation, which is significant at X-band, is not an important issue for the K_{DP} estimator unless there is complete attenuation. The main complications in K_{DP} rainfall estimation at X-band that need to be investigated are (1) the presence of significant d in cases of high rainfall intensities, and (2) the effect of DSD variability and oblateness shape model selection on the estimator parameters. To date, research on the use of polarimetric radar measurements at X-band has been limited to a few theoretical [Chandrasekar *et al.*, 1990; Jameson, 1994] and experimental studies [Matrosov *et al.*, 1999; Tan *et al.*, 1991] but the proposed estimators lack adequate quantitative validation and error analysis.

Thus, if we realize that rainfall estimates based on polarimetric data are uncertain, the task remains to quantify these uncertainties. From this point of view the requirements for validation of radar-rainfall are the same as for single-parameter radar.

1.4 Radar hydrology and rainfall estimation of extreme storms

Radar estimation of extreme rainfall rates plays an important role in a range of applications dealing with the hydrology and hydraulics of flooding. The extreme rainfall rate setting also raises special challenges for development of radar-rainfall estimation algorithms, validation of rainfall algorithms and design of radar-rainfall estimation experiments.

Hudson (1963) presented one of the first experiments designed to measure and parameterize raindrop size distributions in extreme rainfall rate storms (see also [Blanchard and Spencer, 1970; Willis and Tattleman, 1989]). Blanchard and Spencer (1970) concluded that breakup of raindrops controls the raindrop size distribution for extreme rainfall rates and they observed that for rainfall rates in the range between 100 and 700 mm h^{-1}, the median diameter remains relatively constant. These features of dropsize distri-

butions are used to infer that for a given rainfall rate in intense rainfall, a steady-state dropsize distribution develops in which drop growth is balanced by drop breakup. List (1991) presents theoretical arguments supporting an "equilibrium" dropsize distribution in heavy rain and shows that in this case Z and R will be linearly related, that is, the exponent b in the Z-R relation for extreme rainfall rates will be 1.

Uijlenheot *et al.* (2003) show that the linear Z-R relationship holds for extreme rainfall rate drop spectra from Florida (rainfall rates exceeding 100 mm h^{-1}). It is also shown in Uijlenheot *et al.* (2003) that the prefactor of the Z-R relation varies over a large range. It follows that, even under equilibrium conditions for extreme rainfall rates, bias estimation will play an important role in reflectivitybased estimation of extreme rainfall rates. This point is further illustrated in analyses of radar-rainfall estimates from "warm rain process" storms, which produce extreme rainfall rates [Petersen *et al.*, 1997; Smith *et al.*, 1996b,a]. Development of Z-R estimation procedures, as discussed above, will be sensitive to the weighting of observations from the extreme tail of the rainfall rate distribution. For applications in which extreme rainfall rates are of special interest, validation procedures should explicitly characterize the error of rainfall rate estimates as a function of rainfall rate.

The extreme rainfall estimation problem provides one setting in which ideas from the DSD approach and the optimization approach can be usefully combined to enhance radar-rainfall estimation algorithms. The extreme rainfall setting is one in which previous studies provide a strong basis for presuming that variations in DSDs play a significant role in the accuracy of radar rainfall estimates. Information on key aspects of the variability in DSD properties can be obtained from polarimetric measurements, like differential reflectivity and differential phase shift. Including these additional radar observations should lead to significant improvements in estimation of extreme rainfall rates. The framework for including polarimetric measurements, however, should be the optimization approach, in which radar observations aloft are compared with surface measurements of rainfall rate.

The climatology of rainfall rates exceeding 100 mm h^{-1} is heavily influenced by warm season systems of thunderstorms. The climatology of radar reflectivity observations for these storms, in turn, is strongly influenced by hail contamination [Baeck and Smith, 1995, 1998]. The presence of hail in a radar sample volume can severely distort radar-rainfall estimates, due the sixth power dependence of Z on drop diameter. An extreme example of the hail contamination problem is provided by supercell thunderstorms, which are often prolific hail producers and the agents of extreme rainfall rates. The Dallas Hailstorm of 5 May 1995 Smith *et al.* (2002a) was a supercell thunderstorm, which produced hailstones (more than 2 cm in diameter) in close proximity to regions experiencing 15-min rainfall rates exceeding 200 mm h^{-1}. More than 15 fatalities resulted from flash floods produced the Dallas Hailstorm. Smith *et al.* (2002a) argue that supercell thunderstorms play an important role in determining the frequency of extreme rainfall rates in much of the US east of the Rocky Mountains. Hail contamination precludes the development of useful climatologies of extreme rainfall from single parameter radar-rainfall estimates. Polarimetric measurements

could significantly reduce errors in rainfall rates due to hail contamination.

Warm season thunderstorms in urban environments present an important challenge to radar-rainfall estimation procedures. Flood response of small drainage basins in urban environments is particularly sensitive to "fine-scale" temporal and spatial variability of rainfall. The precise scale boundaries will depend on details of the drainage basin (see Smith *et al.*, 2002a, for example), but in many settings the relevant scales of variability are comparable or smaller than the minimum observation scales of operational weather radar systems like the WSR-88D (6 min, 1 km). Experimental programs for radar estimation at rainfall at fine space and time scales will play an important role in advances in urban flood hydrology.

The utility of radar-rainfall estimates for extreme flood analysis can be viewed in terms of enhanced capabilities for modeling flood response of a drainage basin. The potential benefits of high-resolution rainfall estimates have motivated advances in hydrologic modeling [Borga *et al.*, 2000; Corral *et al.*, 2000; Krajewski *et al.*, 1991; Ogden and Julien, 1994; Pessoa *et al.*, 1993]. Advances in operational forecasting and hydrologic design have progressed more slowly although there are exceptions. Radar-rainfall estimates hold particular promise for enhanced flash flood forecasting procedures and for engineering design and management applications in small basins. For these problems, hydrologic processes forced by rainfall rate play a comparable or even more important role than hydraulic processes associated with flood wave propagation. The central difficulty here is often the non-linear response of drainage basins to rainfall rate.

These observations have important implications for development of radar-rainfall estimation procedures. One of the major obstacles to increased utilization of radar-rainfall estimates for hydrologic modeling has been the absence of quantitative assessments of the accuracy of radar-rainfall estimates. As discussed in previous sections, development of formalized procedures for estimating the error structure of radar-rainfall fields and for validating radar-rainfall estimates is of central importance to radar hydrology. In some settings, the hydrologic application may impose useful constraints on the error assessment problem. In particular, assessment of error structure of radar-rainfall estimates that are used for hydrologic modeling should consider the propagation of errors through hydrologic models. The non-linear response of drainage basins to rainfall forcing implies that errors in extreme rainfall rates will play an important role in hydrologic modeling. Quantification and validation of radar-rainfall estimates for extreme rain conditions are also an important challenge for radar hydrology.

The challenges of extreme rainfall estimation are particularly acute in mountainous terrain. Some of the largest measured rainfall accumulations in the United States and the world Costa (1987) have occurred in complex terrain. Landslides and debris flows are added to flooding as major hazards associated with extreme rainfall in mountainous terrain. Radar-rainfall estimation in complex terrain is complicated by ground returns and signal loss associated with beam blockage Joss and Waldvogel (1990) (see also Andrieu *et al.* (1997) for novel approaches dealing with radar sampling problems in complex terrain). An additional problem is that orographic storms may differ from storms forming away from terrain in

terms of microphysical and dynamical properties [Petersen *et al.*, 1997; Smith *et al.*, 1996b]. Despite these difficulties, radar-rainfall estimates hold great promise in improving hazards assessment capabilities in mountainous terrain.

1.5 Typical error sources for the analysis of extreme storms

Anomalous propagation in non-standard atmosphere

The first assumption is that the radar beam is moving through air that cools down at a certain rate with height. The position of the echoes depend heavily on this hypothesis. However, the real atmosphere can vary greatly from the norm.

Super refraction

It is very common to have temperature inversions forming near the ground, for instance air cooling at night while remaining warm aloft. This is not what is expected. As the index of refraction of air increases the radar beam bends toward the ground instead of continuing upward. Eventually, it will hit the ground and be reflected back toward the radar. The processing program will then wrongly place the return echoes at the height and distance it would have been in normal conditions.

This type of false return is relatively easy to spot on a time loop if it is due to night cooling or marine inversion as one sees very strong echoes developing over an area, spreading in size laterally but not moving and varying greatly in intensity. However, inversion of temperature exists ahead of warm fronts and the abnormal propagation echoes are then mixed with real rain.

The extreme of this problem is when the inversion is very strong and shallow, the radar beam reflects many times toward the ground as it has to follow a waveguide path. This will create multiple bands of strong echoes on the radar images.

Under refraction

On the other hand, if the air is unstable and cools faster than the standard atmosphere with height, the beam ends up higher than expected. This places the precipitation at a much higher altitude than it actually is. This situation is very difficult to spot.

Non-Rayleigh targets

If we want to reliably estimate the precipitation rate, the targets have to be 10 times smaller than the radar wave according to Rayleigh scattering. This is because the water molecule has to be excitealpd by the radar wave in order to give a return. This is relatively true for rain or snow as 5 or 10 cm radars

are used. However, for very large hydrometeors, since the wavelength is on the order of stone, the return levels off according to Mie theory. A return of more than 55 dBZ is likely to come from hail but won't vary proportionally to the size. On the other hand, very small targets, like cloud droplets, are too small to be excitealpd and donŠt give a recordable return on common weather radars.

Beam blocking

Beside errors due to Z-R miss calibration other typical problems are found when using weather data for rainfall estimations. To avoid them there are some recommendations to observe during volume scanning performance. Other improvements can be obtained in post processing phase with appropriate algorithms and procedures.

Most error sources derive from radar physics and atmospheric or terrain features. Since radars are continually rotating during data acquirement it is important that the azimuth position is always well known; in general automatic procedures check the North position during rotation, but periodically manual checking can avoid difficult post processing corrections.

Ground clutter can disturb the radar measure, since fixed objects, as an orographic relief, cause back radiation that receiver is not able to distinguish from a rainfall drop scatter signal. Since the velocity of fixed objects is null they can be detected by Doppler methodology, searching pixels with no velocity and removing those data from rainfall estimation fields. Ground clutter at a certain elevation can also be detected by using radar maps obtained with observations in dry condition: when terrain echo is not important (up to 10 dBZ) ground reflectivity can be subtracted to the total one before proceeding with data elaboration; local and sharp clutter pixel reflectivity can be substituted by interpolation of near values. Ground clutter corrections are generally taken in to account by the agency that provides radar data, which generally keeps also raw reflectivity fields.

A radar beam, along its propagation path, can be partially or totally occluded by orography. This problem can be avoided or reduced when the radar location is decided. When working in mountain regions, total occlusion often reduces radar visibility, while partial beam occlusion can be corrected modifying the assumptions in Eq.3.1, and specifically the parameter C witch should varies according to occlusion maps: with no occlusion the total wave power hit atmospheric particles; when part of the beam propagation is interrupted by orography only the non occluded portion of beam power must be taken in to account, so parameter C is reduced by the occlusion factor [Vivekanandan *et al.*, 1999]. Occlusion maps can be derived by DEM elaboration for the specific radar angle elevations [Anagnostou *et al.*, 2008]. In general data from different elevations are available and occlusion decreases when considering higher radar elevations. Choosing the best elevation level is a trade-off procedure between minimizing the beam blockage and the errors due to vertical profile reflectivity variations (see further). Increasing the elevation angle allows to scan meteorological event at a greater distance from the terrain; the higher part of the atmosphere

presents large difference when compared with terrain rainfall estimations.

VPR

One of the greater problems in radar data accuracy is that reflectivity is not homogeneous at different altitudes. Several factors contribute to this feature: evaporation, air turbulence and, above all, water changing from liquid to solid form or vice versa. Despite the fact that radar observations in rain show considerable variety in the shape of echoes, the various reflectivity profiles can be grouped in five classes [Fabry and Zawadzki, 1995].

1. Low level rain, that includes all stratiform rain or drizzle echoes when precipitation forms directly in the liquid state: reflectivity decreases very rapidly with height.

2. Rain with bright band, that is the most common profile in temperate latitudes and at low and moderate rain rates (Figure 1.4 on the next page from Fabry and Zawadzki (1995)): reflectivity is roughly constant from the ground up to the elevation of the melting layer where the reflectivity suddenly increases (the bright band phenomenon); above the melting layer, the reflectivity of snow decreases on average at a rate of about 6 to 7 dB/km in the first kilometre above the bright band.

3. Rain from compact ice: this profile is similar to the previous one except that no clear bright band can be found and the profile undergoes a quick transition from the rain regime to the ice regime through a sudden decrease of Z.

4. Showers: as in case 1 the precipitation forms directly in liquid phase isolated showers and convective rainbands, which are indistinguishable in terms of vertical reflectivity profiles: reflectivity is generally constant from the ground up to 1 km from the echo top beyond which the reflectivity rapidly decreases.

5. Deep convection, exclusively generated by thunderstorms: this type of echo displays the most significant variability in time, and strong reflectivities extending up to several kilometres above the level of the 0° C isotherm.

When the radar beam intersects the melting layer, correctly describing the rate of decrease of reflectivity with height above the bright band can have a considerable impact on the quantitative accuracy of rainfall estimates at longer range [Lewis *et al.*, 2007]. Several correction schemes have been developed to describe the observed profile shape above the bright band using radar data from multiple elevation scans; most methods are based on assuming that the reflectivity expressed in dBZ decreases linearly with height and that the decreasing slope is found by vertical profile of reflectivity (VPR) scansion from the radar. In the events studied in this thesis VPR is not considered since they consist of convective events in the summer

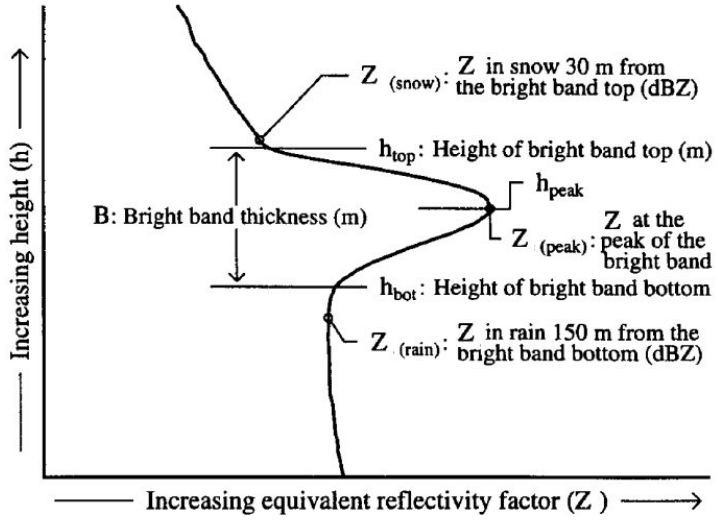

Figure 1.4: representation of reflectivity profile of rain with bright band Fabry and Zawadzki, 1995.

period: combination of high melting layer and low elevations avoids significant variation in VPR. Hail presence is another source of intensity and can lead to local overestimation; when solid precipitation is present or presumed a threshold for Z is chosen to limit overestimation due to high ice surface reflectivity.

Attenuation

Attenuation is another common problem in analyzing reflectivity fields since electromagnetic waves interact with atmospheric gases, clouds and rainfall drops and loose part of their power along the propagation path due to scattering and absorption. Hitschfeld and Bordan (1954) studying attenuation for different wavelengths show that at 10 cm or longer length, attenuation is almost negligible, while its effect becomes increasingly more serious as the wavelength is reduced. In standard radar equation (Eq.3.1) no attenuation effect is taken in to account. If the thickness of the absorbing medium that is traversed is dr, and the drop in the power received dP_r, their relation may be written as:

$$dP_r = -2\Lambda' P_r dr \tag{1.10}$$

where Λ' is the attenuation constant of the medium; the factor 2 arises from the fact that, in case of weather radar, each element of the path is traversed twice: from the antenna to the target and then back to the receiver. Attenuation increases with distance from the radar and varies according to medium characteristic. Integrating Λ' along the path, the attenuation effect can be divided in three different components:

$$\int \Lambda' dr = \int \kappa_1 dr + \int \kappa_2 M dr + \int \kappa R^{\alpha} dr \tag{1.11}$$

respectively referred to atmospheric gases, clouds and precipitation. The three parameters κ, κ_1 , κ_2 and the α exponent can be derived by past studies or calibrated for the specific studied event, while M depends on the cloud density.

The first two terms are negligible for convective storms occurring not too far from the radar, (they are in fact discarded in this work), while the dominant attenuation phenomena are due to rainfall. Hildebrand (1977) presents a method where the attenuated radar reflectivity measurements at distance r are converted to attenuated rainfall rates and to attenuation estimates κ_a (express as the drop in Z due to attenuation across the pixel transport). With appropriate assumptions concerning DSD and temperature, a new estimate of reflectivity fields can be produced with the relation:

$$\log Z'(r) = \log Z(r) + 2 \sum_{x=1}^{r-1} \kappa_a(x) \tag{1.12}$$

and new reflectivity Z' is used to derive revised attenuation estimates $\kappa'_a(r)$. This procedure can be repeated iteratively until the last step doesn't produce any significant change in the reflectivity fields, and the final value of Z is used to calculate rainfall rates corrected for attenuation.

2. Radar rainfall estimation for the post-event analysis of flash flood/debris flow events

2.1 Slovenian case and application of MRT technique

This section is dedicated to event presentation and motivation on application of MRT technique, the description of this attenuation suppression procedure is reported in section 2.1, an other part of the work is focused on the more hydrological aspect for this event, we tried to summarize all these aspects both with the space-time rainfall variation analysis in chapter 5.

The HYDRATE project funded by the European Community (http://www.hydrate.tesaf.unipd.it/) aims at improving the scientific basis of flash flood forecasting by extending the understanding of past flash flood events, advancing and harmonising a European-wide innovative flash flood observation strategy and developing a coherent set of technologies and tools for effective early warning systems. Weather radars offer unprecedented means for observing extreme rain events with space and time resolution relevant with respect to the hydrological dynamics of the affected watersheds [e.g., Smith *et al.*, 1996a; Ogden *et al.*, 2000; Delrieu *et al.*, 2005]. However, the complexity of the radar technology, the variety of uncertainty sources and the variability of precipitation at all scales still make the radar quantitative precipitation estimation (QPE) a very challenging task. This is especially true in mountainous regions [e.g., Joss and Waldvogel, 1990; Andrieu *et al.*, 1997; Germann *et al.*, 2006; Delrieu *et al.*, 2009] due to the impact of the orography on the propagation of the electromagnetic waves (clutter due to the relief and anthropic targets; screening; anomalous propagation). The radar QPE quality depends much on the relative locations of the radar and the rain event, the intervening relief, the radar parameters, the operating protocol and the data processing [Pellarin *et al.*, 2002]. With respect to the extreme event-driven observation strategy promoted in the HYDRATE project, very pragmatic approaches need to be developed to take the best benefit of existing weather radar and raingauge datasets for post-event rainfall estimation in mountainous regions.

This event case is an example with the heavy rains and flash floods that occurred on 18 September 2007 in Slovenia (Figure 2.1 on page 33) causing seven human casualties and damage costs evaluated to 285 millions euros. More than 40 municipalities, i.e. about one third of the country, were concerned by this event. The city of Železniki, located at about 50 km north-west of Ljubljana, was particularly affected by the disaster (3 casualties, 100 millions euros of damages). The flood swept away cars, buses and severely damaged homes, a hospital and a water treatment plant. The Žlezniki city is located on the Selska Sora river. The corresponding watershed has an area of approximately 200 km^2. The unique raingauge within the watershed indicated a rain event mostly concentrated in 5 hours with a total amount of 220 mm. The maximum discharge was estimated to 350 $m^3\ s^{-1}$ from an operational station located downstream of the city. This corresponds to a maximum specific discharge of about 1.75 $m^3\ s^{-1}\ km^{-2}$. Such characteristics motivated a post-event survey, conducted by 21 HYDRATE scientists from different institutions and countries (UK, Italy, France, Greece, Romania, Spain and Slovakia) with the support of the Environmental Agency of the Republic of Slovenia (ARSO; http://www.arso.gov.si/en/). In addition to operational hydrological data, in-situ information was elaborated from cross-section surveys to estimate maximum discharges for ungauged watersheds and from interviews of witnesses to document the chronology of the floods, following the methodology described by Gaume (2006).

The layout of the available rainfall observation system managed by ARSO is displayed in Figure 2.1 on the next page. It includes a network of 47 raingauges (among them, 14 devices provide time series at the hourly time step while the remaining ones are daily raingauges) and a modern volume-scanning Doppler C-band radar located in Lisca at about 80-100 km of the affected watershed. As such, this example is quite representative of the post-event analysis context with radar data coming from a rather remote system, a relatively dense network of daily raingauges and few raingauge time series. The overall strategy is therefore to use the raingauge data to control/assess the radar data processing prior to using the radar QPE space-time series as input in rainfall-runoff models. A first aim of the present contribution is to test the utility of the Mountain Reference Technique (MRT) for quantifying and correcting rain attenuation effects that are likely to severely affect C-band radar measurements in heavy rain [Delrieu *et al.*, 2000]. The MRT refers to the Surface Reference Technique proposed by Meneghini *et al.* (1983) for rainfall measurement at attenuating wavelengths in spaceborne radar configurations. The concept is based on the estimation of path-integrated attenuation (PIA) from the difference between the Earth surface radar return in the presence and in the absence of rain. Such measurements can be used in various ways to estimate the average rain rate over the propagation path and/or to constrain rain rate profiling algorithms [Marzoug and Amayenc, 1994]. Feasibility of applying this technique to ground-based radars with mountain returns was already demonstrated for the X band, a frequency band severely prone to rain attenuation effects [Delrieu *et al.*, 1997; Serrar *et al.*, 2000].

Section 2.1 shows evidence of very significant rain attenuation effects at C-band for the Slovenian

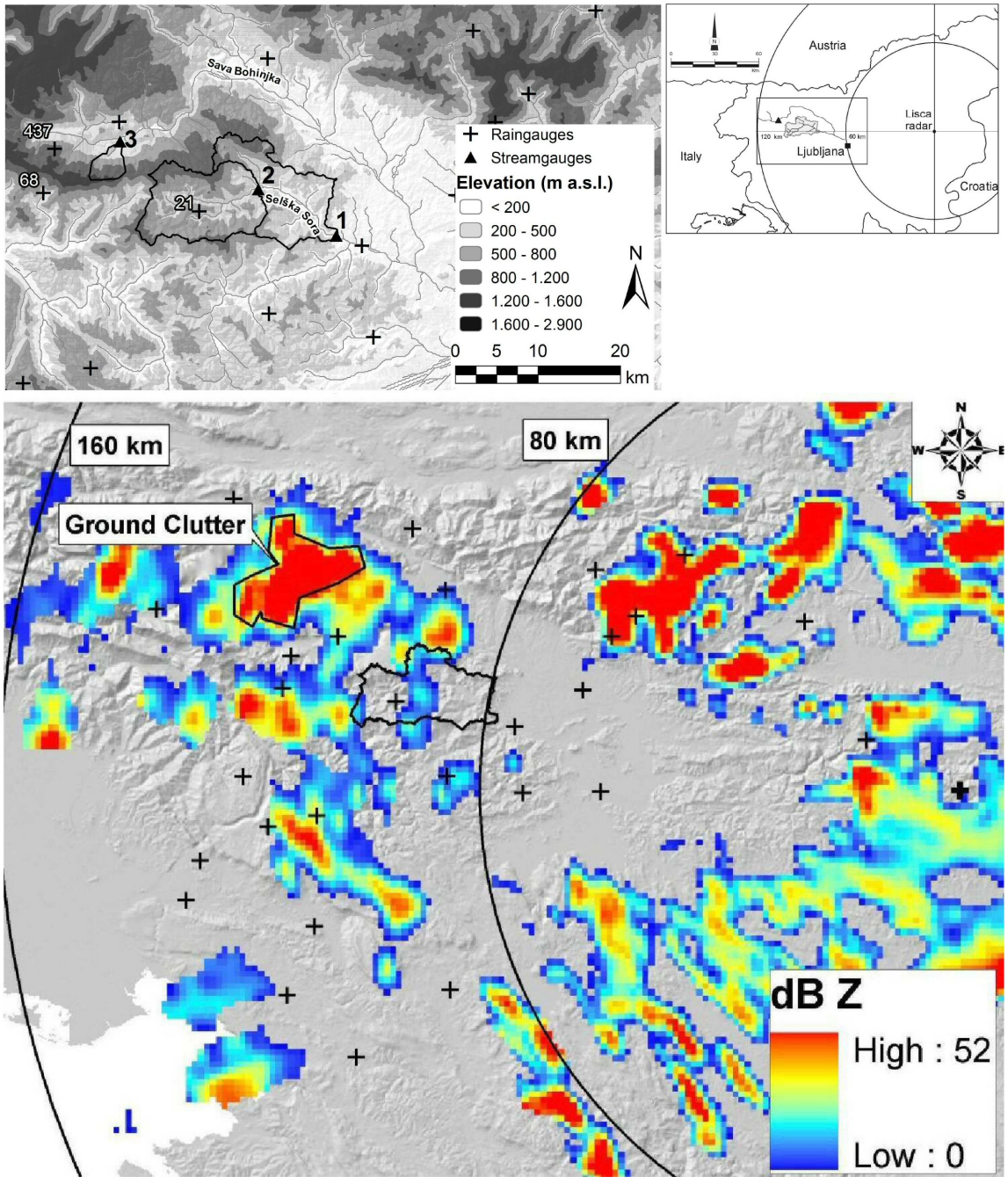

Figure 2.1: Map of the study area in Slovenia. The location of raingauges with a plus sign, the Lisca C-band radar with 80-km range markers. The Železniki watershed is delineated in the center of the image with a black contour. The coloured scale represents the dry-weather clutter (in dBZ) for the lowest elevation angle (0.5°) averaged during seven hours before the 18 September 2007 rain event. It is emphasized the position on the ground clutter used fort he MRT technique.

case. The way such PIAs can be used to correct attenuation over the entire radar detection domain is the subject of Sect. 2.1.1. In Sect. 2.1.3, the attenuation correction is replaced in the broader context of the radar quantitative precipitation estimation, using the TRADHy radar processing system developed at LTHE (Delrieu *et al.*, 2009; TRADHy stands for Traitements Régionalisés et Adaptatifs de données radar pour l'Hydrologie / regionalized and adaptive radar data processing for hydrological applications). Section 2.1.6 provides a series of sensitivity tests and assessments of the radar QPEs with respect to raingauge data. The main results for the radar rainfall estimation are summarized in Section 2.1.7.

Evidence of rain attenuation at C-band using mountain returns

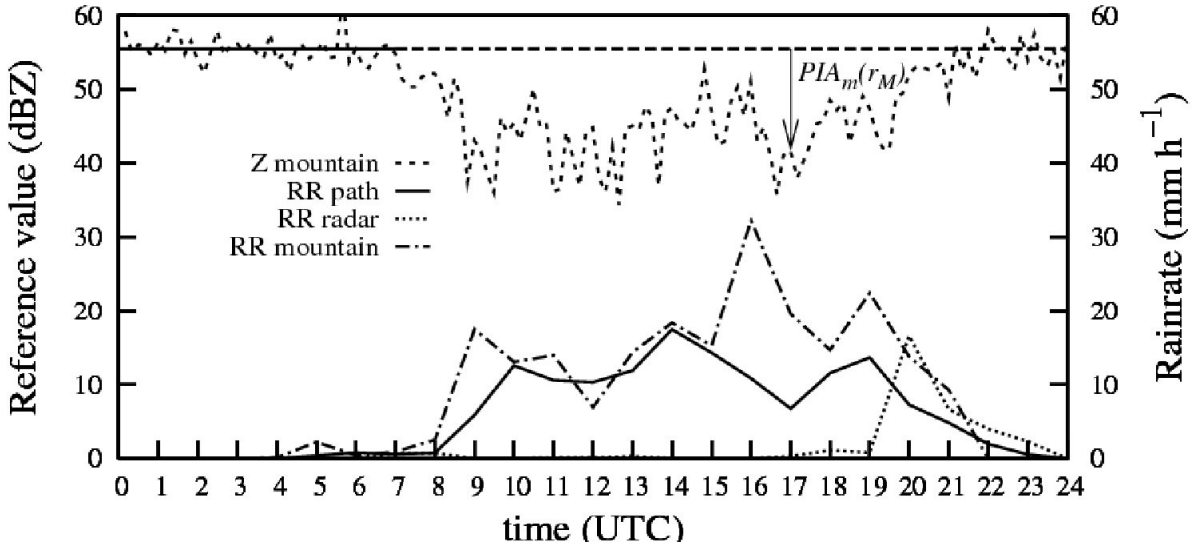

Figure 2.2: Time series of the mountain reference target value (dashed line on top), the average rainrate along the path (bottom part of the graph, continuous line), the rainrate in the vicinity of the mountain (dash-dotted line) and the rainrate close to the radar site (dotted line).

Table 2.1 on the facing page lists the parameters of the Lisca C-band radar. Figure 2.1 on the previous page displays the dry-weather ground clutter for the lowest radar elevation angle (0.5°) averaged over a 7-hour period preceding the 18 September 2007 rain event. It should be noticed that raw reflectivity data is (fortunately) stored by ARSO in polar format, prior to and after implementation of the ground clutter filtering technique. The ground-cluttered reflectivity data is quite naturally not used in any manner in operational practice although we are going to show it contains valuable information for radar QPE.

As the reference target, we selected a strong ground clutter pattern that can be seen at about 20 km in the North-west direction of the Železniki watershed. Figure 2.2 shows the time evolution of the average value of the reference target together with various rainfall indicators derived from the raingauge network measurements: these include (1) the average rainrate along the radar-reference target path obtained with the available hourly raingauges through the Thiessen technique; (2) the rainrate time series of the closest

Parameter	Value(s)
Geographical coordinates	Lat = 46.068° , Lon = 15.290° , Alt = 950 m MSL
Measured parameters	Reflectivity, radial velocity, spectrum width
Wavelength (cm)	5.34
Peak power (kW)	300
PRF (Hz)	600, 1200
Pulse length (μs)	0.8
Minimum detectable signal (dBm)	-110
Antenna diameter (m)	4.2
3-dB beamwidth (°)	0.9
Power gain (dB)	43.8
Operating protocol	12 elevations; revisit time of 10 min
	0.5, 1.0 1.6, 2.4, 3.4, 4.7, 6.3, 8.6 (3 rpm; 600 Hz)
	11.5, 15.5, 20.9, 28.4 (3 rpm; 1200 Hz)
Polar data reflectivity quantization	-30 up to 90 dBZ with 0.5 dBZ increment
Polar data resolution	1000 m (radial); 1° (angular); from 1 to 250 km

Table 2.1: Lisca C-band radar parameters.

raingauge to the reference target and (3) the rainrate time series of the closest raingauge to the radar site. The intensity of the reference target decreases when rain occurs between the radar and the target and it recovers its initial value at the end of the rain event. The PIA reaches maximum values between 15 and 20 dB for path-averaged rain rates between 10 and 15 mm h^{-1} over a 120-km path. Such high PIA values at C-band were already observed [Geotis, 1975] or simulated [Delrieu *et al.*, 2000]. For the hydrologists not familiar with dB units, these PIAs values correspond to multiplicative factors of 31.6 and 100, respectively, on the reflectivity and to multiplicative factors of 10 and 21.5, respectively, on the rain rate if the exponent of the Z-R relationship is equal to 1.5. Compared to the hourly rainrate time series, it is noteworthy that the reference target time series presents a rather high degree of fluctuation from one step to the next. This is related to the fact that the reflectivity measurements are made instantaneously once every 10 min. The rain event was also characterized by fast-moving convective cells, which may also contribute to increase the noise in the reference target time series. Like attenuation measurement with microwave links Leijnse *et al.* (2007), the PIA estimation in the present configuration may also be affected by on-site effects. Since the Lisca C-band radar is equipped with a radome, special care needs to be taken when and after rainfall occurs at the radar site: the presence of a water film on the radome is known to produce attenuation effects of several dB [Collier, 1989]. Fortunately, rainfall occurred at the radar site only at the end of the rain event, well after the intense rainy period in the Železniki area. Rainfall falling over the reference target may also affect the PIA estimation (negative bias) as shown by Delrieu *et al.* (2000) who proposed a simple approach to cope for this effect.

2.1.1 Attenuation correction: principle of the Mountain Reference Technique

In this section is analyzed the principle of the MRT and the way the attenuation correction parameters are estimated. Details may be found in Marzoug and Amayenc (1994); Delrieu *et al.* (1997); Serrar *et al.* (2000).

Let us define the measured rain reflectivity factor profile $Z_m(r)$ mm^{6}m^{-3} as:

$$Z_m(r) = Z(r)\delta_c A(r) \tag{2.1}$$

where r is the range, Z mm^{6}m^{-3} is the true reflectivity factor, δ_c is an eventual radar calibration correction factor, $A(r)$ is the rain attenuation factor along the path from the radar to range r. In equation 2.1, only two sources of error are considered: a possible radar miscalibration supposed to be constant in time (i.e. we assume that the transmitter-receiver unit is stable within the measurement period) and the effect of attenuation by rainfall between the radar and range r.

The PIA factor is given by:

$$A(r) = \exp\left(-0.46 \int_0^r \kappa(s)ds\right) \tag{2.2}$$

where k is the attenuation coefficient [in dB km^{-1}] that depends on the working wavelength and on the rain drop size distribution (DSD) and temperature. We define the PIA in dB units as

$$PIA(r) = -10 \log A(r) \tag{2.3}$$

Assuming that the relation between the reflectivity factor and the attenuation coefficient can be satisfactorily represented by a power law model, with $Z = \alpha\kappa^\beta$, it can be shown [Marzoug and Amayenc, 1994; Delrieu *et al.*, 1997] that:

$$A(r) = \left[A(r_0)^{1/\beta} - \frac{S(r_0, r)}{\delta_c^{1/\beta}}\right]^\beta \tag{2.4}$$

with

$$S(r_0, r) = \frac{0.46}{\beta} \int_{r_0}^r \left[\frac{Z_m(s)}{\alpha}\right]^{1/\beta} ds \tag{2.5}$$

In equation 2.4, r_0 represents the so-called "blind range", that is the range where the reflectivity sampling is started and/or where the reflectivities can be considered as free of ground clutter due to side lobes. The term $A(r_0)$ is related to both radome attenuation and rain attenuation between 0 and r_0 . Equations 2.4 and 2.5 indicate that the PIA factor at any range r can be obtained as a function of the measured reflectivity profile $Z_m(r)$, the coefficients α and β of the Z-k relationship, the blind range attenuation factor $A(r_0)$ and the calibration error δ_c.

If we consider a range r_M where a reference target (a mountain here) is available, the PIA calculated from the measured reflectivity profile ($\text{PIA}_c(r_M)$ hereafter) can be written as:

$$PIA_c(r_M) = -10\log\left[A(r_0)^{1/\beta} - \frac{S(r_0, r_M)}{\delta_c^{1/\beta}}\right]^{\beta} \tag{2.6}$$

The simplest estimator for the PIA from mountain returns can be expressed through the following equation:

$$PIA_m(r_M) = -10\log\left[\frac{Z_{dray}^{ref}(r_M)}{Z_{rain}^{ref}(r_M)}\right] \tag{2.7}$$

where $Z_{dray}^{ref}(r_M)$ and $Z_{rain}^{ref}(r_M)$ are the mean reflectivity of the reference target during dry and rainy time steps, respectively. The practical procedure for estimating $\text{PIA}_m(r_M)$ is described in Delrieu *et al.* (1999b): this includes the definition of a baseline and consideration of rainfall falling over the reference target. The so-called PIA constraint equation stipulates that the PIA calculated at range r_M from the reflectivity profile should be equal to the PIA derived from the mountain return at any time t during the rain event:

$$PIA_c(r_M, t) = PIA_m(r_M, t) \tag{2.8}$$

2.1.2 Parameter estimation

Equations 2.5, 2.6 and 2.7 show that the PIA constraint equation 2.8 depends on three parameters: the coefficients α and β of the Z-k relationship and the radar calibration factor δ_c. Besides the mean reflectivity of the reference target and the measured reflectivity profiles between the radar and the mountain, specification of the blind-range attenuation $A(r_0)$ is required. As already mentioned, rainfall occurred at the radar site only at the end of the rain event Figure 2.2 on page 34. The PIA values of the corresponding time steps were then simply discarded from the optimization procedure. The blind-range attenuation factor

$A(r_0)$ was supposed to be equal to 1 in the calculation of $\text{PIA}_c(r_M)$ for the other time steps.

For the radar calibration factor δ_c optimization, the DSD and the subsequent Z-k relationship are considered to be known (see eg. [Delrieu *et al.*, 1997; Serrar *et al.*, 2000]). Since no DSD data were available for the Slovenian case, we considered a series of Z-k relationships calculated from various DSD models described in the literature and summarized in Delrieu *et al.* (2000). This includes DSD models valid for widespread and thunderstorm rainfall and a Cévennes DSD model established in a French region prone to intense and long-lasting rain events resulting mostly from shallow convection triggered by the orography. The corresponding Z-k and Z-R relationships coefficients calculated for the C-band frequency using the Mie scattering model are listed in Table 2.2.

DSD model	**Z-k relationship** $Z\ [mm^6m^{-3}]$		**Z-R relationship** $Z\ [mm^6m^{-3}]$		δ_c **[-]**	**Nash [-]**	N_{div} **[-]**	N **[-]**
	α	β	a	b				
Widespread rainfall	5.39×10^5	1.16	242	1.43	0.59	0.37	7	51
Cévennes rainfall	4.98×10^5	1.09	362	1.40	0.56	0.33	10	51
Thunderstorm rainfall	4.75×10^5	1.05	533	1.36	0.55	0.28	10	51

Table 2.2: Coefficients of the $Z = \alpha\kappa^\beta$ and $Z = aR^b$ relationships for the C-band frequency and a raindrop temperature of 10° C using the Mie scattering model and DSD models proposed in the literature (see the review in Delrieu *et al.* (2000)). The other columns give the optimal radar calibration factor δ_c, the Nash criterion (Nash) between the measured and calculated PIAs and the number of divergences (N_{div}) of the attenuation equation for the optimal δ_c value; N is the total number of PIA pairs considered for the optimization.

For the optimization, the radar data from the lowest elevation (0.5°) was used. The reflectivity profile was extracted from the ground-clutter processed data and the reference values from the raw reflectivity data. Considering synchronous measurements for the PIA and the reflectivity profiles proved to be important in the present case study due to the fast dynamics of the convective cells. We choose the Nash efficiency between the calculated and measured PIAs as the optimization criterion. It can be noticed however that the PIA can be calculated from equation 2.6 on the previous page only if $S_m(r_0, r_m)/\delta_c^\beta < 1$ (since $A(r_0) = 1$ here). Such a condition may not be fulfilled for a growing number of profiles as δ_c increases. These situations correspond to the well-known divergences of the forward attenuation correction scheme [e.g., Marzoug and Amayenc, 1994], also known as the Hitschfeld-Bordan algorithm. It may happen however that divergences occur for a number of comparison points while the considered δ_c value is optimal for the majority of points. To cope with this problem, we have limited the calculated PIA to the maximum measured value (20 dB) and we have accounted for such capped calculated PIA values in the optimization criterion (illustrations of the optimization procedure for the Cévennes Z-k relationship are presented in Figure 2.5 on page 41). The optimization results are listed in Table 2.2 for the various Z-k relationships. Interestingly, the optimal values are very similar for the three Z-k relationships: the factors are comprised between 0.55 and 0.59 corresponding to a radar underestimation of 2.6 and 2.5 dBZ, respectively. Note that such factors compensate for a radar calibration error and also for the bias

due to an eventual mismatch of the considered Z-k relationship. The similarity of the correction factors from one Z-k relationship to the next does not necessarily mean that such a bias is negligible but rather that the Z-k relationships tested lead to similar PIA values for the range of rainrates observed.

Once the parameters of the attenuation equation have been estimated, Eqs 2.4 and 2.5 form the basis for the Hitschfeld-Bordan algorithm. As already mentioned, such an algorithm may diverge; Delrieu *et al.* (1999a) proposed to limit the maximum PIA to be corrected to a pre-fixed value comprised between 10 and 20 dB, regardless of the considered wavelength. We will test in section 2.1.6 the influence of such an additional parameter in terms of rainfall estimation.

2.1.3 Physically-based data processing for radar QPE

Expanding the weather radar equation [see for instance Doviak and Zrnic (1993)], one may write a more detailed expression for the measured reflectivity factor compared to equation 2.1 on page 36 as:

$$Z_m = \delta_c r^2 \iiint_V \frac{A(s,\theta,\phi)W(s,\theta,\phi)\eta(s,\theta,\phi)}{s^4} dV \tag{2.9}$$

where (s,θ,ϕ) are spherical coordinates of a given elementary volume of atmosphere relative to the radar location and V [L^3] is the radar resolution volume. The reflectivity (sum of the backscattering cross sections of the hydrometeors per unit volume, [L^2L^{-3}]) is proportional to the reflectivity factor Z [L^6L^{-3}]. The function W [-] represents the product of the radial and angular weighting functions associated with the transmitter-receiver and the antenna characteristics, respectively. Let S and A [-] be the screening and the rain attenuation factors, respectively. equation 2.9 is useful to illustrate that:

1. A radar measurement is an integral over a volume (which size and height above the ground evolve as a function of range);

2. More standard expressions for the weather radar equation assume the reflectivity to be homogeneous over the radar resolution volume, while a well-known source of reflectivity heterogeneity is associated with the vertical variation of the temperature and DSD profiles;

3. Screening and rain attenuation may introduce additional sources of heterogeneity along the radial direction. Screening effects generally affect only part of the radar resolution volume.

Non-uniform beam filling was also shown to significantly alter attenuation correction schemes [Gosset and Zawadzki, 2001]. equation 2.9 expresses the complexity of the radar QPE which is likely to be affected by instrumental and sampling errors. These errors are associated with the high variability of rainfall and with environmental factors resulting in significant heterogeneity within the radar resolution volume.

2.1.4 Ground clutter and screening effects

Figure 2.1 shows ground clutter derived from dry-weather radar images. Figure 2.2 on page 34 illustrates the stability of ground clutter prior to and after the rain event, an indication of the probable stability of the transmitter-receiver unit during the rain event. To complement the characterization of the radar detection domain, simulations of the screening effects were realized with a digital terrain according to the procedure described by Delrieu and Creutin (1995). Figure 2.3 on the following page shows the results obtained for the lowest elevation angles (0.5° and 1°).

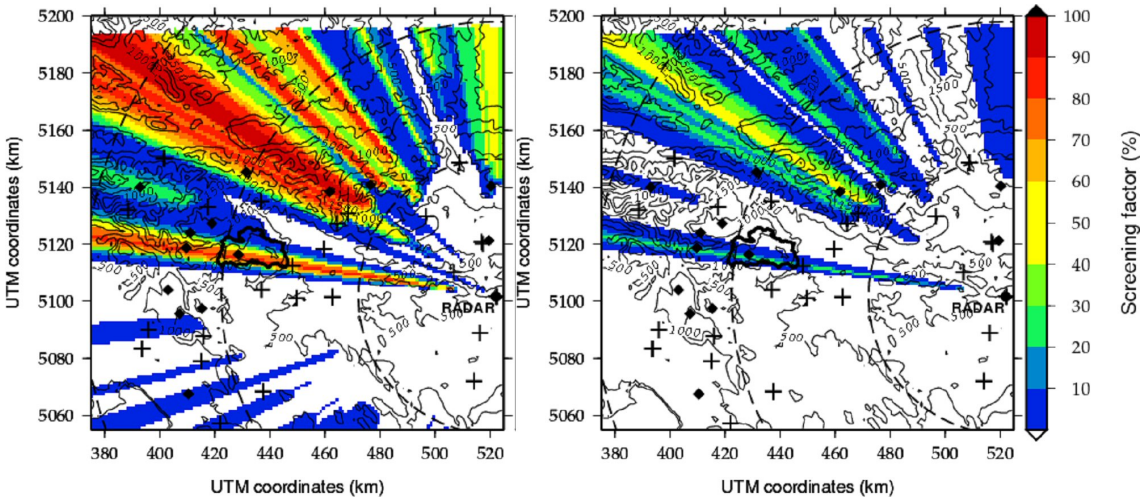

Figure 2.3: Screening factors expressed in percent of the transmitted power for the lowest elevation angles (0.5° left; 1° right). Note that the watershed of interest is severely masked in its southern part.

The mountains induce very significant screening effects. Higher elevation angles are basically free of screening effects. Note that a thin but severe mask affects the Železniki watershed with total occultation over the southern part of the watershed for the 0.5° angle while the maximum screening factor is equal to 30% for the 1° PPI.

In order to solve at best these occlusion problems and also to take in account effects due to apparent VPR we choose to apply the so-called principle of hydrologic visibility as explained by Pellarin *et al.* (2000).

This concept is based on the best choice of the radar data in terms of altitude from soil and in term of partial beam occlusion. First of all it is strongly necessary to have a well defined VPR (see the following section for all the details) calculated for each time step on a one hour floating window in radar time resolution and then couple this with screening effects. This kind of approach (a sort of real time adaptive approach) was not realistically usable in the present case study for problems in term of a great variability of the VPR due to the mainly convective nature of the studied event. So we choose a global apparent VPR that seems to be a good compromise between the requirement of work with the vertical variation of reflectivity and in order to have a not so great variability in terms of correction factors. For each elevation of radar antenna the algorithm used (called VisHydro) calculates the correction coefficients derived of

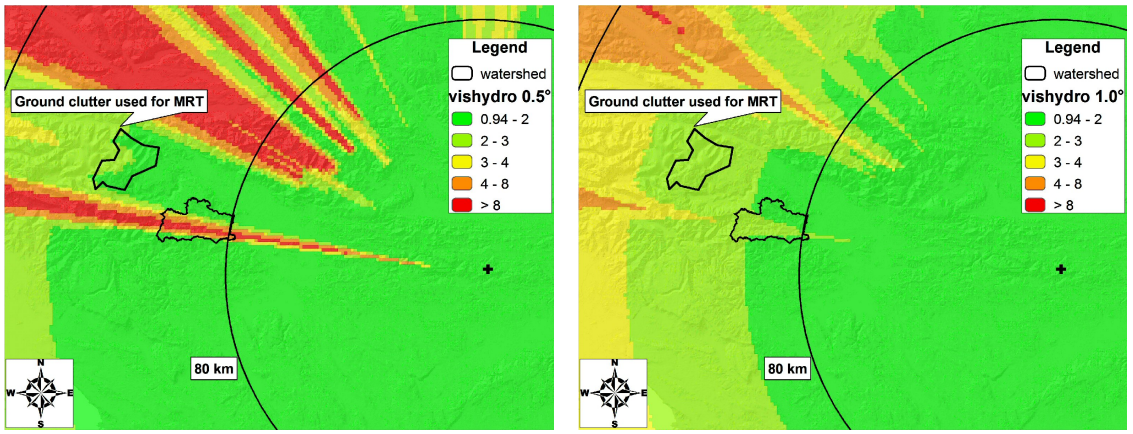

(a) (b)

Figure 2.4: Vishydro correction factors for the lowest elevation angles (0.5° left (a); 1° right(b)).

both screening and VPR analysis for the reflectivity (see Figure 2.4 on page 40), after that we use these coefficients for screening and VPR correction using a simple criterion: for every bin in the radar umbrella, if the value of the correction coefficient is less then 4 the lowest elevation is selected, if not the next elevation is used for rainfall esteem.

2.1.5 Vertical profiles of reflectivity

Figure 2.6 on the facing page displays the vertical profiles of reflectivity estimated for the 18 September 2007 case. We simply consider here apparent VPRs [Delrieu *et al.*, 2009] calculated by averaging measured reflectivities in a given radar range, 20-90 km here. Such profiles are normalized by mean reflectivity values observed close to the ground. We considered an altitude range of 0-1500 m MSL in the present case since the radar altitude is already 950 m MSL. With this basic approach, the VPR shape remains influenced (smoothed) by the beam sampling effects, especially in case of sharp vertical gradients related for instance to the presence of a bright band. The normalized apparent VPRs calculated every 10 min using a one-hour moving time window and the median profile are displayed in Figure 2.6 on the next page. In addition to the VPRs calculated globally over the chosen geographical domain, we realized VPR estimations after separating convective and stratiform regions using variants of the Steiner *et al.* (1995) and Sanchez-Diezma *et al.* (2000) algorithms, respectively. The individual VPRs present a rather high variability with slopes between 0 and -4 dB km^{-1} above 3 km MSL. The median VPRs are very similar for the global and convective cases with a slope of -3.6 dB km^{-1} above 3 km MSL. The median of the stratiform VPRs exhibits a smooth peak between 2000 and 4000 m MSL compatible with the radiosoundings available in Udine, Italy, at about 100 km upstream of the region of interest: the 0° C isotherm varied there from 3800 m MSL on 18/9/2007 0 UTC to 4000 m MSL on 18/9/2007 12 UTC and 2700 m MSL on 19/9/2007 0 UTC. During the most intense part of the rain event (between 0700 UTC and 1400 UTC), convection

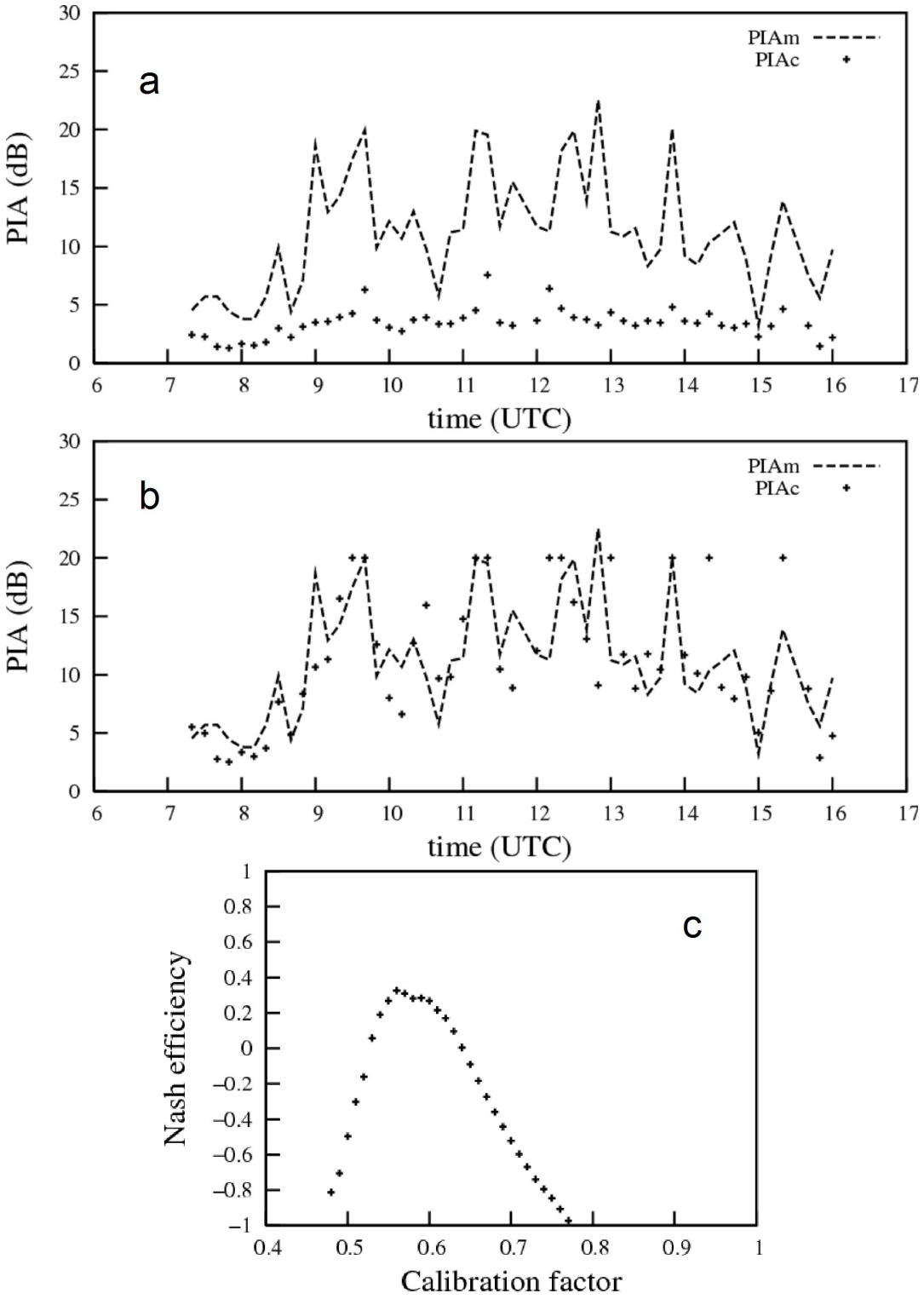

Figure 2.5: Illustration of the δ_c optimization procedure for the Cévennes DSD parameterization. Time series of the measured and calculated PIAs (a) with $\delta_c = 1$ (raw data), (b) with $\delta_c = 0.56$ (optimal value). (c) Evolution of the Nash criterion evaluated between the calculated and measured PIAs as a function of δ_c. Note that PIAs corresponding to divergences of the attenuation equation are artificially set to 20 dB and accounted for in the optimization.

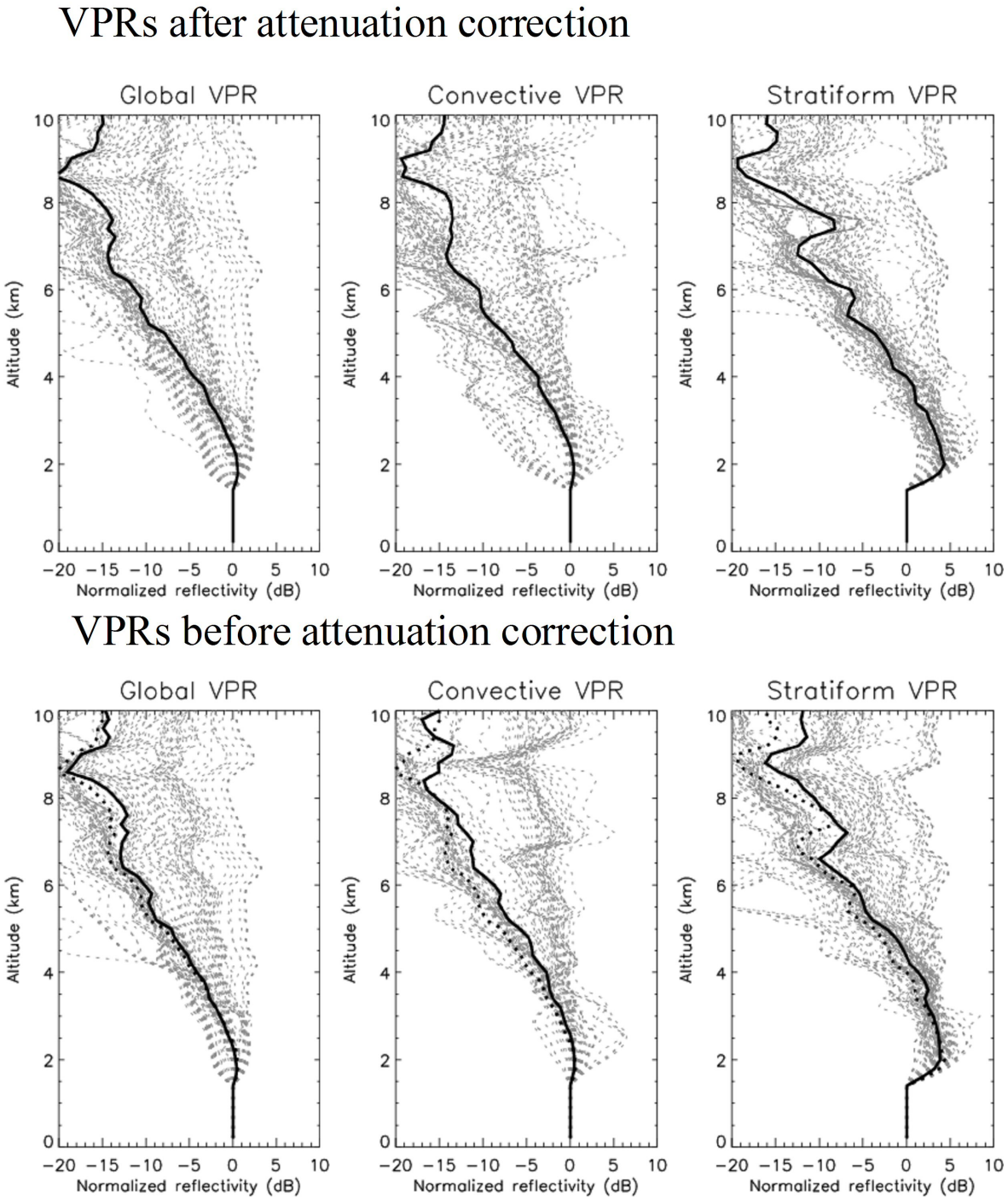

Figure 2.6: Normalized vertical profiles of reflectivity after (top) and before (bottom) attenuation correction, estimated globally (left) and for the convective (center) and stratiform (right) regions of the precipitating system. The grey curves correspond to individual VPRs estimated every 10 min over a 60-min time moving window. The continuous line is the median normalized VPR. In the bottom figures, the black dotted lines show the median normalized VPR shown in top graphs to ease the comparison.

was however the dominant process in the Železniki region, while a generalized stratification of the rain system occurred in the latest stages (after 1700 UTC).

To show the influence of rain attenuation, the VPRs estimated prior to and after the attenuation correction are also displayed in Figure 2.6 on the facing page. Interestingly, the attenuation correction increases the slope of the VPRs for both the convective and stratiform cases. This could be simply explained by the fact that the rain paths are longer for low elevation angles compared to those of upper elevations. In average, the attenuation correction is therefore stronger for low elevation measurements, resulting in higher normalization values for the VPRs, and the observed increased VPR slopes.

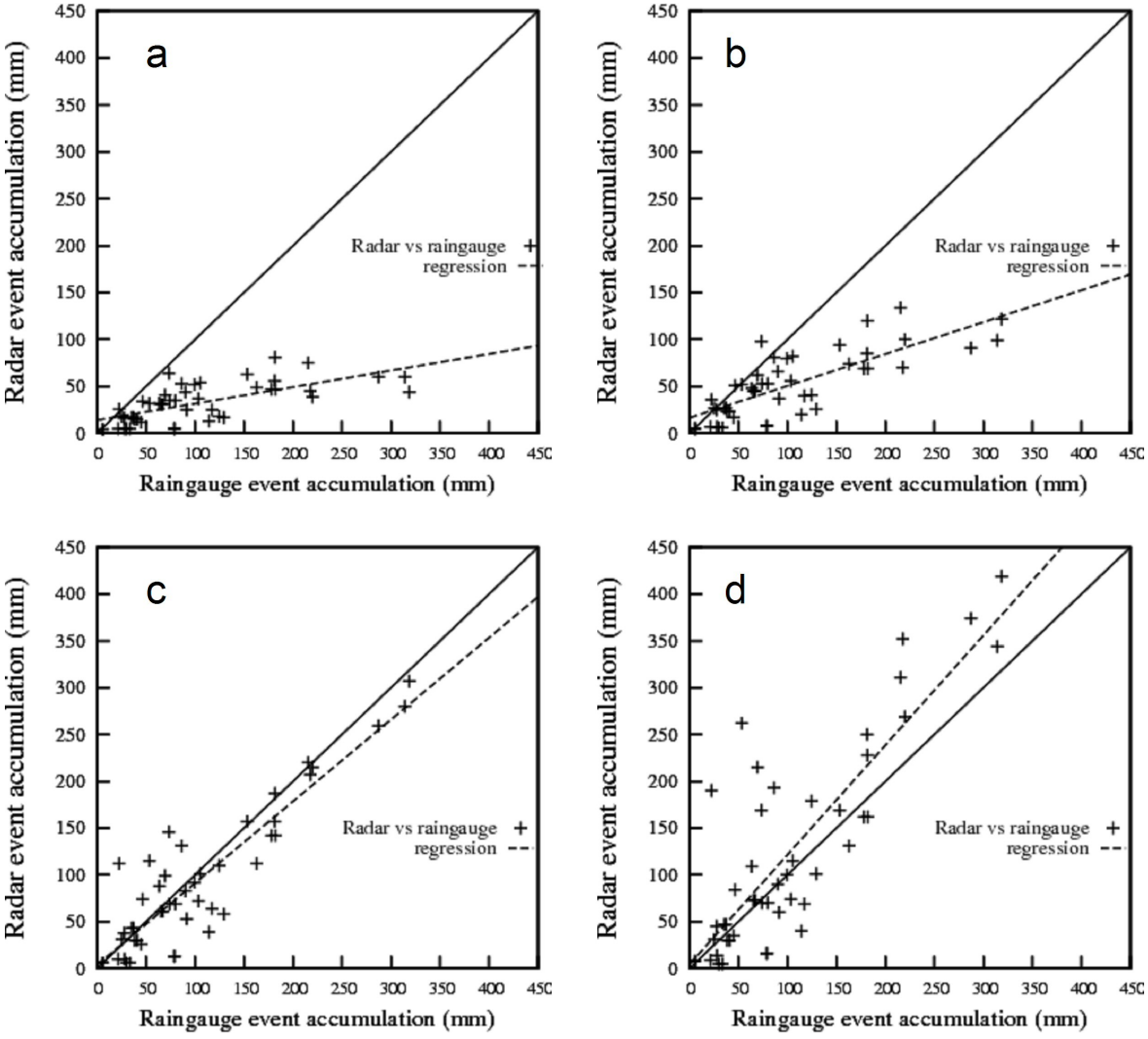

Figure 2.7: Scatterplots of radar versus raingauge measurements at the event time scale with the following radar data processing: (a) screening and VPR correction of the raw reflectivity; (b) in addition, the δ_c correction is performed; (c) in addition, the attenuation correction is performed with a maximum corrected PIA of 10 dB; (d) same as (c) with a maximum corrected PIA of 20 dB. The Cévennes (Z, k, R) relationships are used.

Due to the convection predominance in the region of the affected watershed, the similarity of the

convective and global mean VPRs and the non availability of rain-typed (Z, k, R) relationships, we have used the global VPR to represent the vertical variation of the reflectivity in the following section.

2.1.6 Radar QPE assessment

The radar QPE was implemented for various choices and parameterizations of the processing algorithms. Focus is given hereafter to the sensitivity of the attenuation correction on the (Z, k, R) relationships used, the calibration error and the maximum PIA value considered in the Hitschfeld-Bordan algorithm. The radar QPE performance was assessed with respect to the rain total amounts observed with the ARSO raingauge network. Classical assessment criteria such as the mean error, the determination coefficient (square of the linear correlation coefficient) and the Nash efficiency were evaluated. The values of the assessment criteria are listed in Table 2.3 on the next page; examples of radar-raingauge scatterplots and radar fields are displayed in Figure 2.7 and Figure 2.8, respectively.

The raw reflectivity values, simply corrected for screening and VPR effects and then converted into rainrates with a Z-R relationship, severely underestimate the observed rain amounts (first line in Table 2.3 on the following page; Figs. 2.7a and 2.8a). Application of the correction brings a significant, though insufficient, improvement as can be seen in second line of Table 2.3 on the next page and Figs 2.7a-2.8ab. The attenuation correction proves to be both effective in improving the radar QPE but also very sensitive on the maximum corrected PIA value used (lines 3-5 in Table 2.3 on the following page; Figs. 2.7c-d and 2.8c-d). The better estimations are obtained for the 10 dB maximum PIA for the Cévennes (Z, k, R) relationships. Note in particular that the values greater than 150 mm, corresponding to the most intense rainfall pattern, are almost unbiased and present a small scatter. The higher scatter observed for lower rain amount values is related to poor corrections for both the screening effects in the north-west part of the radar detection domain and for comparison points at ranges greater than 120 km. Although PIA values up to 20 dB were observed between the radar and the mountain reference target (Figure 2.2 on page 34), the well-known instability of the attenuation equation has a dramatic impact on the radar QPE when this threshold is considered (Figs. 2.7d and 2.8d). The assessment criteria are very significantly downgraded compared to both the 10 dB and 15 dB thresholds (Table 2.3 on the following page). As suggested by Delrieu *et al.* (1999a), the former threshold appears as a good compromise here with the implementation conditions considered (adjustment for the radar calibration error, unique set of (Z, k, R) relationships).

Comparison of the results obtained with the three sets of (Z, k, R) relationships indicates that the widespread and Cévennes relationships lead to good and almost equivalent results (with a slight superiority for the widespread relationships parameterization, however) while the radar QPE for the thunderstorm relationships lead to worse results. In particular, although the radar calibration factor was adjusted, the radar QPE remains significantly underestimated in that case for the 10 and 15 dB PIA thresholds while the attenuation equation instability worsen the estimates for the 20 dB PIA threshold. Such results call

(Z, k, R) relationships	δ_c	Attenuation correction	PIA$_{max}$ (dB)	VPR	Nash criterion	Error mean (mm)	Determin. coeff.
Cévennes	1.00	no	-	Median	-0.51	-70.4	0.45
Cévennes	0.56	no	-	Median	0.07	-51.1	0.60
Cévennes	0.56	yes	10	Median	0.80	-9.1	0.82
Cévennes	0.56	yes	10	Time-adaptive	0.77	-15.5	0.81
Cévennes	0.56	yes	15	Median	0.71	2.0	0.77
Cévennes	0.56	yes	20	Median	0.32	21.9	0.70
Widespread	0.59	yes	10	Median	0.80	5.7	0.84
Widespread	0.59	yes	15	Median	0.72	13.1	0.86
Widespread	0.56	yes	20	Median	0.42	23.6	0.78
Thunderstorm	0.55	yes	10	Median	0.69	-24.4	0.79
Thunderstorm	0.55	yes	15	Median	0.62	-11.8	0.68
Thunderstorm	0.55	yes	20	Median	0.33	7.9	0.57

Table 2.3: QPE assessment for various parameterizations of the radar data processing.

for several comments. Firstly, a certain degree of equifinality is likely for the attenuation correction parameterization and the adjustment of the calibration factor allows compensation for part of the eventual inadequacy of the Z-k relationship. It should be noted that since the MRT works with PIA estimates and allows for an adjustment of the radar calibration for a given Z-k relationship, the Z-R conversion is not optimized in any manner in this procedure. Using (Z, k, R) models consistent with the underlying DSDs is therefore particularly critical for such an approach. In this respect however, the fact that the widespread relationships yield the best results for this convective event illustrate the gap between physical parameterizations that can be determined over small volumes with disdrometers and the effective parameterizations at the scale of the radar resolution volume.

As a final test, lines 3 and 4 in Table 2.3 allow comparison of the results obtained by considering a time-adaptive global VPR and the median global VPR. The latter solution yields the better results and it was then preferred in the radar QPE implementation for the other simulations listed in Table 2.3.

2.1.7 Conclusions

This section was dedicated to radar rainfall estimation for the post-event analysis of a Slovenian flash flood that occurred on 18 September 2007. The utility of the Mountain Reference Technique (MRT) was demonstrated to quantify and correct rain attenuation effects that affect C-band radar measurements in heavy rain. Maximum PIAs between 15 and 20 dB were measured thanks to mountain returns for path-averaged rain rates between 10 and 15 mm h^{-1} over a 120 km path. By considering the PIA constraint equation, the MRT allowed estimation of an effective radar calibration correction factor, assuming a DSD model and the subsequent (Z, k, R) relationships to be known. Besides rain attenuation, screening effects were quantified using a geometrical calculation based on a digitized terrain model of the region. A thin

mask affecting the two lowest elevation angles above the Železniki watershed complicated the estimation problem for this region of special interest. The vertical structure of the reflectivity was modelled with the normalized apparent VPR estimated globally without rain type separation.

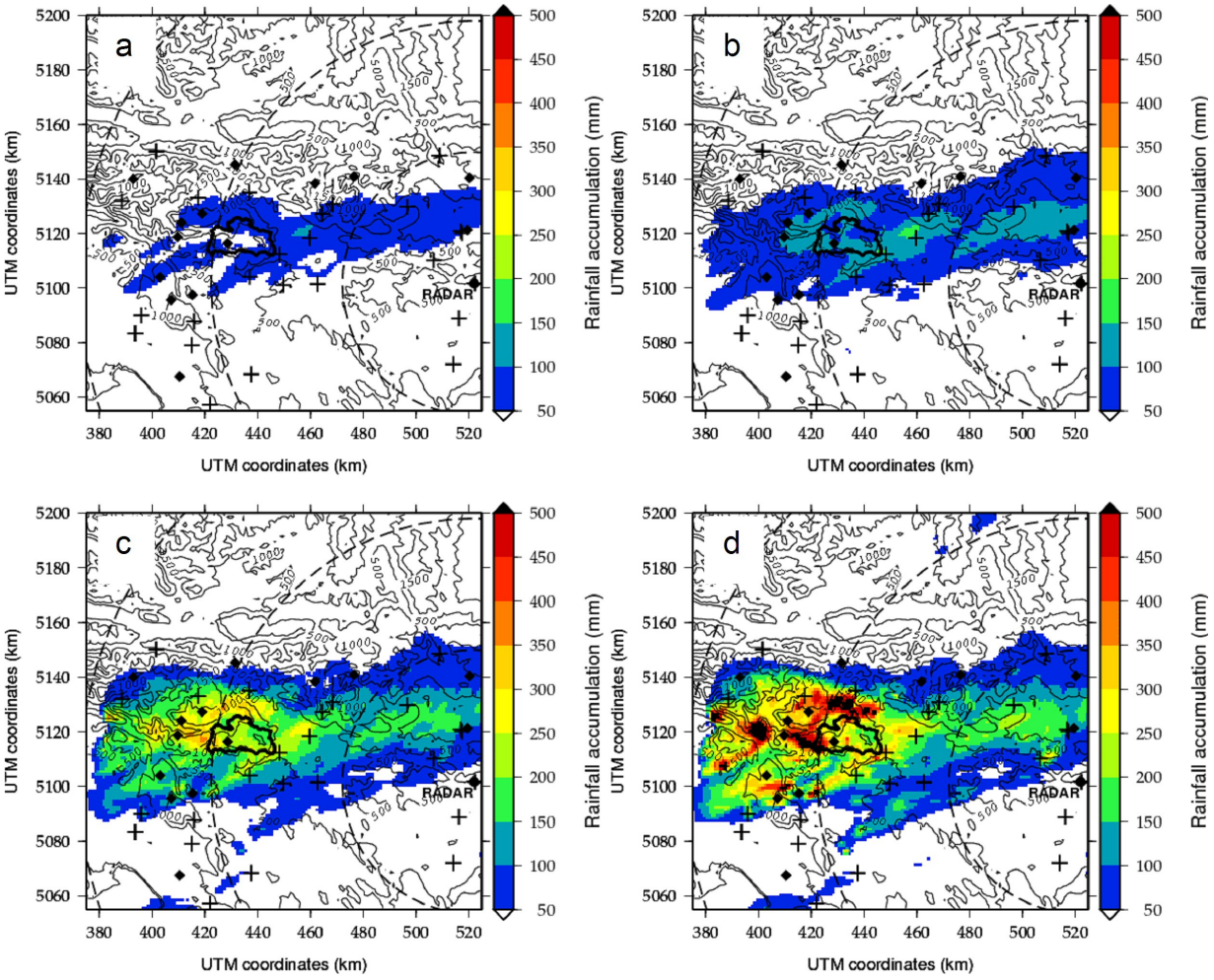

Figure 2.8: Radar fields at the event time scale with the following radar data processing performed with the Cévennes (Z, k, R) relationships: (a) screening and VPR correction of the raw reflectivity; (b) in addition, the δ_c correction is performed; (c) in addition, the attenuation correction is performed with a maximum corrected PIA of 10 dB; (d) same as (c) with a maximum corrected PIA of 20 dB.

Implementation of the radar data processing indicated that:

1. Attenuation correction over the entire detection domain using the Hitschfeld Bordan algorithm allowed obtaining good radar QPEs (Nash criterion of 0.8 at the event time scale), especially for the most intense rainfall pattern;

2. Due to the attenuation equation instability, it is however compulsory to limit the maximum PIA to be corrected to about 10 dB;

3. The results also proved to be sensitive on the choice of the (Z, k, R) relationships.

The convective nature of the precipitation explains the rather good performance obtained. For more contrasted rainy systems with convective and stratiform regions, the combination of the vertical (VPR) and radial (attenuation, screening) sources of heterogeneity yields a still very challenging radar QPE problem.

The big sensitivity of the forward attenuation correction scheme on the maximum PIA, even with an adjusted radar calibration, prevents implementation of such an algorithm in real-time application. However, in the context of post-event studies, this simple method controlled with some raingauge measurements at the event time step proved to be useful. It is worth reminding that backward correction algorithms, starting from a reference target, are very stable and much less sensitive to parameterization errors compared to the forward scheme used herein [Marzoug and Amayenc, 1994]. Such algorithms could be implemented easily if the region of interest was surrounded by a belt of mountain targets.

The radar QPE space-time series are now being used as input for the distributed hydrologic modeling of the Zelezniki flash flood. A striking result of the radar QPE analysis (Figure 2.8c) indicates that maximum rainfall occurred outside the Železniki watershed. This is motivating additional field investigation to assess the flash-flood impacts in this less vulnerable area.

2.2 Anterselva case and the importance of the accurate geo-spatial representation

In this section a case of a strong concentrated in space and time rain event will be presented. No raingauges are available on the small basin involved and only radar wheatear data from Monte Macaion C band radar can be used in order to analyze the storm evolution and the rainfall field.

This event represents a really challenge for his characteristics, a few error in the georeferenciation process can be a source of error that could be determinant and invalidates the entire case study understanding.

It is not so easy to use radar data in a small mountain basin, mainly if the radar antenna is up to 80 km far from the basin location (see Figure 2.9). It seem to be clear that the rain field georeferenciation has to be verified and validated as best as possible. A good way to do that is the use of ground clutter signal in conjunction with the simulated ground signal, performed by the application of the Surfillum algorithm [Delrieu and Creutin, 1995].

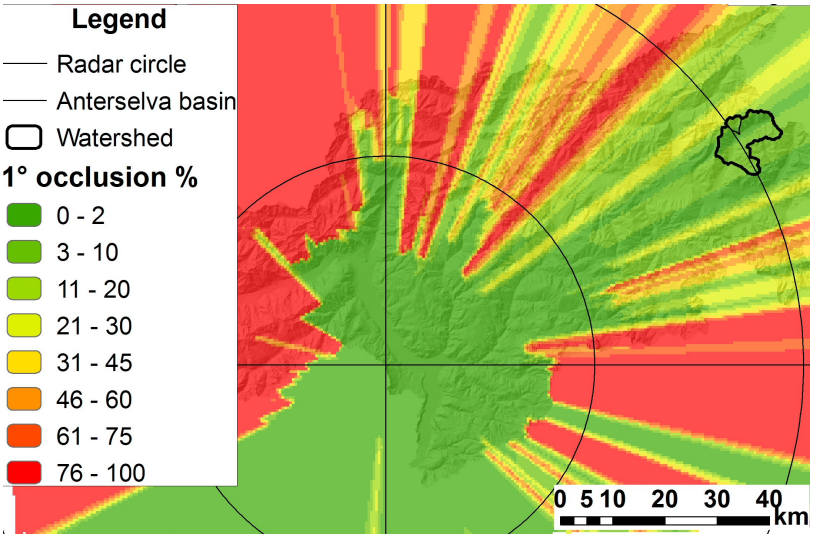

Figure 2.9: Position of Monte Macaion C band radar and Anterselva river basin, it is also presented the radar partial % occlusion at 1° of antenna elevation (radar circles at 40 km).

In Figure 2.10 on the following page the observed and simulated ground clutter pattern are presented, even if this two maps seems to be very similar it is also evident a little miss-positioning of some clutter signal. This effect is amplified when the distance from radar increases. The most probable source of this kind of error is a not perfect orientation with the geographical north of the radar antenna. So when the distance from radar antenna is less then about 40-50 km and the study area greater than some km^2 any possible error due to a non perfect correspondence between radar and DTM north orientation can be neglected.

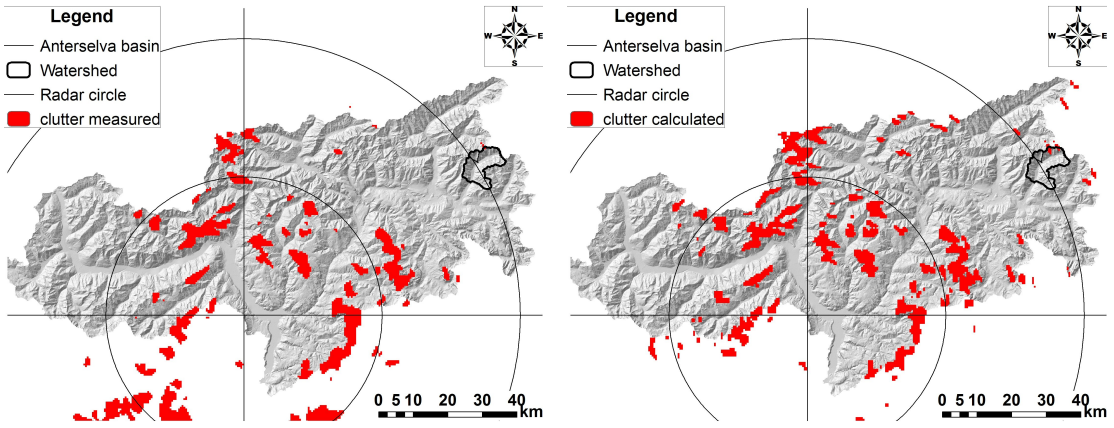

Figure 2.10: (a) Ground clutter observed by Monte Macaion C band radar; (b) ground clutter simulated by Surfillum, Delrieu and Creutin (1995).

On the contrary in this case it becomes underlying to take in account this fact as the prevalent source of georeferenciation error.

In Figure 2.11 two maps of spatial superposition for simulated and measured ground clutter is presented. It appears to be evident that at a distance in range of about 80 km from radar antenna the effect of a non perfect superposition of ground pattern can be a pointer of a significant georeferenciation error. In the case study presented here an error like that, more or less 2° of miss-alignment, can be mean an error of some kilometers in the Anterselva basin area. In Figure 2.19 a-b the total cumulated rainfall map is presented, if in particular we direct our attention to figure 2.19 b the importance of a strongly good radar rainfall pattern positioning appears to be more than evident. After the correction done using the ground clutter pattern and the Surfillum algorithm a good correlation between the thunderstorm event and landslide phenomenon can be found.

2.2.1 Event description

An intense orographic convective system mainly localized in the limited area of Rio Gola basin (6.59 km^2), central Italian Alps, produced locally extreme rainfall peaks in 1.5 hours on August 1, 2005. The storm concentrated on small, rocky and steeply sloping basin where concentrated overland flow feeds ephemeral channels incised in slope deposits. Despite the short duration of the event the storm triggered an unusually large debris flow, with a volume of about 100,000 m^3, producing significant geomorphological impacts and abrupt changes in the extent of incision and channel widening. Hydrometeorological analysis of the storm are based on radar reflectivity observations, raingauge and streamgauge data. The small multicell thunderstorm that triggered the debris flow was not markedly different from other storms in the region which not resulted in debris flows. Detailed geomorphological field surveys, rainfall estimates from radar observations,

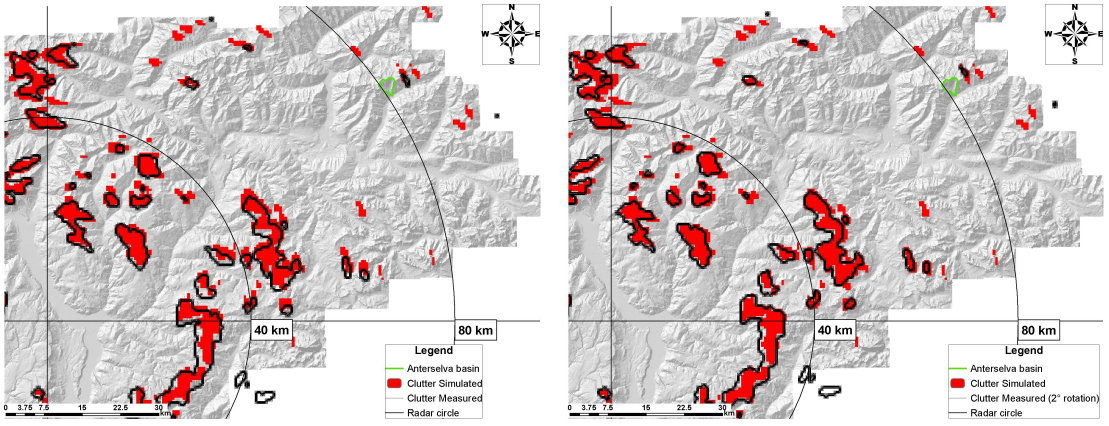

(a) (b)

Figure 2.11: Superposition of simulated (in red) and measured (black lines) ground clutter at 1° of radar antenna elevation: (a) without any correction; (b) with a 2° anticlockwise rotation of radar umbrella.

and the application of a distributed hydrological model in comparison with observed discharge, served as the basis to evaluate erosion processes and quantify the water runoff production at the initiation debris flow area. The hydrological analysis is used to evaluate the consistency among the different observations and to identify the critical factors controlling the debris flow triggering. The hydrological analysis shows that the critical factor is storm concentration on rocky and steeply surfaces and formation of concentrated surface flow at the bottom of channels filled by coarse loose debris.

In mountainous landscapes, where shallow landsliding is the primary erosional process, and often is one of principal causes for the debris flows activation, [Dietrich and Dunne, 1978; Okunishi and Iida, 1981; Johnson and Rodine, 1984; Benda and Dunne, 1997] the rock outcrops play an important role in the activation of slope failures during intense rainfalls [Tarolli *et al.*, 2008]. A relatively common debris flow initiation process in the European Alps is represented by concentrated surface flow at the bottom of channels filled by coarse loose debris. In this case, the shear force of water mobilizes individual particles and the solid concentration increases until it reaches an equilibrium dependant on slope angle and water supply. Debris flows thus initiate when a critical surface discharge, rather than a critical groundwater level, is reached. Debris flows initiated by channel bed mobilization are far less studied and poorly understood compared to landslide-induced debris flows. In particular, a framework to adequately characterize runoff generation, erosion processes, and debris flow generation is still missing.

An intense thunderstorm occurred during the 2005 summer season in a region of the Central Italian Alps triggered a large debris flow with a volume of about 100000 m^3, producing significant geomorphological impacts and abrupt changes in the extent of incision and channel widening. The availability of radar rainfall estimates makes it possible to couple spatially-distributed data on precipitation rate with post-event field observation of type and distribution of geomorphic processes [Hicks *et al.*, 2005; Vivoni *et al.*, 2006]. The post-event field observations suggested that debris flow was initiated at the base of a very steep rocky

area of 500 m in length. The purpose of this study is to document the debris flow activity and the related initiation processes occurred during the intense thunderstorm of summer 2005, specifically:

1. To explore the viability of using ground-based meteorological radar to examine geomorphic processes triggered by specific combination of high intensity rainfall cells and ground characteristics (distribution of rocky outcrops);

2. To assess the role of the initial conditions on the characteristics of the hydrologic and geomorphic response to the storm;

3. To adequately characterize runoff generation at the micro scale of observation in proximity of debris flow initiation area.

2.2.2 Study Area

Physiographic and geologic settings

The area interested by thunderstorm of August 2005 covers a surface of about 6.59 km^2, and it is a small sub-basin of great hydrographic basin of Anterselva (82.7 km^2) (Figure 2.12 on the facing page). Elevations range between 1330 and 3230 m a.s.l., with an average value of about 2000 m a.s.l.. The slope angle has an average value of 30° with maximum values of 70° in proximity of head valleys steeper rocky places. The area presents a morphological step at around 1500 m a.s.l. were the Rio Gola stream reaches its tributary (Figure 2.12 on the next page). The Rio Gola stream contributed to propagate the debris flows materials occurred during the thunderstorm downslope the valley to the junction with main stream of the study area, Rio Anterselva (Figure 2.12 and Figure 2.13). In proximity to Rio Anterselva streams, where low slopes prevail, there are depositional areas of debris flow events frequently observed during last decade. The head of the Rio Gola valley is interested by a 500 m of steep rocky cliffs (Figure 2.12 and Figure 2.13). This place is also the summit (3230 m a.s.l.) of the study area. In proximity of the rocky area is located the small headwater rocky basin (Figure 2.14 on page 55) of 0.22 km^2 where most of rainfall occurred during thunderstorm of August 2005 was concentrated. In proximity of its outlet, within talus deposits area, is located the triggered point of major debris flow analyzed in this study (Figure 2.14 on page 55). This small area was glaciated several times during the Pleistocene. During the little ice age (200 BF) the glaciers have revealed a little increment in surface. Now at the head of the basin only a relict glacier behind erosion deposits is present. This place is usually interested during the summer season by an intense erosion activity due to glacial retreat process.

The bedrocks of Rio Gola basin are structured in two lithologic complexes: the Austroalpine basement on the south, and the Vedrette di Ries pluton on the north. The Austroalpine basement actually has mainly dominant paragneiss and micascisti, with some infiltration of ortogneiss pegmatici, metabasiti, marmi and

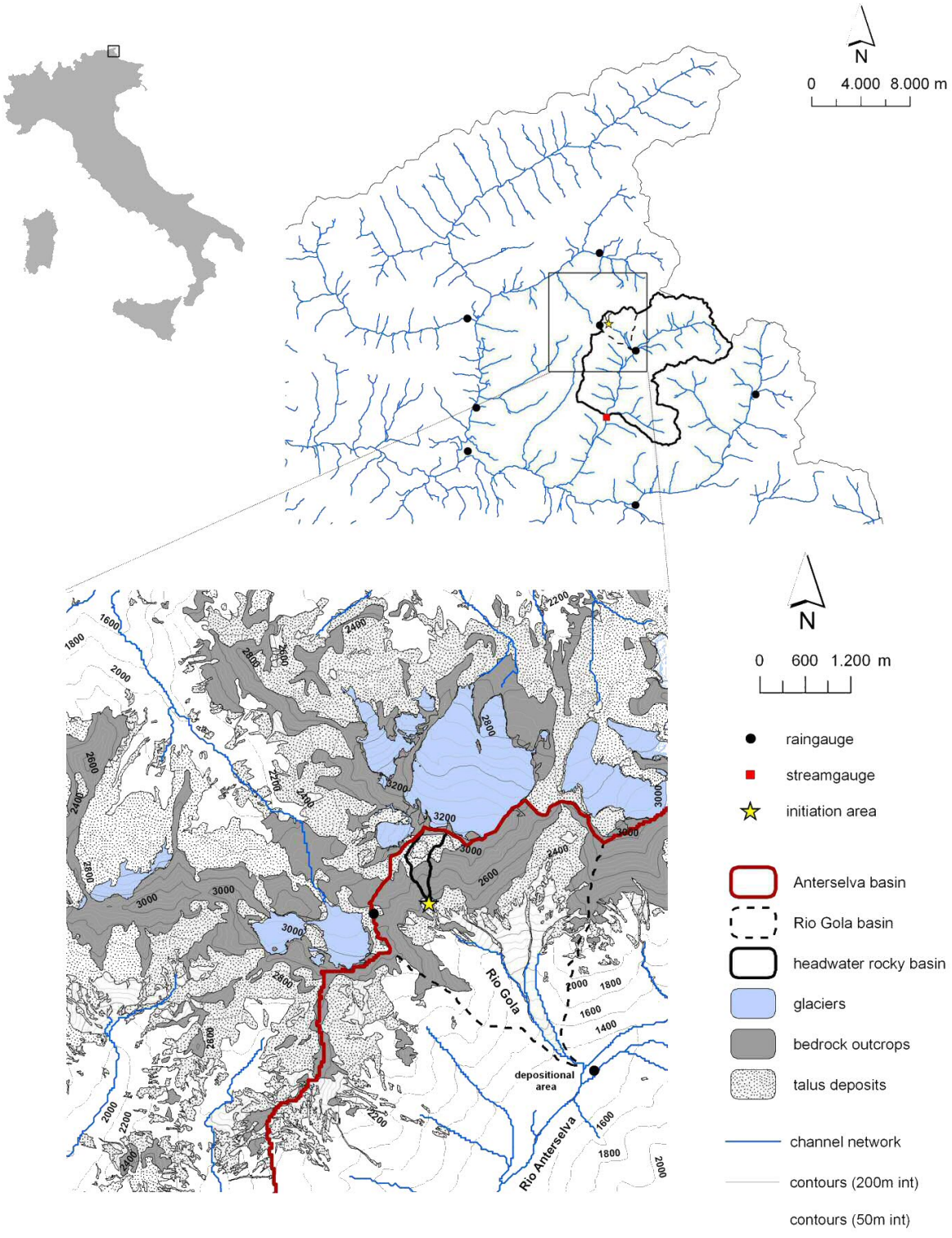

Figure 2.12: Location map of the study area. Figure shows also the location of raingauge and streamgauge.

quarziti [Mager, 1985; Cesare, 1999]. The Vedrette di Ries pluton [Cesare *et al.*, 2004] is an intrusive complex sited in the Austroalpine basement since Pleistocene era (30000 BF).

In the debris flow initiation area substrata has dominant of fine granodiorite. Subvertical faults in the direction N-S are also present. The large Quaternary landslide deposits may presents differences in relation to the elevation and morphologic context. While the debris deposits are equal distributed over the study area and may be vegetated and unvegetated in relation to the elevation, it is possible to distinguish two kind of morainic deposits: a) the relative new and active unvegetated morainic deposits related to the little ice ages (200 BF) and located in places up the 2200 m a.s.l., b) the vegetated morainic deposits related to the last great ice era (Pleistocene).

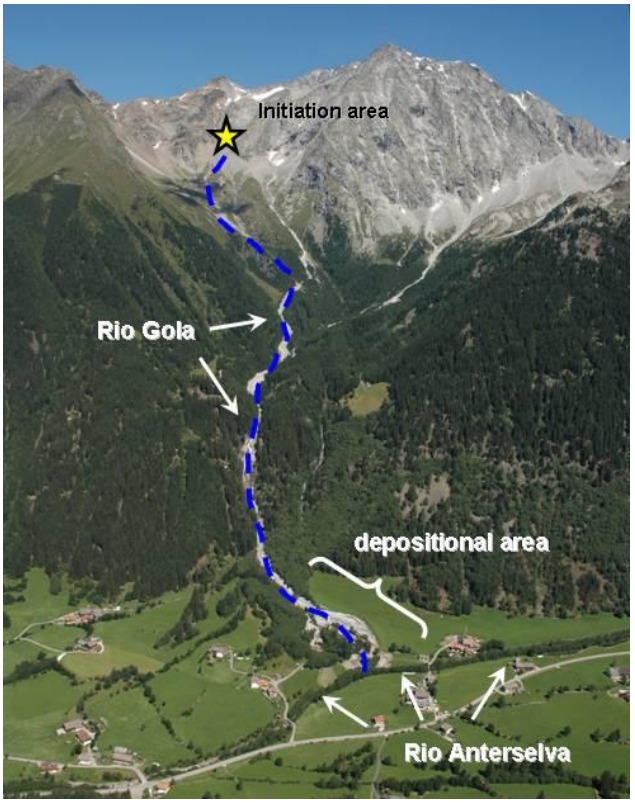

Figure 2.13: Helicopter photograph showing initiation area of debris flows occurred during thunderstorm of summer 2005. In the same figure is showed also the depositional area of triggered material. Photograph taken few days after the thunderstorms of 1 Agugust.

Climate of the region is characterized by dry periods during summer, and a mean annual rainfall of about 1100 mm, ranging from 600 to 1400 mm. Precipitation occurs mainly as snowfall from November to April. Runoff is dominated by snowmelt in May and June but summer and early autumn floods represent an important contribution to the flow regime. In summer storm events are usually intervalled by long dry spell. Vegetation covers 43% of the area and consists of forest stands (52%), shrubs (10%) and mountain grassland (38%); the remaining 57% of the area is vegetated-unvegetated talus deposits, bedrock outcrop,

and glacier.

Figure 2.14: Map showing the small headwater rocky basin at the head of Rio Gola basin. In the same figure is mapped the triggered points of debris flows, debris flow path, and indicated the rocky valley step.

Post event field survey

Field observations aimed at assessing the debris volumes mobilisable by debris were carried out during week immediately after debris flow event in order to determine the contribution of sediment source to the overall sediment budget and to characterise runoff processes. This provided a unique opportunity to evaluate the geomorphic impact of a catastrophic debris flow. The observations indicated that initiation process was function of the abundance of hillside materials. All the slope instability occurred between 2100 and 2700 m a.s.l. at the base of 600 m rocky cliffs. The debris flow path length was about 3080 m starting from the base of rocky cliffs (2580 m a.s.l.) and finishing at the depositional area close to the junction of Rio Anterselva (1350 m a.s.l.). The channel network and the sediment sources on side slopes were surveyed for assessing debris volumes eroded. LiDAR elevation data in addition to high resolution aerial photographs collected after debris flow event served as the basis to give a detailed representation of sediment source areas. In Figure 2.15a is showed the sediment source area where debris flow was initiated, specifically is showed the deep erosion channel causing sediment production, while in Figure 2.15b the map of landform curvature (m/m^2) derived by LiDAR DTM with grid size of 2.5 m. Landform curvature ($\nabla^2 z$) is useful in distinguishing dominant landform processes. In general terms, the divergent-convex landforms ($\nabla^2 z < 0$) are associated with the dominance of hillslope processes and concave-convergent ($\nabla^2 z > 0$)

landforms with fluvial-dominated erosion. The high resolution details given by fine DTM allow to well identify concave-convergent landforms as in our case the sediment source channel, and quantify the are interested by erosion activity, evaluated to be 12,606 m^2.

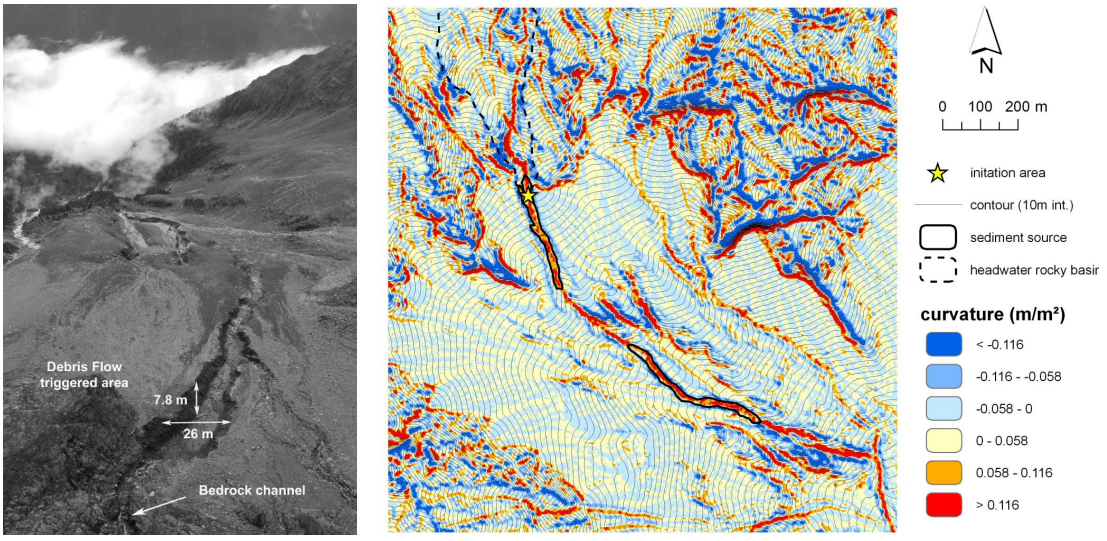

(a) (b)

Figure 2.15: (a) Debris flow channel excavation in proximity of initiation area; (b) map of curvature derived by high resolution LiDAR DTM with 2.5m grid size.

Most of the sediment mobilized by debris flows was deposited by the confluence with Rio Anterselva stream (Figure 2.16 on the facing page): its bed was invaded by transported sediments, one bridge was broken and some fields were totally covered by mud and rocks. The transported and accumulated sediment manly consisted woody debris, mud, gravel, stones and boulders, merged in silt matrix. The grain size diameter of triggered materials ranged from few mm (silt matrix) to values greater than 1 m (2.16 c). The event caused huge damages to the local road system, bridges, and some buildings.

Figure 2.17 on page 58 shows scatterplot of debris-flow magnitude versus drainage basin area [D'Agostino and Marchi, 2001; Marchi and D'Agostino, 2004] of the August 1, 2005 event in the Rio Gola with a sample of 127 debris flows observed since late 19th century in North-eastern Italy. An upper limit can be outlined, which approximately corresponds to a unit value of 70000 m^3 km^{-2}. This limit expresses the maxima that were attained in the considered region due to high intensity storms in basins where large amounts of sediment were available. It is possible to note that debris flow event of summer 2005 is close to upper limit of debris flow magnitude, thus underlining the high intensity of the event under study. Since even small-magnitude debris flows can be very hazardous, e.g. when they affect railways and motorways, attention was also paid to the lower limit of debris-flow volumes. Minimum values of 1000 m^3 are often observed and only in two cases were lower values reported. Debris flows of lower magnitude do occur, but they are reported only for very few basins which were carefully surveyed because of their potential danger

(a)

(b)

(c)

Figure 2.16: (a) depositional area; (b) deposits close to buildings; (c) boulders deposited along the debris flow propagation path of the debris. In the picture it is showed the diameter of the biggest boulder and the height where the mud spray was left along the debris flows path. Photograph taken few days after the last thunderstorm.

[Marchi and D'Agostino, 2004].

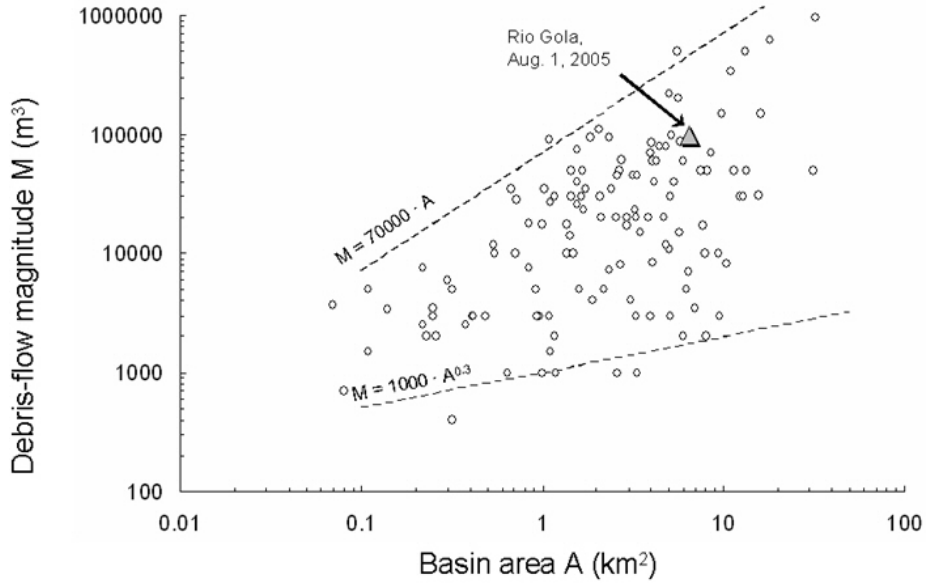

Figure 2.17: Scatterplot of debris-flow magnitude versus drainage basin area (from D'Agostino and Marchi (2001)).

A survey on soil hydraulic properties was carried out during post event field surveys. Values of field saturated hydraulic conductivity were obtained by using a Guelph permeameter at x different sites. In Table 2.4 on page 61 are reported the values of hydraulic conductivity collected under different land use conditions. Scree slopes downslope rocky areas, were randomly selected for analysis of physical characteristics of their deposits. The graphic mean grain diameter was estimated to be -1.8 $\pm$ 1.05 in φ units. Bulk density was determined in the field by the excavation method, and total porosity was calculated from bulk density after particle density of rock fragments was measured. All these analyses provided a basis for parametrization of the distributed rainfall-runoff model and to discriminate land use impact on infiltration potential.

2.2.3 Hydrometeorological analysis

Rainfall

Estimates of the spatial extent of intense rainfall are available from the C-band Doppler radar on the Monte Macaion station (1860 m a.s.l.) located 70 km far from the study area. The radar characteristics consisted in a time resolution of 6 min, and spatial resolution of 250 m in range by 0.9 degree in azimuth. This represent a long range for radar applications in meteorology, therefore it has been observed an under estimation of real precipitation due to the air and rain attenuation of radar beam. Radar reflectivity observations were used to reconstruct the time series of rainfall rate over study area by adjusting for beam

occlusion, wavelength attenuation and by converting reflectivity to rain rate using the convective Z-R relationship. Finally, a bias correction based on comparison with rain gauge observations was applied. The climate of the summer 2005 presented a trend normally observed during the summer season in this Region of the Italian Alps. The July presented a little cold and wet climate for its first part than a warmly and wet second part. The august was variable with a higher convective system activity than July.

On 1 August 2005 an intense orographic convective system affected the study area, starting at 2130 CET (Central European Time) and lasting for approximately 1.5 hours. The storm affected a 10 km^2 wide area. The comparison of rainfall obtained from raingauge and radar-based estimates after adjustment shows a general good agreement; the largest rainfall accumulations are accurately portrayed by radar.

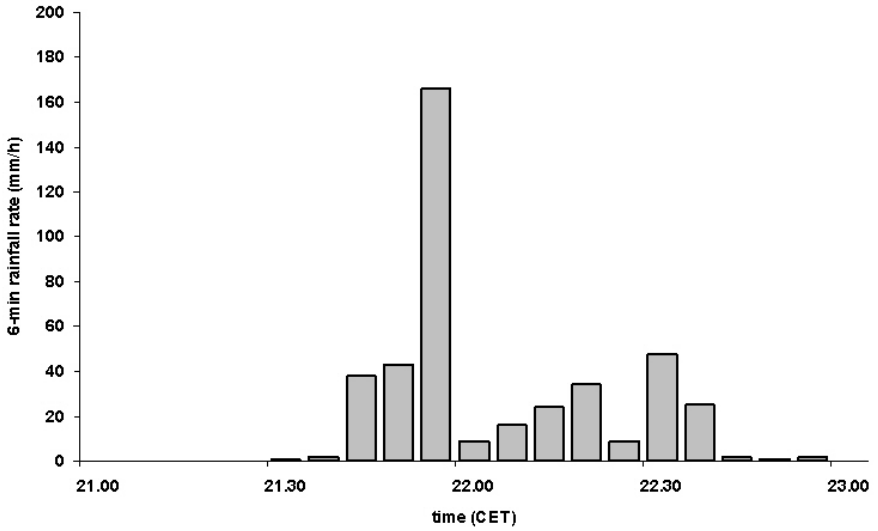

Figure 2.18: The rain rate time series (estimated in mm h^{-1} over 6 minutes) of 1 August thunderstorm, related to the most instense rainfall occurred at the head of headwater rocky basin.

The rain rate time series (estimated in mm h^{-1} over 6 minutes) (Figure 2.18), related to the most intense rainfall occurred at the head of headwater rocky basin, show a sequence of three rainfall pulses. The first pulse, starting at 2130 CET and lasting for half hour, shows a maximum of 166 mm h^{-1} at 2154 CET. A very brief period of lower intensity rainfall was followed by the second pulse of rainfall rates (up to 34 mm h^{-1}) ending at 2218 CET. The third rainfall pulse can be recognized, with a rainrate peak of 48 mm h^{-1} at 2230 CET. Total estimated rainfall was 42 mm. Temperature measured at meteo-station of Vedrette of Ries (2791 m a.s.l) ranged from 8 $^\circ$ C to 10 $^\circ$ C.

A detailed map of total cumulated rainfall is showed in Figure 2.19 on the following page. In the same figure are also mapped the small headwater rocky basin, the Rio Gola basin, the borders of Anterselva basin, in addition with distribution of raingauge stations and debris flow initiation area. Looking at the map it is possible to distinguish a cell with values of total cumulated rainfall greater than 40 mm, at the head of the small rocky basin, upslope the rocky cliffs and in proximity of slope failures.

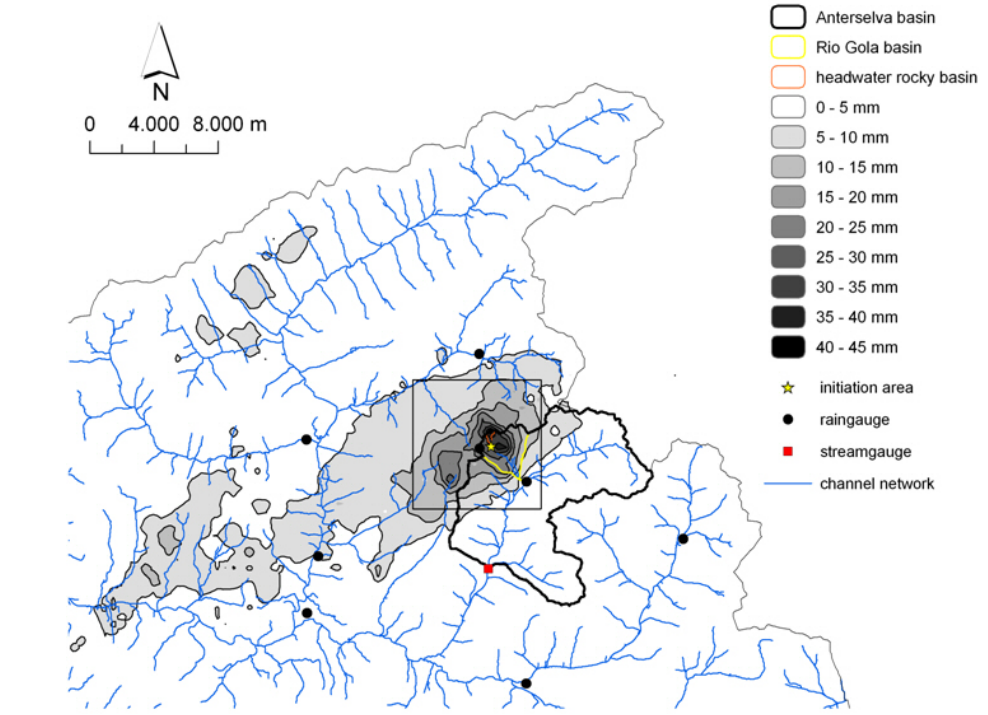

(a)

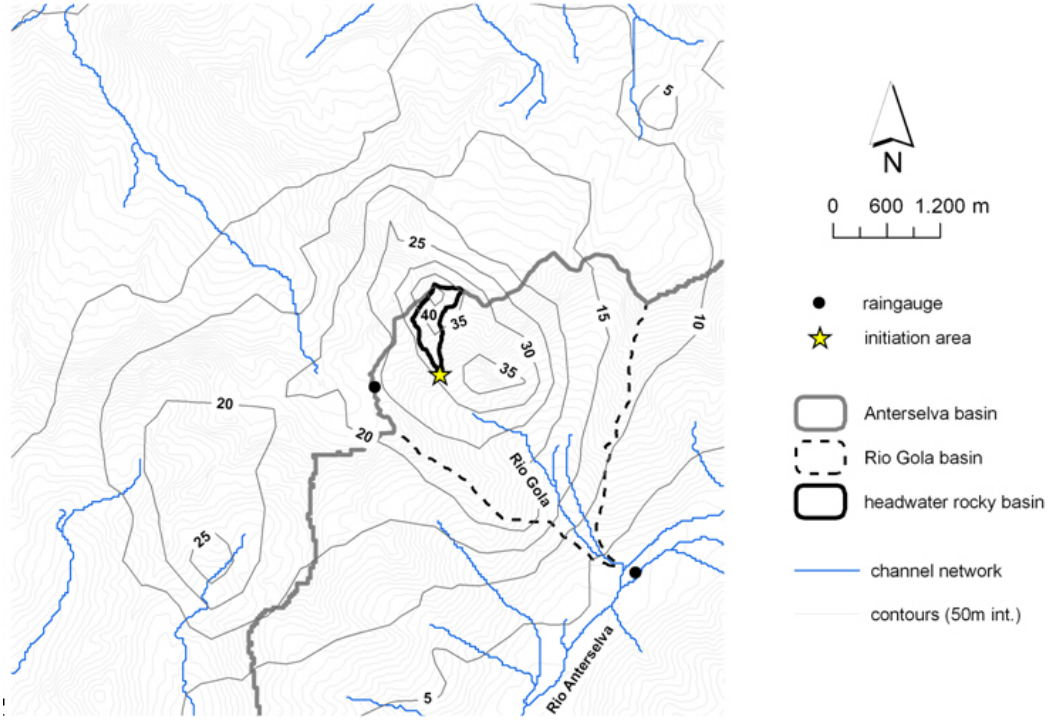

(b)

Figure 2.19: Map of total cumulated rainfall occurred during thunderstorm.

	bedrock outcrops	talus deposits	grassland	forest
Lateral saturated hydraulic conductivity m h^{-1}	0.0	5.0	0.5	1.0
Vertical saturated hydraulic conductivity m h^{-1}	0.0	0.1	0.02	0.02

Table 2.4: Soil hydraulic conductivity observed in the field.

Some intensity vs duration empirical equations proposed in literature [Caine, 1980; Wilson and Wieczorek, 1995; Deganutti and Marchi, 2000; Gregoretti and Dalla Fontana, 2006] were then adopted, and compared with radar estimated rainfalls in order to evaluate the rainfall intensity and duration thresholds that cause slope to fail for analyzed event. The results showed in Figure 2.20 on page 61 suggested that event of 1 August 2005 presented an hazardously condition for debris flow initiation, the values in fact are clearly above the literature threshold-values.

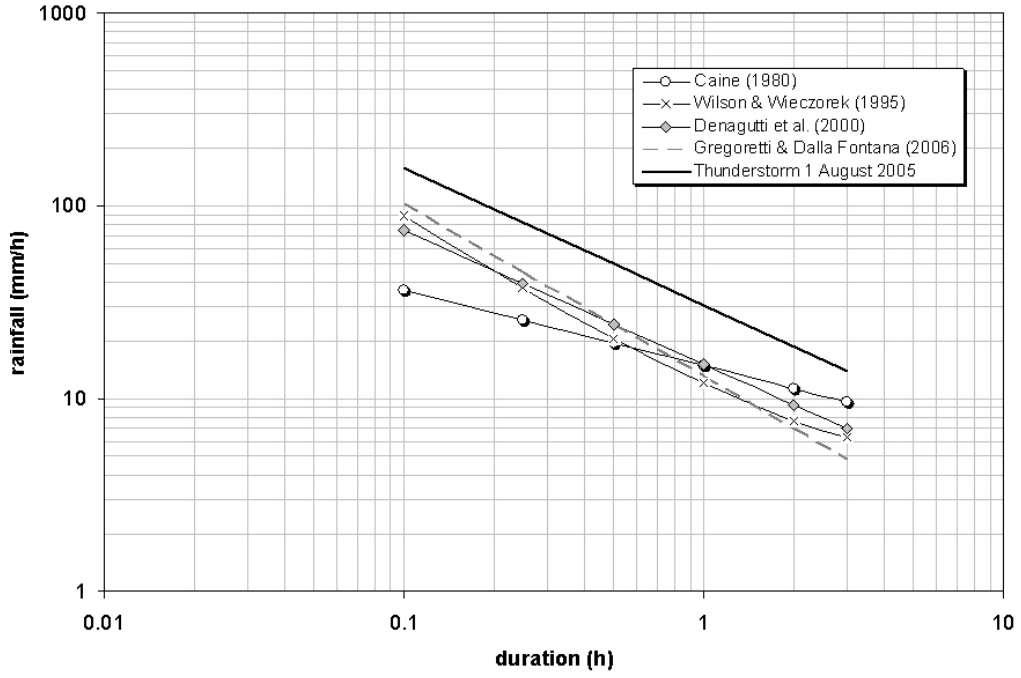

Figure 2.20: Intensity vs duration equations proposed in the literature to define the rainfall thresholds for debris flow initiation. In the Figure is showed also the intensity of rainfall observed for thunderstorm of summer 2005 at the initiation areas of debris flows.

Discharge

In proximity to outlet of Anterselva basin, 9.4 km far from debris flow initiation area it is located the only streamgauge station present in the region. Figure 2.21 on the following page reports observed discharge, rainfall and temperature for the event of 1 August. Hydrograph shows a peak of 19.51 m^3 s^{-1}

at 23:00 CET. Observed rainfall assumes significantly lower values respect to those observed in debris flow initiation area (Figure 2.18 on page 59). This is due to limited area of thunderstorm, mainly localized upslope Rio Gola basin.

Anterselva basin is characterized by a mean annual rainfall and runoff of 1050 mm and 780 mm respectively, with an annual runoff coefficient of 0.74. The mean annual discharge is 12.6 m^3 s^{-1} . Table 2.5 on the facing page shows the historic values of the first eight higher discharges observed at outlet streamgauge station since 1987. Value observed on 1 August 2005 is the fourth higher, thus making the event as one of the most intense in the last two decades.

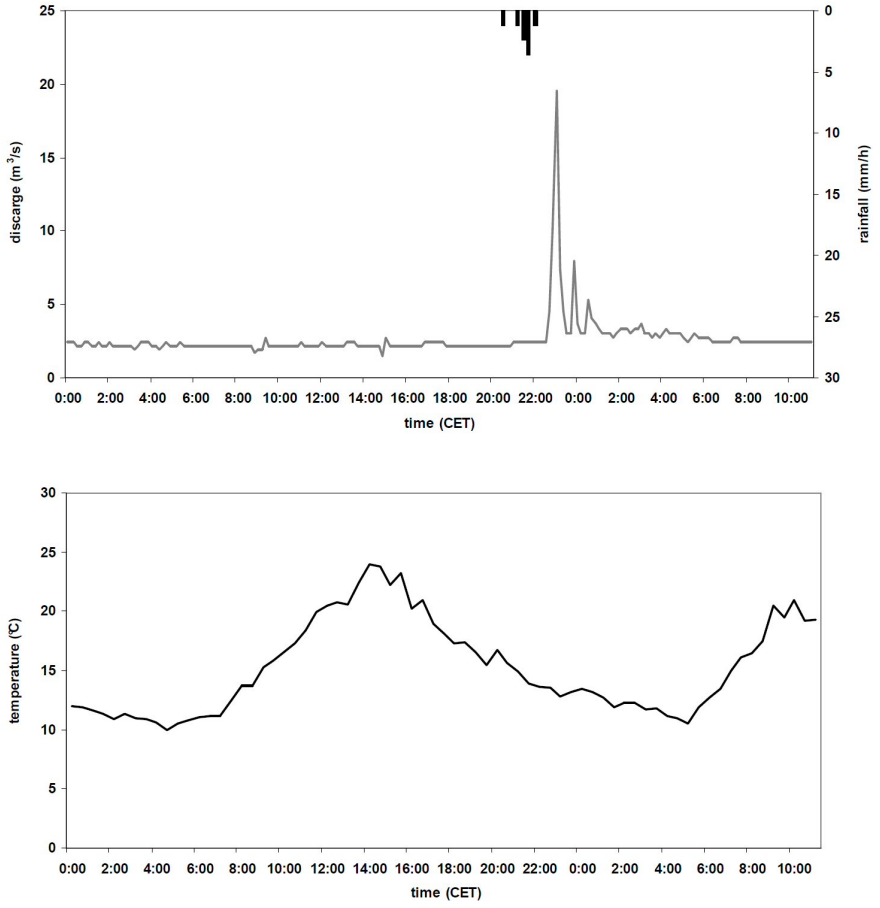

Figure 2.21: Observed discharge, rainfall and temperature for the event of 1 August.

2.2.4 Hydrologic response analysis

Methodology

Hydrologic analysis of flood events under extreme geomorphologic and torrential impacts poses several challenging features. The typical problem of flash flood prediction in ungauged basin is exacerbated by

Date	Time (CET)	$m^3\ s^{-1}$
1987/08/25	07:00	23.12
1994/07/07	00:00	22.68
1991/06/18	01:00	21.56
2005/08/01	23:00	19.5
1987/07/19	18:00	16.8
1991/06/26	22:00	16.19
2000/08/12	19:00	15.97
1998/06/28	01:00	15.58

Table 2.5: Historic values of first eight higher discharge observed at Bagni streamgauge station since 1987.

mass wasting and erosion, so that the assumed geometry and soil properties at the start of the storm change appreciably during the storm. The normal problem for analysis of flash flood events is determining the supply of water to the channel network ("how much" to route). A further question for flood events like the one examined here is "how to route water across and through changing hillslopes and channel systems". This implies that water infiltrated during the early stages of the flood on the channel beds and on side slopes may be quickly mobilised through the process of mass wasting and contribute to the formation of the debris flow peak and volume. On the other side, this means that the channel system must be considered in a dynamic way since flooding and mass movements create new channels and more efficient channels. The methods chosen here for hydrologic response analysis aims therefore to provide estimates for the surface and subsurface water amounts controlling the volume of mobilisable debris.

Flood response to August 2005 storm is examined by using the hydrological model GRISS-2D [Sangati, 2006]. This is a process-based, distributed-parameter, finite-difference hydrologic model that simulates stream flow generated by both infiltration-excess and saturation-excess mechanisms, as well as exfiltration, and subsurface storm flow to streams.

The model operates on a digital elevation model of the catchment, using 5 m grids. The subsurface storm flow component provides a mechanism to allow saturated soil water flow to move within a soil horizon overlying impermeable bedrock toward a receiving stream channel. This component generates return flow from the soil subsurface to the land surface that feeds sheet overland flow toward a receiving stream channel. Since the location of land surface saturation by subsurface storm flow evolves in time and space, this saturated land area becomes a "variable source area" for water flow toward a receiving stream. In this framework, the GRISS-2D model conceptualizes the water contribution from a hillslope into a neighboring stream channel in terms of (1) overland flow; and (2) seepage from subsurface storm flow (which may lead to return overland flow).

The vertical unsaturated flow component, is based upon the Green-Ampt infiltration equation and links the overland flow and the subsurface storm flow components of GRISS-2D. It is capable of estimating the vertical soil water flow rate at different soil depths within the soil root zone above the impeding layer. This

Parameter	Value			
Roughness coefficient (Gauckler-Stickler) Hillslope [$m^{1/3}s^{-1}$]	0.25			
Roughness coefficient (Gauckler-Stickler) Channel [$m^{1/3}s^{-1}$]	0.5			
	bedrock outcrops	talus deposits	grassland	forest
Suction Head [m]	0.0	0.0	0.3	0.3
Effective porosity [-]	0.0	0.35	0.30	0.30
Soil depth [m]	-	3	1.0	1.5

Table 2.6: GRISS-2D parameterization: roughness coefficients and soil hydraulic properties. Hydraulic conductivity is the same reported in Table 2.4 on page 61.

capability of the vertical unsaturated flow model enables it to calculate the accretion rate for subsurface storm flow. The rainfall excess becomes the lateral inflow flux to the hillslope overland flow model. A portion of the infiltrated water becomes subsurface storm flow and the remaining portion is stored within the soil column.

The saturated subsurface flow is simulated according to Wigmosta and Lettenmaier (1981) by using a kinematic wave model [Beven, 1981]. The effects of topography on flow routing are obtained through the direct use of DTM data. Each grid cell can exchange water with its eight adjacent neighbors. Local hydraulic gradients are approximated by local ground surface slopes (kinematic approximation). Thus a given grid cell receives water from its upslope neighbors and discharges to its downslope neighbors. Rise and fall of the subsurface storm flow is taken into account by the unsaturated zone model. In extreme cases the saturated zone may rise to the soil surface; the unsaturated zone disappears; only the saturated flow equations are solved, and seepage from subsurface storm flow can occur.

Once ponding occurs, the overland flow is routed in two orthogonal directions using Gauckler-Strickler equation with the kinematic wave assumption. When overland flow reaches a model grid-cell that contains a defined channel, the flow is passed into the channel and routed using a one dimensional kinematic wave model for surface runoff.

The application of GRISS-2D to the Rio Gola basin is based on parameters values both observed during field surveys, and derived from literature for similar type of soils and conditions. The topography was represented through a raster-type LiDAR derived DTM with grid size of 2.5 m. The model was applied at time intervals of 6'. Table 2.6 shows GRISS-2D input model parameters. The roughness coefficients (Gauckler-Stickler) are taken from literature.

Results

The results of the application of GRISS-2D to the 2005 flood on the three basins (headwater rocky basin, Rio Gola Basin, and Anterselva basin) are shown in Figure 2.22 on the facing page. Since the model is

applied to small areas, spatial rainfall variability is not considered. Rainfall considered in the simulation is the mean areal rainfall calculated for the three considered basins respectively.

- Maximum peak discharge simulated at outlet of the small rocky basin (debris flow initiation area) is 4.87 m^3 s^{-1} and it is reached at 2206 CET. The concentration time was very short (12 min) due to the total impermeable surface on rocky area. The third and second rainfall pulse generated other two runoff peaks with a less simulated unit peak discharge about 1.66 m^3 s^{-1} and 1.89 m^3 s^{-1} respectively. The computed runoff coefficient is around 0.99 [-].

- Maximum peak discharge simulated at outlet of Rio Gola basin, 2.97 km far debris flow initiation area (rocky basin outlet), is 16.26 m^3 s^{-1} and it is reached at 2218 CET. The third and second rainfall pulse here did not generate evident runoff peaks, but just a lower negative gradient (reached at 2242 to 2300 CET) in the receding limb of hydrograph. The computed runoff coefficient of this basin is around 0.24 [-].

- Maximum peak discharge simulated at outlet of Anterselva basin, 9.11 km far debris flow initiation area (rocky basin outlet), is 18.68 m^3 s^{-1} and it is reached at 2300 CET. The third and second rainfall pulse produces a similar trend observed for Rio Gola basin. The computed runoff coefficient is around 0.09 [-]. The simulation is consistent with peak discharge of 19.51 m^3 s^{-1} measured at streamgauge station (black line). Observed discharge shows also two other peaks reached at 2348 CET and at 0030 CET, consisting in 6.99 m^3 s^{-1} and 5.34 m^3 s^{-1} respectively.

This analysis suggests that the major controls of the flood response were i) the cumulated rainfall amount occurred on a restricted steep rocky area, and ii) the large rainfall intensities at temporal scales of up to 2 hour, required to generate high flood response at the considered basin scale.

2.2.5 Conclusions

For the August 2005 debris flow, radar rainfall data, post event field observations, in addition to post event high resolution data such high resolution LiDAR derived DTM, and aerial photographs were important sources of information.

The combination of detailed radar rainfall estimates, topographically based hydrologic model, and flood observation allowed to generate a much more complete picture of the storm and flood environment than would otherwise be available on ungauged basins.

Special attention was reserved at the georeferenciation process of radar rainfall data done using a clutter comparison methodology based on observed and simulated ground echoes. This analysis permitted a good superposition of the two different kind of ground clutter pattern's maps as a prove of an excellent understanding of rain maximum intensity cells positioning.

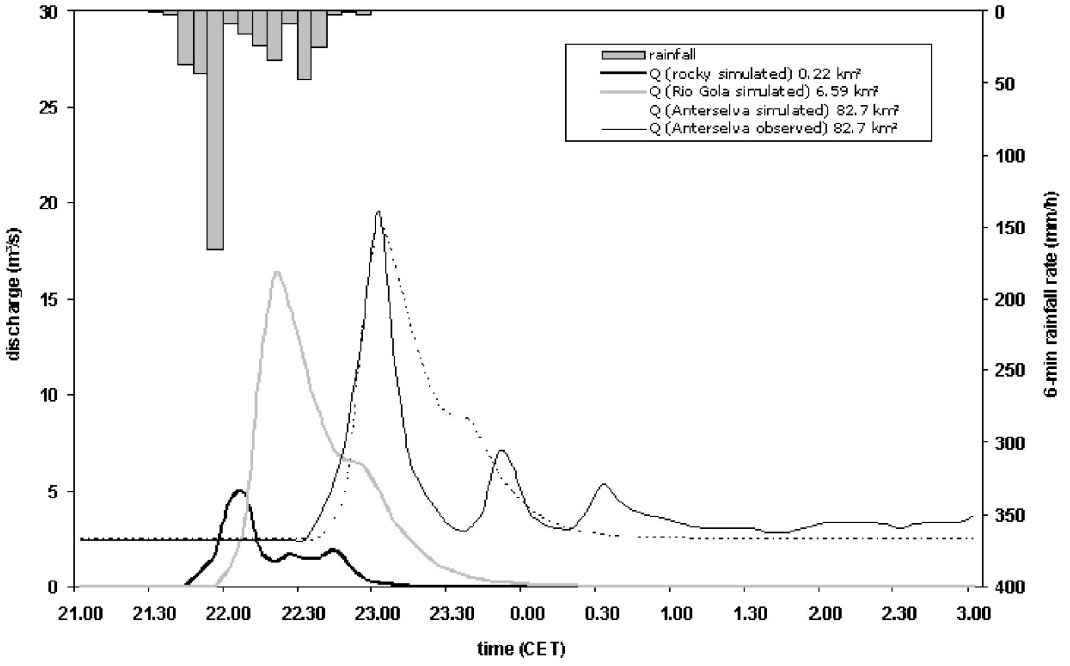

Figure 2.22: Simulated water runoff from the upper headwater rocky basin to debris flow initiation area (bold black line), simulated discharge observed at the Rio Gola outlet (gray line) (depositional area), and at Anterselva outlet (black line), where is also recorded the discharge observed at the outlet of the main basin (dashed black line). In the plot it is reported also the hourly rainfall intensity within 6 minutes of time step.

Our analysis suggested that triggering of the type of debris flow considered in this study is dependent both on high rainfall accumulation and quick generation of runoff on rocky headwater catchment. The debris flow channel collected water from a very small and steep rock basin characterized by a short concentration time. The incoming water took a few minutes to saturate the channel bed material, before excess water began to flow in the initiation area and the debris flow originated. Complete saturation of the material and the presence of flowing water on the surface appear then to be necessary for the initiation of the debris flow; this condition is reached only after intense rainstorms which generate a peak inflow exceeding the capacity of the highly permeable channel bed material.

The analysis proposed here could help to assess the debris flow hazard and understand better the initiation processes behind these phenomena which commonly occur during summer season in this region of the Italian Alps. At the same time we feel that there is more to be explored to gain new informations on debris flow initiation processes during intense and localized rainfalls over a landscape of complex morphology, especially those related to the glaciated/rocky basins and snow-ice melt activity. Future work should be conducted in this way, analyzing such case studies in other to evaluate how topographic signatures of glaciated landscapes and climate change affect debris flow activity.

3. Which rainfall spatial information for flash flood response modelling? A numerical investigation based on data from the Carpathian range, Romania

3.1 Introduction

The influence of rainfall spatial variability on hydrologic response of watersheds has been a recurrent theme in hydrological research over the past 40 years [e.g., Dawdy and Bergmann, 1969; Wilson *et al.*, 1979; Woods and Sivapalan, 1999]. Several distributed modelling studies have considered the impacts of spatial rainfall variability on modelled flood hydrographs [e.g., Wood *et al.*, 1988; Krajewski *et al.*, 1991; Naden, 1992; k. Beven and Wood, 1993; Obled *et al.*, 1994; Ogden and Julien, 1994; Blöschl and Sivapalan, 1995; Bell and Moore, 2000; Moulin *et al.*, 2008; Sangati *et al.*, 2009; Saulnier and Le Lay, 2009]. In a model-based study, Nicotina *et al.* (2008) showed that the sensitivity of catchments to the rainfall spatial patterns is controlled by the structure of the transport process in the hillslopes and river system. They found that when the total travel time of a water parcel is controlled by the travel time on hillslopes system (a basin size of 102 km^2 , accordingly with the results from the study), the runoff response of the catchment does not depend on the specific rainfall pattern. In larger basins, the travel time in the channels is expected to be an important part of the total travel time and as a consequence the runoff response will also be controlled by the specifics of the spatial distribution of rainfall. These results confirm earlier results by a number of studies [Beven and Hornberger, 1982; Naden, 1992; Obled *et al.*, 1994; Andréassian *et al.*, 2001; Smith *et al.*, 2004a,b] who observed that an accurate spatial pattern of rainfall was required

to predict the total volume of runoff correctly rather than the spatial pattern being important in itself. Most of these studies were carried out in relatively small to medium-size catchments where the catchment response is expected to be dominated by the hillslope response. However, based on specific case studies, other investigators found that the spatial variability of rainfall can play a major role in the uncertainty of runoff modelling even at the scale of a small basin [Michaud and Sorooshian, 1994; Faures *et al.*, 1995; Wainwright, 2002; Schuurmans and Bierkens, 2007], hence implying that the sensitivity to spatial rainfall variability cannot be treated as scale dependent relative to the size of the catchment. Results from these modeling studies are therefore quite mixed, being much of the knowledge either site-specific or expressed qualitatively. It is therefore difficult to synthesize it and transfer it to new situations.

A more general approach was taken by Woods and Sivapalan (1999), who proposed a theoretical framework to identify the importance of multiple sources of input and process variability on hydrograph properties (hereinafter referred to as WS model). This was obtained by combining a model of rainfall excess with linear and invariant routing models of hillslopes and channels. The WS model led to emphasise the role of the rainfall excess spatial variability measured along the flow distance, i.e. the distance from a certain point of the catchment to the outlet measured along the flow direction. More specifically, they found that the impact of spatial variability of rainfall excess on simulated hydrograph shapes is controlled by the averaging of space-time rainfall excess fields across locations with equal flow distances. Accordingly with this approach, the sensitivity of hydrograph shapes to rainfall excess spatial variability is related to two parameters: i) the distance from the centroid of the catchment to the centroid of the rainfall excess pattern, and ii) the spreading of the rainfall excess field about its mean position, both measured along the flow distance axis. When the values of these parameters are small, the storm event response is determined more by the drainage network structure and less by rainfall excess spatial pattern, in spite of the intrinsic spatial variability, which may be large.

Space and time scales of flash floods, and the intensity of the relevant rainfall forcing are such that examination of the influence of spatial rainfall variability on flash flood response modelling may help to isolate how rainfall should be organised in space and time to produce a detectable impact in modelling small and medium catchment scales. Moreover, the short duration of these events and the localised character of their rainfall patterns, which are often time-invariant, make them suitable for analysis by means of the methodology proposed by Woods and Sivapalan (1999).

Examination of these issues under flash flood conditions is however made difficult by a number of problems. Flash flood events are difficult to monitor because they develop at space and time scales that conventional measurement networks of rain and river discharges are not able to sample effectively [Creutin and Borga, 2003; Marchi *et al.*, 2009a]. The intensity and the variability of the forcing rainfall may be difficult to estimate even by use of weather radar [Bouilloud *et al.*, 2009]. Moreover, flash floods are relatively rare event at the local scale [Norbiato *et al.*, 2008]. This explains why the investigation of

flash flood events is by necessity event-based and opportunistic as opposed to driven by observations from carefully designed field campaigns. Post-event surveys play a critical role in gathering essential observations to examine how spatial variability of rainfall may influence flash flood response modelling [Borga *et al.*, 2008].

In this work we seek to determine, through careful numerical experiments and based on data from post-event surveys of flash flood events, the characteristics of the rainfall spatial organisation which may be expected to play a relevant role in shaping the main features of flash flood hydrographs at small and medium catchment scales. To this purpose, we extend the analytical approach introduced by Woods and Sivapalan (1999), to develop a coherent framework clarifying the dependence existing between spatial rainfall distribution, basin morphology and runoff response.

High resolution, quality controlled radar rainfall fields and a distributed hydrologic model are used to evaluate the sensitivity of flood response to spatial variability of rainfall. We perform numerical experiments in which modelled flash flood response obtained by using detailed spatial input are contrasted with the corresponding flash flood response obtained by using spatially uniform rainfall. In order to evaluate the effect of the rainfall spatial organisation, the discrepancies between the two responses are related to the structure of the spatial properties of rainfall field measured along the flow distance.

The numerical investigation is based on data from three extreme flash floods occurred on Feernic, Clit and Grinties river basins, in the Carpathian Mountain range (Romania) in the period 2005-2007. The size of the catchments impacted by the flash floods ranges from 36 to 167 km^2 . These events are therefore particularly well suited to represent flash flood dynamics in small to medium size catchments. Data from S-band weather radars, together with a network of raiungauges, are used to quantify the rainfall spatial distribution. Streamflow data are provided by conventional hydrological network and by accurate post-event surveys.

3.2 The flash flood events: hydro-meteorological documentation and analysis

Romania is classified as having a temperate-continental climate, due to its geographic location in the south-eastern Europe. The Carpathians act as a barrier for the Atlantic air masses, restricting the oceanic influences to the western and central part of the country. In the south-western Romanian Plain, the Mediterranean influences determine a milder climate. Multiannual precipitation means display an annual cycle, with a maximum in June and a minimum in February-March, almost all over the country. Accordingly with the mean annual precipitation map (Figure 3.1 on the next page), based on data from 1961 to 2005, the lowest annual precipitation amounts are recorded in the Dobrudja costal area and mostly in the east of the Danube Delta, where less than 400 mm fall on average, whereas the most abundant precipitation

are localized in the Carpathian mountain areas and may exceed 1200 mm.

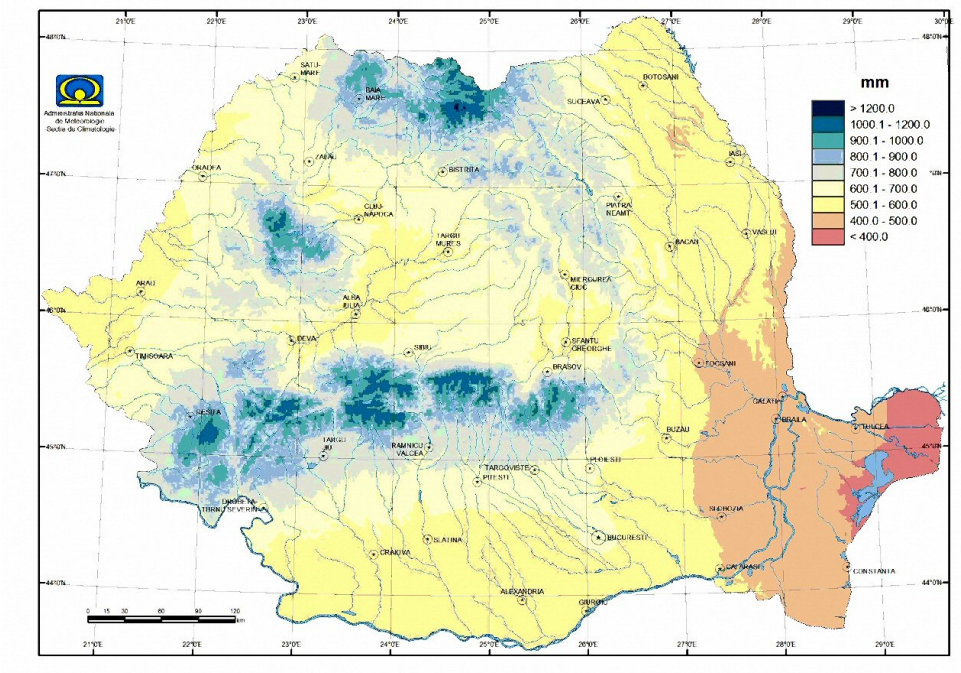

Figure 3.1: Mean annual precipitation distribution over Romania (observation period from 1961 to 2005).

The Carpathian range occupy a distinctive hydroclimatological niche, characterised by a high frequency of organised thunderstorm systems. In this region the annual precipitation maxima typically occur in July and August [Parajka *et al.*, 2009]. Of the largest annual maximum daily precipitation reported for 94 romenian stations in the period 1961-1996, 70 maxima are summer storms [Cazacioc, 2007], and most of these are located in the Carpathian range. Interestingly, the world highest precipitation in 20 min was recorded on July 7 1889 at Curtea-de-Arges in Romania, with 206 mm rain. A consequence of the hydroclimatology of these systems is a sharp seasonal peak in the regional flood frequency in the summer season (June to August). The seasonality of the flash flood occurrence has been examined by Gaume *et al.* (2009), which have noted that in Central Europe (including the Carpathian range) extreme flash floods occur generally in the summer season, while there is a shift towards the fall and winter season when moving to Southern Europe and to the Mediterranean basin. Marchi *et al.* (2009a) have also noted that flash floods in the Carpathian basin tend to be shorter and involve smaller rainfall cumulated depth, with respect to flash floods in Southern Europe. It is therefore not surprising the observation by Gaume *et al.* (2009), who reported that the maximum peak discharges collated in Central Europe are less than half the maximum peak discharges reported for the regions under Mediterranean climatic influence, for a given watershed area. Some very high unit peak discharge values are observed under the inner continental climate but they lie far from the maximum values observed in the Mediterranean area. It is worth reminding that areas of

moderate unit peak flows do not necessarily equate to areas of moderate flood hazard, since the flood hazard for any particular location is in part due to local forecasting, warning, and communication systems, existing flood protection works, as well as the community's social, political, and regulatory setting. Flash flood events in the Carpathian range may result in high loss of human lives and large damages. These effects are exemplified by the flash flood events occurred in the country during 2005 summer season, which led to 76 casualties and to overall economic losses as high as 1.6% of the gross national product [Constantin-Horia *et al.*, 2009].

Three flash flood events, occurred in the period 2005-2007 in the northern portion of the Carpathian range (Figure 3.2), have been documented with the collaboration of the Romanian Meteorological and Hydrological National Services. The area is covered by two S-band radars, and by a fairly dense network of hourly and daily raingauges. Data and observations for the characterisation of these events were collected following the methodology for post-flood survey reported by Marchi *et al.* (2009a). Post-flood analysis methods include a range of procedures for indirect estimation of peak discharges, generally encompassing the following steps: identification of the flow process (which is categorised into the following classes: liquid flow, hyperconcentrated flow, debris flow), high-water marks identification, post-flood river geometry survey, and application of appropriate hydraulic methods for peak flood computation. The methodology incorporates eye-witnesses interviews to reconstruct the time evolution of the flood and uses rainfall-runoff models (usually with radar rainfall input) to check the internal consistency of the information gathered by means of the survey. This approach provides an integral cycle of observations and modelling which affords analysis of the rainfall-runoff processes at small spatial scale during flash floods.

The morphology of the basins is described by a 20-m grid size Digital Elevation Model; land use data have provided at a coarser spatial resolution (1 km) by the Hydrological National Administration. A distributed hydrological model (presented in section 3.2.2 on page 72) has been used to evaluate the consistency of the hydrometeorological information provided for event description and to analyse the influence of rainfall spatial distribution on runoff modelling.

3.2.1 Radar rainfall estimation

Radar rainfall estimation was based on a pragmatic approach, based on a careful analysis of the observation conditions for the radar systems available for the considered cases (Bouilloud *et al.*, 2010). The methodology is therefore based on the availability of original polar data from the Romanian S-band Doppler weather radar, operated at 6 minutes updating time and with a polar element size of 1° 1 km. The two lowest radar beam elevations, which are at 0.5° and 1.5° , were used for constructing the radar rainfall fields, with an aggregation interval of 15 min. The following steps were executed for each storm event:

1. Detailed collection of data and metadata about the radar systems and the raingauge networks (including raingauge data from amateurs and from bucket analysis);

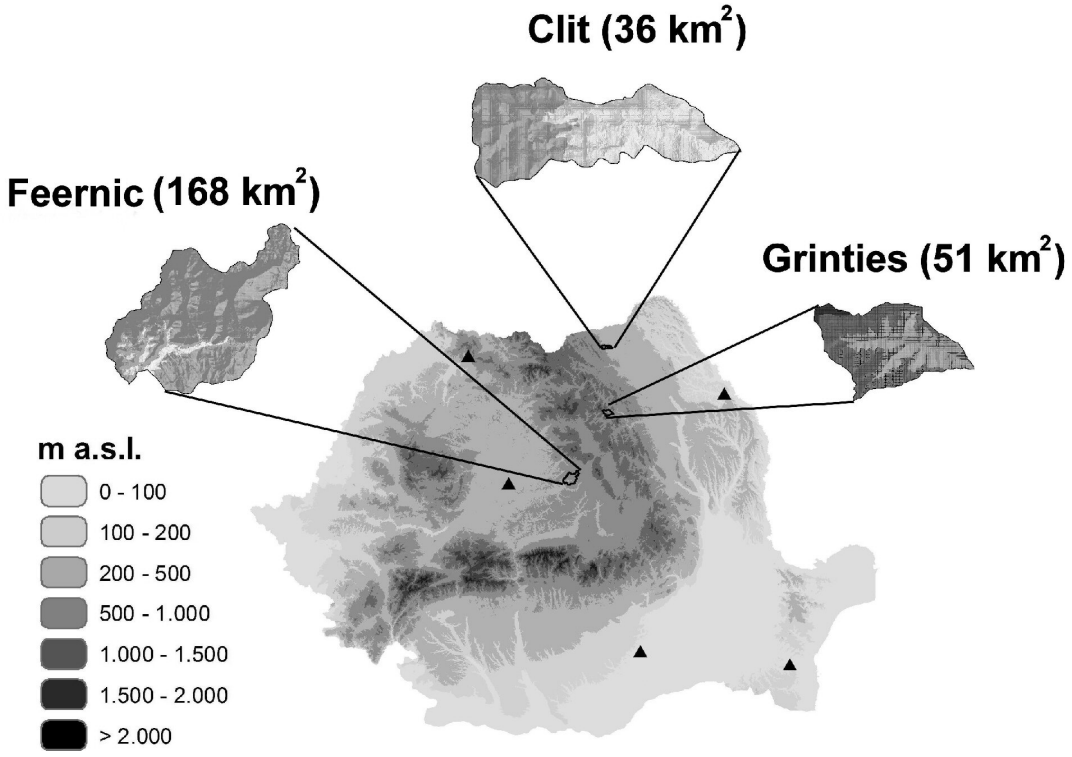

Figure 3.2: Location of the three study basins in Romania with indication of radar coverage and raingauges position .

2. analysis of the detection domain and the ground/anthropic clutter for the considered case [Borga *et al.*, 2002];

3. implementation of corrections for range-dependent errors, such as screening and vertical profiles of reflectivity (attenuation was not an important error source here, given the characteristics of the two S-band radar systems);

4. optimisation of the rainfall estimation procedure by means of radar-raingauge comparisons at the event duration scale [Bouilloud *et al.*, 2009].

The interactions between the radar beam and the relief (ground clutter and screening effects) were characterized thanks to dry-weather observations and simulations based on a digital terrain model of the region of interest. The vertical profile of reflectivity was inferred globally over the detection domain based on available radar volume data. Such information was then used to produce correction factor maps for each elevation angle to be applied to the measured reflectivities to correct for range-dependent errors and estimate the reflectivity close to ground level from the reflectivities measured aloft. Finally, we optimized the parameters of the reflectivity-to-rainrate relationship with reference to the raingauge rain amounts measured at the event time scale over the region impacted by the flood. This procedure is aimed at ensuring the radar rainfall estimates to be unbiased at the event time scale, a crucial condition for

hydrological applications.

3.2.2 The distributed hydrological model

Hydrologic response from the three storm events is examined by using a simple spatially distributed hydrologic model. The distributed model is based on availability of raster information of the landscape topography and of the soil and land use properties. The runoff rate $q(x, y, t)$ [mm h^{-1}] at time t and location x,y is computed from the rainfall rate $P(x, y, t)$ using the Green-Ampt infiltration model with moisture redistribution [Ogden and Saghafian, 1997]. The adopted formulation of the Green and Ampt model has been chosen because it provides a simple, but not simplistic [Barry *et al.*, 2005] and yet physically-based description of the infiltration-excess mechanisms. A simple description of the drainage system response [Da Ros and Borga, 1997] is used to represent runoff propagation. The distributed runoff propagation procedure is based on the identification of drainage paths, and requires the characterization of hillslope paths and channeled paths. A channelization support area (A_s) [km^2] is used to distinguish hillslope elements from channel elements. Discharge at any location along the river network is represented by

$$Q(t) = \iint_A q[x, y, t - \tau(x, y)]dxdy \tag{3.1}$$

where A [km^2] indicates the area draining to the specified outlet location and $\tau(x, y)$ is the routing time from the location (x, y) to the outlet of the basin specified by the region A. The routing time $\tau(x, y)$ is defined as

$$\tau(x, y) = \frac{L_h(x, y)}{\nu_h} + \frac{L_c(x, y)}{\nu_c} \tag{3.2}$$

where $L_h(x, y)$ is the distance from the generic point x, y to the channel network following the steepest descent path, $L_c(x, y)$ is the length of the subsequent drainage path through streams down to the watershed outlet, and ν_h and ν_c [m s^{-1}] are two invariant hillslope and channel velocities, respectively.

The model includes also a linear conceptual reservoir for base flow modeling [Borga *et al.*, 2007]. The reservoir input is provided by the infiltrated rate computed based on the Green-Ampt method. The model framework is based on six calibration parameters: the channelization support area (A_s), two kinematic parameters (ν_h and ν_c), and the three soil hydraulic parameters used by the Green-Ampt method. The model was implemented at 15-min time step and using a 20-m grid size cell for the description of landscape morphology and soil properties.

3.2.3 The August 23, 2005 flood on the Feernic river at Simonesti

Event	Basin area [km^2]	Tot. rain [mm]	Tot. runoff [mm]	Peak dis. [m^3s^{-1}]	Unit peak dis. [$m^3s^{-1}km^{-2}$]	Runoff ratio [-]	Lag time [hr]
Feernic	166.7	76.0	15.9	357.1	2.14	0.21	3.0
Clit	36.0	80.5	28.5	175.0	4.86	0.35	0.50
Grinties	52.0	66.8	7.5	100.0	1.92	0.11	1.25

Table 3.1: Rainfall and runoff for the analysed flash flood events.

The Feernic River at Simonesti (167 km^2) is a small stream in the Mures River catchment, with catchment elevation ranging from 432 to 1049 m a.s.l. (mean elevation 637 m a.s.l.) and mean basin slope 23.5%. The mean annual precipitation ranges between 610 and 650 mm, while the 100-yr 24-hr rainfall slightly exceeds 100 mm. The geological properties are quite varied, with the upper part of the basin characterised by the volcanic lava and pyroclastic rocks of Harghita Mountains, and the lower by the flysch (marls and clays) of the Transylvanian Subcarpathians. Forests (about 20% of the basin surface) are composed by coniferous and beeches on the mountain part of the basin; beeches and chestnut oaks on the hilly part. The percentage of arable soils is 20-25% and the rest of the land is used as pastures and meadows. Two small towns (Lupeni, 4600 inhabitants, and Simonesti, 3600 inhabitants) are located in the floodplain along the river network.

A streamgauge station is in operation in Simonesti since 1961. The highest peak discharge recorded before the 2005 event amounts to 131 m^3s^{-1} measured in 1975, while the average discharge is 1.11 m^3s^{-1}. During the flood event, the station was partially damaged and it went out of order for some time; however, loss of information was relatively minor, and the combination of observed data and of data from a post-event survey carried out in the weeks following the event afforded the reconstruction of the flood hydrograph. The post-event survey enables also estimation of the peak in other two upstream river sections. Only daily raingauge stations are available in the catchment; hence, the rainfall estimation is based on the processing of radar data in combination with these data and hourly raingauge data in the neighbours of the basin.

As a consequence of the flood, 16 people died in Lupeni and Simonesti, and 1400 houses - which correspond to almost all the buildings on the floodplain - were flooded and heavily damaged. Two main bridges collapsed during the flood.

The storm lasted for 5 hours, starting at 1200 UTC, with a catchment average depth of 76 mm (Figure 3.3 on page 76). The basin-average rain rate time series shows a steady increase from 1200 UTC to the precipitation peak at 1530 UTC, followed by a period of lower intensity, ending around 1700 UTC. The period of extreme rainfall began at 1400 till 1530, with values of mean rainfall (for non zero rainfall) between 30 and 50 mm h^{-1} (a rainfall threshold of 1 mm h^{-1} was used to distinguish rain-no rain areas) and coefficient of variation (standard deviation divided by the mean) ranging between 1.0 and 0.8

(Figure 3.4). These values are similar to those reported for other extreme storm events examined by using weather radar [Sangati *et al.*, 2009]. This chronology of storm evolution corresponds with eyewitnesses accounts placing the beginning of extreme rainfall and its rapid transformation to extreme rain rates between 1400 and 1500 UTC. The storm exhibited a striking spatial variability, with the precipitation concentrated in the medium and upper part of the catchment, where rainfall accumulation in some places exceeded 190 mm. This was due to a significant effect of the orography, which played an important role in regulating of atmospheric moisture inflow to the storm and in controlling storm motion and evolution. Small catchments in this area had specific contribution reaching 7-8 m^3 s^{-1} km^{-2} , as confirmed by the post-event analysis. Rainfall was much lower close to the catchment outlet, as shown in Figure 3.3 on the following page. The flood peak at Simonesti was estimated around 370 m^3 s^{-1} , corresponding to 2.2 m^3 s^{-1} km^{-2} (Figure 3.3 on the next page, Table 3.1 on the facing page). Based on the observations gathered for the event, the event runoff coefficient is around 0.22 (Table 3.1 on the preceding page), with values much higher (up to 0.6) in the upper portions of the catchment which received the highest rainfall accumulation and intensities. The soil moisture status at the start of the event was moderately wet, as a consequence of a wetter-than-average 30 days period before the flood (with 177 mm of rain compared to 77 mm resulting from the climatological average over the same period). This explains the relatively low value of initial losses for this event.

The shape, peak discharge, and timing of the model hydrograph (Figure 3.3) are determined by the hillslope and channel flow velocity and by the soil saturated hydraulic conductivity. The two velocities and the saturated hydraulic conductivity were chosen to match estimates of peak discharge and time of peak, both at Simonesti and at two internal river sections were observed data are available. The modeled flow velocities that reproduce observed timing and magnitude of the peak discharge (0.15 m s^{-1} for the hillslope velocity and 2.5 m s^{-1} for the channel velocity) are in the upper end of the range of values (0.003-0.14 m s^{-1}) reported by Dunne (1978). Since the model overland flow velocity is spatially and temporally constant, it must account for sheet flow as well as concentrated overland flow in areas not specified as channels. For this extreme event, overland flow velocities were likely greater than typical due to steep slopes and large amounts of sheet flow. The spatial distribution of saturated hydraulic conductivity was based on the land use information, accordingly with indications by Dunne (1978), who found forests had saturated hydraulic conductivity values up to an order of magnitude greater than hay fields and pasture land.

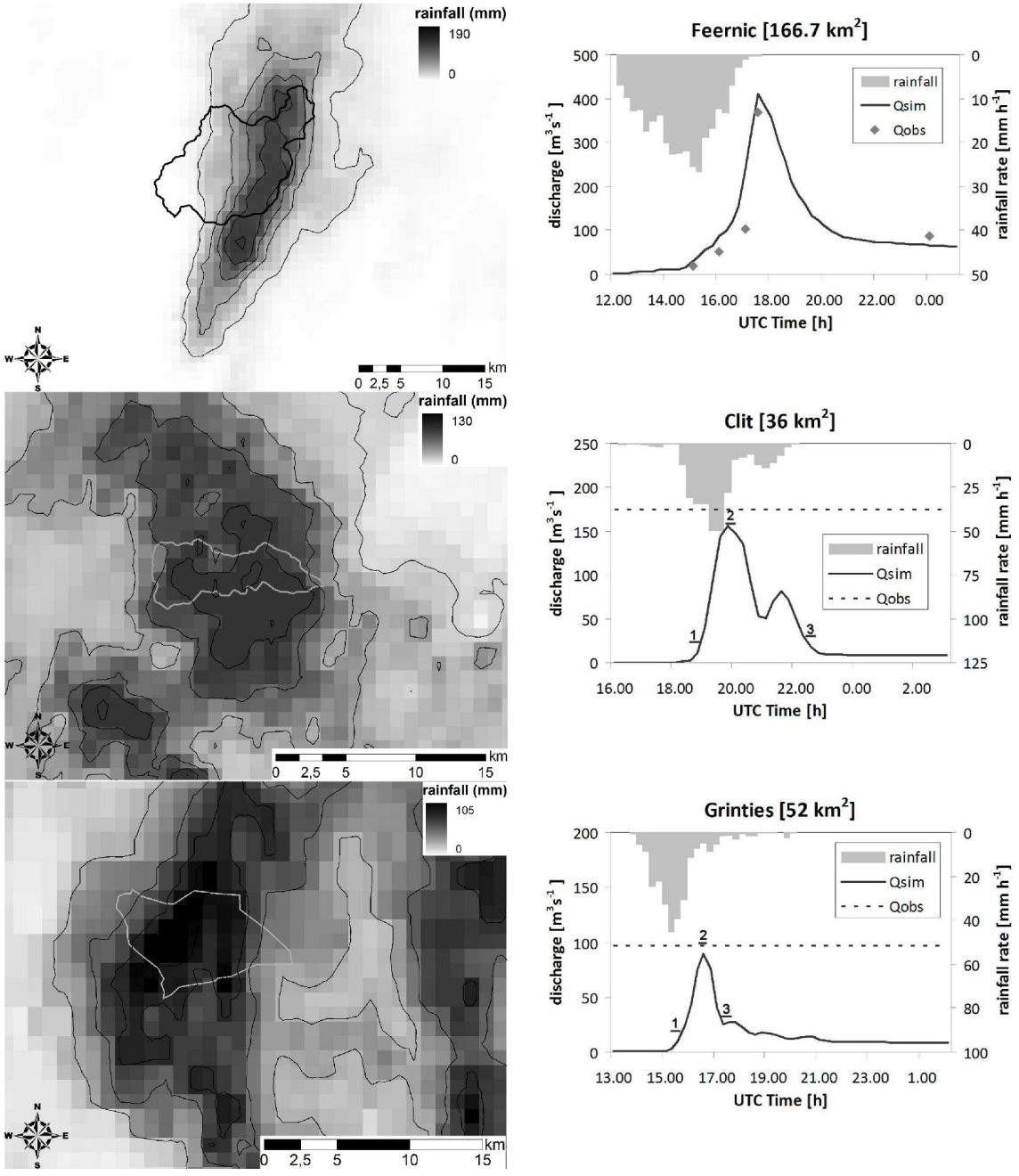

Figure 3.3: Event rainfall accumulation and runoff analysis for the three flash flood events. For the Clit and the Grinties events, the figures report the values of the peak discharges estimated based on post-event analysis, as well as the timing of the flood onset, the peak and the end of the flooding (marked with 1, 2 and 3, respectively), based on eyewitnesses accounts.

3.3 Quantifying the impact of rainfall spatial variability of runoff modeling: the analytical framework

Woods and Sivapalan (1999) proposed an analytical framework for quantifying the effects of space-time variability on catchment flood response. It includes complex space and time variability of both rainfall and runoff generation as well as runoff routing. In the model, rain falls on the catchment and either becomes rainfall excess through the action of a runoff generation process or is stored. Rainfall excess is routed to the channel outlet though a linear and time-invariant model of hillslope and channel routing. In the model (termed WS model in the following), the rainfall excess $R(x, y, t)$ [L T^{-1}] at a point (x,y) and at time t is given by

$$R(x, y, t) = P(x, y, t)W(x, y, t) \tag{3.3}$$

where $W(x, y, t)$ [ ] is the local runoff coefficient, bounded between 0 and 1. Woods and Sivapalan (1999) assume that the space-time distribution of both precipitation and runoff coefficient can be separated into independent multiplicative time and space components. Thus

$$P(x, y, t) = P_{x,y}(t)P_t(x, y) \tag{3.4}$$

and

$$W(x, y, t) = W_{x,y}(t)W_t(x, y) \tag{3.5}$$

where the time series of spatially averaged rainfall rates $P_{x,y}(t)$ and runoff coefficient $W_{x,y}(t)$ is

$$P_{x,y}(t) = \frac{1}{A} \iint_A P(x, y, t)dxdy \tag{3.6}$$

and

$$W(x, y, t) = W_t(x, y)W_{x,y}(t) \tag{3.7}$$

respectively, A [L^2] is the catchment area and the dimensionless spatial pattern of rainfall $P_t(x, y)$ [ ]

and $W_t(x,y)$ [ ] is given by

$$P_t(x,y) = \frac{\int_0^{T_m} P(x,y,t)dt}{\int_0^{T_m} P_{x,y}(t)dt} \tag{3.8}$$

and

$$W_t(x,y) = \frac{\int_0^{T_m} W(x,y,t)dt}{\int_0^{T_m} W_{x,y}(t)dt} \tag{3.9}$$

where T_m [T] is the storm duration.

Based on these assumptions, the model can be used to characterize flood response by means of three quantities: (i) the storm-averaged value of the catchment rainfall excess (i.e., the runoff volume over the catchment), (ii) the mean catchment runoff time (i.e., the time of the center of mass of the runoff hydrograph at the outlet), which is a surrogate for the time to peak, and (iii) the variance of the timing of runoff (i.e., the temporal dispersion of the runoff hydrograph), which is a surrogate for the shape of the hydrograph.

Since the aim of this study is to derive statistics of the rainfall spatial pattern based on the distribution of travel time τ, we modified accordingly the WS model by i) lumping together the hillslope and river channel network travel times, by using the concept of travel time τ, and ii) by assuming that the runoff coefficient is spatially uniform, and thus $W_t(x,y)$ is uniform and equal to 1. The analytical results are summarized below, by focusing on the elements which are essential to derive the rainfall patterns statistics.

3.3.1 Storm and catchment-averaged rainfall excess

The time and catchment-averaged rainfall excess $R_{x,y,t}$ [L T^{-1}] can be expressed in terms of the moments of rainfall P and runoff coefficient W as follows:

$$R_{x,y,t} = [P_{x,y,t}W_{x,y,t} + cov_t(P_{x,y}, W_{x,y})] \tag{3.10}$$

where $P_{x,y,t}$ and $W_{x,y,t}$ are time and catchment-averaged rainfall and runoff generation values, respectively. In Eq. 3.10, the covariance term is as follows:

$$cov_t(P_{x,y}, W_{x,y}) = \frac{1}{T_m}\int_0^{T_m}[P_{x,y}(t) - P_{x,y,t}]\cdot[W_{x,y}(t) - W_{x,y,t}]dt \tag{3.11}$$

Equation 3.10 shows that the storm runoff from the catchment is influenced only by the temporal covariance of the space-averaged P and W. The spatial variability in rainfall has no effect on the volume of rainfall excess, according to this model and to the assumptions.

3.3.2 Mean catchment runoff time

Catchment runoff time is treated as a random variable (denoted T_q), which measures the time from the storm beginning until a drop of water exits the catchments. In the conceptualization of the model, the mean runoff time can be partitioned into two terms of rainfall excess (denoted T_r) and holding time (T_f) as follows

$$E(T_q) = E(T_r) + E(T_f) \tag{3.12}$$

In more detail, this may be given by:

$$E(T_q) = \underbrace{E(T_r)}_{ET_1} + \underbrace{E(\tau)}_{ET_2} + \underbrace{cov[\tau, P^*(\tau)]}_{ET_3} \tag{3.13}$$

where T is time measured since the start of the storm event (treated as a uniform random variable over [0, T_m]) $P*(\tau)$ is defined as the average rainfall at all points with travel time τ (relative to the catchment average rainfall). This quantity is defined as

$$P^*(\tau) = \frac{\frac{1}{A(\tau)}\iint_{\Sigma(\tau)} P_t(x,y)dxdy}{\frac{1}{A}\iint_A P_t(x,y)dxdy} \tag{3.14}$$

where $\Sigma(\tau)$ is the set of points that contribute runoff at travel time τ and $A(\tau)$ is known as the area function. For the conceptualization of $E(T_r)$, which is not central here, we refer to Woods and Sivapalan (1999).

Equation 3.13 has three terms: ET_1, ET_2 and ET_3. The first term ET_1 represent the time from the start of the event to the centroid of the rainfall excess time series, and is independent from the rainfall

spatial variability. The second term ET_2, hereinafter referred to as τ_{mean}, represents the average time to route the rainfall excess from the catchment geographical centroid to the catchment outlet. The third term ET_3 represents the additional time (which can be either positive or negative) taken to route the rainfall excess from the geographical centroid of the rainfall excess spatial pattern to the geographical centroid of the catchment. The third term is therefore the only term which depends on the rainfall spatial variability, and it is computed as follows:

$$cov[\tau, P^*(\tau)] = \frac{1}{A} \iint_A [\tau(x,y) - \tau_{mean}] \cdot [P_t(x,y) - 1] dxdy \tag{3.15}$$

In the following, a dimensionless statistic (ϑ_1, termed normalised time distance in the following) is defined by taking the ratio of the expected value of the catchment holding time $E(T_f)$ with τ_{mean} as follows:

$$\vartheta_1 = \frac{E(T_f)}{\tau_{mean}} = \frac{\iint_A P_t(x,y)\tau(x,y)dxdy}{\iint_A \tau(x,y)dxdy} \tag{3.16}$$

The values of ϑ_1 are defined positive, and are equal to one for the case of spatially uniform precipitation or for a spatially variable precipitation which is concentrated on the catchment centroid. When the travel time is strongly related to the distance from the generic point to the outlet, values of ϑ_1 less than one indicate that rainfall is concentrated towards the outlet, and values larger than one indicate that rainfall is concentrated towards the headwater portion of the basin (as it may when the precipitation is enhanced by orography). Note that the travel time is not always related to the overall distance from the generic point to the outlet, particularly when transport processes along the hillslopes play an important role in the runoff propagation. Based on equation 3.13 on the preceding page, the expected effect of a less-than-one value of ϑ_1 is an anticipation of the mean hydrograph time. This means that when rainfall is concentrated towards the outlet, the hydrograph is anticipated relative to the case of spatially uniform rainfall. The opposite is true for rainfall concentrated towards the periphery of the catchment, with the hydrograph delayed relative to the case of a spatially uniform rainfall.

3.3.3 Variance of catchment runoff time

The variance of the catchment runoff time is estimated by considering the two random variables T_r and T_f as independent, as follows:

$$Var(T_q) = Var(T_r) + Var(T_f) \tag{3.17}$$

This gives the following relation:

$$Var(T_q) = \underbrace{Var(T_r)}_{VT_1} + \underbrace{Var(\tau)}_{VT_2} + \underbrace{\left\{cov[\tau^2, P^*(\tau)] - cov[\tau, P^*(\tau)] \cdot [2E(\tau) + cov(\tau, P^*(\tau))]\right\}}_{VT_3} \tag{3.18}$$

Similarly to equation 3.13 on page 79, equation 3.18 has three terms: VT_1, VT_2 and VT_3. The first term VT_1 measures the variance of the time-varying rainfall excess time series with duration T_m. The second term VT_2 reflects the effect of the runoff routing through the catchment: thus a catchment with a narrow range of travel times is predicted to have a small variance in runoff time (i.e., a sharper hydrograph shape), and vice versa. The third term VT_3 in equation 3.18 estimates the additional variance in runoff time that is caused by the spatial variability in rainfall, relative to the case of spatially uniform rainfall throughout the catchment. As for equation 3.13, this term can be negative, signifying in this case that the rainfall pattern has acted to concentrate the spread of the catchment response time. This occurs for example when the rainfall is concentrated within a short range of travel time values. When, on the contrary, the rainfall excess has a bimodal spatial distribution, with concentration both at the headwaters and at the outlet of the catchment, the third term positively contributes to the overall runoff catchment time variance. The third term may be written as follows:

$$\left\{cov[\tau^2, P^*(\tau)] - cov[\tau, P^*(\tau)] \cdot [2E(\tau) + cov(\tau, P^*(\tau))]\right\} =$$

$$\iint_A (P_t(x,y) - 1) \cdot (\tau(x,y) - \tau_{mean})^2 dxdy + \tau_{mean}^2 - E(T_f)^2 \tag{3.19}$$

The influence of the rainfall spatial variability on the variance of the runoff time is quantified in the following by using the dimensionless statistic ϑ_2 (termed normalised time dispersion in the following), computed as the ratio of $Var(T_f)$ and $Var(\tau)$, as follows:

$$\vartheta_2 = \frac{Var(T_f)}{Var(\tau)} = \frac{\iint_A P_t(x,y)[\tau(x,y) - \tau_{mean}]^2 dxdy + \tau_m^2 - E(T_f)^2}{\iint_A [\tau(x,y) - \tau_{mean}]^2 dxdy} \tag{3.20}$$

As for ϑ_1, the values of ϑ_2 are defined positive and take the value of one when the rainfall field is

spatially uniform. When the rainfall field is spatially concentrated, either towards the outlet or toward the periphery of the catchment, the values of ϑ_2 are less than 1. In the rather rare cases when the rainfall field has a bimodal spatial distribution, with concentration both at the headwaters and at the outlet of the catchment, the values of ϑ_2 are greater than 1. It should be noted that, with the rainfall excess volume remaining unchanged, the effect of decreasing (increasing) the variance of runoff time is to increase (decrease) the flood peak.

3.3.4 The June 30, 2006 flood on the Clit river at Arbore

The Clit River is a tributary of the Solca River in Romania. The Clit catchment closed at Arbore (36 km^2) represents a typical headwater basin of this river system, with elevation ranging from 357 to 928 m a.s.l., and with mean slope of 8.4%. Mean annual precipitation is around 620 mm. The 100-yr 24-hr rainfall is higher than for the Feernic catchment and amounts to 144 mm. The geological properties are rather homogeneous, with almost all the catchment characterised by the semi-permeable rock formation of the mollasse. Forests (about 56% of the basin area) range from coniferous to broad leaves. The percentage of arable soils is 25% and the rest of the land is used as pastures and meadows.

No streamgauge stations are available in the catchment. For this reason, all observations concerning the peak magnitude and timing in the catchment were obtained by means of a post-event survey carried out during the weeks following the event.

On June 30, 2006, the storm event started around 1800 UTC, lasting for 4 hours, although the explosive growth of precipitation occurred in the first two hours. Extreme rainfall amount was measured in the central portion of the catchment, with values around 130 mm. The catchment average rainfall amount was estimated 80.5 mm. During the two hours of extreme precipitation, the mean of non-zero values ranged between 40 and 50 mm h^{-1} (similar to the case of Feernic), whereas the spatial variability was less remarkable, with values ranging between 0.4 and 0.6 (Figure 3.4 on the facing page).

The soil moisture status at the start of the event was moderately wet, as a consequence of a wetter-than-average 30 days period before the flood (with 163 mm of rain compared to 99 mm resulting from the climatological average over the same period). The peak discharge at Arbore was estimated based on the survey of the post-flood river section geometry and by using a critical section method. This led to an estimate of 175 m^3 s^{-1} , corresponding to unit peak discharge of 4.9 m^3 s^{-1} km^{-2} . According to accounts from an eyewitness, flooding started around 1830 with the peak time in the period 1930-2015. Around 2230 the flooding ended and the discharge was less than 50 m^3 s^{-1} (according to observed water levels). As a consequence of the flood, 11 people died in Arbore and heavy damages to both houses and infrastructures were reported. Two main bridges collapsed during the flood.

Figure 3.3 shows the runoff simulation obtained by the distributed hydrological model, which was implemented by using the same approach reported for the Feernic river case study. The runoff coefficient

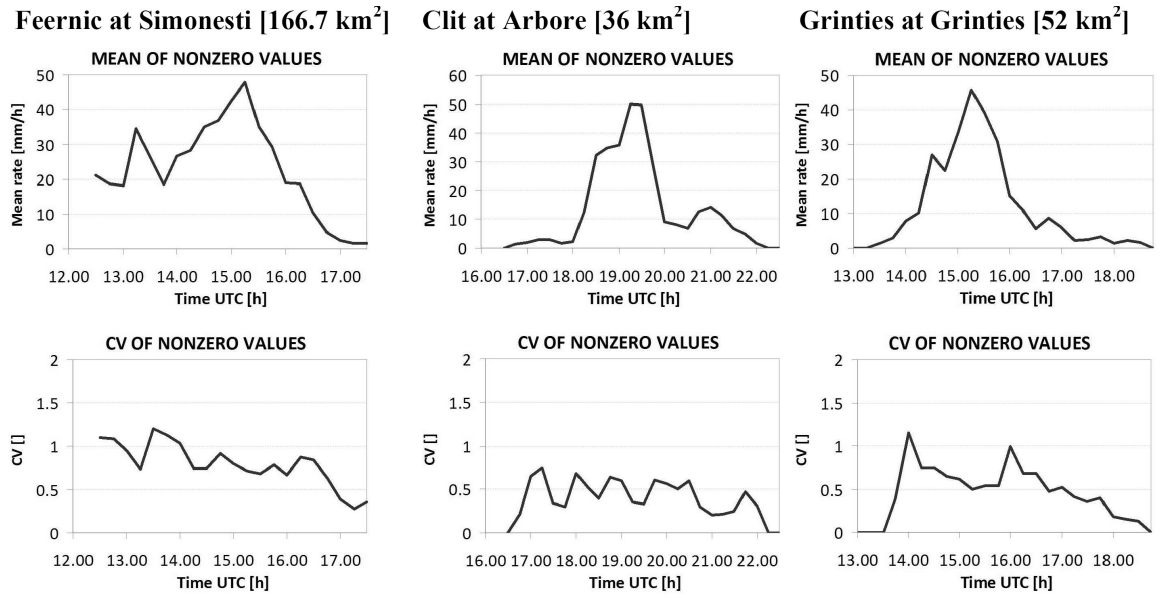

Figure 3.4: Precipitation analysis on the three study catchments. Time series of: (top) mean rain rate of non-zero bins and (bottom) coefficient of variation of non-zero rain rates.

obtained based on the simulated discharges amounts to 0.35.

3.3.5 The August 4, 2007 flood on the river at Grinties

The Grinties River is a tributary of the Bistricioara River in Romania. The Grinties river catchment closed at Grinties (52 km^2) represents the highest headwater basin examined in this work, with elevation ranging from 545 to 1736, and with mean basin slope of 32%. Mean annual precipitation in this area is around 660-700 mm, whereas the 100-yr 24-h rainfall is intermediate between the case of Feernic and that of Clit, amounting to 108 mm. The geological properties are quite diverse, with 36% of the catchment characterised by the flysch formation and 55% by a metamorphic impermeable geology. Forests (about 81% of the basin area) represent the most important land cover, with the remaining land used mainly as pastures.

On August 4, 2007, the storm event started around 1400 UTC, lasting for 3 hours, and 90% of the precipitation falling in 2 hours. The storm rainfall volume was around 66.8 mm, with peaks exceeding 100 mm in the central part of the catchment. Examination of Figure 3.4 shows that during the period of explosive growth of precipitation (between 1430 UTC and 1530 UTC) the mean values of non-zero rainfall ranged between 30 and 45 mm h^{-1} , with values of coefficient of variation ranging between 0.5 and 0.6 (similar to the case of Clit).

The soil moisture status at the start of the event was slightly wet (precipitation in the 30 days period before the flood amount to 130 mm, which has to be compared with the climatological amount in the same period, equal to 103). As no streamgauge stations are available in the catchment, all observations

on the event were collected during a survey organised two months after the flood. The peak discharge at Grinties (a small town of around 800 inhabitants) was estimated based on the survey of the post-flood river section geometry and by using a critical section method. This led to an estimate of 100 m^3 s^{-1} , corresponding to almost 2.0 m^3 s^{-1} km^{-2} . Accounts from a number of eyewitnesses were collected and intercompared. The accounts indicates that flooding started in the period between 1500 and 1530, reaching the peak between 1630 and 1700. Around 1730 the flooding ended and the discharge was less than 50 m^3 s^{-1} (according to observed water levels). One casualty was reported in relation to the event. Moreover, three bridges were destroyed and 36 buildings were flooded and damaged.

Figure 3.3 shows the runoff simulation obtained by the distributed hydrological model, which was computed by using the same approach described above for the Feernc case. The model is able in this way to offer a good match of the flood peak and of the time-to-peak. No observations are available concerning the flood shape. The runoff coefficient obtained based on the simulated discharges amounts to 0.11.

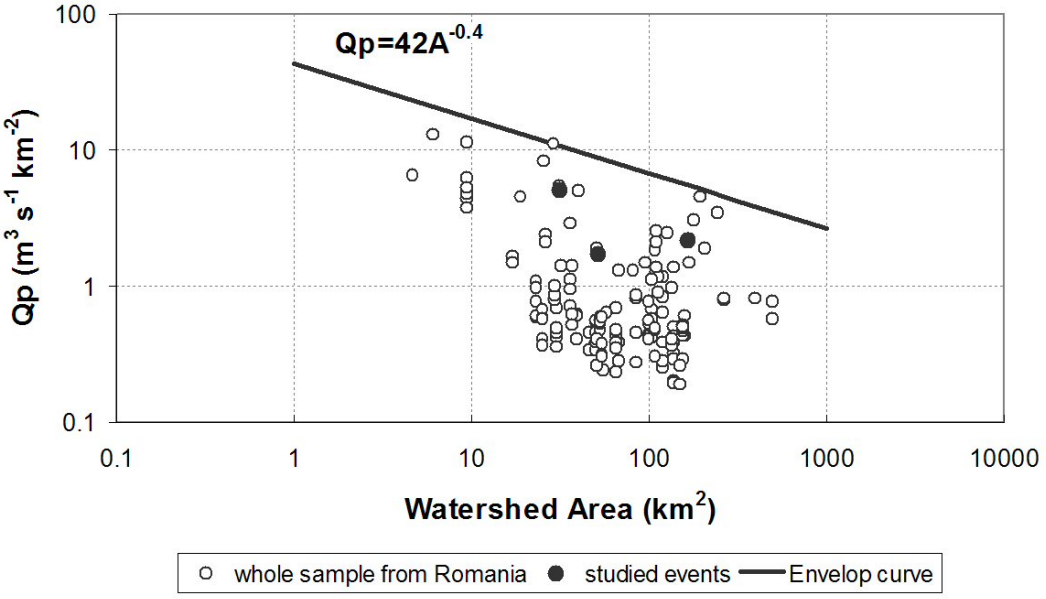

Figure 3.5: Comparison between the unit peak discharges from the three flash flood events considered in this study (full circles) and the unit peak discharges reported in the period 1973-2007 over the whole country (empty circle). The envelope curve is based on the work by Gaume *et al.* (2009).

Figure 3.5 compares the unit peak discharge of the three events considered in this study with a sample of 152 events recorded in the period 1973-2007 over the whole country. Although the events are not exceeding the historical values for the region, anyway they represent very intense cases, with the severity of Simonesti and Clit being exceeded only 2-3 times during the period considered (in the corresponding range of basin size). The case of Grinties is relatively less intense. The runoff coefficients of the flash floods are rather low and in the range reported by Marchi *et al.* (2009b) for flash flood events in the

Continental region of Europe.

3.4 Examination of the rainfall pattern statistics for the three flash flood events

Hereafter we use the methodology presented in section 3.3 on page 77.

The rainfall pattern statistics ϑ_1 "normalised time distance" and ϑ_2 "normalised time dispersion" were computed based on the event-cumulated rainfall pattern for the three flash flood events. Results are reported in Table 3.2 on the following page, together with values of mean travel time and corresponding standard deviation for the three impacted catchments.

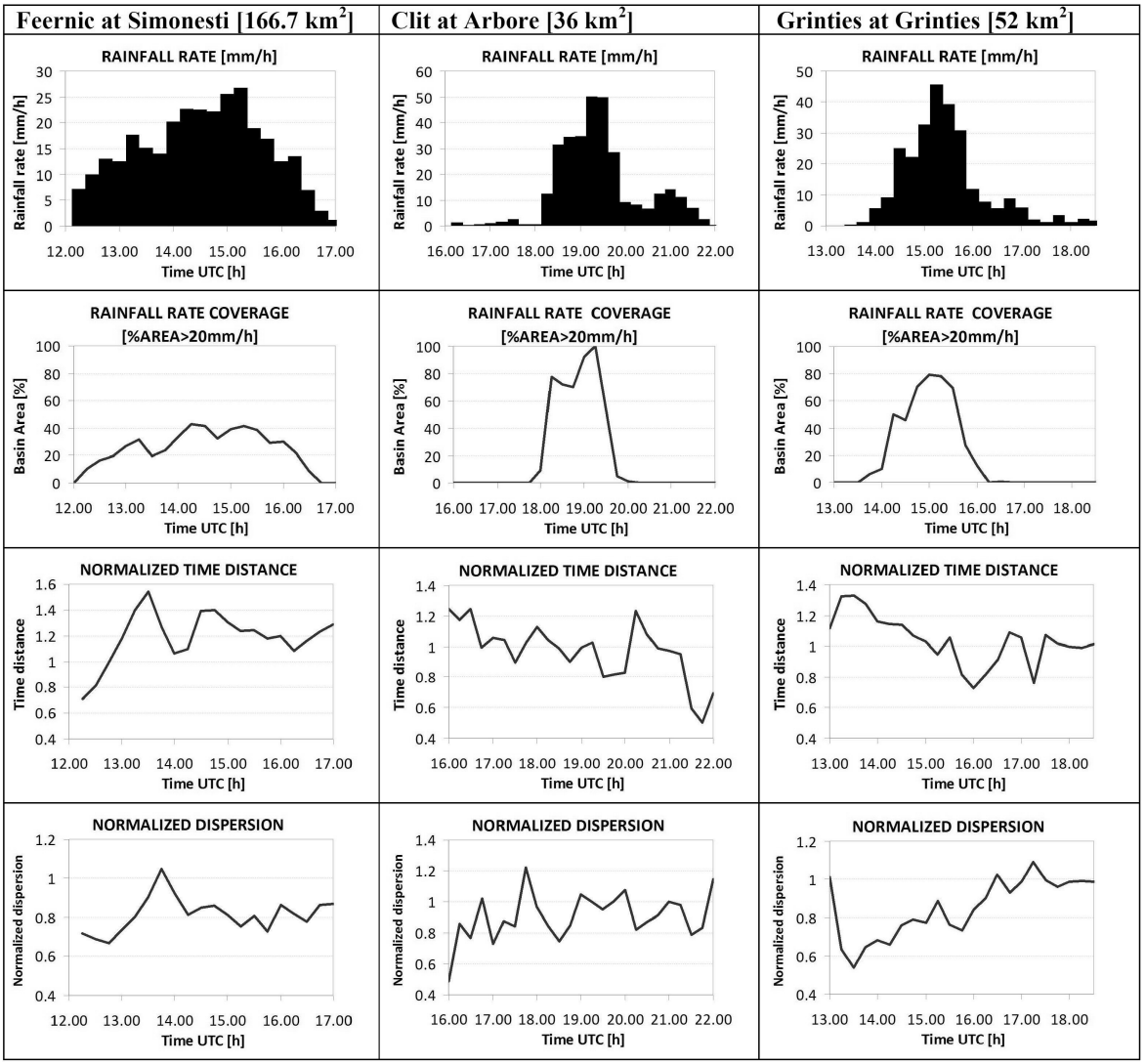

Figure 3.6: Precipitation analysis by using time series of precipitation intensity, coverage (for precipitation intensity > 20 mm h^{-1}), normalised time-distance and normalised time dispersion, for the three flash flood events.

Despite the large variability in rainfall over the Clit and the Grinties, the values of ϑ_1 are close to one, implying that the conditional average value of routing times, given the spatial rainfall distribution, is overall very close to the distribution of routing times in the uniform rainfall case.

For the Clit, normalised time-distance and dispersion are virtually unchanged from uniform rainfall case. For the Grinties, the rainfall spatial concentration over the catchment centroid is rather important and it is reflected in a low value of normalized dispersion. For the Feernic case, the normalized time distance is considerably greater than one, indicating a rainfall pattern focused over the headwaters. The low value of the normalized dispersion for Feernic is a consequence of this concentration.

The rainfall statistics were also computed at each time step (over the 15-min cumulated rainfall patterns) as time series, to examine the variability in time of the statistics. The time series are reported in Figure 3.6, together with the time series of the mean catchment rainfall rate and of the fractional coverage of the basin by rainfall rates exceeding 20 mm h^{-1}, where this threshold has been selected to indicate a flood-producing rainfall intensity. These time series show clearly the differences between the event on the Feernic, with the flood producing rainfall concentrated in a relatively small portion of the catchment, and the other two events of Clit and Grinties, where the rainfall has a more widespread character.

The time series of normalized time distance exhibits a relatively large variability, particularly in the Feernic case, with the time distance varying from 0.8 to 1.6 in the first 80 minutes (with a clear upbasin storm motion, as reflected in increasing values of the statistic) and then decreasing in the following three hours, where a downbasin storm motion can be recognized. The Clit and the Grinties event also reveal a clear downbasin storm motion, with the time distance decreasing from 1.2 to 0.8. The time dispersion generally reflects the trend of the time distance, as expected, with small values of dispersion when time distance is both larger or smaller than one, and values of dispersion close to one when the time distance is also close to unity.

Catchment	ϑ_1	ϑ_2	**Mean travel time [hr]**	**Standard deviation of travel time [hr]**
Feernic	1.22	0.89	2.08	0.98
Clit	0.98	0.96	0.82	0.35
Grinties	1.03	0.87	0.96	0.33

Table 3.2: Rainfall pattern statistics and travel time statistics for the three study catchments. ϑ_1 and ϑ_2 are "normalised time distance" and "normalised time dispersion" respectively.

3.5 Runoff model sensitivity to rainfall spatial variability for the flash flood events

Runoff model sensitivity to rainfall spatial variability was examined by dissecting the three study catchments into a number of similar (in size) nested subcatchments (Figure 3.7). This enables examination for different catchment sizes and rainfall spatial organisations of two questions: i) how different rainfall patterns are portrayed by the statistics of normalised time distance and normalised time dispersion, and ii) how these statistics are related to errors in runoff response modelling arising by neglecting the rainfall spatial variability. The Feernic river was dissected into 9 subbasins, the Grinties into 3 subbasins and the Clit into two subbasins. Overall, 14 catchments were analysed by using the rainfall-runoff model and deriving the rainfall statistics; the catchment size ranges between 5 and 167 km^2. For the Feernic, the subcatchments corresponded also to the river section where post-event analysis where available and where the runoff model was evaluated against reconstructed peak flow values.

In the first step of the analysis, we checked the impact of assuming the runoff coefficient as spatially uniform in the derivation of the equation for ϑ_1. To this purpose, we computed the values of ϑ_1 "normalised time distance" based on distributed event runoff amount (instead of rainfall amount), computed as surface runoff by the rainfall-runoff model. Then, we compared these values with those obtained based on the event-cumulated rainfall field (Figure 3.8a, where $\vartheta_{1,R}$ indicates the statistic computed on runoff and $\vartheta_{1,P}$ indicates the one obtained from the precipitation field).

Examination of Figure 3.8a shows that there is a fairly good linear correspondence between $\vartheta_{1,R}$ and $\vartheta_{1,P}$, implying that assuming the runoff coefficient as spatially uniform is relatively realistic, as far as it concerns the derivation of this statistic. However, one may notice that the non-linear character of the rainfall-runoff transformation influences the range of the values, with the values of $\vartheta_{1,P}$ ranging between 0.95 and 1.22, and $\vartheta_{1,R}$ ranging in the wider interval 0.8-1.25.

The relationship between the statistics $\vartheta_{1,P}$ and $\vartheta_{2,P}$, both computed based on precipitation, is explored in Figure 3.8b. Inspection of this figure shows that generally $\vartheta_{2,P}$ is close to one when $\vartheta_{1,P}$ is also close to one, indicating that in these cases the normalised time-distance and dispersion are virtually unchanged from uniform rainfall case. $\vartheta_{2,P}$ is considerably less than one when $\vartheta_{1,P}$ is either considerably larger or smaller than one, as expected. However, in one case $\vartheta_{2,P}$ is considerably less than one when $\vartheta_{1,P}$ is close to one. In this case the rainfall field is spatially concentrated close to the centroid of the catchment, with a corresponding low value of dispersion. In the second step of the analysis, we quantified the effect of neglecting the rainfall spatial variability on the rainfall-runoff model application. For each subcatchment, the flash flood event was simulated by using the actual rainfall spatial variability and then by using spatially uniform precipitations, hence obtaining two different hydrographs. The differences between the two simulated hydrographs were examined by using two statistics:

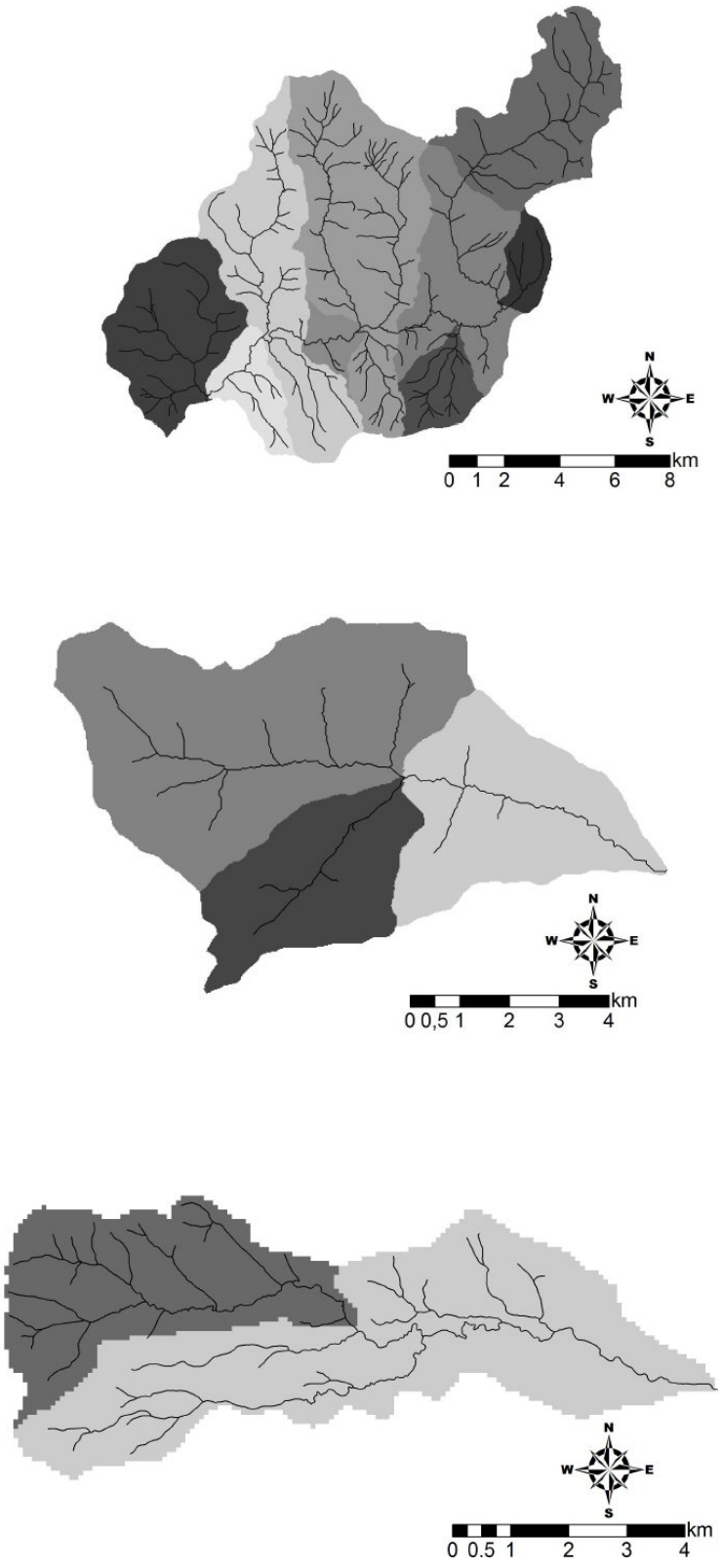

Figure 3.7: Subdivision of the study catchments into nested sub-basins.

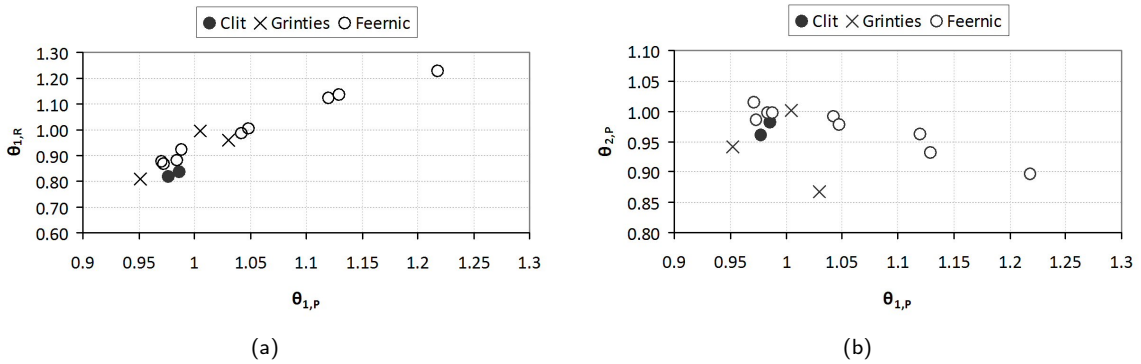

(a) (b)

Figure 3.8: (a) Relationship between the normalised time distance computed based on event precipitation ($\vartheta_{1,P}$) and that computed based on event runoff ($\vartheta_{1,R}$), for the 14 sub-basins considered in the study. (b) Relationship between normalised time distance ($\vartheta_{1,P}$) and normalized time dispersion ($\vartheta_{2,P}$), both computed based on event precipitation, for the 14 sub-basins considered in the study.

- the time difference between the two hydrograph centroids (hereinafter referred to as Δt_n), normalised by taking the ratio with the corresponding mean travel time in order to afford comparison among different catchments. A positive (negative) value of Δt_n implies a positive (negative) shift in time of the hydrograph generated by uniform rainfall with respect to the one produced by spatially distributed precipitation;

- the Nash Sutcliffe efficiency (hereinafter referred to as NS), computed as follows:

$$NS = 1 - \frac{\sum_{i=1}^{n}(Q_i^r - Q_i^\mu)^2}{\sum_{i=1}^{n}(Q_i^r - Q_{ave}^r)^2} \tag{3.21}$$

where Q_i^r is the $i-th$ reference discharge computed by using the actual spatial rainfall variability, Q_i^μ is the simulated discharge computed by using uniform precipitation, and Q_{ave}^r is the mean value of the reference discharges. The coefficient of efficiency was selected because it is dimensionless and is easily interpreted. If there are no differences between the two hydrographs, then E=1. If E<0 then the errors due to ignoring the rainfall spatial variability are such that the model's predictive power is worse than simply using the average of the reference values.

The relationships between the statistics Δt_n and NS and the rainfall statistic $\vartheta_{1,P}$ are reported in Figure 3.9a,b, respectively. Figure 3.9a shows that there exists a fairly good linear relationship between the value of $\vartheta_{1,P}$ and Δt_n, as expected based on equation 3.13 on page 79, at least for positive values of $\vartheta_{1,P}$ (corresponding to cases of precipitation concentrated towards the headwater of the basin). This means that the runoff generated by a precipitation concentrated towards the upstream periphery of the basin

tends to arrive later at the outlet with respect to a uniform one, and that the delay is corresponding to the time difference statistic. Values less then 1 of $\vartheta_{1,P}$ correspond to negative values of Δt_n, as expected, but the linear relationship cannot be recognized anymore. This reflects the behavior of the smallest basins in our sample, with values of time difference between hydrograph's centroids which are small in absolute terms. However, since their mean travel time (used as a normalizing quantity) is also small, values of Δt_n become larger, and thus even small differences in the hydrograph shapes are emphasized with this comparison.

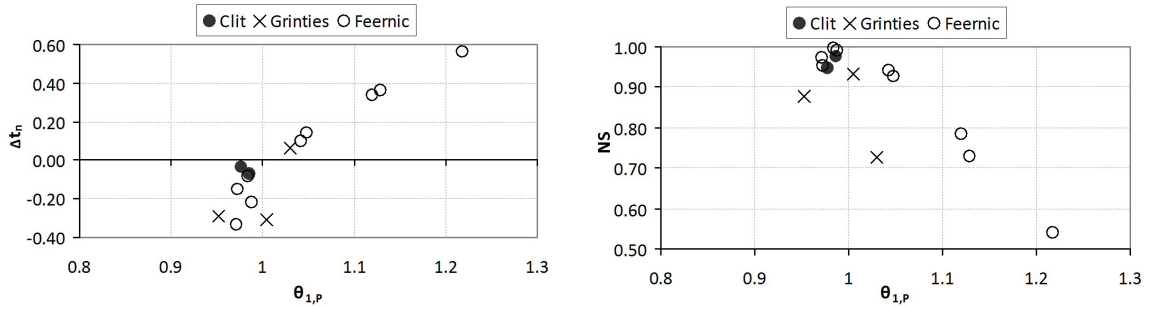

Figure 3.9: (a) relationship between the normalised time distance $\vartheta_{1,P}$ and the time delay Δt_n; (b) relationship between the normalised time distance $\vartheta_{1,P}$ and the Nash-Sutcliffe efficiency statistics NS.

Figure 3.9b shows the impact of neglecting the spatial rainfall variability on the efficiency statistics. Several important features can be recognized in this figure. Ignoring the spatial rainfall variability results in a considerable loss of simulation efficiency (NS less than 0.8) in almost 30% of the cases (four cases out of 14), with NS less than 0.6 in one of the cases. This provides a significant documentation of the influence of the spatial rainfall variability on runoff modeling for catchment scale less than 150 km^2. All the cases with low NS values are characterized by either high values of $\vartheta_{1,P}$ ($\vartheta_{1,P}$>1.1), implying focusing of precipitation towards the headwater portions of the catchments, or low values of $\vartheta_{2,P}$ ($\vartheta_{2,P}$<0.9) (the case of Grinties with Figure 3.8b), implying a strong spatial concentration of precipitation. All the cases with both values of $\vartheta_{1,P}$ and $\vartheta_{2,P}$ close to one are characterized by high values of efficiency. This shows that these rainfall statistics, used in combination, are able to capture the features of rainfall spatial variability which have significant impact on runoff simulation.

3.6 Conclusions

In this work we modify the framework proposed by Woods and Sivapalan (1999) to develop a set of statistics which may effectively clarify the dependence existing between spatial rainfall distribution, basin morphology and runoff response. The two statistics are represented by:

1. A scaled measure of the time taken to route the rainfall from the geographical centroid of the rainfall spatial pattern to the geographical centroid of the catchment, ϑ_1;

2. A scaled measure of the additional variance in runoff time that is caused by the spatial variability in rainfall, relative to the case of spatially uniform rainfall throughout the catchment, ϑ_2.

The statistics are based on the observation that runoff routing through branched channel networks imposes an effective averaging of spatial rainfall excess at equal travel time, in spite of the inherent spatial variability. This implies that rainfall organisation measured along the river network by using the travel time coordinate may be a significant property of rainfall spatial variability when considering flood response modelling.

The analysis reported in chapter 3 suggests that the two statistics are effective in i) describing the degree of spatial organisation which is important for runoff modelling, and ii) quantifying the effects of neglecting the spatial rainfall variability on flood modelling. The use of these statistics enables linking different sources of errors emerging when the spatial rainfall variability is neglected, such as timing error and shape error. Moreover, the methodology analytically derived provides an avenue to revisit and express prior results. For example, the special averaging operator defined in equation 3.14 on page 79 is a special case of the soil-weighting function proposed by Naden (1992). The statistics defined in this thesis are similar to those developed by Zhang *et al.* (2001) and by Smith *et al.* (2005, 2002b,a). These researchers, in a series of monographs on extreme floods and flash flood events, systematically employed a scaled measure of distance from the storm centroid and a scaled measures of rainfall variability to quantify the storm spatial organisation and variability from the perspective of a distance metric imposed by the river network. However, they found that, despite the large variability in rainfall when viewed from a Euclidean perspective, the variability measured along the flow distance was small, suggesting that the storm event response was strongly determined by the drainage network structure and less by rainfall spatial variability.

A similar approach was taken by Smith *et al.* (2004a), who developed a set of diagnostic indicators that can be used to formulate inferences on the nature of a basin's response for basins in the Distributed Model Intercomparison Project [Smith *et al.*, 2004b]. One of the indicators was represented by a rainfall location index computed based on of the distance from the centroid of the catchment to the centroid of the rainfall pattern. Analogously, Syed *et al.* (2003) evaluated the ability of simple geometric measures of thunderstorm rainfall in explaining the runoff response from a 148 km^2 watershed. They also used a location index similar to that introduced by Smith *et al.* (2004a). They observed that the position of the storm core relative to the watershed outlet becomes more important as the catchment size increases, with storms positioned in the central portion of the watershed producing more runoff than those positioned near the outlet or near the head of the watershed. Sangati *et al.* (2009); Sangati and Borga (2009) examined the influence of rainfall spatial resolution on flood response simulation by using the flow distance as a

spatial coordinate to measure the rainfall organisation. They found that increasing rainfall resolution may affect significantly runoff simulation, even at catchment scales as low as 250 km^2, for those cases when the distance to the storm centroid (measured along the river network) was systematically larger than the distance to the catchment centroid. These events were related to cases of strong convection enhanced by orographic uplifting and their analysis highlighted the capability of these measures to provide a metric for the effect of orography on storm organisation and on runoff modelling.

Use of travel time instead of flow distance in the formulation of the statistics affords a more general quantification of the runoff propagation characteristics. The flow distance has two components: the distance on hillslopes from the pixel to the channel network, and the distance from the channel network to the outlet. When no distinction is made between the travel velocities over hillslopes and over the channel network, the two concepts necessarily coincide. However, when the two velocities are represented by using different values, use of travel time enables analysis of the effects of the hillslope response on the statistics. On-going investigations are aimed to illustrate these aspects.

Other aspects of the work require further investigation. This concerns for instance the possibility of quantifying the evolution in time of the normalized travel time values, as a way to illustrate the catchment-scale rainfall effective velocity along the river network (either downstream or upstream). The importance of storm movement on surface runoff has been investigated for nearly four decades [Maksimov, 1964; Niemczynowicz, 1984; Singh, 1998; De Lima and Singh, 2002, among others]. However, most of this knowledge have been derived from simulation experiments, due to difficulties in isolating and quantifying the effective dynamics of the observed rainfall patterns at the catchment scale (as opposed to the kinematics of the single storm elements). The statistics introduced in this work may be used to derive in a direct way these dynamics, as shown in the formulation developed by Viglione *et al.* (2010a,b). On a different avenue, use of the normalized time distance and the normalized time dispersion rainfall statistics may provide a useful framework to quantify the impact of catchment shape in accounting for rainfall spatial variability. Nicotina *et al.* (2008) highlighted for instance the larger sensitivity of elongated catchments with respect to catchments characterized by more compact shapes.

4. Hydrometeorological Analysis of the 29 August 2003 Flash Flood in the Eastern Italian Alps

4.1 Introduction

The eastern Italian Alps (Figure 4.1 on the next page) in the Friuli region of Italy has been a workshop for hydrologists and geomorphologists to study the hydrological and geomorphological effects of extreme storms [Deganutti and Marchi, 2000; Marchi and D'Agostino, 2004]. The region includes the upper Tagliamento River basin as the major river system and is characterized by frequent heavy precipitation. Daily rainfall amounts exceeding 500 mm may be locally recorded in this area in a 20-30-yr time span [Villi *et al.*, 1986; Ceschia *et al.*, 1991]. During late fall, winter, and spring, heavy precipitations are normally related to synoptic circulations and to southerly humid flows. During summer and partially during fall, the contribution from convective or mesoscale rainfall becomes significant or even prevailing. Because of the rugged topography of the region, together with its densely fractured bedrock and its high seismicity [Querini, 1977], heavy convective precipitations result often in flash floods, associated with diffused landsliding, debris flows, and sediment trans- port.

On 29 August 2003, at the end of a prolonged drought, a mesoscale convective system affected the study area, starting at 1000 local standard time (LST) and lasting for approximately 12 h. Prior to the development of convection, the atmosphere was characterized by strong instability as evidenced by the very high CAPE value on the Udine radio sounding of 29 August 2003 at 0700 LST (about 4000 J kg^{-1} for the CAPE computed based on the most unstable parcel). Precipitable water computed for this radio sounding amounts to 44 mm and shows that the humidity content of the atmosphere was already high. The storm affected a 1500 km^2 area, and caused loss of lives and substantial disruption of the local economy, with damages close to 1 billion euro [Tropeano *et al.*, 2004].

Radar rainfall observations, combined with data from 15 rain gauges, provide high temporal (5 min)

and spatial (1 km^2) representation of rainfall from the August 2003 storm. A noticeable characteristic of the precipitation event was its organization in well-defined banded structures. The steadiness of these rainbands led to highly variable precipitation accumulations.

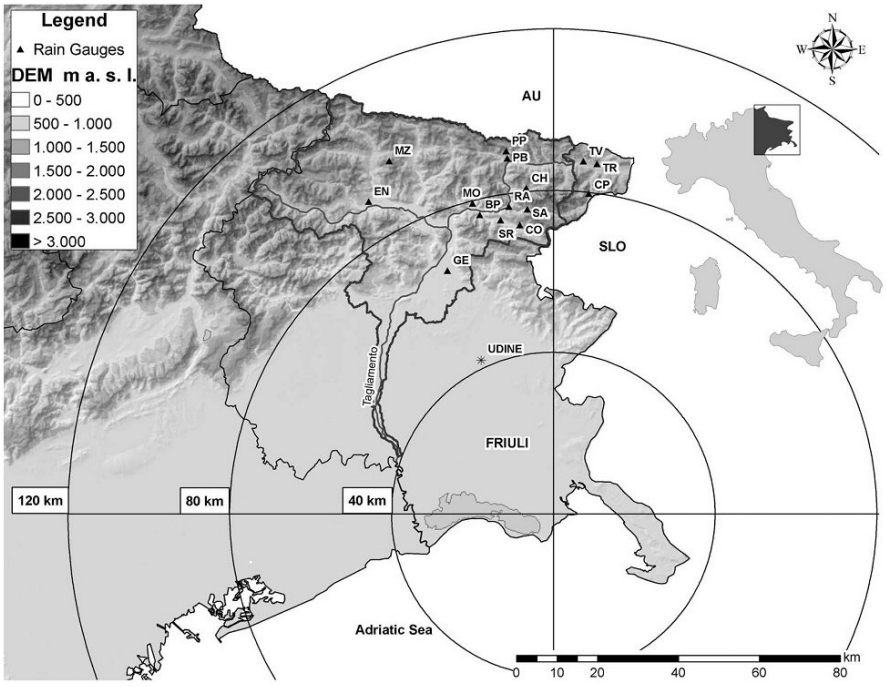

Figure 4.1: Location of the OSMER radar and the Tagliamento River basin with digital terrain model (DTM) of northeastern Italy. The locations of the rain gauge stations used in the study are also reported.

Time series of river stage at a number of gauging stations were combined with indirect discharge measurements to produce flood hydrographs at several river sections. Extensive post-event surveys of peak flows and interviews were carried out to characterize the spatial variability of flood response.

The 29 August 2003 flood is also of particular interest because it provides an end member in the spectrum of impacts of antecedent soil moisture on extreme floods. The event resulted indeed as a combination of two extreme events, since very large accumulations of rainfall over 3-6 h occurred at the end of a climatic anomaly of prolonged drought and warm conditions in Europe and over the Mediterranean. Analysis of temperature records over Europe shows that the 3-month period June-August 2003 has been probably the warmest since 1500 over western Europe [Casty *et al.*, 2005]. The drought culminated in August, but precipitation accumulations were below average since the beginning of the year. At the Udine rain gauge station, close to the study area, the cumulative precipitation total for the first eight months of 2003 was around 50% of the climatological average. As a consequence, the soil water content was very low at the beginning of the event. A heavy localized thunderstorm that occurred the day before the flood on a portion of the Fella River system introduced elements of spatial variability in the pattern of soil moisture initial conditions.

Whereas it is generally recognized that antecedent soil moisture is of little importance in determining the magnitude of extreme floods [Wood *et al.*, 1990], the August 2003 flood provides a counterexample of the possible role of low antecedent soil moisture conditions, when combined with high soil moisture capacity, on the flood response of extreme storms. This impact is in terms of enhanced nonlinearity, that is, nonlinear variation of runoff with storm total, and mitigation of flood peak magnitude with respect to rainfall magnitude. Large initial losses and nonlinearities related to the wetting-up processes and to the extension of the river network to unchannelized topographic elements are examined in this study.

In line with previously published flash flood monographs [e.g., Smith *et al.*, 1996a; Ogden *et al.*, 2000; Gaume *et al.*, 2003; Hicks *et al.*, 2005], this work aims at documenting the 29 August 2003 flash flood. The objectives of this study are as follows: (1) to identify the aspects of storm structure, motion, and evolution that control the spatial and temporal distribution of extreme rainfall and flooding; (2) to provide estimates of peak discharge and to examine how peak discharge varied with basin scale; (3) to analyze the impact of space-time precipitation variability and of antecedent soil moisture conditions on flood response.

4.2 Study region and data

The region considered in this study (Figure 4.1 on the facing page) includes a portion of the central chain of eastern Alps and of the Alpine foreland region. The arc-shaped mountainous range of the eastern Alps constitutes the major topographic feature within the analysis domain. The most prominent valleys are aligned along the main ridge in the west-east direction for some tens of kilometers. The area is included within the Friuli-Venezia Giulia region, which borders to the north with Austria, to the east with Slovenia, and to the west with Veneto. The region is characterized by three distinct pluviometric regimes: (i) the upper plain area, with mean annual precipitation (MAP) ranging from 1200 to 1500 mm; (ii) the Alpine foreland area, where MAP locally increases up to 3300 mm, which represents the highest mean values for the Alps; (iii) the inner Alpine area, where MAP decreases to 1600-1800 mm, due to rain shadow effect of the southern ridges.

A description of the climatology of extreme subdaily rainfall is provided by the maps of the point average values of annual precipitation maxima (APM) for duration of 1, 3, and 6 h (Figure 4.2 on the next page). These maps are computed based on annual maxima from 36 stations, with an average usable record length of 39.5 yr. The maps show clearly (i) the relatively high values of these rainfall accumulations, and (ii) the orographic control on the spatial distribution of the average values. It is interesting to note that the highest values for 6h duration are located on the Alpine foreland area, while for 1h duration high values are also found on the southeastern coastal plain. The maps reveal also a marked decrease of the average APM values (for all durations) in the inner Alpine region.

The 29 August 2003 storm on the upper Tagliamento River basin is examined here as a prototype for

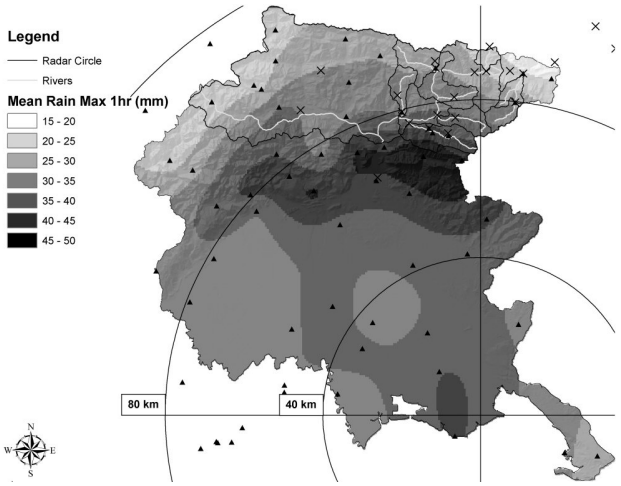

(a)

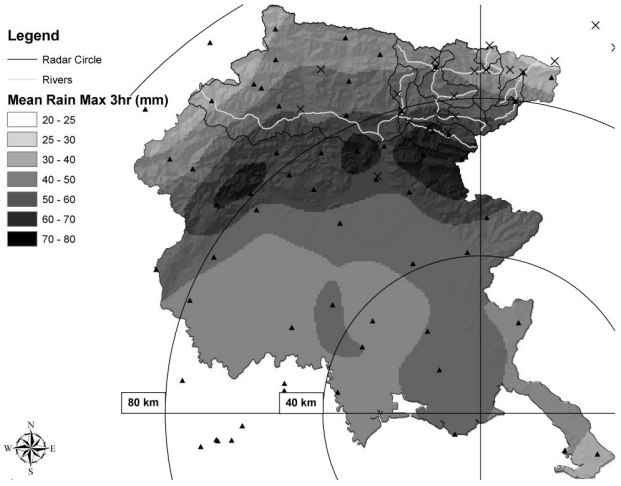

(b)

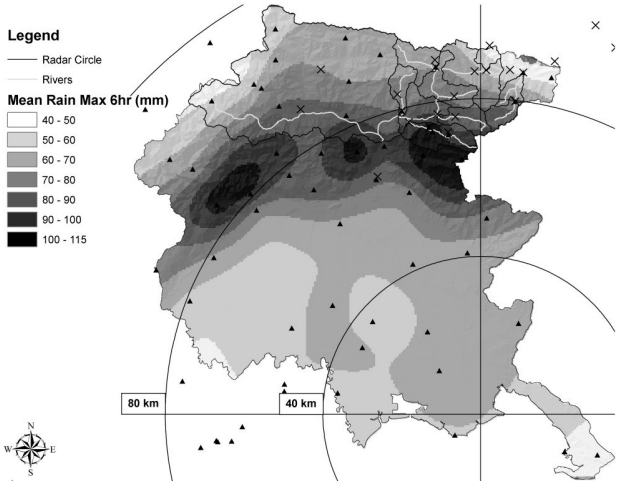

(c)

Figure 4.2: Maps of point average of maximum yearly rainfall for durations of a) 1, b) 3, and c) 6 h, for the Friuli region. Triangles represent the position of the stations used to draw the maps.

organized convective systems that are likely responsible for the majority of flash flood peaks in this area of the eastern Italian Alps. Previous similar flash flood events occurred in this region on 22 June 1996 and on 11 September 1983. Figure 4.3 on the following page show the APM empirical regional growth curves based on APL plotting position [Stedinger *et al.*, 2002] for the three durations of 3, 6, and 12 h. The data are obtained from 11 rain gauge stations located in the area of the Fella basin. It is interesting to note in these figures that all the normalized quantiles exceeding a value of 3.0 resulted from the aforementioned storms, which dominate therefore the upper tail of the precipitation frequency distribution.

The Tagliamento is the dominant river system in the analysis domain. From north to south (a linear distance of <100 km), the Tagliamento traverses four major regions: (i) the Julian and Carnian Alps, (ii) Alpine foreland area, (iii) the upper and lower Friulian plain, and (iv) the coast (Figure 4.1 on page 94). The alpine area of Friuli mainly consists of limestone, with a spatial sequence of Silurian, Devonian, Triassic, Jurassic, and Cretaceous formations north to south [Cucchi *et al.*, 2000]. Some portions of the regions are characterized by karstified limestone. The catchment is tectonically active, continuously developing faults and overthrusts. Many tributary streams, like the Fella, have sharp bends following the direction of these faults (Figure 4.4 on page 99). The pre-alpine mountains mainly consist of limestone (Jurassic-Cenozoic) and Flysch (calcareous flysch, molasse) [Ward *et al.*, 1999].

The Tagliamento is characterized by a flashy pluvio-nival flow regime, with the highest average discharges in spring (snowmelt runoff) and autumn (rainy period). At Pioverno (catchment area around 1866 km^2) the average annual precipitation amounts to 2150 mm and average discharge is 91 m^3 s^{-1} . The August 2003 flood focused on the 705 km^2 Fella basin (Figure 4.4 on page 99), which is a major left-hand tributary of the Tagliamento River system. This basin has a mean altitude of 1140 m above sea level (ASL), with an average annual precipitation of 1920 mm. Major subbasins of the Fella River are Pontebbana (70 km^2) and Aupa (50 km^2) (right-hand tributaries) and Dogna (47 km^2), Raccolana (63 km^2), and Resia (107 km^2) (left-hand tributaries). In the Fella watershed, the main carbonate complexes influenced by karst phenomenon are located around Monte Canin, in the upper Resia and Raccolana basins.

During the August 2003 flood, exceptional rainfall rates and accumulations were observed on the right-hand tributaries of the Fella, whereas the left-hand tributaries received much less rainfall, imposing a contrasting flood response to the different elements of the river system. On 28 August 2003, the day before the flood, a localized convective storm generated almost 100 mm of precipitation on areas of the left-hand tributaries of the Fella River system. This added to the various nonlinearities sources in the hydrologic response, introducing elements of spatial variability in the pattern of antecedent soil moisture conditions.

Postflood surveys were important source information for the flood analysis. Surveys were concentrated in the upper Fella basin and included (i) collection of rainfall data, (ii) indirect peak flood estimation, (iii) mapping of geomorphic effects, (iv) collection of hydraulic saturated conductivity values in a number

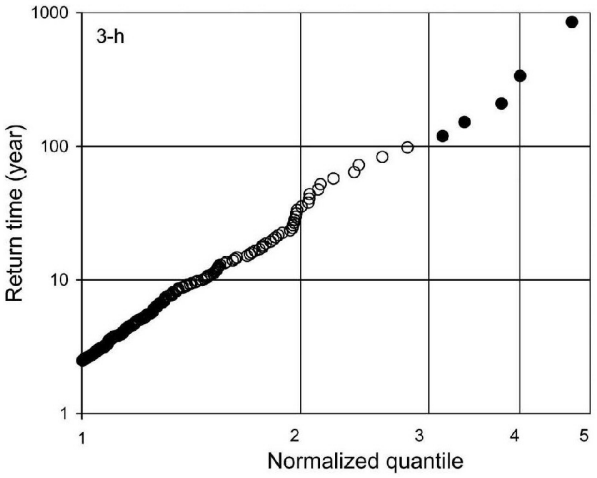

(a)

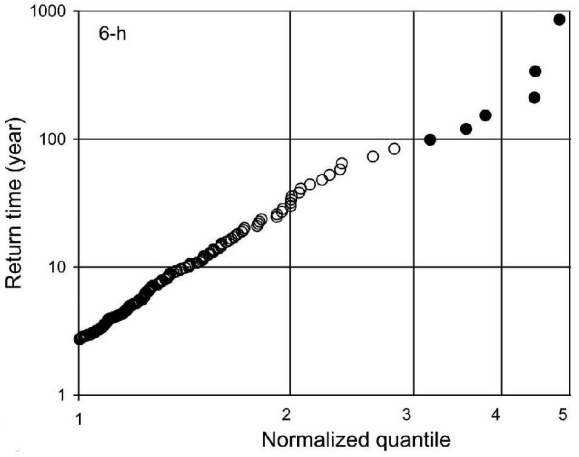

(b)

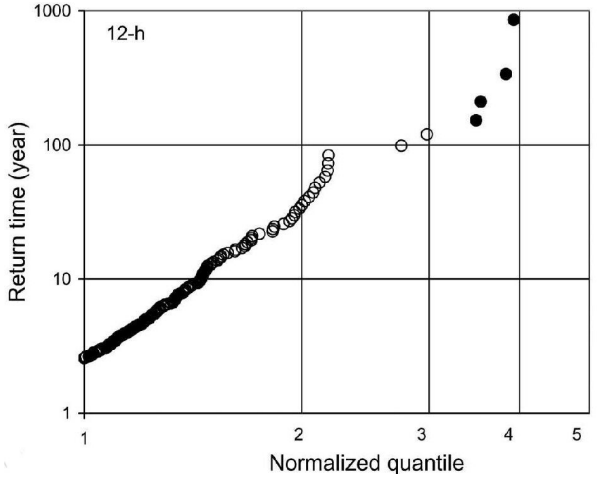

(c)

Figure 4.3: Empirical regional growth curves of precipitation annual maxima for the three durations of (a) 3, (b) 6, and (c) 12 h. Quantiles marked in bold result from the storms of 29 Aug 2003, 22 Jun 1996, and 11 Sep 1983.

of sites, and (v) postflood interviews.

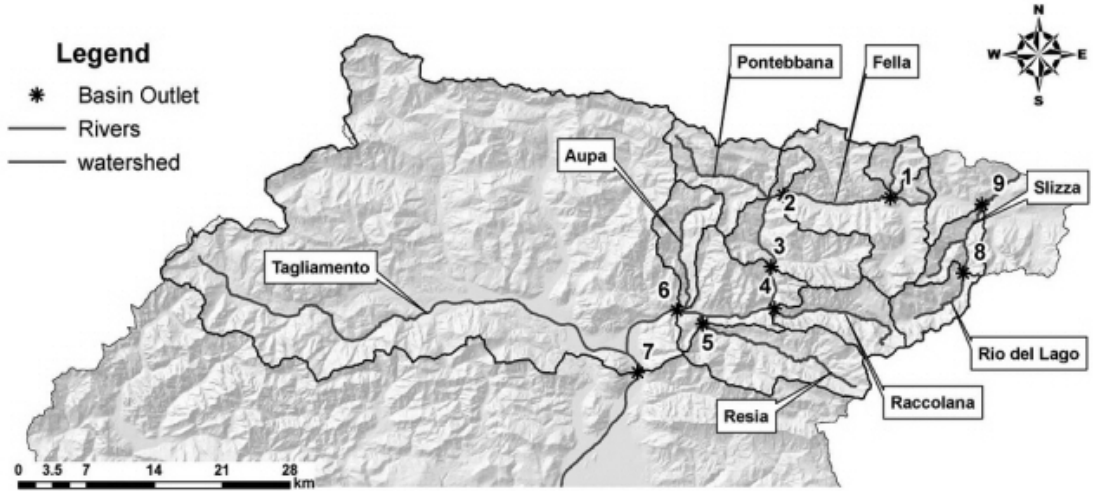

Figure 4.4: Catchment map of the upper Tagliamento River basin, with subcatchments of the Fella River basin: 1) Uqua at Ugovizza; 2) Fella at Pontebba; 3) Fella at Dogna; 4) Raccolana at Raccolana; 5) Resia at Borgo Povici; 6) Fella at Moggio Udinese; 7) Tagliamento at Venzone; 8) Rio del Lago at Cave del Predil; 9) Slizza at Tarvisio.

4.2.1 Rainfall data collection and elaboration

Radar and rain gauge observations are used to derive rainfall fields for the August 2003 storm. Five-minute rain gauge data were collected at 15 rain gauges (Figure 4.1 on page 94), whereas storm total rainfall was available at six additional daily rain gauges. Twelve out of the 15 rain gauges are located within the Fella watershed closed at Moggio Udinese (623 km^2) and the nearby Slizza watershed (73.1 km^2), that is, an average density of about one rain gauge per 50 km^2. Note that the network density is not homogeneous and that some gaps are evident in the northwest part of the Fella basin. Radar and rain gauge observations are used to derive rainfall fields for the August 2003 storm. Five-minute rain gauge data were collected at 15 rain gauges (Figure 4.1 on page 94), whereas storm total rainfall was available at six additional daily rain gauges. Twelve out of the 15 rain gauges are located within the Fella watershed closed at Moggio Udinese (623 km^2) and the nearby Slizza watershed (73.1 km^2), that is, an average density of about one rain gauge per 50 km^2. Note that the network density is not homogeneous and that some gaps are evident in the northwest part of the Fella basin.

Volume scan reflectivity data from the Doppler, dual-polarized C-band OSMER radar station, located at Fossalon di Grado (Figure 4.1 on page 94) (time resolution of 5 min and spatial resolution of 250 m in range by 0.9° in azimuth), were used to derive radar rainfall rates. The radar measures the reflectivity in two orthogonal (horizontal and vertical) polarizations, Z_h and Z_ν, respectively. When the two reflectivities are measured in an approximately simultaneous fashion, the differential reflectivity (in decibels) can be derived by dB Z_{DR}=$10\log 10(ZH/ZV)$. In this study, rainfall rates were estimated based on horizontal-polarized

observations; Z_{DR} values were use to discriminate ground clutter from rainfall observations.

A number of procedures were applied to the reflectivity data to correct for the following error sources: (i) ground clutter; (ii) partial beam occlusion; (iii) path attenuation; and (iv) wind drift. Hail was not observed during the event, so no correction was implemented to remove hail contamination.

An algorithm based on a three-step decision tree, based on Doppler velocity, clear-air echo statistics, and Z_{DR} variance, was used to flag clutter-contaminated data in the polar volumes [Bechini *et al.*, 2002]. Correction for beam occlusion is based on offline computation of the percentage of beam power intercepted by the orography by using a model of beam propagation and a digital description of the orography [Borga *et al.*, 2000; Pellarin *et al.*, 2002]. Path attenuation due to precipitation (which can generate large errors at C band at high rainfall rates; Delrieu *et al.*, 2000) is corrected by using a variational method with gauge accumulations as external constraints and the Hitschfeld and Bordan (1954) equation as model [Berenguer *et al.*, 2002].

Wind drift was a major error source in the comparison of radar estimates to rain gauge measurements, due to the strong winds and to the sharp local differences in rainfall accumulation. Wind drift correction was carried out by taking into account horizontal wind velocity and drops fall time to compute the rainfall advection. We adopted a bulk-advection approach, by assuming the same fall speed for all drops in a radar pixel.

Rainfall estimation was based on reflectivity observations from the 2.06° beam elevation, which is the lowest elevation affected by minimal beam occlusion over the study area. Effects due to nonuniform reflectivity along the vertical were not included in the analysis and correction procedure, due to the difficulties of separating the effects of attenuation from those generated by vertical variability of reflectivity and of beam occlusion for localized storms. After correction, the reflectivity factor Z was converted to rainfall rate R through an empirical R-Z power function of the form:

$$R = aZ^b \tag{4.1}$$

The R-Z parameters used are a=0.022 and b=0.67 for R in mm h^{-1} and Z in mm^6 m^3 . These parameter values are used in this region for estimation of convective events and are similar to those used in the so-called Next Generation Weather Radar (NEXRAD) convective relationship [Ogden *et al.*, 2000].

Figure 4.5 on the next page show the scatterplot between the 15 rain gauges rain measures and the corresponding radar estimates. The plot shows a general good agreement; the squared correlation coefficient for hourly accumulation is 0.73, while for rainfall accumulation on 12 h it raises to 0.94. The radar estimates are generally positively biased, with an overestimation around 10%. A few hourly rates are strongly overestimated by radar. It is difficult to identify clearly the origins of these differences, even though

some of them are related to a less-than-optimal correction for attenuation. Of particular importance is the capability of radar to delineate heavy rainfall areas. Figure 4.6 on page 102 summarizes the results obtained over a region centered on the Fella basin by intercomparing gridded gauge accumulations (obtained by using the spline technique) with radar estimates in terms of exceedance areas, that is, the areas over which a given amount of rainfall was exceeded in the region of interest. From the gauge network one infers that the area exceeding 350 mm is around 12 km^2, in contrast to a radar derived value of 55 km^2 . The accuracy of storm total radar rainfall accumulations was confirmed by comparison with values from daily rain gauges (BZ06).

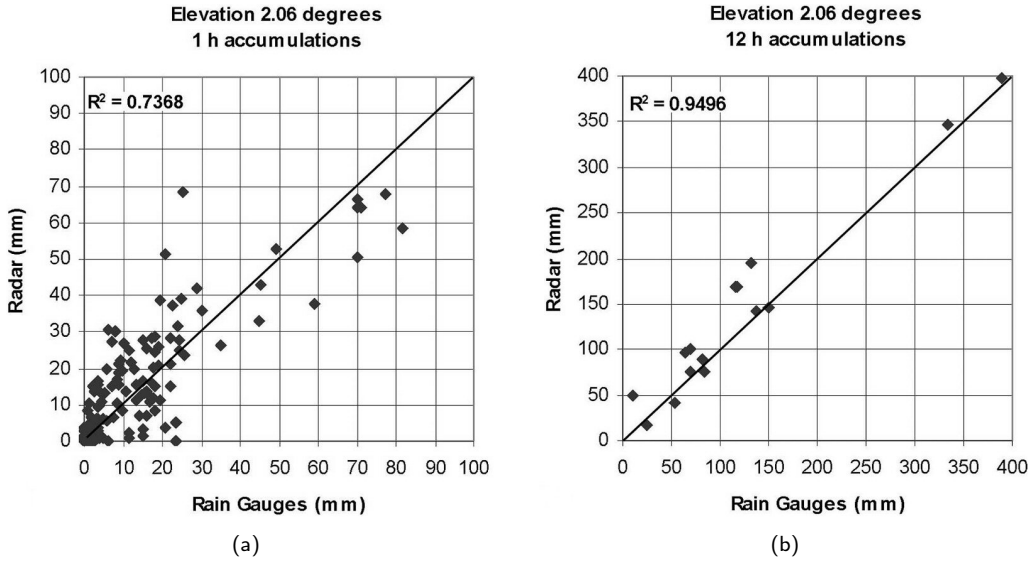

(a) (b)

Figure 4.5: Scatterplot of radar estimates and rain gauge accumulations at (a) hourly time steps and (b) 12-h time steps.

4.3 Precipitation analyses

Precipitation was analyzed by using animations of both the instantaneous rain rates at the 5-min time steps and the cumulated rain amounts over a given period. A synthesis of this information is provided by the following four figures: Figure 4.7 on the next page, which provides the storm total precipitation; Figure 4.8 on page 104, which reports the rain amounts during three main phases of the event; Figure 4.9 on page 105, which reports tracking-based representations of rainfall cells motion; and Figure 4.10 on page 105, which illustrates the spatial patterns of local maximum rainfall accumulations for 1 and 6 h.

The storm total precipitation (Figure 4.7 on the next page) exhibits three local peaks of rainfall accumulations exceeding 320 mm. The most extended accumulation is over the upper Aupa basin and the mid-Pontebbana basin; the second peak is close to the Uqua basin and near the Italian-Austrian border; the third one (and also the less extended) is located over the extreme eastern portion of the study area. The

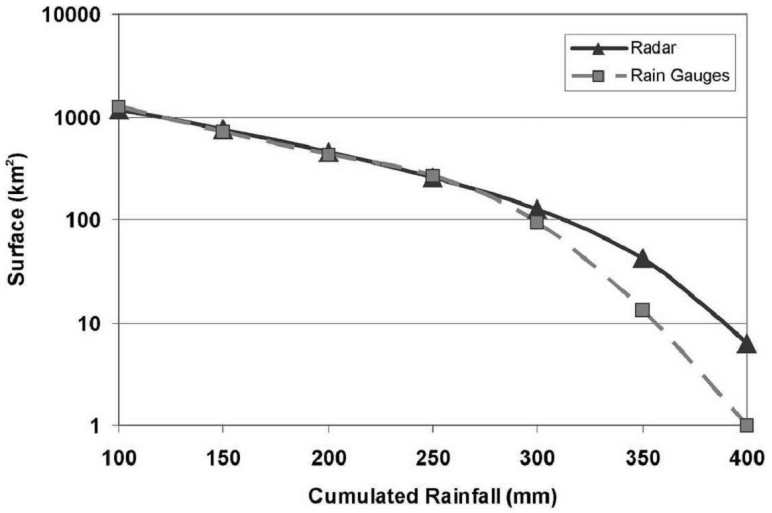

Figure 4.6: Curves of exceedance areas, i.e., the areas over which various rain thresholds were exceeded, using gridded rain gauge-based interpolation and radar-based estimates.

storm total rainfall distribution reflects southwest-northeast motion of the storm elements and west-east shift of the tracks of the storms. This evolution can be distinguished in Figure 4.8 on page 104, with the storm accumulation in three phases.

In the initial period (1000-1300 LST) the rainfall maxima (60-70 mm) extended over an elongated region at the western periphery of the Tagliamento, close to the Veneto-Friuli border. A secondary rainfall accumulation maximum extends over the right-hand tributaries of the Fella, from Aupa to Uqua, and over part of the Resia.

In the second period (1300-1900 LST) an explosive growth of precipitation can be recognized over the right-hand tributaries of the Fella River system, associated with orographic enhancement. A maximum of 350 mm is identified over the region comprised between Pontebbana and Uqua. Because of the west-east shift of storm tracks, precipitation extends also to the left-hand Fella tributaries, with accumulation up to 70 mm.

In the last phase (1900-2200 LST) the precipitation accumulation splits in three regions, with maximum of precipitation still concentrated over the Aupa and a less organized precipitation focused over the Slizza River system, at the eastern border of the Tagliamento River basin.

A striking characteristic of the event is its organization in four well-defined banded structures. The bands can be distinguished in Figure 4.10 a, which reports the maximum hourly values throughout the storm event. Some of the bands persisted in the same locations for the duration of the event, as evidenced in Figure 4.8 on the next page. The steadiness of these rainbands led to highly variable precipitation accumulations with extreme spatial gradients up to 70 mm km^{-1} .

The spatial organization of the bands of the August 2003 storm was analyzed based on the instan-

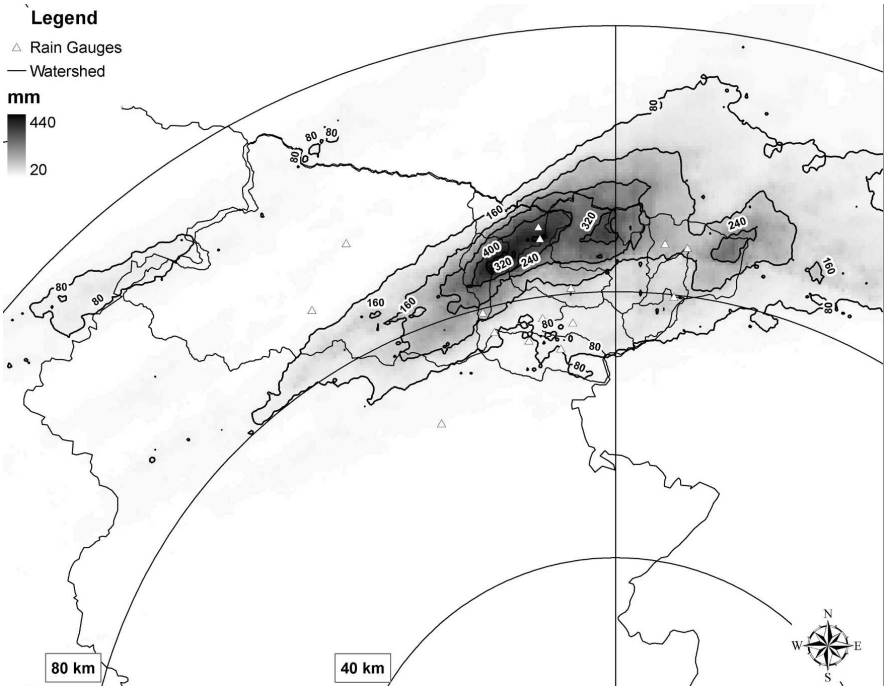

Figure 4.7: Storm total rainfall (mm) for the 29 Aug 2003 event.

taneous reflectivity observations. Mean band alignment, measured counterclockwise relative to the east, is comprised between 30° and 35° , and is almost parallel to the orographic flanks of the Veneto region (Figure 4.1 on page 94). Mean width, defined as distance between 5-dBZ contours on the flanks of individual precipitation bands, is around 9 km. Mean spacing, that is, distance between adjacent bands, measures 13 km. Although some of the bands appear to form over and downstream of small-scale peaks on the gradually sloping barrier, others form past valleys or have no clear connection to obvious small-scale topographic features.

The patterns of the maximum precipitation for 1 and 6 h (Figure 4.10 on page 105) show clearly that on all four bands precipitation reached local hourly rates exceeding 40 mm, but only the central band [passing over Pontebba (PB in Figure 4.1 on page 94) and Pramollo (PP) rain gauge stations] lasted in a quasi-stationary way to give accumulations exceeding 400 mm in 6 h.

The tracks of the convective cells through the region have been objectively identified by using the procedure developed by Bacchi *et al.* (1996); the tracks are reported in Figure 4.9 on page 105 for three different periods of the most intense phase of the storm (1300-1900 LST). The motion vector reported for each cell is obtained from cell locations computed for each volume scan. New cells formed repeatedly over the foothills of the Alps and intensified while being lifted onto the orographic barrier; this caused the quasi-stationary and persistent banded pattern. Direction and velocity of the cells are strikingly similar during the event; velocities of these storm elements are in the order of 70 km h^{-1} for most of the event.

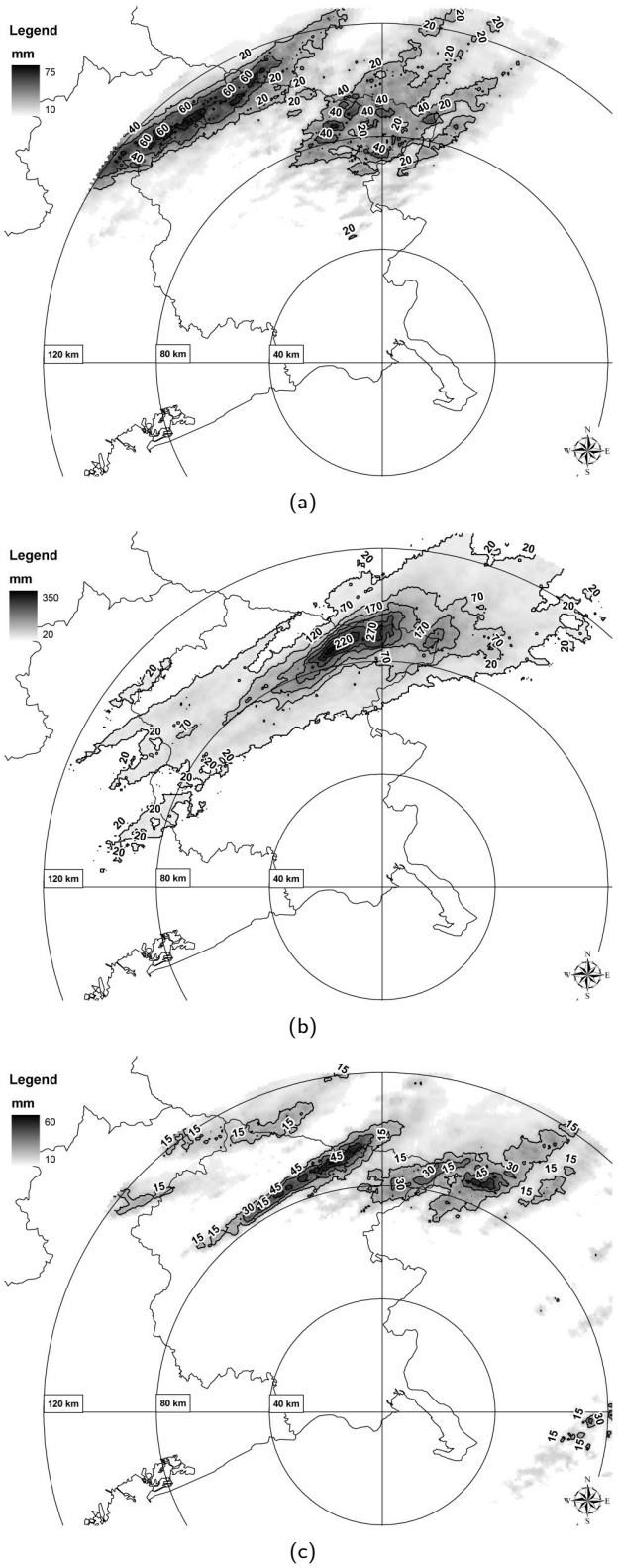

Figure 4.8: Rain accumulations (mm) for three phases of the 29 Aug 2003 storm: (a) 1000-1300, (b) 1300-1900, (c) 1900-2200 LST.

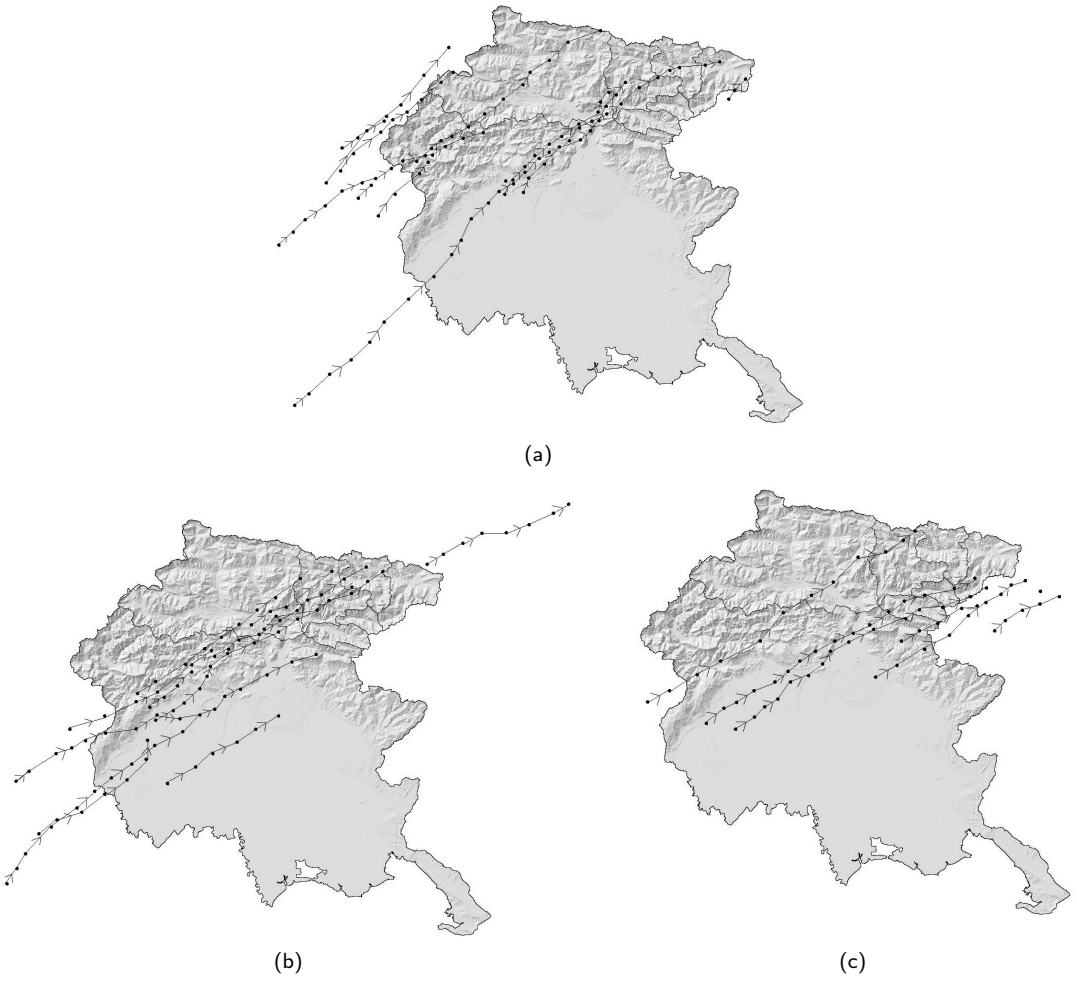

(a) (b) (c)

Figure 4.9: Tracks of the rainfall cells for the 29 Aug 2003 storm: (a) 1300-1500, (b) 1500-1700, and (c) 1700-1900 LST.

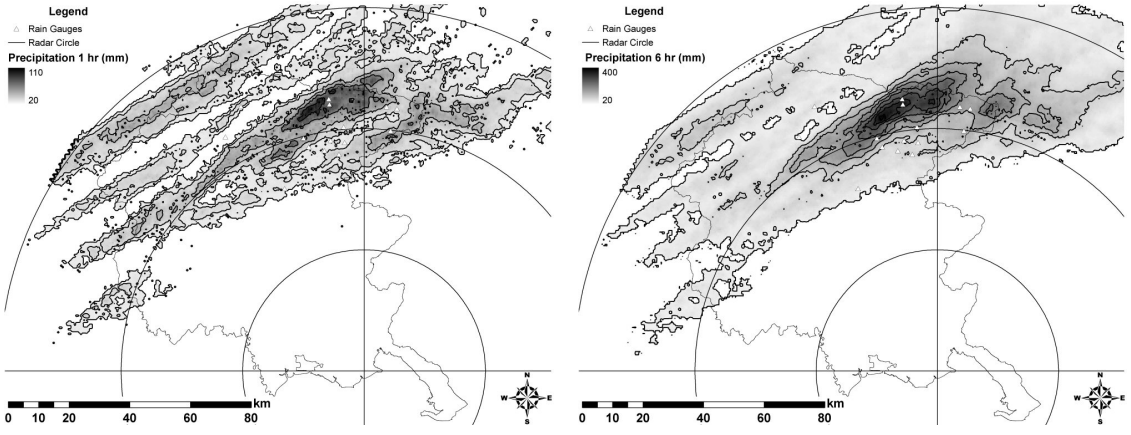

(a) (b)

Figure 4.10: Analysis of rainfall maxima: spatial patterns for rainfall maxima over (a) 1 h, with contour intervals equal to 20 mm and (b) 6 h, with contour intervals equal to 50 mm.

The composite effects of storm structure, storm evolution, and orographic enhancement of precipitation on the regional distribution of precipitation are illustrated in Figure 4.11 through the relationship between storm total rainfall and maximum 30-min rainfall rates (in Figure 4.11 a) and storm total rainfall and the fraction of storm total produced by heavy rainfall rates (30-min rainfall rates exceeding 20 mm h^{-1}) (Figure 4.11 b). Rainfall intensity >20 mm h^{-1} exceeds the 20% quantile of the cumulative distribution of saturated hydraulic conductivity values collected in the higher portions of the Fella basin by using a Guelph permeameter. Even though point values of saturated hydraulic conductivity may be affected by large spatial variability, this value suggests the potential for significant infiltration excess runoff.

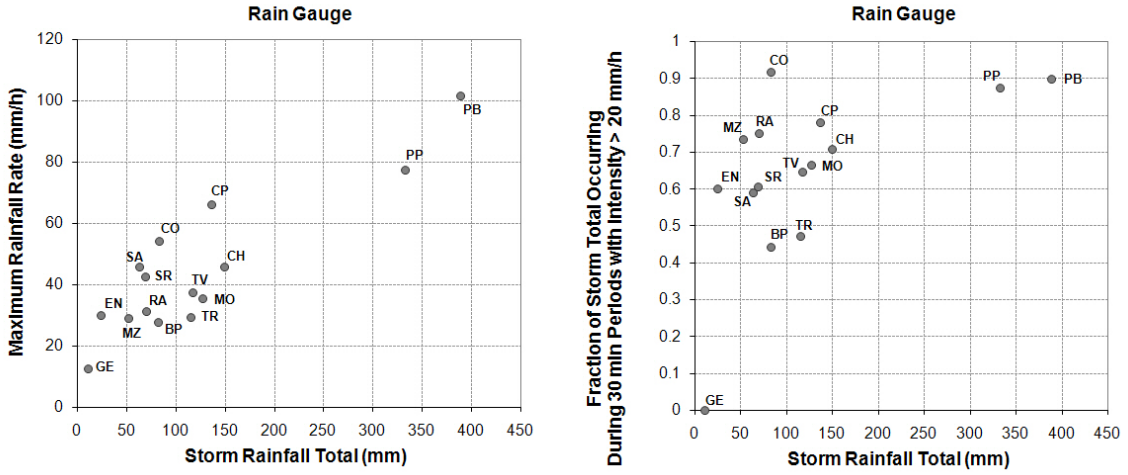

(a) (b)

Figure 4.11: Precipitation analysis: (a) storm total rainfall and maximum 30-min rainfall rates; (b) storm total rainfall and the fraction of storm total produced by heavy rainfall rates (30-min rainfall rates exceeding 20 mm h^{-1}).

In these figures one should note that only the two rain gauges located in PP and PB were under the influence of the major convective precipitation band. This can be noted in Figure 4.11 a, where the two rain gauges are characterized by highest rainfall accumulation and rates. This shows clearly that the central convective band was associated with the intensification of rainband precipitation in the upper watersheds, due to orographic enhancement, leading to the largest rainfall rates and accumulations. The lowest rainfall accumulations and rates occurred in portions of the region that were not under the influence of the convective bands. The quasi-stationary character of the storm is outlined in Figure 4.11 b, where most of the stations (with the exception of those with low rainfall accumulations) are characterized by high values of the fraction of storm total rainfall with 30-min intensity >20 mm h^{-1} . Rainfall rates greater than 20 mm h^{-1} accounted for >70% of the rainfall measured for half of the stations, including some of those measuring 50-100 mm rainfall accumulations.

4.4 Analysis of flood response

Rainfall produced by the August 2003 storm resulted in severe flooding throughout the Fella River basin. The storm produced catastrophic flooding at drainage areas up to 80-90 km^2, with dominance of debris floods [Slymaker, 1988] at basin scale up to some tens of kilometers. These debris floods were essentially extreme streamflows with large quantities of mauds, rocks, and debris, including woody debris. The extremely intense rainfall of August 2003 storm provided not only additional materials by creating new and reactivating old landslides but also high peak streamflows required for occurrence of debris floods. According to Tropeano *et al.* (2004), the debris and sediment mass mobilized and deposited downslope and over the valley bottom may be roughly estimated at 1 million cubic meters. Fluvial impact of the August 2003 flood includes significant stream widening and incision.

Stream gauge data and observations from post-event surveys, combined with hydraulic modeling, were used to examine hydrologic response to the storm. Stream gauge data were available at eight sites (Figure 4.4 on page 99 and Table 4.1 on page 109). Two out of the eight sites belong to the Slizza River system, which is a tributary of the Drava and of the Danube, while the other six belong to the Fella River system. Almost all these gauges are located either close or at bridge crossing sites, where measurements are taken by means of ultrasound sensors. Hydraulic modeling, combined with surveys of the post-flood river section geometry and data about preflood geometry, was used to derive stage-discharge relationships at these river sections. Furthermore, hydraulic modeling was used to estimate peak discharges based on surveyed high watermarks and postflood channel geometry at another three sites (including the site at the outlet of Uqua basin; Table 4.1 on page 109) and to confirm the estimates at the gauged sections. Information on runoff volumes and flood peak concerning the Vorderberg River (located in Austria, bordering the Uqua basin, on the northern side of the mountain range) were obtained from Moser (2003). It was not feasible to extend indirect flood peak estimation to basins with drainage area less than 20 km^2, due to the difficulties in establishing the actual flood channel geometry in river reaches subject to substantial erosion and/or deposition. Furthermore, the character of the flow process places essential limitations to traditional procedures for indirect peak estimation, which are likely to be flawed in case of debris flows.

Twentytwo local residents, mostly located close to the Uqua River basin and its fan, were interviewed about the severity of the storm and such factors as wind and timing of rainfall. Comments on the rate of stream rise and timing of peak stage were also noted.

4.4.1 The flood response model and properties

Hydrologic response to August 2003 storm is examined by using a simple spatially distributed hydrologic model [Kinematic Local Excess Model (KLEM); Cazorzi and Dalla Fontana, 1992]. The distributed model

is based on availability of raster information of the landscape topography and of the soil and vegetation properties. In the model, the SCS-Curve Number (SCS-CN) procedure [US-SCS, 1986] is applied on a grid-by-grid way for the spatially distributed representation of runoff generating processes, while a simple description of the drainage system response [Da Ros and Borga, 1997; Giannoni *et al.*, 2003] is used to represent runoff propagation.

The general SCS-CN runoff equation is

$$\begin{cases} q = \dfrac{(P - I_a)^2}{(P - I_a + S)} & \text{for} \quad P \geq I_a \\ q = 0 & \text{for} \quad P < I_a \end{cases} \tag{4.2}$$

where q (mm) is the direct runoff depth, P (mm) is the event rainfall depth, I_a (mm) is an "initial abstraction"or event rainfall required for the initiation of runoff, and S (mm) is a site storage index defined as the maximum possible difference between P and q as $P \to \infty$. $P - I_a$ is also called "effective rainfall," or P_e. The SCS-CN method can be applied by specifying a single parameter called the curve number, CN, which is function of the hydrologic soil-cover complex and ranges in principles from 1 to 100. The spatial distribution of the CN values was obtained from previous investigations on the study area [Cazorzi and Bincoletto, 2005]. Following Ponce and Hawkins (1996), the value of S for a given soil is related to the curve number as:

$$S = C\left(\frac{100}{CN} - 1\right) \tag{4.3}$$

where C is a calibration parameter (mm), called infiltration storativity. The use of the parameter C allows one to use the spatial distribution of CN values, which represents an input data in this work, and to simulate correctly, at the same time, the observed flood water balance. In the original SCS-CN equation the value of C is 254 mm and the initial abstraction is specified as a percentage of S. Given the exceptionally low soil moisture initial conditions, the proportionality factor between I_a and S (herewith called X) was considered as a further parameter in this study.

The distributed runoff propagation procedure is based on the identification of drainage paths and requires the characterization of hillslope paths and channeled paths. We used a channelization support area (A_s) (km^2), which is considered constant at the subbasin scale, to distinguish hillslope elements from channel elements. Discharge at any location along the river net- work is represented by:

$$Q(t) = \int_A q[t - \tau(x), x]dx \tag{4.4}$$

where A (km^2) indicates the area draining to the specified outlet location, $q(t,x)$ is the runoff at time t and location x, and $\tau(x)$ is the routing time from x to the outlet of the basin specified by the region A. The routing time $\tau(x)$ is defined as:

$$\tau(x) = \frac{L_h(x)}{\nu_h} + \frac{L_c(x)}{\nu_c} \tag{4.5}$$

where $L_h(x)$ is the distance from the generic point x to the channel network following the steepest descent path, $L_c(x)$ is the length of the subsequent drainage path through streams down to the watershed outlet, and ν_h and ν_c (m s^{-1}) are two invariant hillslope and channel velocities, respectively.

The model includes also a linear conceptual reservoir for base flow modeling, whose structure was kept invariant over all basins. The reservoir input is provided by the infiltrated rate computed based on the CN-SCS method; the method is applied at the subbasin scale. The model framework is based on six calibration parameters: the channelization support area (A_s), two kinematic parameters (ν_h and ν_c), the parameter C required for the calibration of the SCS-CN procedure, and the parameter I_a required for the specification of the initial abstraction. The model was implemented at 15-min time step and using a 20-m grid size cell for the description of landscape morphology and soil properties.

Basin	**River system**	**Basin area (km^2)**	**Type of information available**
Uqua a Ugovizza	Fella	23.9	Peak estimate (post-event survey)
Fella a Pontebba	Fella (Tagliamento)	164.5	River stage time series; stage-discharge (post-event survey)
Fella a Dogna	Fella (Tagliamento)	329.8	River stage time series; stage-discharge (post-event survey)
Raccolana a Raccolana	Fella (Tagliamento)	61.6	River stage time series; stage-discharge (post-event survey)
Resia a Borgo Povici	Fella (Tagliamento)	102.1	River stage time series; stage-discharge (post-event survey)
Fella a Moggio Udinese	Fella (Tagliamento)	623.1	River stage time series; stage-discharge (post-event survey)
Tagliamento a Venzone	Tagliamento	1843.4	River stage time series
R. del Lago a Cave del Predil	Slizza (Drava)	40.6	River stage time series; stage-discharge (post-event survey)
Slizza a Tarvisio	Slizza (Drava)	73.1	River stage time series; stage-discharge (post-event survey)
Vorderbergbach	Gail (Drava)	26.9	Peak estimates and estimation of runoff volumes post-event survey; Moser 2003

Table 4.1: Characteristics of the surveyed river sections and of the corresponding drainage basins.

The KLEM model was applied to the nine different basins of the Fella and Slizza River system for which data and observations are available for model calibration and verification.

Basin	Total rain (mm)	Total runoff (mm)	Peak discharge (m^3s^{-1})	Unit peak discharge ($m^3s^{-1}km^{-2}$)	Runoff ratio (-)	Lag time (h)
Uqua a Ugovizza	287	NA	200	8.36	NA	2.0
Fella a Pontebba	247	49.4	680	4.13	0.18	2.0
Fella a Dogna	237	-	805	2.44	-	2.0
Raccolana a Raccolana	96	3.8	27	0.43	0.04	4.0
Resia a Borgo Povici	71	6.4	54	0.53	0.09	3.0
Fella a Moggio Udinese	189	28.3	1290	2.1	0.15	3.5
Tagliamento a Venzone	110	NA	NA	NA	NA	3.5
R. del Lago a Cave del Predil	122	7.3	15	0.37	0.06	1.5
Slizza a Tarvisio	132	9.2	38	0.52	0.07	2.0
Vorderbergbach	260	65.0	125	4.65	0.25	NA

Table 4.2: Rainfall and runoff for the surveyed basins (NA: not available).

These data are summarized in Table 4.2 on the following page to permit water balance and response time analysis. Data reported in Table 4.2 on the next page show that there are systematic differences among the surveyed basins. Maximum rainfall accumulations were recorded along the Fella main stream down to Dogna and on the Vordergergbach. These four basins are all located under the central convective rain- band. Much of the lower accumulations were received by Resia and Raccolana, which were only partially located under a rainband. The runoff ratio ranges between 0.25 for 260 mm total rainfall to less than 0.1 for the smallest rainfall totals. The low values of runoff ratios point out the impact of the dry antecedent soil moisture conditions.

The strong influence of the initial conditions is confirmed by results obtained from the water balance analysis of the 22 June 1996 flood (Table 4.3 on the facing page). This flood, for which only rain gauge data were available for rainfall estimation, was characterized by two very intense consecutive storm episodes and a total duration of 54 h. Initial conditions were much wetter than for the August 2003 flood. These two characteristics translate into much more uniform rainfall totals over the various subbasins (with totals ranging from 220 to almost 300 mm) and larger runoff ratios, ranging from 0.34 to 0.52. It should be noted that estimates reported in Table 4.3 on the next page are obtained through application of the rainfall-runoff model, which was verified on the Venzone observed hydrograph. At that time, postflood surveys were not carried out for indirect peak estimation.

The large influence of the initial soil moisture condition on the August 2003 flash flood is not unexpected, due to the combination of the exceptionally dry summer 2003 and high soil moisture capacity characterizing the study area. In this region, soil moisture storage capacity is closely linked to the presence of densely fractured bedrock and of relatively thick surficial deposits, developed from colluvium and underlined by carbonate rocks [Mosetti, 1983]. The ratio of daily discharge which is exceeded 90% of the time to the mean daily flow, Q_{90}/Q_A, ranges between 0.31 to 0.46 in the upper Tagliamento basin, with

Basin	**Total rain** (mm)	**Total runoff** (mm)	**Runoff ratio** (-)
Uqua a Ugovizza	257	NA	NA
Fella a Pontebba	266	122	0.46
Fella a Dogna	277	130	0.47
Raccolana a Raccolana	275	143	0.52
Resia a Borgo Povici	281	133	0.48
Fella a Moggio Udinese	293	145	0.50
Tagliamento a Venzone	220	75	0.34
R. del Lago a Cave del Predil	249	118	0.47
Slizza a Tarvisio	225	102	0.46
Vorderbergbach	NA	NA	NA

Table 4.3: Rainfall and runoff for the surveyed basins for the 22 Jun 1996 flood event (NA: not available).)

values ranging between 0.33 to 0.36 for the Fella basin. These are relatively high values and correspond to large groundwater storage. The flood response in the Fella basin suggests that the combination of high soil moisture storage capacity and low antecedent soil moisture conditions is an important factor determining land surface response to extreme rainfall.

In addition to nonlinearities in the storm event water balance, there are also pronounced heterogeneities in the hydraulics of basin response. Lag time, obtained as the time difference between the discharge peak and the rainfall mass center, is comparatively very short for the basins with large rainfall accumulations, irrespective of basin area, whereas it is relatively large for the watersheds characterized by low storm totals. This pattern reflects the systematic decrease of basin response with increasing the rainfall accumulation. Two major factors controlling this process are the expansion of stream network to unchanneled topographic elements during the flood and the increase of flow velocity with discharge.

The KLEM model parameters were estimated simultaneously over multiple catchments by means of a combination of manual and automatic calibration to minimize an integrated normalized integrated root-mean-square error over the flood hydrograph. The basin average values of the spatially variable CN parameter given as input to the model ranges between 41 and 49 across the various basins, with larger values for the upper basins and lower values for the lower portions of the Fella watershed. This pattern is due to the development of bare rock surfaces on the upper portions of the Fella. The degree of nonlinearity arising from the available data could not be reproduced by the flood response model with a basin-invariant parametrization. The rainfall spatial distribution was the most important factor preventing the use of an invariant parametrization. Actually, the rainfall and runoff values reported in Table 4.2 on the facing page can be easily reproduced by using S=350 mm and I_a=0.2S, which means by using spatially uniform values for both rainfall and CN.

Three different parameter sets were identified, stratified according to the basin average rainfall accumulation (Table 4.4 on page 114). Figure 4.13 on page 113 show model results for the basins of Uqua at Ugovizza, Fella at Pontebba, and Fella at Moggio Udinese. Results concerning flood peak and time

to peak are reported in Table 4.5 on page 114, and point out the reasonable accuracy of the simulations provided by the hydrological model.

Some patterns in the model parameters may be noted in Table 4.4 on page 114. For the basins characterized by the largest rainfall accumulations, the extracted river network reflects a smaller support area, with an elaboration of the drainage network into unchannelized swales during the extreme event. For these basins, the modeled overland flow velocities (0.2 m s^{-1}) that reproduce observed timing and magnitude of the flood peaks exceed the upper end of the range of values (0.003-0.14 m s^{-1}) reported by Dunne (1978). Since the model overland flow is spatially and temporally constant, it must account for sheet flow as well as concentrated overland flow in areas not specified as channels. For this extreme event, overland flow velocities were likely greater than typical due to steep slopes and large amount of sheet flow.

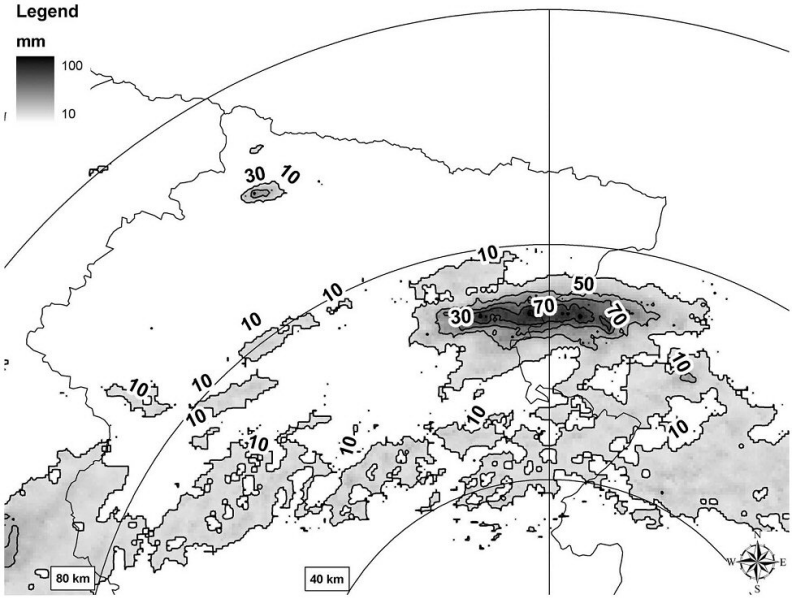

Figure 4.12: Storm total rainfall (mm) for the 28 Aug 2003.

As reported in section 4.2, on 28 August 2003, the day before the flood, a localized convective storm generated almost 100-mm precipitation on areas of the left-hand tributaries of the Fella River system. The precipitation was focused on the basins of Resia (32 mm of cumulated basin-averaged rainfall) and Raccolana (12 mm of cumulated rainfall). It is likely that this localized thunderstorm introduced elements of spatial variability in the pattern of soil moisture initial conditions. For instance, the runoff ratio appears to be higher for the Resia basin, which was affected by larger previous precipitation amounts, than for the nearby Raccolana basin for similar rainfall totals. However, the runoff ratio is very low for both basins and in the same range of other basins with similar rainfall amount. The initial soil moisture conditions were probably dry enough to mitigate the influence of spatial heterogeneity in the antecedent precipitation. On the other hand, uncertainties in both rainfall and runoff observed amounts propagate in large uncertainties

Cum. prec. P (mm)	A_{th} (km^2)	$\nu_c(ms^{-1})$	$\nu_h(ms^{-1})$	(x) (-)	$I_a(mm)$	$C(mm)$
P<100	0.05	2.5	0.03	0.03(Rac.)	43-61	1626.0 (Rac.)
				0.1(Resia)		279.4 (Resia)
$100 \leq$ P $<$ 200	0.03	4.5	0.04	0.2	80-117	508
P $\geq$ 200	0.01	5.0	0.2	0.4	142-169	254.0

Table 4.4: KLEM parametrization, stratified according to basin-average precipitation accumulation. Rac. means Raccolana.

in the model parameters, particularly for these basins.

4.4.2 Influence of space-time precipitation variability at the catchment scale

To characterize the influence of temporal and spatial variability of rainfall on flood response, we utilized 30-min, 1-km radar rainfall fields to compute the following quantities:

1. the mean rainfall rate over the catchment at time t during the storm, $M(t)$;
2. the fractional coverage of the basin by rainfall rates exceeding 20 mm h^{-1}, $F(t)$;
3. the normalized time distance of rainfall from the basin outlet, ϑ_1; and
4. the normalized dispersion of rainfall, ϑ_2.

The mean rainfall rate and fractional coverage time series provide basic information on rainfall mass balance and distribution of rainfall rates over the catchment. They do not provide information on the spatial distribution of rainfall relative to the basin network structure, however. The drainage network, as represented by the routing time $\tau(x)$, provides a natural metric for analyzing the spatial distribution of rainfall, as shown previously by Zhang *et al.* (2001); Smith *et al.* (2005); Skoien *et al.* (2001). The routing time incorporates both geometric and kinematic properties in its determination. The routing time is therefore a more convenient measure with respect to purely geometric values, such as the distance, when runoff propagates through the network at spatially variable velocities.

The normalized time distance at time t, $\vartheta_1(t)$, is a function of the rainfall field $R(t,x)$ and the routing time $\tau(x)$. It is defined as the ratio of the rainfall-weighted centroid routing time $D_l(t)$ and the mean routing time d_{mean}. The time distance $\vartheta_1(t)$ can be represented as:

$$\vartheta_1(t) = |A|^{-1} \int_A w(t,y)\tau(y)dy \tag{4.6}$$

where A is the spatial domain of the drainage basin and the weight function $w(t,y)$ is given by:

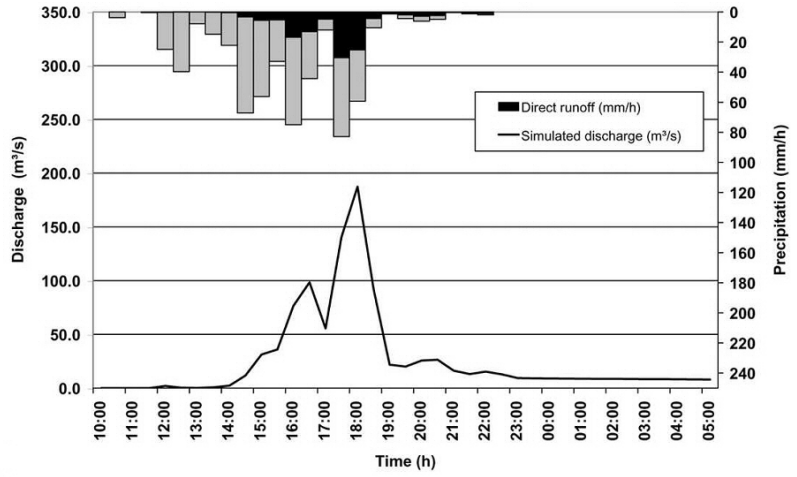

(a)

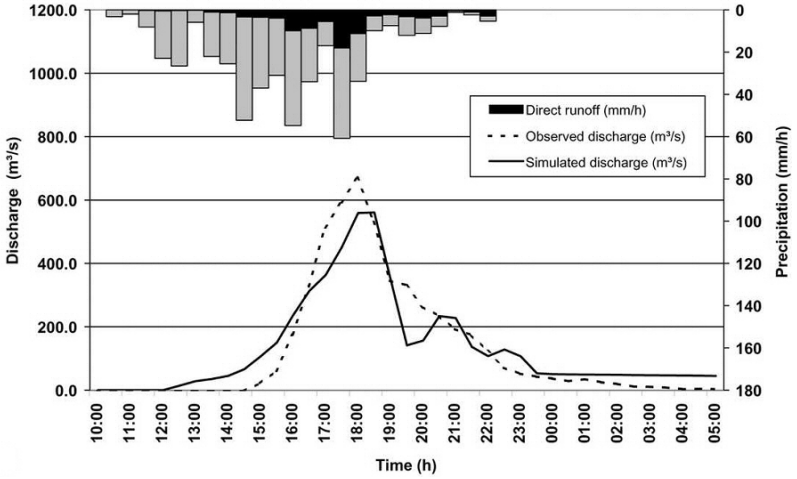

(b)

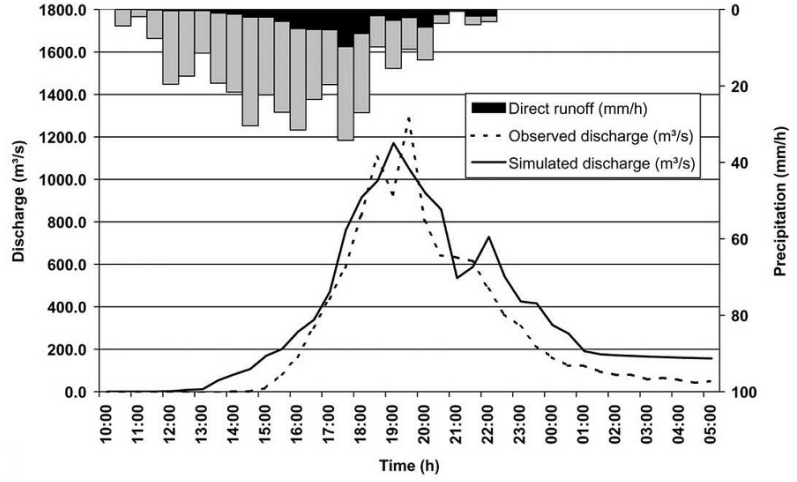

(c)

Figure 4.13: Results of KLEM application for the three nested Fella basins closed at (a) Ugovizza (Uqua), (b) Pontebba, and (c) Moggio Udinese.

Basin	**Simulated peak discharge** (m^3s^{-1})	**Estimated peak discharge** (m^3s^{-1})	**Error in time to peak (h)**
Uqua a Ugovizza	187.0	200	0
Fella a Pontebba	560.5	680	0.5
Fella a Dogna	1053.9	805	0
Raccolana a Raccolana	29.6	27	-0.5
Resia a Borgo Povici	60.2	54	0
Fella a Moggio Udinese	1170.8	1290	-0.5
Tagliamento a Venzone	1303.1	NA	1.0
R. del Lago a Cave del Predil	21.7	15	0
Slizza a Tarvisio	39.2	38	0

Table 4.5: Simulated and estimated flood peaks and errors in time to peak (NA: not available).

$$w(t,y) = \frac{R(t,y)}{|A|^{-1}\int_A R(t,y)dy} \tag{4.7}$$

Values of $\vartheta_1(t)$ close to 1 reflect a rainfall distribution either concentrated close to the mean time distance or homogeneous, with values less than 1 indicating that rainfall is distributed near the basin outlet, and values greater than 1 indicating that rainfall is distributed to- ward the periphery of the drainage basin.

The rainfall-weighted flow time-distance dispersion is given by:

$$S(t) = \left\{ \int_A w(t,y) \left[\tau(y) - D_l(t)\right]^2 dy \right\}^{0.5} \tag{4.8}$$

The dispersion for uniform rainfall is defined by:

$$S_l = \left\{ \int_A [\tau(y) - d_{mean}]^2 dy \right\}^{0.5} \tag{4.9}$$

and the normalized dispersion is given by:

$$\vartheta_2(t) = \frac{S(t)}{S_l} \tag{4.10}$$

Values of $\vartheta_2(t)$ close to 1 reflect a uniform-like rainfall distribution, with values less than 1 indicating that rainfall is characterized by a unimodal peak, and values greater than 1 indicating cases of multimodal rainfall peaks close and far from the basin outlet.

Basin	Area (km^2)	Mean travel time (h)	Std dev. of travel time (h)
Uqua at Ugovizza	23.9	0.46	0.18
Fella at Pontebba	164.5	1.01	0.39
Fella at Moggio Udinese	623.1	2.52	1.3

Table 4.6: Mean travel time and standard deviation for Uqua at Ugovizza, Fella at Pontebba, and Fella at Moggio.

Results are reported for the nested Fella basins of Rio Uqua at Ugovizza, Fella at Pontebba, and Fella at Moggio Udinese (Figure 4.14 on page 117). Note that the watershed of Fella at Moggio includes two important left-hand tributaries: Raccolana and Resia (Figure 4.4 on page 99). Values of mean routing time and standard deviation are reported in Table 4.6 for the three basins.

Flood producing rainfall for the Uqua and the Fella at Pontebba was concentrated over a period of 4 h, lasting from 1430 to 1830 LST. Rainfall peaked from 1900 to 2100 LST over Raccolana and Resia, thus extending the storm period over the Fella basin at Moggio for 2 h and half. Three hourly peak values of basin-averaged rainfall can be recognized for the Uqua basin and the Fella at Pontebba. These peaks, which were synchronous over the two basins, occurred at 1430, 1600, and 1730 LST, with two hiatuses of 30 min, and increased with time, from 60 to 71 mm, over the Uqua. This condition is a typical trigger for diffused landsliding and debris flow, as documented by Montgomery *et al.* (2002).

The fractional coverage of heavy rainfall (greater than 20 mm h^{-1}) displays three peaks: the first at 1230 LST, the second for the period from 1430 to 1630 LST, and the last at 1800 LST. For the Fella at Moggio an increasing trend can be recognized (up to 1800 LST) in the peaks of fractional coverage.

Despite the large variability in rainfall over the Fella basin, the "conditional" distribution of routing times, given the spatial rainfall distribution, was close to the distribution of routing times in the uniform rainfall case, particularly for the Uqua and the Fella at Pontebba. For the Uqua, normalized time distance and dispersion are virtually unchanged from uniform rainfall case. Moving from Uqua to Pontebba and then to Moggio, a downbasin storm motion can be recognized, as reflected in decreasing values of normalized time distance. This is in contrast to the fast upstream motion of the convective cells, and partially explains why the flood peak was recorded at the same time (around 1800 LST) at Ugovizza and Pontebba. At Moggio two peaks were recorded: the first at 1830 LST and the second at 1930 LST. The first is associated with the flood response from the nearby Aupa basin (according to interviews collected from local residents), whereas the second peak is associated to the upstream Fella River response. Our runoff model is unable to accurately portray the specific response time of each basin. For this reason, the double peak was not reproduced in the simulation (Figure 4.13 c).

The increase of normalized time distance and of dispersion at Moggio after 1800 LST is related the storm event over Raccolana and Resia, which are characterized by a relatively slow response.

4.4.3 Scale dependent flood response

A fundamental research topic in hydrology is to understand the physical basis of observed scaling statistic relating flood peaks with their drainage areas [Furey and Gupta, 2005]. Observational flash flood studies and model analyses of hydrologic response illustrate how storm structure and evolution translate into scale dependent flood response.

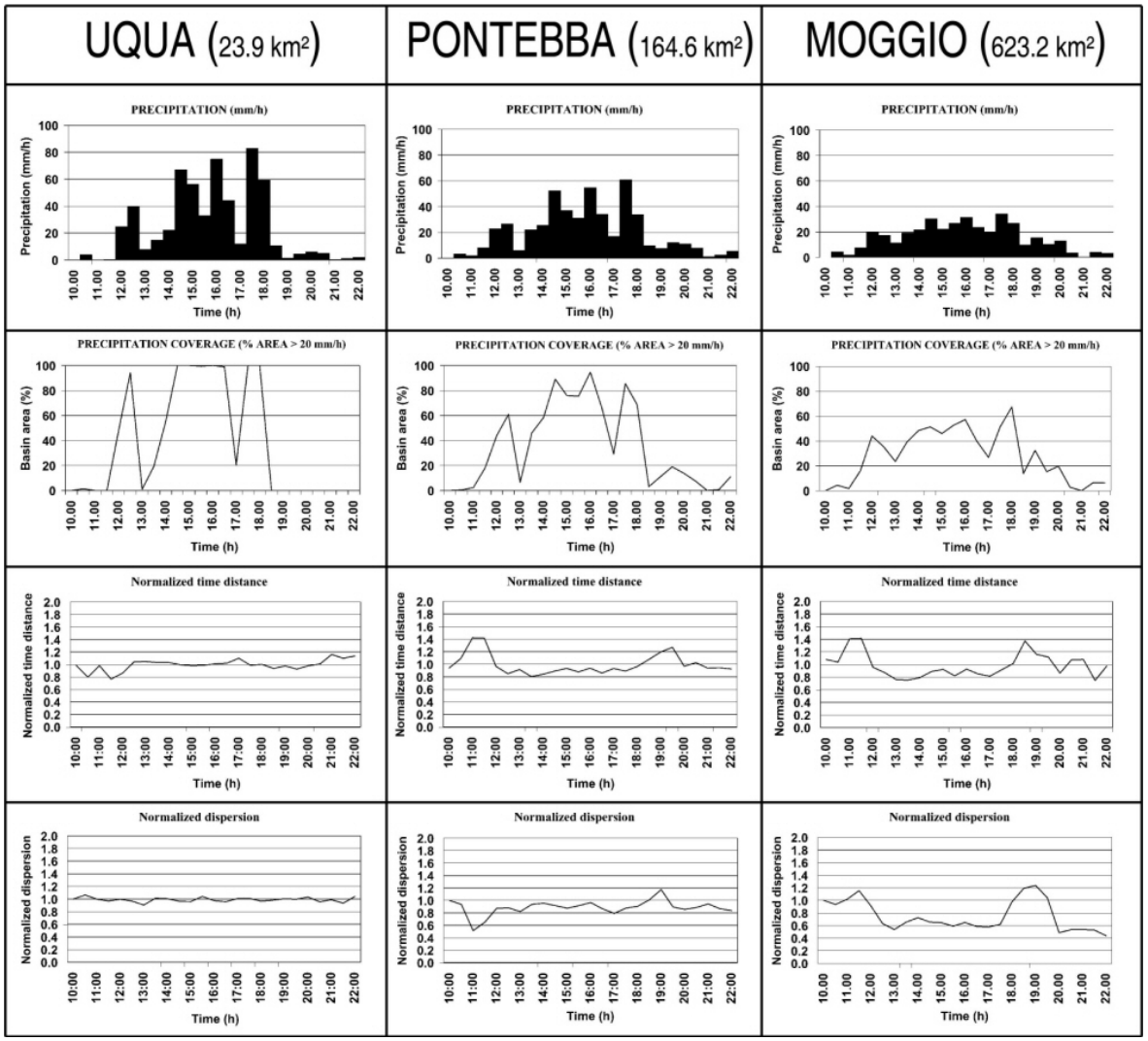

Figure 4.14: Precipitation analyses by using time series of precipitation intensity, coverage (for precipitation intensity >20 mm h^{-1}), and normalized time distance, for the three nested Fella basins closed at Ugovizza, Pontebba, and Moggio Udinese

Based on observations and model analyses, peak discharges were computed at regular intervals along stream network. For each of these model gaging stations, the upstream drainage area, the peak discharge and the rainfall accumulations were computed [Zhang *et al.*, 2001] (Figs. 4.15 a,b). Figure 4.15 a shows the relationship of the rainfall accumulations with upslope basin area, whereas Figure 4.15 b shows the

same relationship for peak unit discharge. To understand how the space-time structure of precipitation controls scale-dependent flood response, the maximum intensity averaged over the basin time response was computed for each basin included in the envelope of peak unit discharge (Figure 4.15 c).

It is possible to identify two regions in the pattern of maximum unit peak discharges: (a) basin scale ranging from 1 to 90 km^2 , with unit discharges decreasing from 19 to 5 m^3 s^{-1} km^{-2} ; (b) basin scale ranging from 90 to 600 km^2, with smaller unit discharges, decreasing from 4 to 2 m^3 s^{-1} km^{-2}. The first region reproduces the shape of the central convective band, with a mean width of 9 km. The region of peak storm total accumulation in the upper portion of the Fella River basin (Uqua and Pontebbana River basins) is the location of the largest model discharges at small drainage area. Results reported in Figure 4.15 c show that a major factor controlling the shape of the scale dependency of peak unit discharges is the reduction with basin area of the maxi- mum rainfall intensity averaged over basin response time. The pattern of the scale dependent averaged precipitation intensity reproduces the two regions identified for the scale-dependent flood response (from 1 to 90 km^2 , and from 90 to 600 km^2) and the different scaling with area within the two regions.

4.5 Conclusions

There are six principal observations from our work,

1. The August 2003 storm system, which produced record storm accumulations, flood peaks, and impressive geomorphic changes, provides a model for mesoscale convective systems that are likely responsible for the majority of flash flood peaks in the upper Tagliamento River basin. Extreme rainfall from the August 2003 storm was produced by quasi-stationary convective banded structures. Some of the bands persisted in the same locations for the duration of the event. The steadiness of these rain- bands led to highly variable precipitation accumulations and runoff. The characteristic spatial scale of the convective bands is around 9 km, which results in a dominant spatial scale for rainfall accumulation and flooding of around 100 km^2 .

2. Antecedent soil moisture distribution appears to have played an important role in flood response. Measured peak discharges were large, but not as exceptional as implied by the measured rainfall. The exceptionally dry summer season of 2003, combined with the high soil moisture storage capacity that characterizes the basins in the upper Tagliamento watershed, resulted in low runoff ratios and emphasized the nonlinearity of the flood response. These findings are confirmed by comparison with a previous extreme flood occurred on 22 June 1996.

3. Pronounced contrasts in flood response between different basins of varying catchment size are related to (a) effect of the spatial organization of the banded convection, (b) contrasting fractional coverage

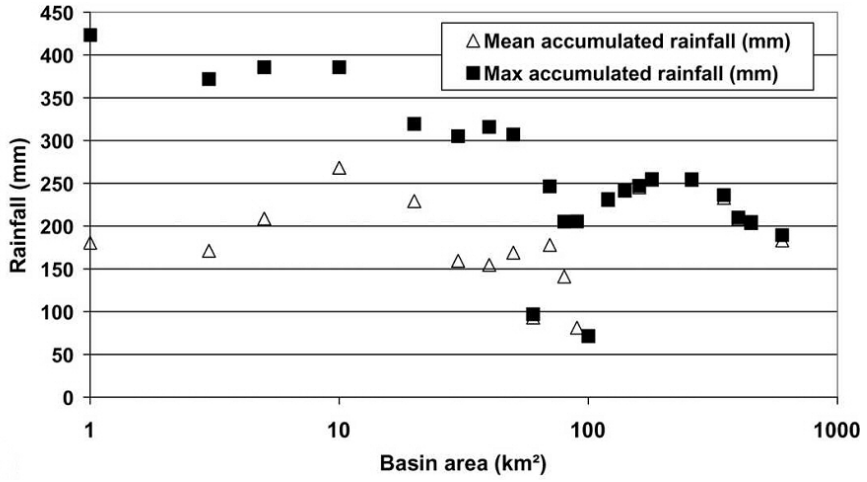

(a)

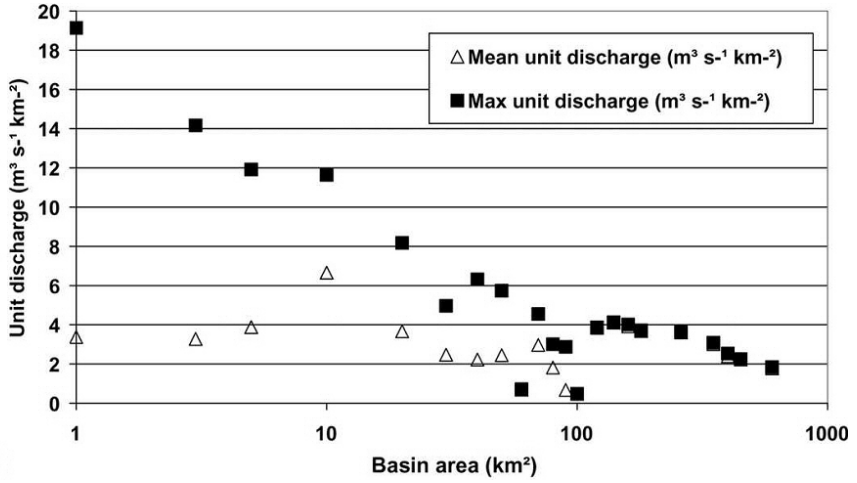

(b)

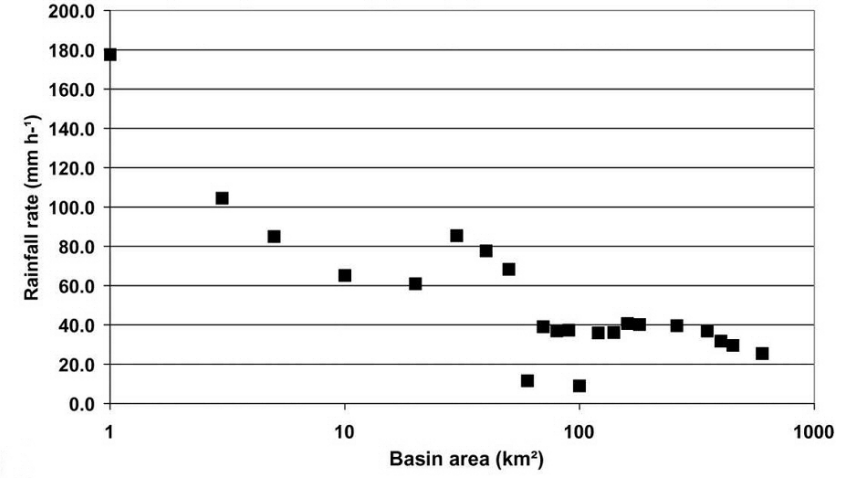

(c)

Figure 4.15: The relationship between (a) accumulated rainfall, (b) peak unit discharges, and (c) maximum rainfall rate averaged over basin response time, with drainage area. Unit discharges are derived from the hydrological model simulations

of rainfall following from basin size and structure, and (c) differential response due to the highly nonlinear relationship between rainfall and runoff. An important source of nonlinearity is related to the strong dependency of basin response time to storm accumulation.

4. The storm event response can be reasonably well reproduced with a simple distributed hydrologic model, using high resolution rainfall observations. However, application of the model to the case study required stratification of parametrization according to precipitation accumulation at the sub-basin scale. The degree of nonlinearity arising from the available data could not be reproduced by the flood response model with invariant parametrization.

5. Model analysis of hydrologic response for the August 2003 storm illustrate the role of storm structure, motion, and evolution for scale-dependent flood response. A major factor controlling the shape of the scale dependency of peak unit discharges is the spatial extent of the major convective band.

6. For the August 2003 flood, postflood interviews, field observations, and surveys were important sources of information. The combination of detailed radar rainfall estimates, readily available GIS data, hydrologic and hydraulic modeling, postflood surveys, and interviews with local residents allowed us to generate a much more complete picture of the storm and flood environment than would otherwise be available on ungauged basins.

5. Hydrological analysis of a flash flood across a climatic and geologic gradient: the September 18, 2007 event in Western Slovenia

5.1 Introduction

A fundamental issue in flash flood science is to identify the landscape and climate variables which control the runoff response to heavy rainfall. This question has important practical implications concerning the accuracy of flood predictions for ungauged basins, which is often driven by observation of specific and measurable catchment attributes as indicators of hydrological similarity.

Such flood predictions may underpin flash flood warning procedures in real-time and form a key role in the design and planning of flood risk management measures. For example, Doswell III *et al.* (1996), reviewed the meteorological processes that lead to flash floods and gave a crude guideline based on observational experience that flooding commences when rainfall rates are at least 25 mm h^{-1} sustained for at least 1 hour. They stressed, however, that what may be a rainfall threshold for flash flood triggering in one hydrometeorological setting may not be important in another. They recommeded that reconnaissance studies should focus on which hydrometeorological and climate variables control the rainfall threshold and the runoff response more in general.

There exists a substantial body of work on physical flood processes in small research catchments where processes can be observed by field campaigns and detailed instrumentation [e.g., Dunne, 1983; Anderson and Burt, 1990; Peschke *et al.*, 1999; Grayson and Blöschl, 2001]. However, a central problem in the study of extreme floods and flash floods is that investigations are focused precisely in the realm of events that rarely occur [see Smith *et al.*, 1996a; Sturdevant-Rees *et al.*, 2001; Wood *et al.*, 1990]. Dunne (1978)

characterizes this problem by noting that "within a particular basin, the dominant runoff process may vary with the characteristics of rainstorms. Even the highest infiltration capacities of forest soils will not accommodate the highest recorded rainfall intensities". Documenting runoff response to extreme storms provides a guidance to extend hydrological predictability with increasing storm severity [Blöschl and Zehe, 2005].

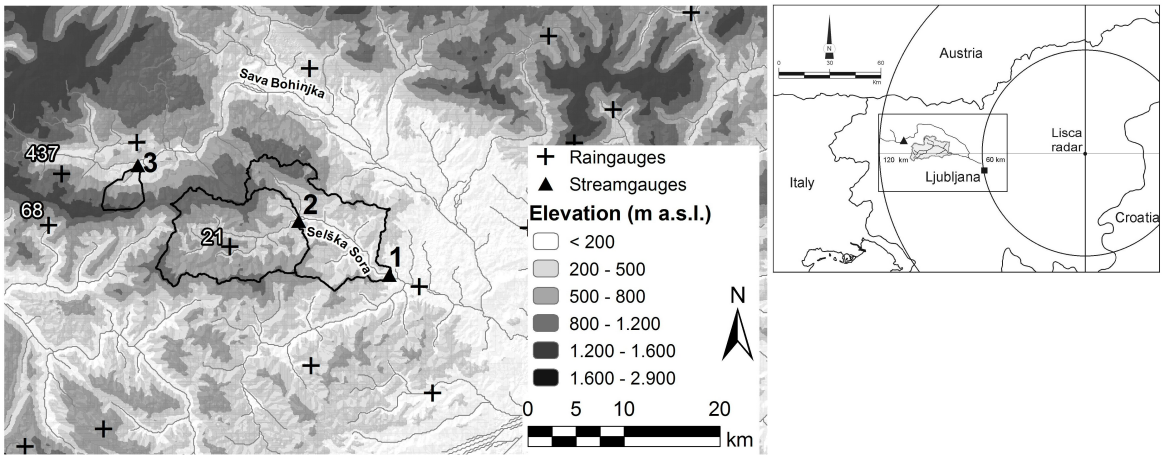

(a)

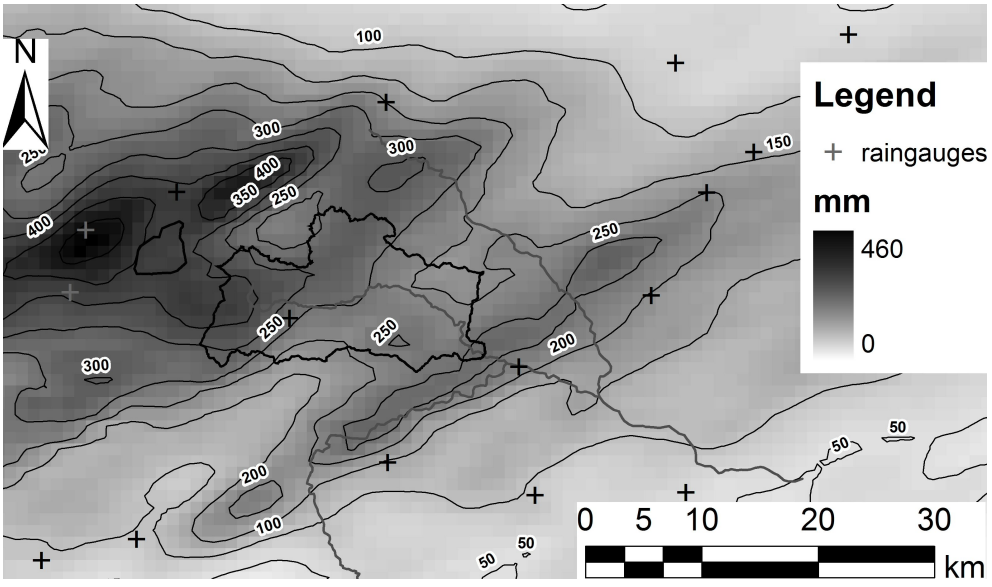

(b)

Figure 5.1: a) Location of the Selška Sora and Sava Bohinjca watersheds and of the Lisca weather radar, with the topography of the study basins (Streamgauges: 1: Selška Sora basin at Vester; 2: Selška Sora basin at Železniki; 3: Bohinjska Bistrica basin at Bistrica; Raingauges: 21: Davča; 68: K. Ravne; 437: Vogel); b) event cumulated rainfall of the September 18, 2007 storm.

Investigation on extreme flash floods requires that field work is focused on specific extreme events rather than on specific watersheds. Post-event flash flood surveys [Borga *et al.*, 2008; Marchi *et al.*,

2009b] are specifically valuable to collect and collate the observations to address the questions posed by extreme flash floods. The key methodological development involves i) use of radar rainfall estimates for water balance and hydrologic response analysis; ii) post event survey to document geomorphic effects and peak discharges; iii) eye-witnesses interviews to establish the timing of storm and peak flows.

This study combine analysis of results from post-event survey with hydrological modelling to investigate the runoff response of an extreme flood event occurred in western Slovenia on 18^{th} September 2007. This event was one of the major flood events occurred in the last century in the country, and motivated the organisation and execution of a survey by an international team of experts in the context of the European Project HYDRATE (http://www.hydrate.tesaf.unipd.it), funded by the EU Commission, Sixth Framework Programme [Marchi *et al.*, 2009a].

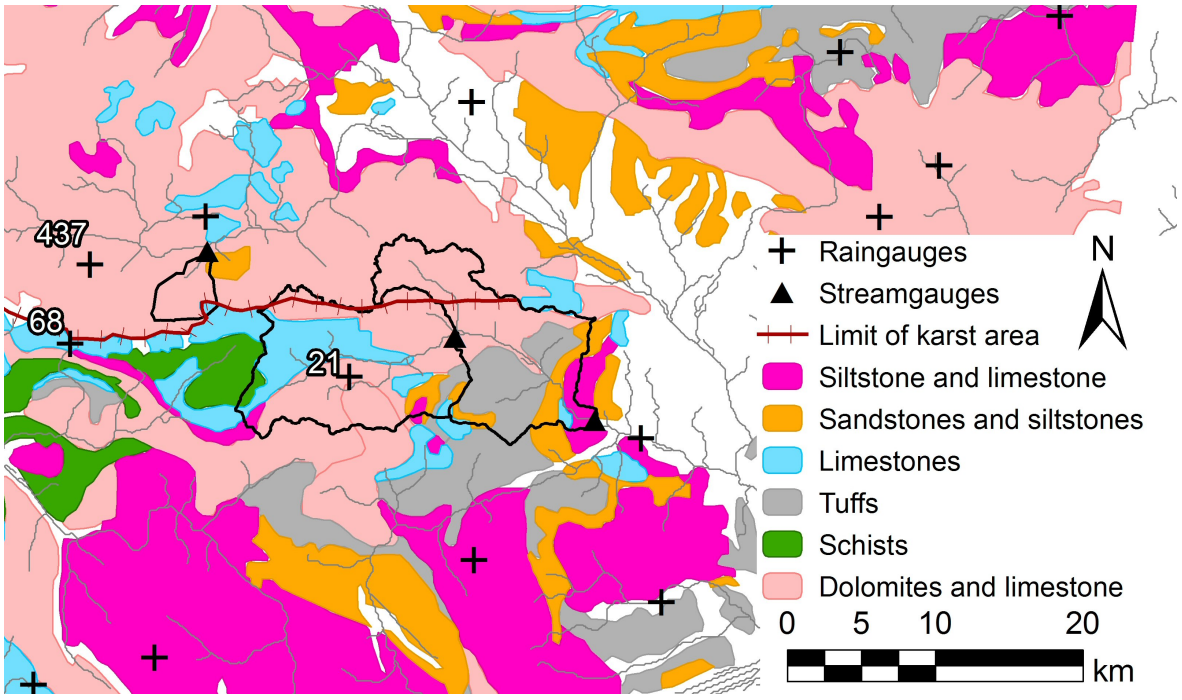

Figure 5.2: Simplified geological map of the region affected by the September 2007 event.

Figure 5.1 on the facing page shows the region impacted by the event in north-western Slovenia. The region is characterised by climatic variability and diversity in terms of geological characteristics. The variability of climatic characteristics at relatively short distances can be associated to distinctively high topographic variability which influences the occurrence of heavy rainfall events. This leads to a pronounced west-east decrease in mean annual precipitation as well as in the extreme rainfall statistics. Geological heterogeneities are associated mostly to the presence of karst features, with alpine karstified limestone prevailing in the north-western part of the region. The geological and climate properties had a pronounced influence on the runoff response of the event. The region which received the largest rainfall amounts

is characterised by a well developed karstified aquifer. Although the rain rates and accumulation were extreme in this area, runoff response was mainly due to groundwater flow from the aquifer and saturation excess mechanism in the floodplain. This led to reduced runoff response and damages compared to other sites. On the other hand, extreme flooding impacted the upper Selška Sora river, located in a region which received comparatively less precipitation and is less interested by karstified aquifers. Due to the reduced extension of the river network in the karst areas, the post event field activities were focused in the area of the upper Selška Sora.

Questions which motivate this study include the following. How do heterogeneities in geological and climatic properties influence storm event response? How the disparate observed data collected during the survey provide a consistent description of the runoff response to the storm event? What are the elements of spatial rainfall variability that control observed and modelled flood response? These questions are examined through empirical and model-based studies of September 18, 2007 storm event response.

5.2 Study region and data

The northwest part of Slovenia is characterised by the extension of the Julian Alps with many peaks above 2000 metres. Mean annual precipitation reaches very high values in the upper Soca river with accumulations up to 3300 mm, which represents the highest mean value for the Alps [Frei and Schär, 1998]. The precipitation decreases in the west-east direction, due to the rain shadow effect of the mountain ranges. A description of the climatology of extreme subdaily rainfall is provided in Table 5.1 by the mean values of annual precipitation maxima (herewith called APM) for duration of 1, 3, 6, 12 and 24 hours for three stations (stations n. 21, 68 and 437, located respectively at Davča, K. Ravne and Vogel) whose locations are reported in Figure 5.1 on page 122. We used the mean values of APM due to the short samples available, which makes quite uncertain use of higher statistical moments.

Station	1-h	3-h	6-h	12-h	24-h
21 Davča	30.0	49.3	59.5	78.7	97.6
68 K Ravne	40.5	70.1	92.0	124.3	152.4
437 Vogel	37.7	69.6	101.5	143.4	194.9

Table 5.1: Mean values of the annual maximum precipitation for the three stations and the five durations (1h, 3h, 6h, 12h, 24 h), see Figure 5.1 on page 122 for gauges position.

Inspection of these values shows both (i) the relatively high values of these rainfall accumulations, and (ii) the orographic control on the spatial distribution of the average values, with a marked decrease of the average APM values in the west-east direction. The decrease is more remarkable with increasing the rainfall duration, as expected. For an intermediate duration of 6 hours, the average of APM decreases from 101.5 mm at Vogel to 59.5 mm at Davča, 13 km eastward.

The main river systems affected by the storm event are the Sava Bohinjka and the Selška Sora watersheds (Figure 5.1 on page 122), which are both important tributaries of the Sava river system. The Sava Bohinjka is an alpine watershed, characterized by steep topographical relief (400-2864 m) and rather thin soils (0-50 cm) on the hillslopes. The Selška Sora, and in particular the catchment closed at Železniki, has similar topography and soils structure. For both catchments, the land use is dominated by forests, with grassland and grazing in the floodplain. The area is tectonically active and characterised by significant seismic activity, developing faults and overthrusts. Even though the two catchments exhibit similar topography, the rock formations are characterised by significant differences (Figure 5.2 on page 123). The lithological constituents of the catchment of Sava Bohinjka are upper Triassic carbonate rocks, the major part being Dachstein layered karstified limestones. At overthrust base are impermeable Carnian layers of marks and mudstones. In the Selška Sora mainly Miocene clastic rocks prevail and karst features are observed only in relatively small catchments, generally located in the northern portions where some alpine karst plateau are found. The limit of karst area reported in Figure 5.2 on page 123 shows the southern border of the main karstified limestone, as determined based on geophysical measures and tracers [Trisic *et al.*, 1997, M. Bat, personal communication, October 2009].

The impact of variations in the karst terrain influence on estimates of the mean residence time (MRT) between these two river system has been documented by Ogrinc *et al.* (2008). They used stable isotope measurements of oxygen and hydrogen (δ^{18}O and δD) in stream waters and precipitation to investigate hydrological pathways and residence times in the River Sava catchment in Slovenia. The shortest MRT of 0.40 year was observed on the Sava Bohinjka, which showed the highest δ^{18}O variability and the lowest mean δD value. According to the authors, the short residence time reflects the influence of the rapid subsurface response of the watershed due to high proportion of precipitation in this easily permeable karstified catchment. On the contrary, the second largest MRT value (1.85 year) was estimated on the Selška Sora river system, implying a less considerable influence of the karstified aquifers.

The boundaries of the Bohinjska Bistrica watershed at Bistrica (13.4 km^2) as reported in Figure 5.1 on page 122, are derived based on topographic analysis. However, one should borne in mind that in the area of Sava Bohinjka, hydrological catchment boundaries are highly uncertain and the topographic catchments rarely corresponds to the karst hydrological or hydrogeological drainage basins (for instance, the Slovenian Environmental Agency, which is responsible for hydrological surveying in Slovenia, does not report the catchment areas for the streamgauge stations located in this region). Tracer experiments carried out in the upper Sava Bohinjka, showed that the tracer injected in the plateau of Vogel emerged in the distant karstic spring of the Bistrica (Figure 5.1 on page 122) [Trisic *et al.*, 1997]. The position of the watershed limit depends upon the groundwater level, which can change very quickly, especially during and after high-intensity precipitation which may cause flash flooding. Generally at very high groundwater levels fossil and inactive conduits and springs are activated, which cause intercatchment overflow and the

redistribution of catchment areas [Bonacci *et al.*, 2006].

5.3 The September 18, 2007 flash flood: rainfall data collection and elaboration

On 18 September 2007 a Mesoscale Convective System affected the study area, starting around 06:00 local time (Central European Time, CET, corresponding to UTC+1) and lasting for twelve hours. The storm triggered extreme flooding in selected basin, causing 6 casualties and substantial disruption of the local economy, with damages close to 0.3 billion Euro [Rusjan *et al.*, 2009; Marchi *et al.*, 2009b].

A noticeable characteristic of the precipitation event was its organization in well defined banded structures, 60-70 km in length and 8-12 km in width, from west to east over the country. The precipitation gradients in the directions orthogonal to the bands were significant, with differences in hourly precipitation accumulations of up to 50 mm within 7 km. The convective cells propagated quickly (60-70 km/hr) through the convective band. The natural consequence of these precipitation patterns, which are relatively common in this climatic setting [Borga *et al.*, 2007], is that neighbouring watersheds received distinctly different rainfall amounts and therefore exhibited contrasting responses to the event.

Radar and raingauge observations were used to derive rainfall fields for the September 2007 storm. The rainfall observation resources include a network of 47 raingauges (Figure 5.1 on page 122) (among them, 14 devices provide time series at the hourly time step while the remaining ones are daily raingauges) and a modern volume-scanning Doppler C-band radar located in Lisca at about 80 to 100 km of the affected watersheds [Bouilloud *et al.*, 2009]. Rough data from the original volume scan data (12 elevations, with time resolution of 10 min, and spatial resolution of 1000 m in range by 1.0 degree in azimuth) were made available for radar rainfall estimates. This afforded the application of an integrated set of procedures, aiming to detect and correct for the following error sources: (i) partial beam occlusion; (ii signal attenuation; (iii) vertical profile of reflectivity, (iv) radar hardware miscalibration. Hail was not observed during the event, so no correction was implemented to remove hail contamination. The correction procedures are described in detail in section 2.1; a summary is provided below. Due to the extremely high rain rates, and the characteristics of the weather radar, a specific attention was devoted to the correction of the signal attenuation by means of the Mountain Reference Technique (MRT, hereinafter) [Delrieu *et al.*, 1997, 2000]. By applying the MRT, maximum path integrated attenuation (PIAs) between 15 and 20 dB were measured thanks to mountain returns for path-averaged rain rates between 10 and 15 mm h^{-1} over a 100-km path. By considering the PIA constraint equation, the MRT allowed estimation of an effective radar calibration correction factor, assuming a DSD model and the subsequent reflectivity-rain rate-attenuation relationships to be known. Besides signal attenuation, screening effects were quantified using a numerical model of radar beam propagation in the atmosphere and the terrain model of the region.

The vertical structure of the reflectivity was modelled with the normalized apparent VPR estimated globally without rain type separation into convective and stratiform precipitation. The final step of the processing chain consisted of generating rainfall accumulation from the instantaneous surface rainfall rate estimation.

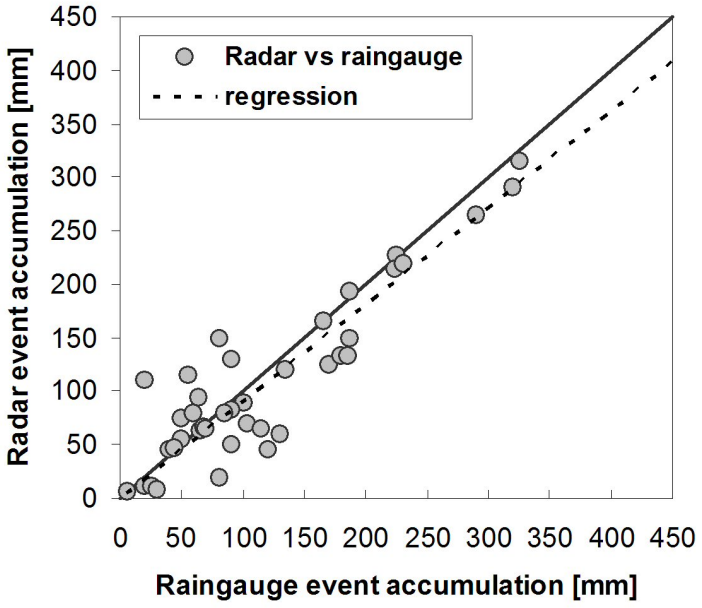

(a)

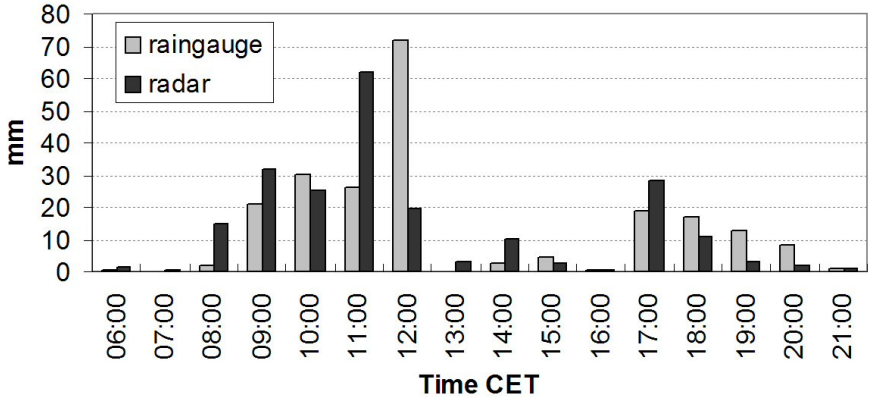

(b)

Figure 5.3: a) Scatterplot of adjusted radar versus raingauge measurements at the event time scale; b) comparison between hourly adjiusted radar and raingauge accumulations for the Davča raingauge station.

To achieve this, the surface rainfall rate estimation was advected using the advection field obtained by comparing successive rain maps. This oversampling allows for the smoothing of the rainfall accumulation map and the suppression of stroboscopic effects that were visible for this case of rapidly moving cell system.

Radar rainfall estimates obtained in this way were evaluated by comparing them with raingauge ob-

servations (which were considered as reference values) at the event time scale, and considering only the raingauges located at distance less than 110 km from the radar antenna (Figure 5.3a). The comparison was carried out by means of performance criteria like the Nash-Sutcliffe efficiency (which was found equal to 0.79) and the mean relative error (-2.9%). This overall comparison shows that, at least up to 110 km range, the adjusted radar rainfall match quite well the raingauge values in an almost unbiased way. The comparison between radar estimates and the reference values at the Davča raingauge station (Figure 5.3b), which is centrally located in the upper Selška Sora catchment at Železniki, shows that in general the time distribution and structure of the precipitation is well described by the radar observations. The highest hourly rainfall accumulation (72 mm) appears well reproduced by the radar (63 mm), even though it appears anticipated by 30 min in the radar observations. Inspection of the radar data at 10 min time interval shows that the radar peak was observed between 0930 and 1000 UTC; hence a slight mismatch in the timing of the raingauge may explain this time error.

Even though the radar-raingauge comparison shows good results, the uncertainties in reproducing fine features of the highly variable precipitation pattern should be borne in mind. This is mainly related to the rather high radar beam altitude with respect to the terrain and to the assumptions used in the radar correction procedure. These uncertainties may be rather large at ranges further than 110 km, where range effects are combined with severe path attenuation effects.

5.4 Rainfall analysis

Precipitation was analysed by using animations of both the instantaneous rain rates at the 10 min time steps and the cumulated rain amounts over a given period. A synthesis of this information is provided by Figure 5.4 on the next page, which provides the storm total precipitation and the rain amounts during the three main phases of the event.

The storm total precipitation (Figure 5.1b) exhibits two local peaks of rainfall accumulations exceeding 350 mm over the upper Sava Bohinjka. Whereas this is the area which received the highest rainfall amount (the highest precipitation from a raingauge, 303 mm, was recorded at the station of Vogel, which is located 15 km East of the Selška Sora Basin), it is likely that the radar estimates at ranges exceeding 110 km are affected by overestimation induced by the correction for the effects of path attenuation. Other peaks, less extended, are observed on the upper Selška Sora and close to the outlet of the same basin at Vester. Interestingly enough, the regions of extreme precipitation accumulations include only marginally the Selška Sora watershed at Železniki, where extreme flooding was observed. The storm total rainfall distribution reflects south west - north east motion of the storm elements and west-east shift of the tracks of the storms. This evolution can be distinguished in Figure 5.4 on the facing page, which describes the three main phases of the storm event.

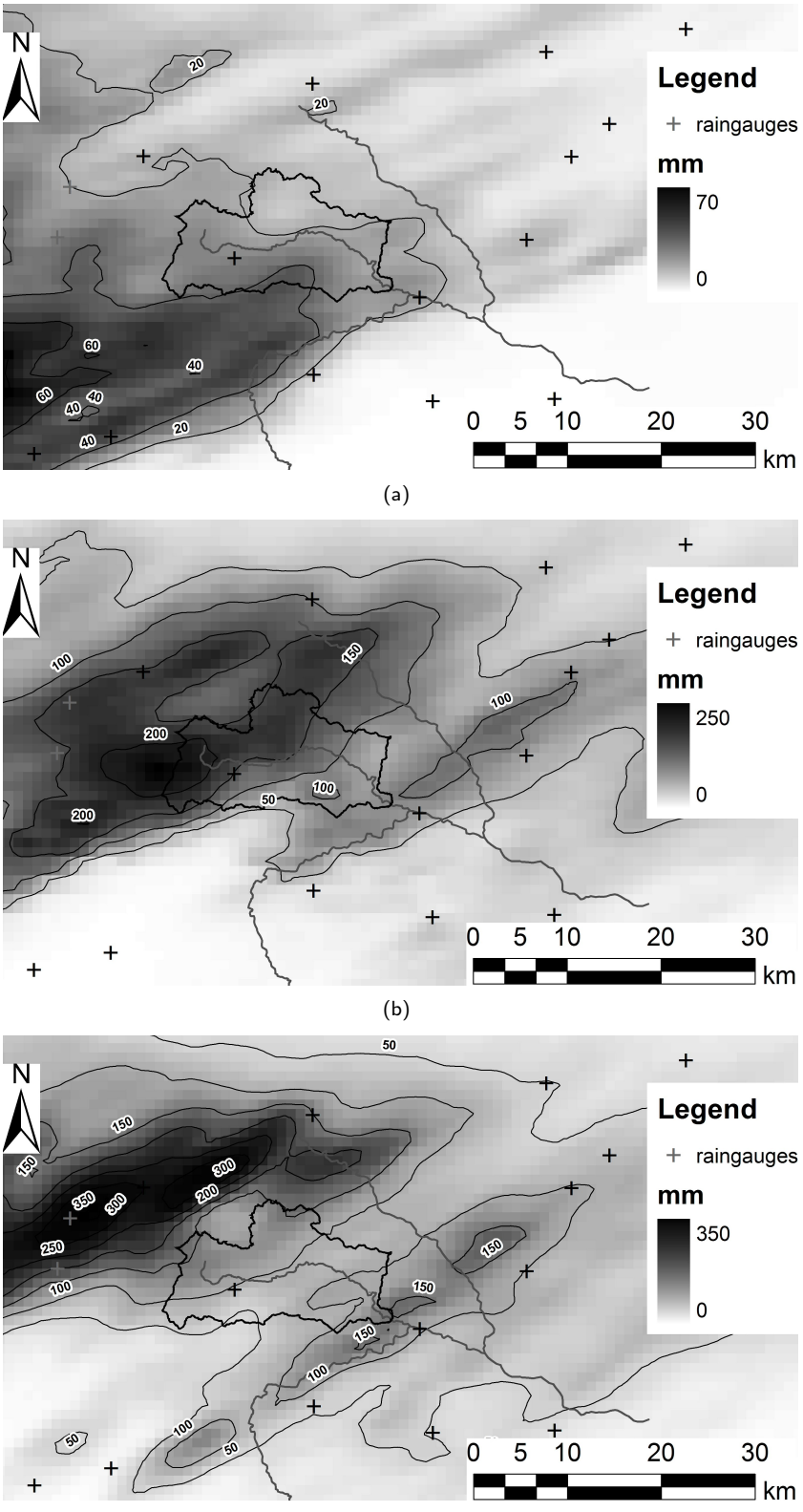

Figure 5.4: Rain accumulations (mm) for three phases of the September 18, 2007 storm: (a) 0600-0800 CET, (b) 0800-1230 CET, (c) 1230-1730 CET.

In the initial period (0600-0800 CET) the rainfall maxima, with values up to 60 mm, extended over an elongated region at the southern periphery of Selška Sora at Vester.

In the second period (0800-1230 CET), after a period with less intense rain, a convective band established over the upper Sava Bohinjka and the upper Selška Sora, becoming quasi-stationary. This led to an explosive growth of precipitation between 1130 and 1230 CET, with the Davča raingauge measuring extreme rainfall accumulations at 5-min, 30 min and 60 min, equal to 17.5 mm, 57.9 and 84.0 mm, respectively.

In the last phase (1230-1730 CET)) the precipitation accumulation splits in two regions, with a maximum of precipitation concentrated over the upper Sava Bohinjka and a convective band focused over the Vester area. The precipitation contribution from this band insisted on the area already impacted during the initial period, thus leading to very high event accumulation on the Vester area. However, the 2-hours hiatus of precipitation between 1030 and 1230 CET reduced the runoff generation potential from these accumulations in this area. In the period 1230-1330 CET, extreme rainfall concentrated over the area of the stations of Vogel and K. Ravne, with values which are strikingly similar to those observed one hour earlier at the Dacča raingauge. As an example, the K. Ravne raingauge measured max rainfall accumulations at 5 min, 30 min and 60 min, equal to 16.7 mm, 53.0 and 83.8 mm, respectively.

Station	**1-h**	**3-h**	**6-h**	**12-h**	**24-h**
21 Davča	84.0 (2.8)	49.3	155.0 (2.6)	214.0 (2.7)	97,6
68 K Ravne	84.0 (2.1)	70,.1	240.0 (2.6)	279.0 (2.2)	152.4
437 Vogel	78.0 (2.1)	69.6	215.0 (2.1)	289.0 (2.0)	194.9

Table 5.2: Values of the rainfall maxima and of the normalised maxima for durations of 1 h, 6 h and 12 h and for the three raingauge stations.

Even though the rainfall maxima from 30 min to 12 hours are decreasing from west to east (as shown in Table 5.2 for the three stations of Vogel, K. Ravne and Davča), the decrease is less than the one exhibited by the mean APM for the same durations. As a result, it is possible to note that the severity of the rainfall maxima varies, accordingly with the climate characteristics, in the opposite way. Table 5.2 reports the rainfall maxima at durations for 1 h, 6 h and 12 h, normalised by using the mean APM at the same durations. Inspection of these values shows that only at the Davča station the normalised values exceed the value 2.5 consistently for all rainfall durations up to 12 hours, providing an indication that for this station the rainfall accumulations at various durations were particularly high relative to the local climate. For the other two stations, the normalised values are considerably lower for both 1 h and 12 hours. Whereas a more thorough statistical examination of the severity of the storm is on going and will be reported later, these observations provide a first explanation for the extreme runoff response in the upper Selška Sora watershed.

5.5 Post event survey and runoff response data collection

Rainfall produced by the September 2007 storm resulted in severe flooding of the upper Selška Sora basin and, at a lesser degree, of the Sava Bohinjka. In the Selška Sora the storm produced catastrophic flooding at drainage areas up to 80-90 km^2 , with debris flows at basin scale up to some km^2 . Streamgauge data were available for three catchments: for the Selška Sora at Železniki and at Vester, and for the Bohinjska Bistrica catchment (Sava Bohinjka) at Bistrica. Note, however, that the equipment of the streamgauge in Železniki was out of order during the most intense phase of the flood. A distributed runoff model was therefore combined with observations of peak discharges at multiple locations to examine the flood response properties to the storm.

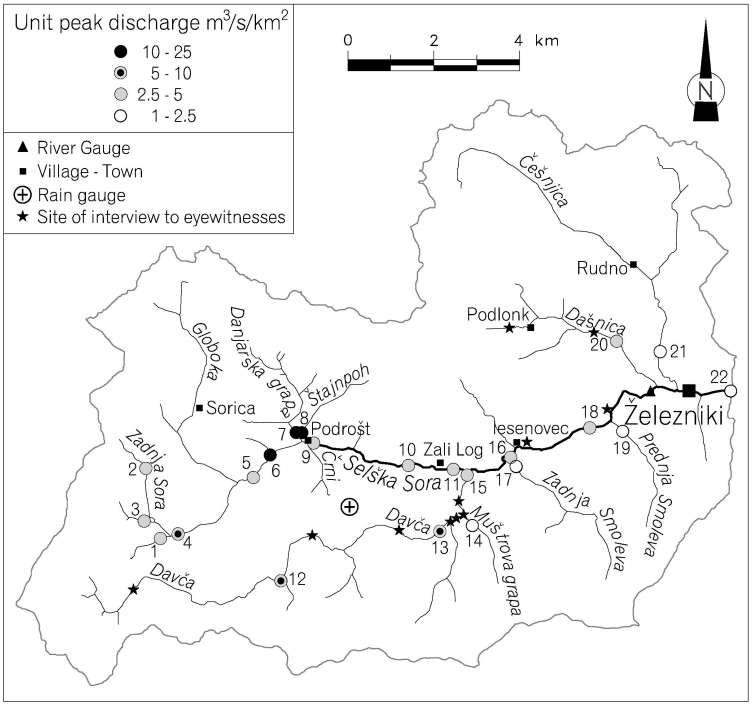

Figure 5.5: Selška Sora watershed with 22 locations of discharge estimates, interviews to eye-witnesses and central values of unit peak discharge estimates.

A detailed post event survey was carried out two months after the flood on the Selška Sora catchment at Železniki [Marchi *et al.*, 2009a]. High water marks (HWMs) and post-flood river cross-section surveys were carried out in order to compute the flood peak discharge at 22 locations along the river network (Figure 5.5). The surveys were located in reaches where the flow process was identified as water flood according to the results of a previous hydrogeomorphic survey. The steps of the post event surveys are detailed by Marchi *et al.* (2009a). In this study, the slope-conveyance method Gaume (2006) was used for discharge estimation: this requires the survey of the post-flood cross section, identification of HWMs to define flood depth and local water slope, estimation of flow roughness and computation of the discharge by

means of the one-dimensional Manning-Strickler equation. Depending on the vegetation in the river bed and on the banks, the selected Manning roughness values typically ranged from 0.1 to 0.066 for streams of width smaller than 5 meters and from 0.066 to 0.05 for larger streams. Froude numbers were generally less than 1 or close to 1, implying that the flow regime was either subcritical or close to critical flow.

Witnesses were interviewed in order to identify the timing of onset and end of rainfall, the presence of hail, the time of rise, peak and recession of the flood, and the nature of the flow process (either water flood or debris flow). The locations referred to in the interviews are reported in Figure 5.5 on the preceding page. This helped to reconstruct the dynamics of the event: start of the rising, time of the peak, duration of the recession. Witnesses provided also useful information on the rainfall-runoff processes (observation of surface runoff, origin of the runoff, extent of soil saturation ...) and the local flow characteristics (presence of woody debris, approximated surface water flow velocities, blockages formed during the flood, timing of the collapse of bridges and dykes).

5.6 Flood response analysis

Flood response properties are investigated by i) contrasting the flood hydrographs observed on the Selška Sora at Vester and on the Bistrica at Bohinjska Bostrica, and by ii) combining the results from a distributed rainfall-runoff model with data from the streamgauge stations in Vester and with results from the post-event survey. The model was not applied over the Bistrica catchment, due to difficulties implied by the subsurface karst circulation, which prevented the definition of catchment boundaries in the area and hence the determination of the rainfall input.

5.6.1 Contrasting runoff response on Selška Sora and on Bistrica river systems

The two flood hydrographs measured on Selška Sora at Vester (212 km^2) and on Bohinjska Bostrica at Bistrica are reported in Figure 5.6 on page 135, together with the corresponding rainfall input. For the case of Bistrica, the rainfall input is provided by the radar rainfall estimates over the corresponding topographic catchment (13.6 km^2). However, as repeatedly reported above, the extent of this topographic catchment is thought to be much less with respect to the actual, but unknown, hydrologic catchment. The Vester hydrograph shows a double peak, corresponding to two distinct rainfall peaks, whereas the Bistrica hydrograph is characterised by one single marked peak. However, it is the recession limb which displays the most striking differences between the two flood responses. The recession limb of hydrograph of Bistrica is characterised by unique characteristics: i) an exponential decrease immediately following the peak, ii) an inflection point followed by a convex upward period and (iii) another inflection point followed by further exponential recession. The recession curve is very long and it takes around 30 hours for the discharge to recede to 30% of the peak discharge. This behaviour has been frequently observed in

other karst systems, as reported by Herman *et al.* (2008) and by Long and Derickson (1999). The flood response at Vester is sharp and peaky, displaying a comparatively much important more contribution of "fast" contributing runoff, even though the subsurface component appears to be significant anyway. On this river system, it takes around 8 hours for the discharge to recede to 30% of the flood peak, which is 26% of the corresponding time required on the Bistrica. The recession on the Selška Sora catchment is therefore faster than in the Bistrica, even though the floodplains of that catchment were interested by extensive inundation, which was scarcely observed over the Bistrica. Floodplain inundation generally act to slow the recession dynamics, as reported by Jothityangkoon and Sivapalan (2003). Overall, these observations support the view that the extreme rainfall accumulations which impacted the area interested by karstified aquifer were in general quickly infiltrated into the karst underground. As the capacity of karst voids is not very large in the study area, groundwater level rising was fast, but anyway delayed with respect to the storm event.

5.6.2 Runoff response analysis on the Selška Sora catchment: the flood response model

A detailed analysis is presented here about the relationship between rainfall and runoff as obtained by combining the discharge data from the Vester and Železninki streamgauge and the flood peak data from the post-event survey with a distributed rainfall-runoff model.

The hydrological model is based on availability of raster information of the landscape topography and of the soil and land use properties. The runoff rate $q(x, y, t)$ [L T^{-1}] at time t and location x, y is computed from the rainfall rate $P(x, y, t)$ [L T^{-1}] using the Green-Ampt infiltration model with moisture redistribution [Ogden and Saghafian, 1997]. The adopted formulation of the Green and Ampt model has been chosen because it provides a simple and yet physically-based description of the infiltration-excess mechanisms. A simple description of the drainage system response [Da Ros and Borga, 1997] is used to represent runoff propagation. The distributed runoff propagation procedure is based on the identification of drainage paths, and requires the characterization of hillslope paths and channeled paths. A channelization support area (A_s) [L^2] is used to distinguish hillslope elements from channel elements. Discharge $Q(t)$ [L^3 T^{-1}] at any location along the river network is represented by:

$$Q(t) = \iint_A q[x, y, t - \tau(x, y)]dxdy \tag{5.1}$$

where A [L^2] indicates the area draining to the specified outlet location and $\tau(x, y)$ [T] is the routing time from the location (x, y) to the outlet of the basin specified by the region A. The routing time $\tau(x, y)$ is defined as

$$\tau(x,y) = \frac{L_h(x,y)}{\nu_h} + \frac{L_c(x,y)}{\nu_c} \tag{5.2}$$

where $L_h(x,y)$ [L] is the distance from the generic point x,y to the channel network following the steepest descent path, $L_c(x,y)$ [L] is the length of the subsequent drainage path through streams down to the watershed outlet, and ν_h and ν_c [L T^{-1}] are two invariant hillslope and channel velocities, respectively.

Ref.	Section	Wat. area [km^2]	Peak disch. [m^3 s^{-1}]	Unit peak disch. [m^3 s^{-1} km^{-2}]
1	Selška Sora upstream Zadnja Sora inflow	1.9	6-8	3.2-4.2
2	Zadnja Sora upstream Rovtarjev grapa inflow	2.3	7-12	3.0-5.2
3	Rovtarjev grapa	2.6	10-15	3.8-5.8
4	Selška Sora downstream Zadnja Sora inflow	9.0	50-70	5.6-7.8
5	Selška Sora downstream Globoka inflow	24.7	85-125	3.4-5.1
6	Tributary between Globoka and Danjarska grapa inflows [1]	0.2	5	25.0
7	Danjarska grapa [2]	9.2	80-120	8.7-13.0
8	Štajnpoh [3]	3.9	30-50	7.7-12.8
9	Selška Sora downstream Danjarska grapa inflow	40.7	125-155	3.1-3.8
10	Selška Sora upstream Zali Log	44.8	140-200	3.1-4.5
11	Selška Sora between Zali Log and Davča inflow	46.8	170-230	3.6-4.9
12	Davča upstream reach	9.8	50-60	5.1-6.1
13	Davča upstream Mustrova grapa inflow	21.4	140-170	6.5-7.9
14	Muštrova grapa	4.2	6-9	1.4-2.2
15	Davča upstream the confluence with Selška Sora	31.8	80-120	2.5-3.8
16	Selška Sora upstream Zadnja Smoleva inflow	80.4	290-350	3.6-4.4
17	Zadnja Smoleva	7.5	14-18	1.9-2.4
18	Selška Sora upstream Prednja Smoleva inflow	95.5	330-430	3.5-4.5
19	Prednja Smoleva	5.7	7-10	1.2-1.7
20	Dašnica in Železniki	10.8	25-40	2.3-3.7
21	Češnjica in Železniki	25.8	35-50	1.4-1.9
22	Selška Sora downstream Železniki	147.2	260-320	1.8-2.2

Table 5.3: Peak discharge estimates from field survey. Section reference numbers are shown on map in Figure 5.5 on page 131.

The model includes also a linear conceptual reservoir for base flow modeling [Borga *et al.*, 2007]. The reservoir input is provided by the infiltrated rate computed based on the Green-Ampt method. The model framework is based on six calibration parameters: the channelization support area (A_s), two kinematic parameters (ν_h and ν_c), and the three soil hydraulic parameters used by the Green-Ampt method. The model was implemented over the Selška Sora catchment at Vester at 15 min time step and using a 12.5 m grid size cell for the description of landscape morphology and soil properties.

The runoff model parameters were calibrated by using data from the streamgauge station at Vester for the September 2007 floods and for a number of floods recorded at this station in the last 20 years.

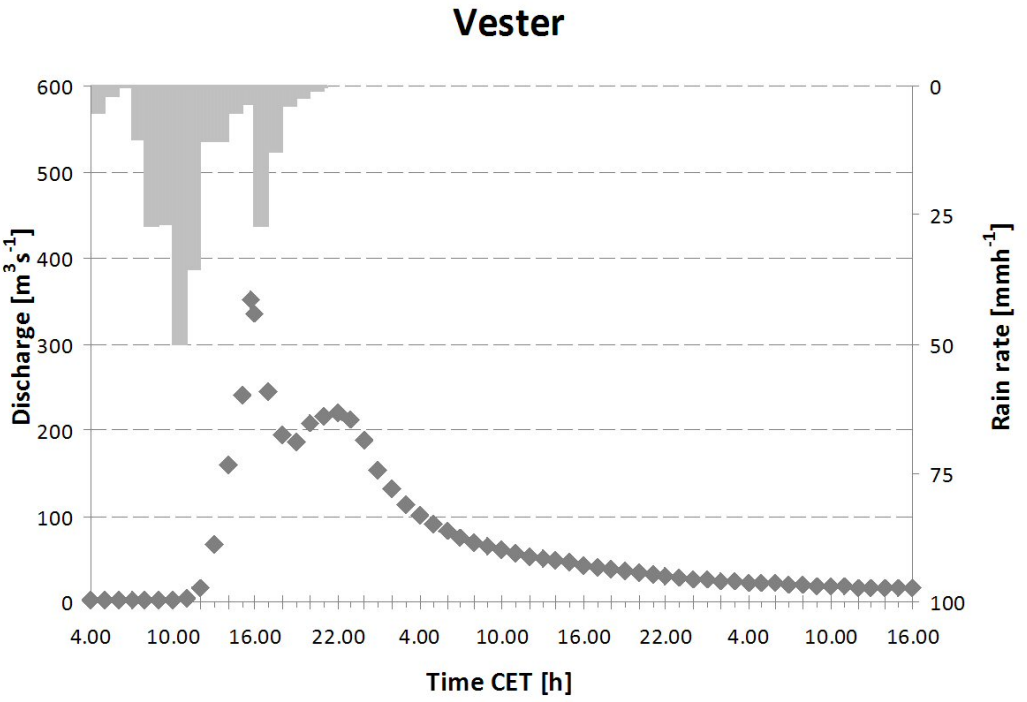

(a)

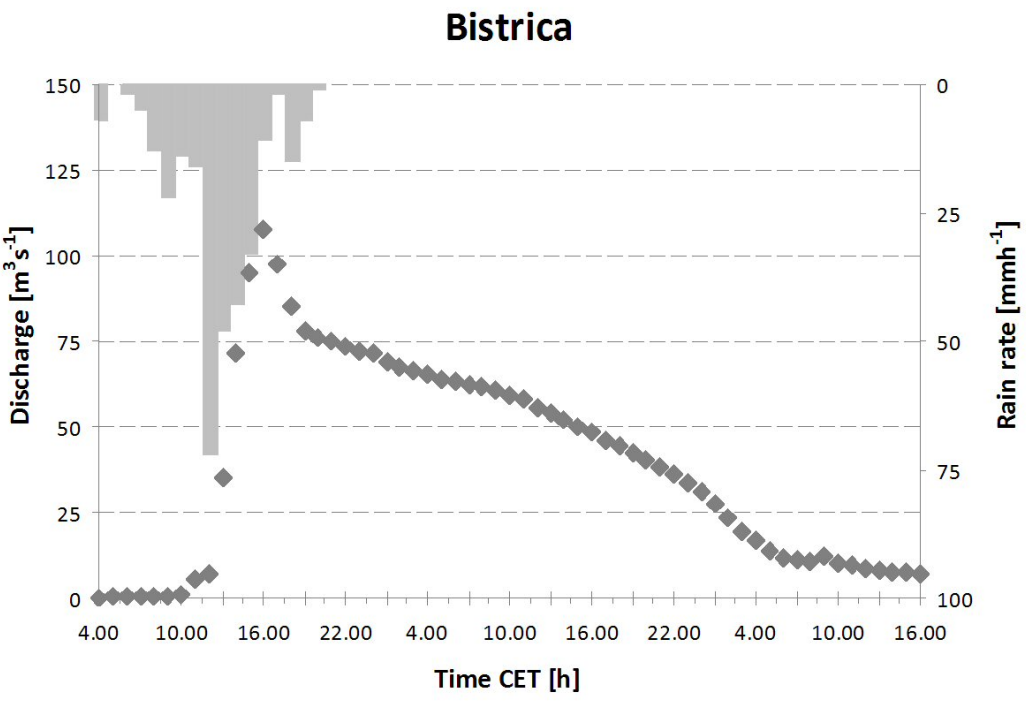

(b)

Figure 5.6: Observed hydrographs on Selška Sora at Vester and on Bohinjska Bostrica at Bistrica.

A methodology involving a combination of manual and automatic calibration to minimise an integrated normalised integrated root mean square error over the flood hydrograph was used. The accuracy of the measured flood hydrograph was considered good enough to afford model calibration. The return time of the flood peak at Vester ranges between 20 and 30 years [Rusjan *et al.*, 2009]. Even though some degree of uncertainty is involved in the extrapolation of the available rating curve [Di Baldassarre and Montanari, 2009], the measured peak discharge was found consistent with application of an hydraulic model at the site. The shape, peak discharge, and timing of the model hydrograph are determined by the hillslope and channel flow velocity and by the soil saturated hydraulic conductivity. The two velocities and the saturated hydraulic conductivity were chosen to match estimates of peak discharge and time of peak. The initial conditions were used to calibrate the initial value of the subsurface store. The results from the application of the runoff model at Vester are reported in Figure 5.7a, whereas Figure 5.7b reports the spatial pattern of event cumulated rainfall. The rainfall map shows that the precipitation is characterised by sharp variability in space, ranging from 170 to almost 400 mm and with gradients of 200 mm in less than 6 km. The hydrological simulation describes well the rising part of the hydrograph, the time and value of the peak, as well as the recession curve. However, a second peak is simulated at 2130 CET which is not observed. This is likely due to errors in the rainfall estimation in the area close to the stream gauge station in the third phase of the storm (between 1230 and 1730 CET). The recession dynamics shows the significance of the subsurface stormflow for this event.

5.6.3 Flood response properties

The relationship between the distribution of the observed unit peak discharges and the properties of the rainfall forcing (spatial average of event cumulate rainfall and of max hourly rainfall for each surveyed catchment) is reported in Figure 5.8 on page 138. The figure shows that the highest unit peak discharges are located in the area of largest total rainfall which also correspond to the areas affected by the highest instantaneous rainfall intensities. The lowest unit peak discharges correspond to areas with lower accumulated rainfall. However, some differences can be noted for the three Sections numbered 7, 8 and 13. The tributaries corresponding to Section 7 and 8 (Danjarska grapa, cross-section no. 7, Štajnpoh, cross-section no. 8) experienced relatively high unit peak discharge, compared to the relevant rainfall. Marchi *et al.*, 2009b reported that the survey of the Danjarska grapa and the Štajnpoh sections showed high bed load transport (Danjarska) and almost hyperconcentrated flow (Štajnpoh). This may have led to overestimation of flood discharge, especially for Štajnpoh. At the same time, one should note that the two tributaries are very close to the area heavily impacted by one of the convective band, and that underestimation of rainfall rates by weather radar could play a role here. Also for Section 13, located on the Davča valley, uncertainty in the discharge observations may be due difficulties in the survey. A wide range in peak discharge for catchments characterised by similar precipitation amounts may be also observed in Figure 5.8 on page 138.

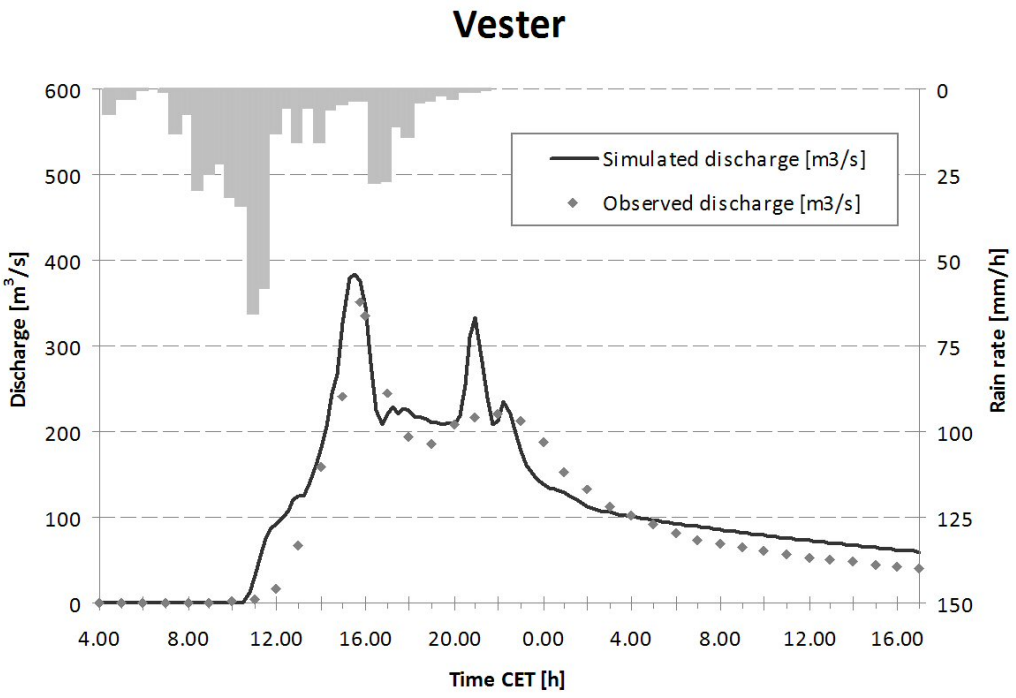

(a)

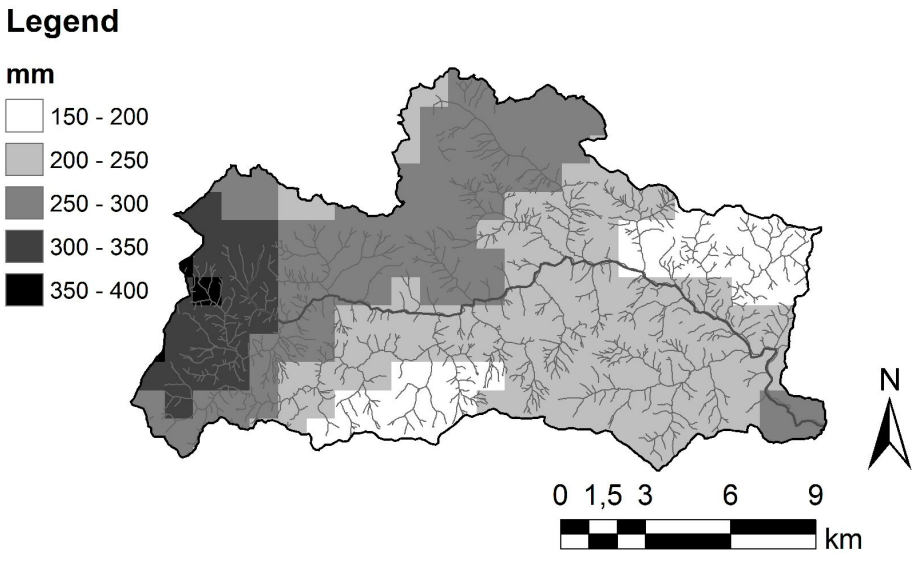

(b)

Figure 5.7: Sora at Vester: a) results of runoff model application; b) event rainfall spatial distribution over the catchment.

This may point out to heterogeneity in the catchment properties or errors in the observations. A likely case of heterogeneity in catchment properties is represented by the Češnjica sub-basin (cross-section no. 21), with a relatively low runoff response with respect to high rainfall amount. This may be explained by the karst geology of this portion of the catchment, which may have had an impact on the runoff response.

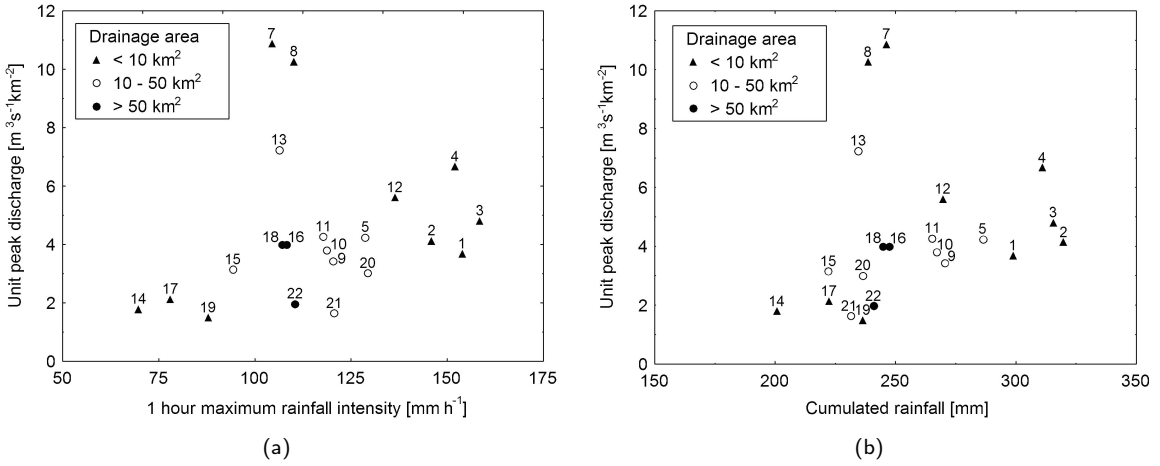

Figure 5.8: Relationship between observed unit peak discharges and rainfall characteristics on the corresponding catchments: a) max hourly rainfall; b) event cumulated rainfall.

The surveyed peak discharges are in general hydraulically consistent, with flow values in downstream cross sections which are larger than those observed in the upstream sections. Whereas this is expected, given the simultaneous arrival of flood peaks at the confluence points (inferred by eyewitnesses reports and consistent with rainfall analyses), this also points out to the good accuracy of the survey. However, hydraulic inconsistency is shown when comparing in Table 5.3 on page 134 the peak discharge estimated just downstream of Železniki (cross-section no. 22, with central value of 290 $m^3\ s^{-1}$) with the upstream values measured at cross-sections 16 (320 $m^3\ s^{-1}$) and 18 (380 $m^3\ s^{-1}$). While uncertainty in the surveys plays certainly a role here, inundation of the floodplain and flooding of the town may provide a physical justification for the observed flood peak attenuation. The runoff model, as calibrated based on Vester discharge data, was applied to simulate peak discharges over the 22 subcatchments and on the Železniki streamgauge section. Corresponding results are reported in Figures 5.9 5.10 and 5.11.

Figure 5.9a,b shows the comparison between observed and simulated peak discharges and unit peak discharges, respectively. The results show a good fit between simulated and observed peak discharges, with a squared correlation equal to 0.87 and Nash-Sutcliffe efficiency equal to 0.83 (Table 5.4).

This suggest that the hydrological model provides a reasonably good description of the flood event. The success in the hydrological simulation may be ascribed to the rather homogeneous soil and morphological properties in the basin upstream Vester, and in the strong forcing of the rainfall, which was estimated with good accuracy for the study basin. Analysis of the results obtained for the unit peak discharges

(Figure 5.9a) affords closer examination of the simulations for the smaller basins. The analysis allows to isolate the behaviour of the tributaries corresponding to Section 7 and 8 (Danjarska grapa, cross-section no. 7, Štajnpoh, cross-section no. 8), which are characterised by simulated peak values considerably less than the observed ones. This support the view that either the observed values were overestimated (due to the large proportion of sediments) or the rainfall values were underestimated for these small catchments, as reported above. When a rainfall-runoff model is used to link the disparate rainfall and runoff observations, one should borne in mind that the two errors have different characteristics. An error in the survey of a peak discharge at a certain cross-section does not affect downstream flow values; on the other hand, rainfall underestimation over a certain sub-basin should translates as runoff underestimation to downstream cross section. The observation that simulated peak flows at a number of downstream cross sections (namely 11, 13, 16 and 18 in Table 5.3) show consistent underestimation with respect to observed peak flows supports the view that rainfall was likely underestimated over the tributaries of Danjarska grapa, cross-section no. 7, Štajnpoh, cross-section no. 8.

INDICI		
Obs-sim(distr)	**Peak**	**Unit peak**
Correlation^2	0.87	0.00
Nash	0.83	-0.59
Obs-sim(mean)		
Correlation^2	0.77	0.08
Nash	0.70	-1.24
Sim(distr)-Sim(mean)		
Correlation^2	0.94	0.20
Nash	0.93	-0.36

Table 5.4: Statistical results.

To investigate the significance of the accurate spatial rainfall portray, simulations were repeated over the 22 catchments involved in the survey by using the spatially averaged rainfall over the largest catchment closed at Section 22 (with a catchment area of 147.2 km^2).

Results are reported in Figure 5.10a,b, which shows the comparison between observed and simulated peak discharges and unit peak discharges, respectively. The comparison shows a significant decrease in Nash-Sutcliffe simulation efficiency, which amounts here to 0.70 with a reduction of 16% with respect to simulations obtained by using the actual rainfall spatial variability. Taking into account that in both cases the model was used in 'validation mode', the important consequence is that the good flood peak simulation reported in Figure 5.9a,b is due to the right reason, i.e. to the availability of reasonably accurate precipitation patterns. Examination of the simulations obtained for the unit peak discharges shows that, as expected, the accuracy decreases strongly particularly for the small basins (less than 10 km^2).

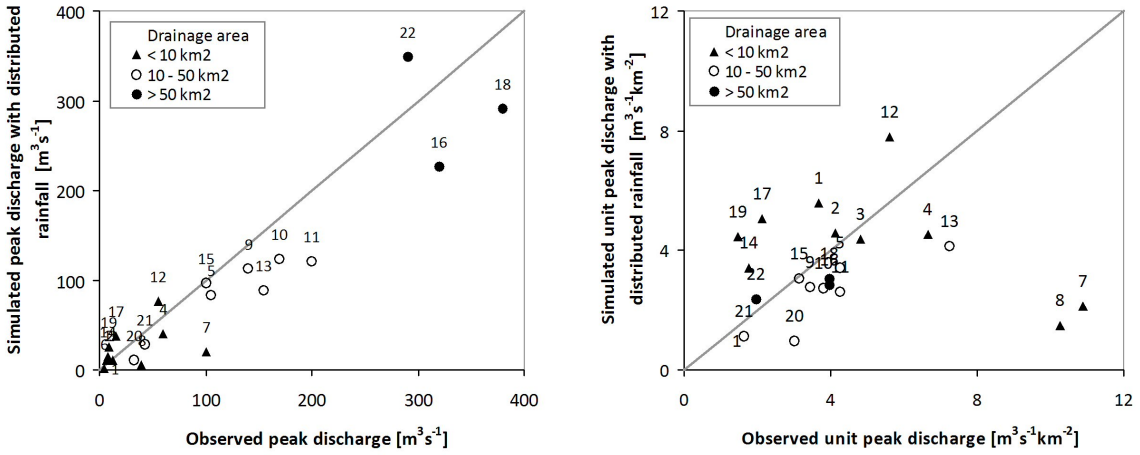

Figure 5.9: Result from runoff model applications over the 22 IPEC catchments on the S. Sora river: a) observed versus simulated peak discharges; b) observed versus simulated unit peak discharges.

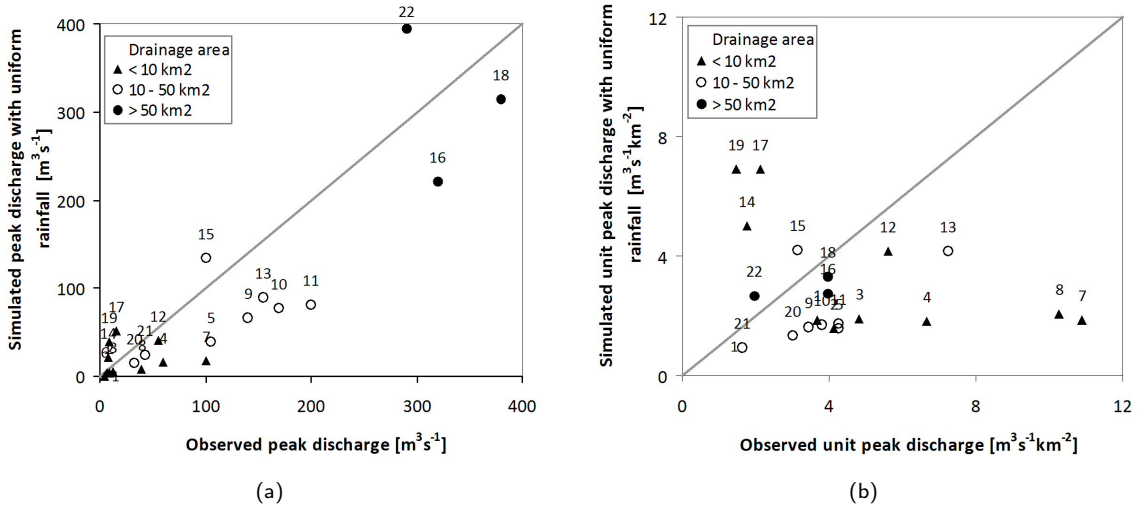

Figure 5.10: Result from runoff model applications over the 22 IPEC catchments by using spatially uniform rainfall on the S. Sora river: a) observed versus simulated peak discharges; b) observed versus simulated unit peak discharges.

5.6.4 Water balance and response time analysis

Three nested catchments of the Selška Sora (the Selška Sora closed at Železniki, the Davča and the Upper Sora subcatchments) are considered with more details. For these catchments, we report simulated flood hydrograhs (Figure 5.10 on the preceding page) and water balance and response time analysis (Table 5.5). The flood response from these catchments is contrasted with the response observed for the Bistrica at B Bistrica.

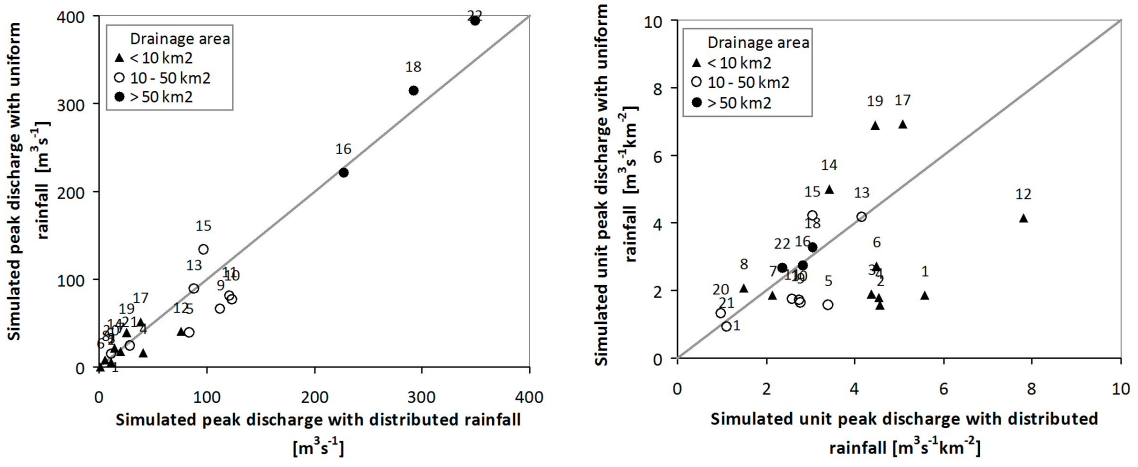

(a) (b)

Figure 5.11: Result from runoff model applications over the 22 IPEC catchments by using spatially distributed and spatially uniform rainfall on the S. Sora river: a) observed versus simulated peak discharges; b) observed versus simulated unit peak discharges.

Basin	Area [km^2]	Rain [mm]	Runoff [mm]	Peak disch. [m^3 s^{-1}]	Unit peak disch. [m^3 s^{-1} km^{-2}]	Runoff ratio [-]	Lag time [hr]
Davča[1]	31.9	217.2	50.0	97.0	3.1	0.23	1.9
Upper Sora[1]	46.7	258.4	41.0	120.0	2.7	0.16	1.9
Železniki[1]	103.3	238.5	55.0	312.0	3.0	0.23	2.2
Vester[2]	212.0	236.5	43.5	351.7	1.6	0.18	5.2

Table 5.5: Rainfall and runoff for the three basins.[1]: analysis obtained from model simulated values; [2]: analysis obtained from observed flow values.

The town of Železniki was flooded during the event; so, a number of cross-checked observations are available to evaluate the quality of the simulations. The conveyance of the river in the town is ranging around 160 m^3 s^{-1} . According to notes from eyewitnesses, flooding started around 1115 CET and lasted for 0130 hours to 0200 hours. The flow peak was reached around 1230 CET. After 1330 CET, no more flooding was observed in the town and the flow showed a quick decrease. Inspection of simulations for Železniki in Figure 5.10 on the preceding page shows that the simulation provides a rather good match of the notes from the observers, with the exception of the second peak. It is likely that there was a

second peak, however it was not as intense as reported in the model simulation (the second peak did not exceed the flooding threshold in the town). The simulated peak flow is larger than that obtained from the post-event survey; however, one should note that the flooding in the area of the town and in the upstream river reaches was likely to attenuate the flood peak. Eyewitnesses notes showed also that the timing of the simulated flow peak for the catchments of Davča and Upper Sora was accurate within $\pm$ 15 min.

These data are summarised in Table 5.5 on the preceding page to permit water balance and response time analysis. Inspection of the values reported in this table shows that the runoff coefficient (computed as the ratio between runoff and rainfall) is always rather low for the four catchments, ranging between 0.16 for the Davča and 0.23 for Železniki and the Upper Sora, with Vester in intermediate position.

The values reported for the runoff coefficient are slightly larger than the mean value computed on the sample of flood events available for analysis in Železniki. It is interesting to note the different response from the Davča and the Upper Sora, with the Davča receiving less rainfall and generating relatively more runoff. As reported before, the runoff peak simulations provide a rather good match to the observations collected during the post event survey; hence, given that also the shape of the flood appears to have been reasonably well simulated (at least for the catchment of Železniki), it is likely that the simulated runoff coefficients are close to the actual values. In the simulations, the difference between the Davča and the upper Sora is due to the different parametrisation of the soil hydraulic properties, with the Upper Sora considered more permeable than the Davča, and to the different characteristics of the rain forcing, with the Davča receiving less rainfall, but more intense. We speculate that the actual behaviour is also influenced by karst terrain that may influence the hydrological response of the Upper Sora close to its northern and western border.

Very close values of time lag are reported for the three upper basins; these are not unexpected, given the homogeneity of the geomorproperties of the river network in the three basin, and the synchronous characteristics of the rainfall forcing.

5.7 Influence of space-time precipitation variability at the catchment scale

To characterize the influence of temporal and spatial variability of rainfall on flood response, we utilized 30-min, 1-km radar rainfall fields to compute the following quantities:

1. the normalized time distance of rainfall from the basin outlet, $\vartheta_1(t)$; and
2. the normalized dispersion of rainfall, $\vartheta_2(t)$.

The drainage network and its kinematic properties, as represented by the routing time $\tau(x)$, provides a natural metric for analyzing the spatial distribution of rainfall, as shown previously by Zhang *et al.* (2001);

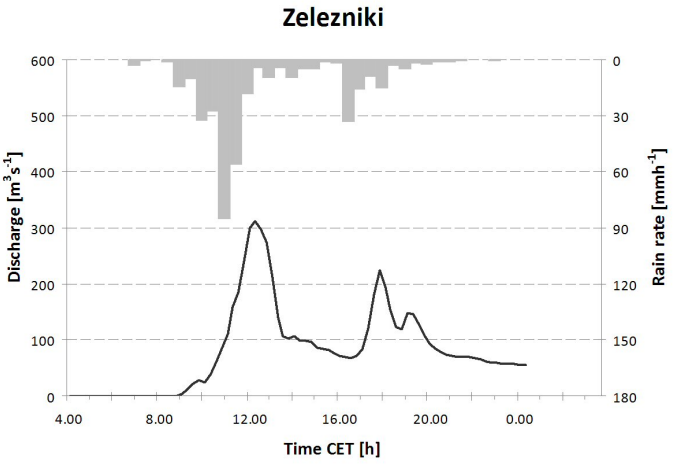

(a)

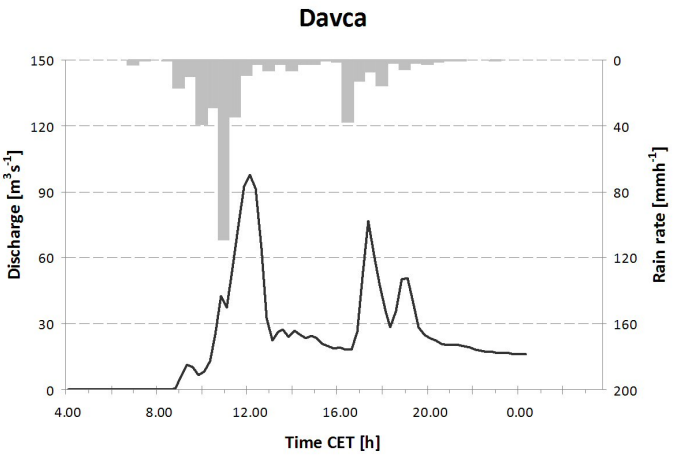

(b)

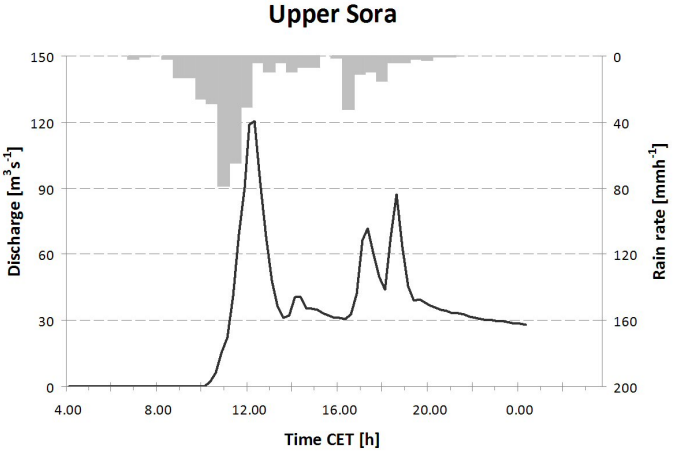

(c)

Figure 5.12: Model simulations for the S Sora at the river sections of: a) Železniki, b) outlet of Dav{c a subcatchment; outlet of Upper Sora subcatchment.

Smith *et al.* (2005); Skoien *et al.* (2001). The routing time incorporates both geometric and kinematic properties in its determination. The routing time is therefore a more convenient measure with respect to purely geometric values, such as the distance, when runoff propagates through the network at spatially variable velocities..

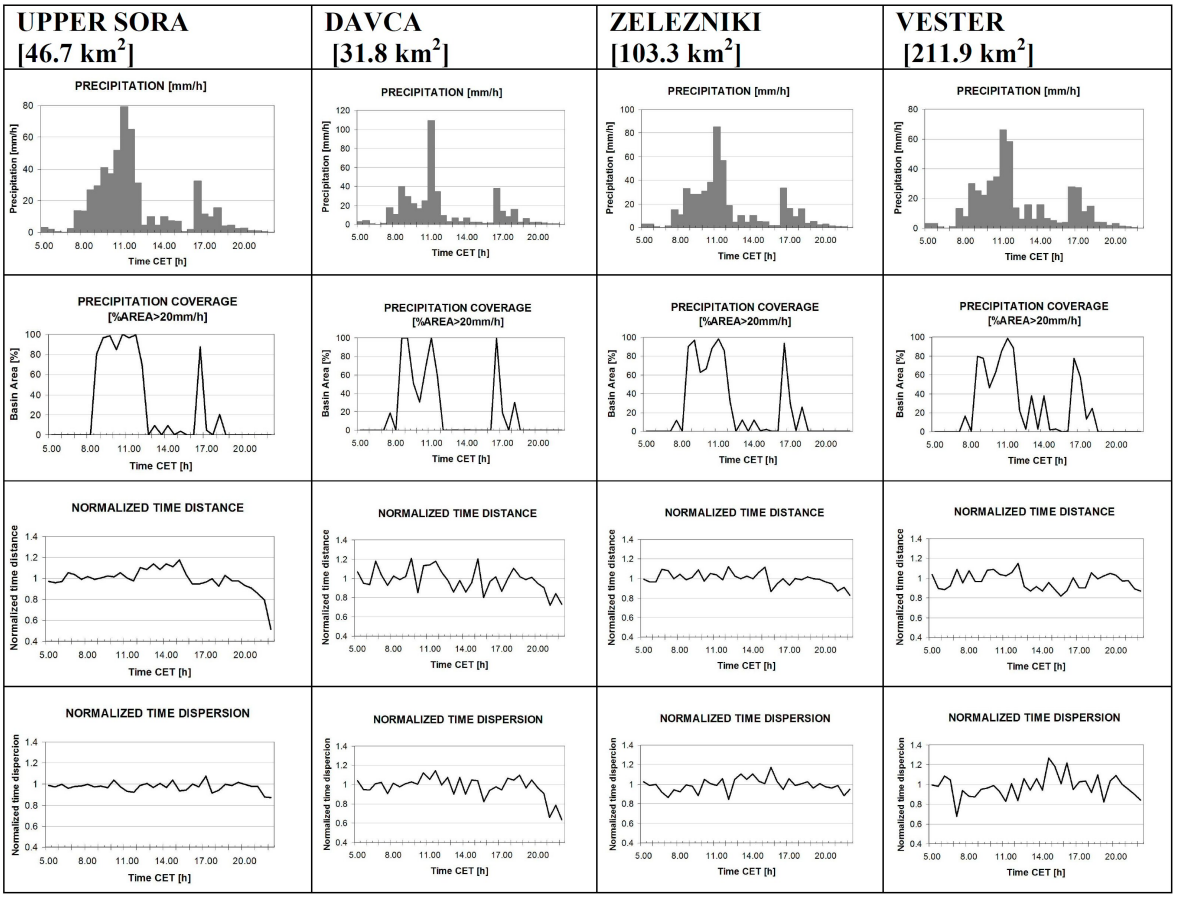

Figure 5.13: Precipitation analysis by using time series of precipitation intensity, coverage (for precipitation intensity > 20 mm h^{-1}), and normalized time-distance, for the three nested S Sora basins closed at Vester, Železniki and Davča

The normalized time-distance at time t, $\vartheta_1(t)$, is a function of the rainfall field $P(t,x,y)$ and the routing time $\tau(x,y)$. It is defined as the ratio of the rainfall-weighted centroid routing time and the mean routing time. The time-distance $\vartheta_1(t)$ can be represented as

$$\vartheta_1(t) = \frac{\int_A w(t,x,y)\tau(x,y)dxdy}{|A|d_{mean}} \tag{5.3}$$

where A is the spatial domain of the drainage basin and the weight function $w(t,x,y)$ is given by:

$$w(t,y) = \frac{P(t,x,y)}{|A|^{-1}\int_A P(t,x,y)dxdy} \tag{5.4}$$

and d_{mean} is the mean value of the routing time over the basin.

Values of $\vartheta_1(t)$ close to 1 reflect a rainfall distribution either concentrated close to the mean time-distance or homogeneous, with values less than 1 indicating that rainfall is distributed near the basin outlet, and values greater than 1 indicating that rainfall is distributed towards the periphery of the drainage basin.

The rainfall-weighted flow time-distance dispersion is given by:

$$S(t) = \left\{\int_A w(t,x,y)\left[\tau(x,y) - d_{mean}\right]^2 dxdy\right\}^{0.5} \tag{5.5}$$

The dispersion for uniform rainfall is defined by:

$$S_l = \left\{\int_A \left[\tau(x,y) - d_{mean}\right]^2 dxdy\right\}^{0.5} \tag{5.6}$$

and the normalized dispersion is given by:

$$\vartheta_2(t) = \frac{S(t)}{S_l} \tag{5.7}$$

Values of $\vartheta_2(t)$ close to 1 reflect a uniform-like rainfall distribution, with values less than 1 indicating that rainfall is characterised by a unimodal peak, and values greater than 1 indicating cases of multimodal rainfall peaks close and far from the basin outlet.

Results are reported for the nested Selška Sora basins of Upper Sora, Davča, Železniki and Vester (Figure 5.13 on the preceding page). Examination of the fractional coverage of heavy rainfall (greater than 20 mm h^{-1}) shows that flood producing rainfall for the four basins is concentrated over a period of 4 hours and half, lasting from 0800 to 1230 CET, followed by a second peak around 1700 CET. These peaks are synchronous over the two headwater basins, Upper Sora and Davča, with the Davča exhibiting a very intense peak around 1100 CET (the mean areal rainfall rate over this 30 min period exceeds 100 mm h^{-1}). Being the two basins of similar size, their flood peaks at the outlet were also synchronous, leading to the flooding of Železniki around 1230 CET. One should also note the increasing of the rainrate with time, which is a typical trigger for diffused landsliding and debris flow, as documented by Montgomery *et al.*, 2002 and Borga *et al.*, 2002 and as observed in the field.

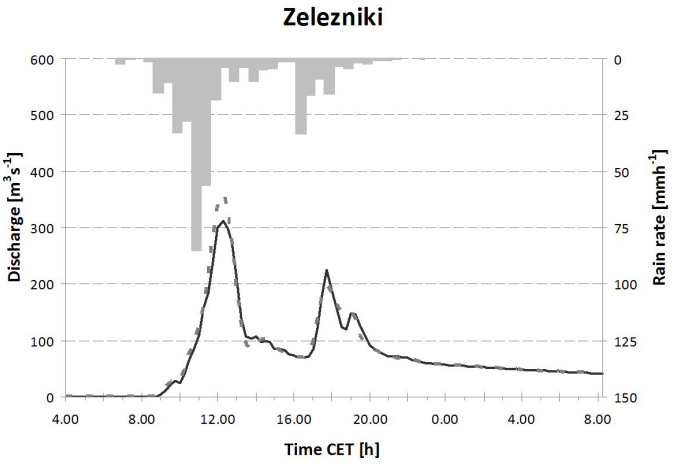

(a)

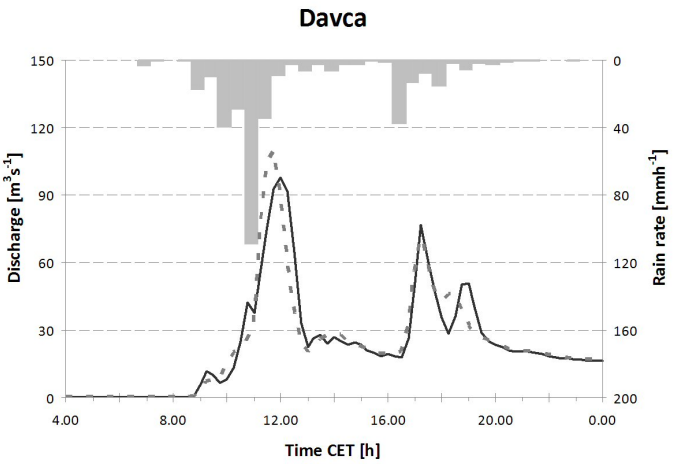

(b)

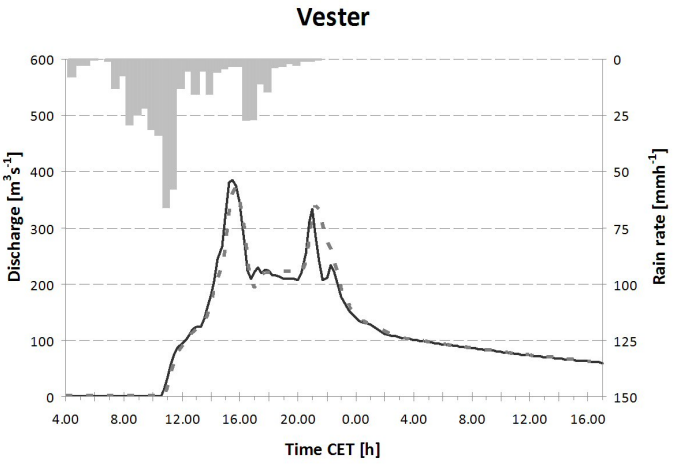

(c)

Figure 5.14: Runoff model results obtained by using spatially averaged rainfall rates (dashed line) and spatially distributes rainfall rates (continuous line) for the three nested S Sora basins closed at Davča, Železniki and Vester.

Despite the large spatial variability in rainfall over the Selška Sora basin, the "conditional" distribution of routing times, given the spatial rainfall distribution, is close to the distribution of routing times in the uniform rainfall case.

For the Upper Sora, Železniki and Vester, normalised time-distance and dispersion are virtually unchanged from uniform rainfall case Table 5.6. The variability in time of the normalised time distribution is particularly marked for the Davča catchment, due to the shifting of the convective band over this basin. The convective band, centered over upper Selška Sora catchment during the flood producing rainfall period 0800-1230 CET and displaying a south-west to north-east direction, sometimes shifted in the orthogonal direction, thus interesting more extensively the Davča catchment. Interestingly enough, the normalised dispersion exceeds unity for both the Upper Sora catchment and for the catchment closed at Vester. In both cases, this is due to the characteristics of the spatial rainfall pattern, which exhibits a double peak, one (larger) corresponding to the headwater basins and the other (smaller) close to the outlet.

Catchment	**"normalised time distance"** ϑ_1	**"normalised time dispersion'** ϑ_2
Davča	1.07	1.07
Upper Sora	1.02	0.96
Železniki	1.02	1.00
Vester	1.00	1.06

Table 5.6: Rainfall pattern statistics for the four nested S Sora catchments.

In the second step of the analysis, we quantified the effect of neglecting the rainfall spatial variability on the rainfall-runoff model application. For each catchment, the flash flood event was simulated by using the actual rainfall spatial variability and then by using spatially uniform precipitations, hence obtaining two different hydrographs (Figure 5.14 on the preceding page). The comparison between the two modelled hydrographs shows that the differences are negligible. As identified by the examination of the time distance parameter, differences are less negligible for the Davča catchment, which is indeed characterised by the largest values of time distance (1.07) among the catchments considered in the study. This value reflects a concentration of precipitation towards the headwater basins. Hence, it is expected that the runoff generated by a precipitation concentrated towards the upstream periphery of the basin tends to arrive later at the outlet with respect the same rainfall input taken uniformly distributed over the basin. This is clearly reported in the figure, which shows that the flood peak corresponding to uniform rainfall anticipates by 30 min that obtained by considering the actual spatial rainfall distribuition.

5.8 Conclusions

Even tough karst geological formations are important in many countries, and especially around the Mediterranean sea where they represent more than half of the drainage basin [Ganoulis, 2003], only few studies

documented the influence of this geology on flood and flash flood development [Fabre, 1990; Ganoulis, 1995; Bonacci *et al.*, 2006; Marechal *et al.*, 2008; Norbiato *et al.*, 2009]. Overland flow is generally rare in karst terrain, due to the influence of permeable soils, strong interaction between the circulation of surface water and groundwater, and well-developed underground drainage system. While these features generally reduce the runoff response to high rainfall rates, karst systems are also known to exhibit a threshold-like response when the retention capacity of the groundwater is exhausted by continuing precipitation [Gaume *et al.*, 2004; Marechal *et al.*, 2009]. This may lead to back flooding, saturation excess runoff formation and very quick development of flood discharges in a terrain that hardly experienced any surface runoff.

There are five principal observations from this work:

1. The September 2007 storm system over Western Slovenia, which produced record storm accumulations, flood peaks and intense debris flows, was characterised by quasi-stationary convective banded structures which are similar, even though less persistent, to the studied flash flood event occurred over north-eastern Italy (upper Tagliamento river basin) on 29 August 2003 (see Chapter 4). The steadiness of these rainbands led to highly variable precipitation accumulations and runoff.

2. The highly variable lighological properties of the region provides a major control on runoff response to extreme rainfall accumulations and intensities. The area which received the highest rainfall accumulations is characterised by a permeable karstified aquifer, which led to an attenuated runoff response. Peak discharges in this area were high, but not as exceptional as implied by the measured rainfall. On the other hand, runoff response in the area of Selška Sora, characterised by a less fractured aquifer, was very intense and led to widespread flooding, with a pronounced contrast in flood response at short geographical distance.

3. Pronounced contrasts in flood response between different basins at short distance are related to: (a) effect of the spatial organization of the banded convection, (b) contrasting fractional coverage of rainfall following from basin size and structure and (c) differential response due to highly non linear relationship between rainfall and runoff due to karstic terrain features.

4. For the September 2007 flood, postflood interviews, field observations, and surveys were important sources of information. The combination of detailed radar rainfall estimates, readily available GIS data, hydrologic and hydraulic modeling, postflood surveys and interviews with local residents allowed to generate a much more complete picture of the storm and flood environment than would otherwise be available on ungauged basins.

5. The storm event response over the Selška Sora basin can be reasonably well reproduced with a simple distributed hydrologic model, using high resolution rainfall observations and parameter calibration at large scale. The simulated flood peaks provide an accurate reproduction of the observed flood peaks

at 22 cross sections surveyed after the flash flood event. Combined use of the hydrological model and observations from the post-event survey led to an improved understanding of the hydrometeorological processes involved in the flash flood event.

6. Conclusions and implications for flash flood risk management

The work thesis demonstrated the value of high resolution radar rainfall estimates, obtained by weather radar and raingauge network, for the objective to understand the hydrometeorological processes leading to flash floods and to improve the procedures for flash flood forecasting. Data from different environments and different instruments have been exploited to this purposes:

- Weather radar observations and post event surveys data from a location (Anterselva) impacted by a high intensity debris flow;
- Data from Romania, where a network of S-band weather radar provided the required reflectivity observations and data from a raingauge network has been used to adjust the radar rainfall estimates for an ensemble of localised and dramatic flash floods (leading to more than 20 casualties overall);
- Data from Western Slovenia, where the value of applying the MRT to adjust for signal attenuation has been demonstrated. Moreover, these radar rainfall estimates have been used, together with a rather simple, but not simplistic, distributed hydrological model, to establish the consistency of the post event survey for the 18 September 2007 flash flood event (which caused 6 casualities);
- Radar, raiungauge, streamgauge and survey observation data from the flash flood event of 29 September 2003, which caused 2 casualties.

The main results from this study are summarised below.

- The utility of the Mountain Reference Technique (MRT) has been demonstrated to quantify and correct signal attenuation effects that affect C-band radar measurements in the typical heavy rain conditions which dominate flash floods. Besides rain attenuation, screening effects were quantified using a geometrical calculation based on a digitized terrain model of the region. The vertical structure of the reflectivity was modelled with the normalized apparent VPR estimated globally without rain type separation. Implementation of the radar data processing indicated that: i) attenuation

correction over the entire detection domain using the Hitschfeld Bordan algorithm allowed obtaining good radar QPEs (Nash criterion of 0.8 at the event time scale), especially for the most intense rainfall pattern; ii) due to the attenuation equation instability, it is however compulsory to limit the maximum PIA to be corrected to about 10 dB; iii) the results also proved to be sensitive on the choice of the (Z, k, R) relationships. The convective nature of the precipitation explains the rather good performance obtained;

- Two spatial pattern statistics have been introduced which may effectively clarify the dependence existing between spatial rainfall distribution, basin morphology and runoff response. The two statistics are represented by i) a scaled measure of the time taken to route the rainfall from the geographical centroid of the rainfall spatial pattern to the geographical centroid of the catchment, and ii) a scaled measure of the additional variance in runoff time that is caused by the spatial variability in rainfall, relative to the case of spatially uniform rainfall throughout the catchment. The statistics are based on the observation that runoff routing through branched channel networks imposes an effective averaging of spatial rainfall excess at equal travel time, in spite of the inherent spatial variability. This implies that rainfall organisation measured along the river network by using the travel time coordinate may be a significant property of rainfall spatial variability when considering flood response modelling;

- The analysis reported for the Romenian flash floods suggests that the two rainfall spatial pattern statistics are effective in i) describing the degree of spatial organisation which is important for runoff modelling, and ii) quantifying the effects of neglecting the spatial rainfall variability on flood modelling. The use of these statistics enables linking different sources of errors emerging when the spatial rainfall variability is neglected, such as timing error and shape error. Overall, the analysis reported here shows that neglecting the spatial rainfall variability results in a considerable degradation of simulation Nash-Sutcliffe (NS) efficiency in almost 30% of the cases (NS less than 0.8), with NS less than 0.6 in one of the cases. This provides a significant documentation of the influence of the spatial rainfall variability on runoff modeling for catchment size less than 160 km^2. Failing to consider spatial variability of rainfall adequately in model calibration will likely lead to errors in the values of the model parameters which will be wrongly adjusted to compensate for errors in the rainfall input data. When the timing error is dominant, it is likely that the adjustment of the channel and hillslope velocity parameters may compensate for errors due to neglecting the spatial rainfall information. However, this compensation will be strongly event-dependent, and will induce uncertainty in model calibration when multiple events (likely characterized by mixed spatial rainfall organization) will be used for model calibration;

- The analysis of the August 2003 storm system, which produced record storm accumulations, flood

peaks and impressive geomorphic changes, provides a model for Mesoscale Convective Systems that are likely responsible for the majority of flash flood peaks in the upper Tagliamento river basin (North-eastern Italy) Extreme rainfall from the August 2003 storm was produced by quasi-stationary convective banded structures. Some of the bands persisted in the same locations for the duration of the event. The steadiness of these rainbands led to highly variable precipitation accumulations and runoff. The characteristic spatial scale of the convective bands is around 9 km, which results in a dominant spatial scale for rainfall accumulation and flooding of around 100 km2. Antecedent soil moisture distribution appears to have played an important role in flood response. Measured peak discharges were large, but not as exceptional as implied by the measured rainfall. The exceptionally dry summer season of 2003, combined with the high soil moisture storage capacity which characterises the basins in the upper Tagliamento watershed, resulted in low runoff ratios and emphasised the non-linearity of the flood response. These findings are confirmed by comparison with a previous extreme flood occurred on June 22, 1996. Pronounced contrasts in flood response between different basins of varying catchment size were related to: (a) effect of the spatial organization of the banded convection, (b) contrasting fractional coverage of rainfall following from basin size and structure and (c) differential response due to highly non linear relationship between rainfall and runoff. An important source of non-linearity is related to the strong dependency of basin response time to storm accumulation;

- Examination of the cases occurred in Romania, Slovenia and on the Taglaimento river basin, showed that the storm event response can be reasonably well reproduced with a simple distributed hydrologic model (based on use of Green-Ampt equation and constant flow velocity on hillslope and channel reaches), provided that high resolution rainfall observations are used. However, application of the model to the Fella case study in eastern Italy required stratification of parametrisation according to precipitation accumulation at the sub-basin scale. The degree of non-linearity arising from the available data could not be reproduced by the flood response model with invariant parametrisation. The other cases showed a less degree on rainfall-runoff nonlinearity, implying a more robust application of the distributed model;

- For all the cases considered here, postflood interviews, field observations, and surveys were important sources of information. The combination of detailed radar rainfall estimates, readily available GIS data, hydrologic and hydraulic modeling, postflood surveys and interviews with local residents allowed to generate a much more complete picture of the storm and flood environment than would otherwise be available on ungauged basins. Concerning the organisation and execution of the post-flood survey, a number of lessons should be recognised: i) The availability of quality-controlled weather radar observations enable the coupling of field collection of observations with the rainfall-runoff

modelling of the same experimental setting. This triggers an integral cycle of observation and modelling, which may be iterated to provide more accurate understanding of the discrepancies between observations and model outcomes. ii) Post-flood geomorphological observations are a pre-requisite for peak discharge estimation, particularly in mountainous areas with abundant sediment supply. The geomorphological survey is essential to elucidate the nature of the flow (water flood versus debris flow and hyperconcentrated flow) and to uncover the potential for flood surges related to the collapse of temporary dams formed during the event. ii) The systematic collection of information from interviews to eyewitnesses is capable to generate a reliable picture of the time evolution of the flood and may provide essential information to check the quality of the observations;

- Finally, the post-flood documentation campaign demonstrated the high educational potential of the post-flood survey concept. The survey gives to graduate and post-graduate students in hydrology and geosciences the opportunity to improve their field skills in collecting the interdisciplinary observations necessary to characterize flash flood processes and responses. The integral cycle of observations and modelling enables the participants in the surveys to grasp the uncertainty sources in the model input (the rainfall forcing), in the model structure, and in the flood response observations. This provides insights on both limitations of data and model outcomes and on the gain generated by interpreting data and models in the field settings where hydrologic problems arise and where decisions must be made. This is an essential ingredient in the education and training of next-generation hydrologists, as it was for the work carried out for this thesis.

A. Statistical indicators

Correlation:

$$Corr = \frac{\frac{1}{N_t N_s} \sum_{i,j=1}^{N_t N_s} (R_{i,j} - \overline{R})(G_{i,j} - \overline{G})}{\sigma_R \sigma_G} \tag{A.1}$$

Bias:

$$bias = \frac{\frac{1}{N_t N_s} \left(\sum_{i,j=1}^{N_t N_s} G_{i,j} - \sum_{i,j=1}^{N_t N_s} R_{i,j} \right)}{\frac{1}{N_t N_s} \sum_{i,j=1}^{N_t} G_{i,j}} \tag{A.2}$$

Fractional Standard Error (FSE):

$$FSE = \frac{\sqrt{\frac{1}{N_t N_s} \sum_{i,j=1}^{N_t N_s} (G_{i,j} - R_{i,j})^2}}{\frac{1}{N_t N_s} \sum_{i,j=1}^{N_t N_s} G_{i,j}} \tag{A.3}$$

Mean Absolute Error (MAE):

$$MAE = \frac{\frac{1}{N_t N_s} \sum_{i,j=1}^{N_t N_s} |R_{i,j} - G_{i,j}|}{\frac{1}{N_t N_s} \sum_{i,j=1}^{N_t N_s} G_{i,j}} \tag{A.4}$$

Mean relative error (MRE)

$$MRE = \frac{\frac{1}{N_t N_s}\sum_{i,j=1}^{N_t N_s}(R_{i,j} - G_{i,j})}{\frac{1}{N_t N_s}\sum_{i,j=1}^{N_t N_s} G_{i,j}} \tag{A.5}$$

where N_t is the number of hours in the storm event, N_s is the number of raingauge station used in the evaluation, $G_{i,j}$ and $R_{i,j}$ are the raingauge measurement and the corresponding radar estimate at time step i and for the raingauge station j.

Nash-Sutcliffe model efficiency coefficient

$$E = 1 - \frac{\sum_{t=1}^{T}(Q_o^t - Q_m^t)^2}{\sum_{t=1}^{T}(Q_o^t - \bar{Q}_o)^2} \tag{A.6}$$

where Q_o is observed discharge, and Q_m is modeled discharge. Q_o^t is observed discharge at time t.

List of Figures

List of Tables

Bibliography

Anagnostou, M. N., Krajewski, W. F., Seo, D. J., and Johnson, E. R. (1998). Meanfield radar rainfall bias studies for wsr-88d. asce. *J. Eng. Hydrol.*, **3**, 149–159.

Anagnostou, M. N., Kalogeros, J., Tarolli, M., Anagnostou, E. N., Borga, M., and Papadopoulos, A. (2008). Rainfall measurements of x-band polarimetric weather radar in complex terrain. *proceeding for ERAD - the 5th European conference on radar in meteorology and hydrology*.

Anderson, M. G. and Burt, T. P. (1990). Process studies in hillslope hydrology. *John Wiley, Hoboken, N. J.*, page 539 pp.

Andréassian, V., Perrin, C., Michel, C., Usart-Sanchez, I., and Lavabre, J. (2001). Impact of imperfect rainfall knowledge on the efficiency and the parameters of watershed models. *Journal of Hydrology*, **250**, 206–223.

Andrieu, H., Creutin, J. D., Delrieu, G., and Faure, D. (1997). Use of a weather radar for the hydrology of a mountainous area. part i: Radar measurement interpretation. *J. Hydrol*, **193**, 1–25.

Bacchi, B., Ranzi, R., and Borga, M. (1996). Statistical characterization of spatial patterns of rainfall cells in extratropical cyclones. *J. Geophys. Res.*, **101**(D21), 26277–26286.

Baeck, M. L. and Smith, J. A. (1995). Climatological analysis of manually digitized radar data for the united states. *Water Resour. Res.*, **31**, 3033–3049.

Baeck, M. L. and Smith, J. A. (1998). Estimation of heavy rainfall by the wsr-88d. *Weather Forecast*, **13**, 416–436.

Barry, D., Parlange, J. Y., Li, L., Jeng, D. S., and Crapper, M. (2005). Green-ampt approximations. *Adv. Water. Res*, **28**, 1003–1009. doi:10.1016/j.advwatres.2005.03.010.

Battan, L. J. (1973). Radar observation of the atmosphere. *University of Chicago Press*, page 324 pp.

Bechini, R., Gorgucci, E., Scarchilli, G., and Dietrich, S. (2002). The operational weather radar of fossalon di grado (gorizia, italy): Accuracy of reflectivity and differential reflectivity measurements. *Meteor. Atmos. Phys.*, **79**, 275–284.

Bell, V. A. and Moore, R. J. (2000). The sensitivity of catchment runoff models to rainfall data at different spatial scales. *Hydrology and Earth System Sciences*, **4**(4), 653–667.

Benda, L. and Dunne, T. (1997). Stochastic forcing of sediment supply to channel networks from landsliding and debris flow. *Water Resources Research*, **33**, 2849–2863.

Berenguer, M., Lee, G. W., Sempere-Torres, D., and Zawadzki, I. (2002). A variational method for attenuation correction of radar signal. *Proceedings of ERAD*, pages 11–16.

Berne, A., Delrieu, G., Creutin, J. D., and Obled, C. (2004). Temporal and spatial resolution of rainfall measurements require for urban hydrology. *J. Hydrol.*, **299**, 166–179.

Beven, K. J. (1981). Kinematic subsurface stormflow. *Wat. Res. Res.*, **33**, 2849–2863.

Beven, K. J. and Hornberger, G. M. (1982). Assessing the effect of spatial pattern of precipitation in modeling stream flow hydrographs. *Water Res. Bulletin*, pages 823–829.

Blanchard, D. C. and Spencer, A. T. (1970). Experiments of the generation of raindrop size distributions by drop breakup. *J. Atmos. Sci.*, **27**, 101–108.

Blöschl, G. and Sivapalan, M. (1995). Scale issues in hydrological modelling: a review. *Hydrological Processes*, **9**, 251–290.

Blöschl, G. and Zehe, E. (2005). On hydrological predictability. . *Hydrol. Process.*, **19**, 3923–3929.

Bonacci, O., Ljubenkov, I., and Roje-Bonaci, T. (2006). Karst flash floods: an example from the dinaric karst (croatia). *Nat. Hazards Earth Syst. Sci.*, **6**, 195–203.

Borga, M., Anagnostou, E. N., and Frank, E. (2000). On the use of real-time radar rainfall estimates for flood prediction in mountainous basins. *J. Geophys. Res*, **105**(D2), 2269–2280.

Borga, M., Dalla Fontana, G., and Cazorzi, F. (2002). Analysis of topographic and climatic control on rainfall-triggered shallow landsliding using a quasi-dynamic wetness index. *J. Hydrol.*, **268**(1-4), 56–71.

Borga, M., Boscolo, P., Zanon, F., and Sangati, M. (2007). Hydrometeorological analysis of the august 29, 2003 flash flood in the eastern italian alps. *Journal of Hydrometeorology*, **8**, 1049–1067.

Borga, M., Gaume, E., Creutin, J. D., and Marchi, L. (2008). Surveying flash floods: gauging the ungauged extremes. *Hydrological Processes,*, **22**(18), 3883–3885.

Bouilloud, L., Delrieu, G., Boudevillain, B., Borga, M., and Zanon, F. (2009). Radar rainfall estimation for the post-event analysis of a slovenian flash-flood case: application of the mountain reference technique at c-band frequency. *Hydrology and Earth System Sciences*, **13**, 1349–1360.

Bouilloud, L., Delrieu, G., Boudevillain, B., and Kirstetter, P. E. (2010). Radar rainfall estimation in the context of post-event analysis of flash floods. *Journal of Hydrology*. submitted.

Bringi, V. N., Goddard, J. W. F., and Cherry, S. M. (1982). Comparison of dual polarization radar measurements of rain with ground based disdrometer measurements. *J Appl Meteor*, **21**, 252–254.

Caine, N. (1980). The rainfall intensity duration control of shallow landslides and debris flows. *Geogr. Ann.*, **62**(1-2), 23–37.

Casty, C., Wanner, H., Luterbach, J., Esper, J., and Böhm, R. (2005). Temperature and precipitation variability in the european alps since 1500. *Int. J. Climatol.*, **25**, 1855–1880.

Cazacioc, L. (2007). Spatial and temporal variability of extreme daily precipitation amounts in romania. *Romanian Journal of Meteorology*, **9**(1-2), 34–46.

Cazorzi, F. and Bincoletto, L. (2005). Modellazione dei processi idrologici. la prevenzione del rischio idrogeologico nei piccoli bacini montani della regione: Esperienze e conoscenze acquisite con il progetto catchrisk (in italian). *Convegno finale del Progetto CATCHRISK, Udine, Italy*, **INTERREG IIIB**, 45–74.

Cazorzi, F. and Dalla Fontana, G. (1992). L'utilizzo dei sistemi informativi geografici nello studio idrologico di bacino (in italian). *Quaderni di idrologia montana*, **12**, 83–115.

Cesare, B. (1999). Multi stage pseudomorphic replacement of garnet during polymetamorphism: Microstructures and their interpretation. *Journal of Metamorphic Geology*, **17**, 723–734.

Cesare, B., Fioretti, A., and Rosenberg, C. (2004). The periadriatic intrusion of vedrette di ries - rieserferner (eastern alps): petrology, emplacement mechanisms and contact aureole. *32nd IGC, B17 Field Trip Guide Book. Published by APAT*, **17**, 723–734. Italian Agency for the Environmental Protection and Technical Services - Via Vitaliano Brancati, 48 - 00144 Roma - Italy, 36pp.

Ceschia, M., Micheletti, S., and Carnie, R. (1991). Rainfall over friuli venezia giulia: High amounts and strong geographical gradients. *Theor. Appl. Climatol*, **43**, 175–180.

Chandrasekar, V., Bringi, V. N., Balakrishnan, V. N., and Zrnic, D. S. (1990). Error structure of multiparameter radar and surface measurements of rainfall. part iii: Specific differential phase. *J Atmos Oceanic Technol*, **7**, 621–629.

Collier, C. G. (1989). Applications of weather radar systems. *Ellis Horwood*, page 294 pp.

Constantin-Horia, B., Simona, S., Gabriela, P., and Adrian, S. (2009). Human factors in the floods of romania. in: Threats to global water security, nato science for peace and security series c: Environmental security. *Eds: J. Anthony A. Jones, Trahel G. Vardanian and Christina Hakopian*, pages 187–192.

Corral, C., Torres, D. S., Revilla, M., and Berenguer, M. (2000). A semidistributed hydrological model using rainfall estimates by radar. application to mediterranean basins. *Phys Chem Earth Part B: Hydrol Oceans Atmos*, **25**, 1133–1136.

Costa, J. E. (1987). Hydraulics and basin morphometry of the largest flash floods in the conterminous united states. *J Hydrol*, **93**(313-338).

Creutin, J. D. and Borga, M. (2003). Radar hydrology modifies the monitoring of flash flood hazard. *Hydrological Processes*, **17**(7), 1453–1456. Invited commentary. 10.10002/hyp.5122.

Cucchi, F., Piano, C., Marinetti, E., Massari, G., Oberti, S., and Zini, L. (2000). Studies for the realization of the hydrogeological map of friuli-venezia giuli. *Ipogea*, **3**, 57–71.

Da Ros, D. and Borga, M. (1997). Use of digital elevation model data for the derivation of the geomorphologic instantaneous unit hydrograph. *Hydrol. Processes*, **11**, 13–33.

D'Agostino, V. and Marchi, L. (2001). Debris flow magnitude in the eastern italian alps: data collection and analysis. *Physics and Chemistry of the Earth, Part C*, **26**(9), 657–663.

Dawdy, D. R. and Bergmann, J. M. (1969). Effect of rainfall variability on streamflow simulation. *Water Resour. Res.*, **5**, 958–969.

De Lima, J. and Singh, V. (2002). The influence of the pattern of moving rainstorms on overland flow. *Advances in Wat. Res.*, **25**, 817–828.

Deganutti, A. and Marchi, L. (2000). Rainfall and debris-flow occurrence in the moscardo basin (italian alps). *Proc. of the second International Conference on Debris flow hazards mitigation, Taipei August*, pages 26–72.

Delrieu, G. and Creutin, J. D. (1995). Simulation of Radar Mountain Returns Using a Digitized Terrain Model. *Journal of Atmospheric and Oceanic Technology*, **12**, 1038–1049.

Delrieu, G., Caoudal, S., and Creutin, J. D. (1997). Feasibility of using mountain return for the correction of ground based x-band weather radar data. *Journal of Atmospheric and Oceanic Technology*, **14**, 368–385.

Delrieu, G., Hucke, L., and Creutin, J. D. (1999a). Attenuation in rain for x- and c- band weather radar systems operating in heavy rainfall: sensitivity with respect to the drop size distribution. *Journal of Applied Meteorology*, **38**, 57–68.

Delrieu, G., Serrar, S., Guardo, E., and Creutin, J. D. (1999b). Rain measurement in hilly terrain with x-band radar systems: Accuracy of path-integrated attenuation estimates derived from mountain returns. *Journal of Atmospheric and Oceanic Technology*, **16**, 405–416.

Delrieu, G., Andrieu, H., and Creutin, J. D. (2000). Quantification of path-integrated attenuation for x and c-band weather radar systems operating in mediterranean heavy rainfall. *Journal of Applied Meteorology*, **39**, 840–850.

Delrieu, G., Ducrocq, V., Gaume, E., Nicol, J., Payrastre, O., Yates, E., Kirstetter, P. E., Andrieu, H., Ayral, P. A., Bouvier, C., Creutin, J. D., Livet, M., Anquetin, A., Lang, M., Neppel, L., Obled, C., du Chatelet, J. P., Saulnier, G. M., Walpersdorf, A., and Wobrock, W. (2005). The catastrophic flash-flood event of 8-9 september 2002 in the gard region, france: a first case study for the cévennes-vivarais mediterranean hydro-meteorological observatory. *Journal of Hydrometeorology*, **6**, 34–52.

Delrieu, G., Boudevillain, B., qnd B. Chapon, J. N., Kirstetter, P. E., Andrieu, H., and Faure, D. (2009). Bollène 2002 experiment: radar rainfall estimation in the cévennes-vivarais region, france. *Journal of Applied Meteorology and Climatology*. in press.

Di Baldassarre, G. and Montanari, A. (2009). Uncertainty in river discharge observations: a quantitative analysis. . *Hydrology and Earth System Sciences Discussion*, **6**, 39–61. www.hydrol-earth-syst-sci-discuss.net/6/39/2009/.

Dietrich, W. E. and Dunne, T. (1978). Sediment budget for a small catchment in mountainous terrain. *Zeitschrift für Geomorphologie*, **29**, 191–206.

Doswell III, C. A., Brooks, H. E., and Maddox, R. A. (1996). Flash-flood forecasting: an ingredients-based methodology. *Weather Forecast*, **11**, 360–381.

Doviak, R. J. and Zrnic, D. S. (1993). Doppler radar and weather observations, 2nd edition. *Academic Press Inc.*, page 562 p.

Dunne, T. (1978). Field studies of hillslope flow processes. *Hillslope hydrology, M. J. Kirkby, Ed., John Wiley*, pages 227–293.

Dunne, T. (1983). Relation of field studies and modeling in the prediction of storm runoff. . *J. Hydrol.*, **65**, 24– 48.

Fabre, G. (1990). La catastrophe hydrologique éclaire de nîmes (3 octobre 1988). the nimes flash flood on october 3, 1988. *Bulletin de l'Association des Géographes Français*, **67**(2), 113–122.

Fabry, F. and Zawadzki, I. (1995). Long-term radar observations of the melting layer of precipitation and their interpretation. *J. Atmos. Sci.,*, **52**, 838–851.

Faures, J. M., Goodrich, D. C., Woolhiser, D. A., and Sorooshian, S. (1995). Impact of small-scale spatial rainfall variability on runoff modeling. *Journal of Hydrology*, (173), 309–326.

Frei, C. and Schär, C. (1998). A precipitation climatology of the alps from high-resolution rain-gauge observations. *Int. J. Climatol.*, **18**, 873–900.

Furey, P. R. and Gupta, V. J. (2005). Effects of excess rainfall on the temporal variability of observed peak-discharge power laws. *Adv. Water Resour.*, **28**, 1240–1253.

Ganoulis, J. (1995). Floodplain protection and management in karst areas, in gardiner. *J. et al. (ed.), Defence from Floods and Floodplain Management. NATO ASI Series, Vol. 299, Kluwer Academic, Dordrecht*, pages 419–428.

Ganoulis, J. (2003). Risk-based floodplain management: A case study from greece. *Intl. J. River Basin Management*, **1**(1), 41–47.

Gaume, E. (2006). Post flash-flood investigation - methodological note. floodsite european research project. *Available at http://www.floodsite.net/, report D23.2*, page 62 p.

Gaume, E., Livet, M., and Desbordes, M. (2003). Study of the hydrological processes during the avène river extraordinary flood (south of france): 6-7 october 1997. *Phys. Chem. Earth.*, **28**, 263–267.

Gaume, E., Livet, M., Desbordes, M., and Villeneuve, J. P. (2004). Hydrological analysis of the river aude, france, flash flood on 12 and 13 november 1999. *Journal of Hydrology*, **286**(1), 135–154.

Gaume, E., Bain, V., Bernardara, P., Newinger, O., Barbuc, M., Bateman, A., Blaskovicova, L., Blöschl, G., Borga, M., Dumitrescu, A., Daliakopoulos, I., Garcia, J., Irimescu, A., Kohnova, S., Koutroulis, A., Marchi, L., Matreata, S., Medina, V., Preciso, E., Sempere-Torres, D., Stancalie, G., Szolgay, J., Tsanis, J., Velasco, D., and Viglione, A. (2009). A compilation of data on european flash floods. *Journal of Hydrology*, **367**, , 70–78. doi:10.1016/j.jhydrol.2008.12.028.

Geotis, S. G. (1975). Some measurements of the attenuation of 5-cm radiation in rain. *Preprints 16th Conf. on Radar Meteorology, Houston, TX, Amer. Meteor. Soc.*, pages 63–66.

Germann, U., Galli, G., Boscacci, M., and Bolliger, M. (2006). Radar precipitation measurement in a mountainous region. *Q. J. R. Meteorol. Soc.*, **132**, 1669–1692.

Giannoni, F., Smith, J. A., Zhang, Y., and Roth, G. (2003). Hydrologic modeling of extreme floods using radar rainfall estimate. *Adv. Water Resour.*, **26**, 195–200.

Gosset, M. and Zawadzki, I. (2001). Effect of nonuniform beam filling on the propagation of the radar signal at x-band frequencies. part i: Changes in the k(z) relationship. *Journal of Atmospheric and Oceanic Technology*, **18**(7), 1113–1126.

Grayson, R. and Blöschl, G. (2001). Spatial patterns in catchment hydrology: Observations and modelling. *Cambridge Univ. Press, New York*, (404 pp.).

Gregoretti, C. and Dalla Fontana, G. (2006). The triggering of debris flow due to a channel-bed failure in four alpine basins of dolomites. part ii: rainfall analyses. Submitted.

Herman, H. K., Toran, L., and White, W. (2008). Threshold events in spring discharge: Evidence from sediment and continuous water level measurement. *Journal of Hydrology*, **351**, 98– 106.

Hicks, N. S., Smith, J. A., and Nelson, P. A. (2005). Catastrophic flooding from an orographic thunderstorm in the central appalachians. *Wat. Res. Res.*, **41**. , W12428, doi: 10.1029/2005WR004129.

Hildebrand, P. H. (1977). Iterative Correction for Attenuation of 5 cm Radar in Rain. *Journal of Applied Meteorology*, **17**, 508–514.

Hitschfeld, W. and Bordan, J. (1954). Errors inherent in the radar measurement of rainfall at attenuationg wavelenghts. *J. Meteorol.*, **11**, 58–67.

Hubbert, J. and Bringi, V. N. (1995). An iterative filtering technique for the analysis of copolar differential phase and dual-frequency radar measurements. *J. Atmos. Ocean. Technol.*, **12**, 643–648.

Hudson, N. W. (1963). Raindrop size distribution in high intensity rain. *Rhod J Agric Res*, **1**, 6–11.

Jameson, A. R. (1994). An alternative approach to estimating rainfall rate by radar using propagation differential phase shift. *J Atmos Oceanic Technol*, **11**(122-131).

Johnson, A. M. and Rodine, J. R. (1984). Debris flow. *In Slope Instability, Brundsen D, Prior DB (ed.). John Wiley, Hoboken, N. J.*, pages 257–361.

Joss, J. and Gori, E. G. (1978). Shapes of raindrop size distributions. *J. Appl. Meteor.*, **17**, 1054–1061.

Joss, J. and Waldvogel, A. (1968). Raindrop size distribution and sampling size errors. *J. Atmos. Sci.*, **26**, 566–569.

Joss, J. and Waldvogel, A. (1990). Precipitation measurement and hydrology. *Radar in Meteorology: Battan Memorial and 40th Anniversary Radar Meteorology Conference, D. Atlas, Ed., Amer. Meteor. Soc.*, pages 577–606.

Jothityangkoon, C. and Sivapalan, M. (2003). Towards estimation of extreme floods: Examination of the roles of runoff process changes and floodplain flows. *Journal of Hydrology*, **281**, 206–229.

Journel, A. and Huijbregts, C. (1978). Mining geostatistics. *Academic Press, London.*

k. Beven and Wood, E. F. (1993). Flow routing and the hydrological response of channel networks. In: Beven, K.J., Kirkby, M.J. (Eds.). Channel Network Hydrology, John Wiley, Chichester, pp. 99.

Keenan, T. D. (1998). The bmrc/ncar c-band polarimetric (cpol) radar system. *J Atmos Oceanic Technol*, **15**, 871–886.

Krajewski, W. F. (1995). Rainfall estimation using weather radar and ground stations. *Proceedings of the III International Symposium on Weather Radars*. San Paulo, Brazil.

Krajewski, W. F., Lakshmi, V., Georgakakos, K. P., and Jain, S. C. (1991). A monte-carlo study of rainfall sampling effect on a distributed catchment model. *Water Resour Res*, **27**, 119–128.

Leijnse, H., Uijlenhoet, R., and Stricker, J. N. M. (2007). Rainfall measurements using radio links from cellular communications networks. *Water Resources Research*. 43, W03201, doi:10.1029/2006WR005631.

Lewis, H. W., Harrison, D. L., and Kitchen, M. (2007). Local vertical profile corrections using data from multiple scan elevations, met. office, united kingdom. *Proceedings for 33rd Conference on Radar Meteorology*.

List, R. (1991). A linear radar reflectivity rain rate relationship for steady tropical rain. *J. Atmos. Sci.*, **45**, 3564–3572.

Long, A. J. and Derickson, R. G. (1999). Linear systems analysis in a karst aquifer. *Journal of Hydrology*, **219**(3-4), 206–217.

Mager, D. (1985). Geologische karte des rieserfernergruppe zwischen magerstein und windschar (südtirol). *Der Schlern*, **6**. Bozen.

Maksimov, V. A. (1964). Computing runoff produced by a heavy rainstorm with a moving center. *Soviet Hydrology*, **5**, 510–513.

Marchi, L. and D'Agostino, V. (2004). Estimation of debris-flow magnitude in the eastern italian alps. *Earth Surface Processes and Landforms*, **29**(2), 207–220.

Marchi, L., Borga, M., Preciso, E., Sangati, M., Gaume, E., Bain, V., Delrieu, G., Bonnifait, L., and Pogancik, N. (2009a). Comprehensive post-event survey of a flash flood in western slovenia: observation strategy and lessons learned. *Hydrological Processes*, **23**(26), 3761–3770. DOI: 10.1002/hyp.7542.

Marchi, L., Cavalli, M., Sangati, M., and Borga, M. (2009b). Hydrological controls and erosive response of a major alpine debris flow. *Hydrological Processes*. in print.

Marchi, L., Borga, M., Preciso, E., , and Gaume, E. (2010). Characterisation of selected extreme flash floods in europe and implications for flood risk management. *Journal of Hydrology*. Under review.

Marechal, J. C., Ladouche, B., and Dörfliger, N. (2008). Karst flash flooding in a mediterranean karst, the example of fontaine de nîmes. *Eng. Geol.*, **99**, 138–146.

Marechal, J. C., Ladouche, B., and Dörfliger, N. (2009). Analyse hydrogéologique de la contribution de l'eau souterraine à la crue éclair des 6 et 8 septembre 2005 à nîmes (hydrogeological analysis of groundwater contribution to the 6-8 september 2005 flash flood in nîmes). *La Houille Blanche*, **2**, 88–93.

Marshall, J. S. and Palmer, W. K. (1948). The distribution of raindrop size to intensity. *J. Meteor.*, **5**(165-166).

Marzoug, M. and Amayenc, P. (1994). A class of single and dual-frequency algorithms for rain rate profilimg from a spaceborne radar, part 1, principle and tests from numericalò simulations. *J. Atmos. Oceanic Technol*, **11**, 1480–1506.

Matrosov, S. Y., Kropfli, R. A., Reinking, R. F., and Martner, B. E. (1999). Prospects for measuring rainfall using propagation differential phase in x and ka-radar bands. *J Appl Meteor*, **38**, 766–776.

Mc Collum, J. R., Krajewski, W. F., Ferraro, R. R., and Ba, M. B. (2002). Evaluation of biases of satellite rainfall estimation algorithms over the continental united states. *J Appl Meteor*, **41**(11), 1065–1080.

Meneghini, R., Eckerman, J., and Atlas, D. (1983). Determination of rain rate from a spaceborne radar using measurements of total attenuation. *IEEE Trans. Geosci. and Remote Sensing*, **GE-21**, 34–43.

Michaud, J. and Sorooshian, S. (1994). Effect of rainfall-sampling errors on simulations of desert flash floods. *Water Resources Research*, **30**(10), 2765–2775.

Montgomery, D. R., Dietrich, W. E., and Heffner, J. T. (2002). Piezometric response in shallow bedrock at cb1: Implications for runoff generation and landsliding. *Water Resour. Res.*, **38**, 1274, doi:10.1029/2002WR001429.

Moser, J. (2003). Hochwasser am vorderberger wildbach (in ger- man). *Amt der Kärntner Landesregierung, Abteilung 18 Wasserwirtschaft*, page 15 pp.

Mosetti, F. (1983). Sintesi sull'idrologia del friuli-venzia giulia, quaderni dell'ente tutela pesce del friuli-venzia giulia (in italian). *Rivista di Limnologia*, **6**, 1–295.

Moulin, L., Gaume, E., and Obled, C. (2008). Uncertainties on mean areal precipitation: assessment and impact on streamflow simulations. *Hydrol Earth Syst Sci Discuss*, **5**, 2067–2110.

Naden, P. S. (1992). Spatial variability in flood estimation for large catchments: the exploitation of channel network structure. *Journal des Sciences Hydrologiques*, **37**(1), 53–71.

Nicotina, L., Celegon, E. A., Rinaldo, A., and Marani, M. (2008). On the impact of rainfall patterns on the hydrologic response. *Water Resources Research*, **44**. W12401.

Niemczynowicz, J. (1984). Investigation of the influence of rainfall movement on runoff hydrograph: Part i. simulation of conceptual cathcment. *Nordic Hydrology*, **15**, 57–70.

Norbiato, D., Borga, M., Esposti, S. D., Gaume, E., and Anquetin, S. (2008). Flash flood warning based on rainfall depth-duration thresholds and soil moisture conditions: an assessment for gauged and ungauged basins. *Journal of Hydrology*, **362**, 3–4.

Norbiato, D., Borga, M., Merz, R., Blöschl, G., and Carton, A. (2009). Controls on event runoff coefficients in the eastern italian alps. *J. Hydrology, in print*.

Obled, C. H., Wendling, J., and Beven, K. (1994). The sensitivity of hydrological models to spatial rainfall patterns: an evaluation using observed data. *Journal of Hydrol.*, **159**, 305–333.

O'Connor, J. E. and Costa, J. E. (2004). Spatial distribution of the largest rainfall-runoff floods from basins between 2.6 and 26,000 km^2 in the united states and puerto rico. *Water Resources Research,*, **40**(W1107).

Ogden, F., Sharif, L. H. O., Senarath, S. U. S., Smith, J. A., Baeck, M. L., and Richardson, J. R. (2000). Hydrologic analysis of the fort collins, colorado flash flood of 1997. *J. Hydrol*, **228**, 82–100.

Ogden, F. L. and Julien, P. Y. (1994). Runoff model sensitivity to radar rainfall resolution. *Journal of Hydrology*, **158**, 1–18.

Ogden, F. L. and Saghafian, B. (1997). Green and ampt infiltration with redistribution. *J. Irrig. Drain. Eng.*, **123**(5), 386–393.

Ogrinc, N., Kanduc, T., Stichler, W., and Vreca, P. (2008). Spatial and seasonal variations in $\delta^{18}o$ and δd values in the river sava in slovenia. *Journal of Hydrology*, **359**, 303–312. doi:10.1016/j.jhydrol.2008.07.010.

Okunishi, K. and Iida, T. (1981). Evolution of hillslopes including landslides. *Transactions, Japanese Geomorphological Union*, **2**, 291–300.

Orlanski, I. (1975). A rational subdivision of scales for atmospheric processes. *Bull. Am. Meteorol. Soc.*, **56(5)**, 527–530.

Parajka, J., Kohnová, S., Bálint, G., Barbuc, M., Borga, M., Claps, P., Cheval, S., Gaume, E., Hlavcová, K., Merz, R., Pfaundler, M., Stancalie, G., Szolgay, J., and Blöschl, G. (2009). Seasonal characteristics of flood regimes across the alpine-carpathian range. *Journal of Hydrology*. submitted.

Pellarin, T., Delrieu, G., Creutin, J. D., and Andrieu, H. (2000). Hydrologic visibility of weather radars operating in high-mountainous regions: A case study for the toce catchment (italy) during the mesoscale alpine programme. *Physics and Chemistry of the Earth, Part B: Hydrology, Oceans and Atmosphere*, **25**, 953–957.

Pellarin, T., Delrieu, G., Saulnier, G. M., Andrieu, H., Vignal, B., and Creutin, J. D. (2002). Hydrologic visibility of weather radar systems operating in mountainous regions: Case study for the ardèche catchment (france). *J. Hydrometeor.*, **3**, 539–555.

Peschke, G., Etzenberg, C., Muller, G., Topfer, J., and Zimmermann, S. (1999). Das wissensbasierte system flab-ein instrument zur rechnergestützten bestimmung von landschaftseinheiten mit gleicher abflussbildung. *IHI-Schr. 10, Int. Hochsch. Zittau, Zittau, Germany*.

Pessoa, M. L., Bras, R., and Williams, E. (1993). Use of weather radar for flood forecasting in the sieve river basin: A sensitivity analysis. *Journal of Applied Meteorology*, **32**, 462–475.

Petersen, W. A., Carey, L. D., Rutledge, S. A., Knievel, J. C., Doesken, N. J., and Johnson, R. H. (1997). Mesoscale and radar observations of the fort collins flash flood of 28 july 1997. *Bull Am Meteorol Soc*, **80**, 191–216.

Ponce, V. M. and Hawkins, E. R. H. (1996). Runoff curve number: Has it reached maturity? *J. Hydrol. Eng.*, **1**, 11–19.

Querini, R. (1977). L'influenza del terremoto sulla torrenzialità nei bacini montani del friuli (in italian). *Annali dell'Accademia Italiana di Scienze Forestal*, **26**, 139–185.

Rusjan, S., Kobold, M., and Mikos, M. (2009). Characteristics of the extreme rainfall event and consequent flash floods in w slovenia in september 2007. *Natural Hazards and Earth System Sciences*, **9**, 947–956. www.nat-hazards-earth-syst-sci.net/9/947/2009/.

Sanchez-Diezma, R., Zawadzki, I., and Sempere-Torres, D. (2000). Identification of the bright band through the analysis of volumetric radar data. . *J. Geophys. Res.*, **105**(D2), 2225–2236.

Sangati, M. (2006). Analisi e modellazione di piene improvvise in ambiente montano (in italian). *University of Padova, Dept. TESAF, unpublished report.*

Sangati, M. and Borga, M. (2009). Influence of rainfall spatial resolution on flash flood modelling. *Nat. Hazards Earth Syst. Sci.*, (9), 575–584. www.nat-hazards-earth-syst-sci.net/9/575/2009/.

Sangati, M., Borga, M., Rabuffetti, D., and Bechini, R. (2009). Influence of rainfall and soil properties spatial aggregation on extreme flash flood response modelling: an evaluation based on the sesia river basin, north western italy. *Advances Water Resources*, **32**(7), 1090–1106.

Saulnier, G. and Le Lay, M. (2009). Sensitivity of flash-flood simulations on the volume, the intensity, and the localization of rainfall in the cevennes-vivarais region (france). *Water Resources Research*, **45**. W10425, doi:10.1029/2008WR006906.

Schilling, W. (1991). Rainfall data for urban hydrology: what do we need? *Atmos. Res.*, **27**(1-3), 5–21.

Schuurmans, J. M. and Bierkens, M. (2007). Effect of spatial distribution of daily rainfall on interior catchment response of a distributed hydrological model. *Hydrology and Earth System Sciences*, **11**(2), 677–693.

Sekhon, R. S. and Srivastava, R. C. (1970). Doppler radar observations of rain drop distributions in a thunderstorm. *J. Atmos. Sci.*, **28**, 983–994.

Seo, D. J. and Breidenbach, J. P. (2002). Real-time correction of spatially nonuniform bias in radar rainfall data using rain gauge measurements. *J Hydrometeorol*, **3**(93-111).

Seo, D. J., Breidenbach, J. P., Fulton, R., Miller, D., and O'Banon, T. (2000). Real time adjustment of range dependent biases in wsr-88d rainfall estimates due to nonuniform vertical profile of reflectivity. *J Hydrometeorol*, **1**(222-240).

Serrar, S., Delrieu, G., Creutin, J. D., and Uijlenhoet, R. (2000). Mountain reference technique: Use of mountain returns to calibrate radars operating at attenuating wavelengths. *Journal of Geophysical research*, **105**(D2), 2281–2290.

Singh, V. P. (1998). Effect of the direction of storm movement on planar flow. *Hydrological Processes*, **12**, 147–170.

Sivapalan, M. (2006). Pattern, process and function: Elements of a unified theory of hydrology at the catchment scale, encyclopedia of hydrological sciences- part 1. theory, organization and scale.

Skoien, J. O., Merz, R., and Bloeschl, G. (2001). Top-kriging: Geostatistics on stream networks. *Hydrol. Earth Syst. Sci.*, **10**, 277–287.

Slymaker, O. (1988). The distinctive attributes of debris torrents. *Hydrol. Sci.*, **33**, 567–573.

Smith, J., Baeck, A. M. L., Steiner, M., and Miller, A. J. (1996a). Catastrophic rainfall from an upslope thunderstorm in the central appalachians: The rapidan storm of 27 june 1995. *Water Resour. Res.*, **32**(10), 3099–3113.

Smith, J. A. and Krajewski, W. F. (1991). Estimation of the mean field bias of radar rainfall estimates. *J Appl Meteor*, **30**, 397–412.

Smith, J. A., Seo, D. J., Baeck, M. L., and Hudlow, M. D. (1996b). An intercomparison study of nexrad precipitation estimates. *Water Resour Res*, **32**, 2035–2045.

Smith, J. A., Baeck, M. L., Zhang, Y., and Doswell Jr, C. A. (2002a). Extreme rainfall and flooding from supercell thunderstorms. *Journal of Hydrometeorology*, **2**(5), 469–489.

Smith, J. A., Baeck, M. L., Morrison, J. E., Sturdevant-Rees, P. L., Turner-Gillespie, D. F., and Bates, P. D. (2002b). The regional hydrology of extreme floods in an urbanizing drainage basin. *Journal of Hydrometeorology*, **3**(3), 267–282.

Smith, J. A., Seo, D. J., Koren, V. I., Reed, S. M., Zhang, Z., Duan, Q., Moreda, F., and Cong, S. (2004a). The distributed model intercomparison project (dmip): motivation and experiment design. *Journal of Hydrology*, **298**(1-4), 4–26.

Smith, J. A., Baeck, M. L., Meierdiercks, K. L., Nelson, P. A., Miller, A. J., and Holland, E. J. (2005). Field studies of the storm event hydrologic response in an urbanizing watershed. *Water Resour. Res.*, **41**(W10413, doi:10.1029/2004WR003712).

Smith, M., Koren, V., Zhang, Z., Reed, S., Pan, J., and Moreda, F. (2004b). Runoff response to spatial variability in precipitation: an analysis of observed data. *Journal of Hydrology*, (298), 267–286.

Stedinger, J. R., Voge, R. M., and Foufoula-Georgiu, E. (2002). Frequency analysis of extreme events. *Handbook of Hydrol.*, pages 18.1–18.66. D. R. Maidment, Ed., McGraw-Hill.

Steiner, M., Houze, R. A., and Yuter, S. E. (1995). Characterization of three dimensional storm structure from operational radar and rain gauge data. *J. Appl. Meteor.*, **34**, 1978–2007.

Sturdevant-Rees, P., Smith, J. A., Morrison, J. E., and Baeck, M. L. (2001). Tropical storms and the flood hydrology of the central appalachians. *Water Resources Research*, **37**(8), 2143 – 2168.

Syed, K., Goodrich, D., Myers, D., and Sorooshian, S. (2003). Spatial characteristics of thunderstorm rainfall fields and their relation to runoff. *Journal of Hydrology*, **271**, 1–21.

Tan, J., Holt, A. R., and Hendry, A. (1991). Bebbington dho. extracting rainfall rates from x-band cdr radar data by using differential propagation phase shift. *J Atmos Oceanic Technol*, **8**(790-801).

Tarolli, P., Borga, M., and Dalla Fontana, G. (2008). Analyzing the influence of upslope bedrock outcrops on shallow landsliding. *Geomorphology*, **93**, 186–200. doi:10.1016/j.geomorph.2007.02.017.

Trisic, N., Bat, M., Polajnar, J., and Pristov, J. (1997). Water balance investigations in the bohinj region. *Tracer Hydrology. Rotterdam*.

Tropeano, D., Turconi, L., and Sanna, S. (2004). Debris flow triggered by the 29 august 2003 cloudburst in val canale, eastern italian alps. *Proc. Int. Symp. INTERPRAEVENT 2004 Riva del Garda, Italy.*, pages 121–132.

Uijlenheot, R., Smith, J. A., and Steiner, M. (2003). The microphysical structure of extreme precipitation as inferred from ground-based raindrop spectra. *J. Atmos. Sci.*, **60**, 1220–1238.

Ulbrich, C. W. (1983). Natural variations in the analytical form of the raindrop size distribution. *J. Clim. Appl. Meteor.*, **22**, 1764–1775.

US-SCS (1986). Department of agriculture urban hydrology for small watershed. *U.S. Department of Agriculture Tech. Release*, **55**, 164 pp.

Viglione, A., Chirico, G. B., Woods, R., and Blöschl, G. (2010a). Generalised synthesis of 851 space-time variability in flood response: 1. analytical framework. *Journal of Hydrology*. Under review.

Viglione, A., Chirico, G. B., Komma, J., Woods, R., Borga, M., and Blöschl, G. (2010b). Generalized synthesis of space-time variability in flood response: Dynamics of flood event types. *Journal of Hydrology*. Under review.

Vignal, B. and Krajewski, W. F. (2001). Large sample evaluation of two methods to correct range-dependent error for wsr-88d rainfall estimates. *J Hydrometeorol*, **2**(5), 490–504.

Vignal, B., Andrieu, H., and Creutin, J. D. (1999). Identification of vertical profiles of reflectivity from voluminal radar data. *J Appl Meteor*, **38**, 1214–1228.

Vignal, B., Galli, G., Joss, J., and Germann, U. (2000). Three methods to determine profiles of reflectivity from volumetric radar data to correct precipitation estimates. *J Appl Meteor*, **39**, 1715–1726.

Villi, V., Caleffa, G., Gatto, G., and Mori, G. (1986). Distribuzione spazio temporale delle piogge intense nel triveneto cartografia. *Quaderni di ricerca C.N.R and Regione Veneto*, **7**, 1–444.

Vivekanandan, J., Yates, D. N., and Brandes, E. A. (1999). The influence of terrain on rainfall estimates from radar reflectivity and specific propagation phase observations. *J. Atmos. Oceanic Technol.*, **16**, 837–845.

Vivoni, E. R., Bowman, R. S., Wyckoff, R. L., Jakubowski, R. T., and Richards, K. E. (2006). Analysis of a monsoon flood event in an ephemeral tributary and its downstream hydrologic effects. *Wat. Res. Res.*, **42**. W03404, doi: 10.1029/2005WR004036.

Wainwright, K. M. J. (2002). Modelling the effects of hillslope channel coupling on catchment hydrological response. *Earth Surface Processes and Landforms*, **27**(13), 1441–1457.

Waldvogel, A. (1974). The n0 jump of raindrop spectra. *J. Atmos. Sci.*, **31**, 1067–1078.

Ward, J. V., Tockner, K., Edwards, P. J., Kollmann, J., Bretschko, G., Gurnell, A. M., Petts, G. E., and Rossaro, B. (1999). A reference system for the alps: The "fiume tagliamento.". *Regul. Rivers*, **15**, 63–75.

Wigmosta, M. S. L. W. and Lettenmaier, D. P. (1981). A distributed hydrology-vegetation model for complex terrain. *Wat. Res. Res.*, **30**, 1665–1679.

Willis, P. T. and Tattleman, P. (1989). Drop-size distributions associated with extreme rainfall. *J Appl Meteor*, **28**(3-15).

Wilson, C. B., Valdes, J. B., and Rodriquez-Iturbe, I. (1979). On the influence of the spatial distribution of rainfall on storm runoff. *Water Res. Res.*, (15(2)), 321–328.

Wilson, R. C. and Wieczorek, G. F. (1995). Rainfall thresholds for the initiation of debris flow at la honda, california. *Environ. Eng. Geosci.*, **1**(1), 11–27.

WMO (1994). (world meteorological organization) (1994): Guide to hydrological practices. *WMO-164, WMO, Geneva (5th edn), WMO-N.168, Geneva, Switzerland.*

Wood, E. F., Sivapalan, M., Beven, K., and Band, L. (1988). Effects of spatial variability and scale with implications to hydrologic modeling. *Hydrological processes*, **102**, 29–47.

Wood, E. F., Sivapalan, M., and Beven, K. (1990). Similarity and scale in catchment storm response. *Review of Geophysics*, **28(1)**, 1–18.

Woods, R. A. and Sivapalan, M. (1999). A synthesis of space-time variability in storm response: Rainfall, runoff generation and routing. *Water Resour. Res.*, **35**(8), 2469–2485.

Zhang, Y., Smith, J. A., and Baeck, M. L. (2001). The hydrology and hydrometeorology of extreme floods in the great plains of eastern nebraska. *Adv. Water Resour.*, **24**, 1037–1050.

Zrnic, D. S. and Ryzhkov, A. V. (1996). Advantages of rain measurements using specific differential phase. *J Atmos Oceanic Technol*, **13**, 454–464.

Zrnic, D. S. and Ryzhkov, A. V. (1999). Polarimetry for weather surveillance radars. *Bull Am Meteorol Soc*, **80**, 289–406.

Ringraziamenti/Acknowledgments

Ringrazio tutti quelli che hanno reso possibile questo lavoro, quelli che hanno lavorato insieme a me in questi anni e quelli con cui ho condiviso esperienze e fatiche.

Al chiudersi di un ciclo di lavoro e di vita è sempre bello e dal sapore agrodolce fare un bilancio di quello che si è fatto e di quello che si è vissuto, ricordare le difficoltà e le vittorie, le cadute e i successi, che per quanto piccole e limitate alla vita di ciascuno di noi, sono l'essenza e la sostanza che rendono la vita piena e ne fanno una piccola avventura quotidiana.

Certo ci sono state difficoltà, periodi meno felici e forse qualche arrabbiatura che non sono riuscito a far passare inosservata. Perdonino coloro cui erano rivolte le rare maleparole e siano comprensivi quelli che non sopportano gli improperi, anche a loro dico grazie. Grazie di aver sopportato, grazie della pazienza. Per tutti gli altri momenti, quelli belli, ringrazio per la partecipazione, per l'aiuto e per il supporto morale, intellettuale e materiale che ho ricevuto. Spero di essere stato un buon compagno di viaggio per tutti voi e di aver guadagnato la vostra stima.

Se mi volgo a guardare indietro e faccio scorrere la memoria lungo questi anni, posso vedere i volti di molte persone e di molti amici che hanno riempito la mia vita durante il mio "periodo Padovano". Spero che continiuate a farne parte e che col tempo l'amicizia cresca ancora. Non posso che essere felice di aver conosciuto e frequentato persone così speciali, non farò alcun nome; non ve ne è bisogno, sono certo che coloro che ringrazio sanno che queste parole sono per loro. Vi voglio bene,

Francesco